

An Integrated Method for Detection and Mitigation of Ice Accretion on Wind Turbine Blades

by
© Ezieddin Ahmed Madi
BEng, MEng

A thesis submitted to the School of Graduate Studies in partial fulfillment of the
requirements for the degree of

Doctor of Philosophy

Faculty of Engineering and Applied Science

Memorial University of Newfoundland

May 2023

St. John's, Newfoundland and Labrador, Canada

Abstract

Ice formation on structures, particularly on the leading edges of curved surfaces such as cylinders and airfoils, can be dangerous, and it is necessary to use an ice sensor combined with an ice mitigation system to prevent ice from forming on these surfaces. Wind turbine blades, which are commonly used in cold climate regions, are particularly susceptible to ice accumulation due to their sensitivity to changes in aerodynamic performance. To address this issue, it is necessary to have an integrated system for detecting and mitigating ice formation on wind turbine blades. Various ice detection and mitigation techniques for wind turbine blades in cold regions are reviewed and categorized based on key parameters. The conceptual design of integrating ice sensing and mitigation systems is also investigated, along with the advantages and disadvantages of these systems. A new technique for estimating the volume of frozen water droplets on a cold solid surface based on the contact angle and thermal images is presented. This technique takes into consideration factors such as temperature, surface roughness, and droplet size. An integrated ice tracking and mitigation technique using thermal imaging and heat elements along the stagnation line of a cylindrical surface is developed. This technique, which employs IR camera to monitor ice buildup, de-icing, and relaxation, is validated using an optical camera. The average uncertainty of ice thickness determined from thermal and optical images is about 0.16 mm during ice buildup and about 0.1 mm during ice mitigation, making it suitable for many cold environment applications. Finally, the relationship between ice thickness at the stagnation line and ice thickness at the heater edge is investigated in order to control ice accumulation mass and limit the heat energy required for de-icing. It is shown through de-icing experiments that the heat energy needed to remove the ice accumulation on the surface of a cylinder can be reduced by controlling the ice thickness at the heater's edge.

Acknowledgements

All praises are due to almighty Allah who has given me the opportunity and patience to complete this thesis. It is my honor to acknowledge several institutions and individuals for their contribution, guidance, and support throughout my Ph.D. journey.

First, I would like to offer my sincere thanks to my Libyan government for their financial support by offering me a scholarship to complete my Ph.D. program.

I would like to thank my supervisors (Dr. Kevin Pope and Dr. Weimin Huang) and supervisor committee member (Dr. Tariq Iqbal) for all their support, guidance, and encouragement throughout my program.

I would like to extend my thanks to the department of graduate studies at Memorial University for providing me with such a great opportunity to complete this work.

Lastly, I would like to thank my parents, wife, sons, daughters, brothers and sisters for their prayers, support, and encouragement. Special thanks to my wife whose efforts enabled me to make this journey. I also would like to thank my beloved sons and daughters for their patience and understanding.

Table of Contents

Abstract	ii
Acknowledgements	iii
Table of Contents	iv
List of Symbols & Abbreviations	vii
List of Figures	ix
List of Tables	xiii
Chapter 1: Introduction and Overview	1
1.1 Introduction and Motivations	1
1.2 Research Objectives	5
1.3 Research Contributions	6
1.4 Thesis Structure	7
1.5 References	9
Chapter 2: A Review of Integrating Ice Detection and Mitigation for Wind Turbine Blades.....	10
2.1 Introduction	11
2.2 Sensing of Ice Accretion on Wind Turbine Blades.....	13
2.2.1 Sensing Techniques Based on Reaction of Blade to Ice	13
2.2.2 Sensing Techniques Based on Reaction of a Signal to Ice.....	15
2.2.3 Sensing Techniques Based on Reaction of Electric Field Towards Ice	22
2.3 Ice Mitigation for Wind Turbine Blades	26
2.3.1 Thermal Ice Mitigation Techniques	27
2.3.2 Mechanical Ice Mitigation Techniques	34
2.4 Integrated Ice Sensing and De-icing Systems for Wind Turbine Blades	38
2.4.1 Integrated Systems Based on Hot Air Ice Mitigation Techniques:	38
2.4.2 Integrated Systems Based on Thermal Resistors Ice Mitigation Techniques:	39
2.4.3 Integrated Systems Based on Microwave Ice Mitigation Techniques:	40
2.4.4 Integrated Systems Based on Ultrasonic Ice Mitigation Techniques:	41
2.4.5 Integrated Systems Based on Flexible Boot Ice Mitigation Technique:	42
2.5 Conclusions	43
2.6 References	44

Chapter 3: Estimating the Volume of Frozen Water Droplets on A Cold Surface During the Phase Change With Thermal Image Processing	49
3.1 Introduction	50
3.2 The Relation of The Droplet Shape and its Contact Angle.....	56
3.3 Analyzing the Thermal Image of An Object.....	67
3.4 Experimental Method.....	73
3.4.1 Contact Angle Estimation and Equivalent Diameter Extraction Methods	76
3.4.2 Validation of the Estimated Results	79
3.5 Results and Discussion.....	80
3.6 Conclusions	105
3.7 References	106
Chapter 4: An integrated Ice Tracking and Mitigation System on the Stagnation Line of A Cylindrical Surface Based on Thermal Imaging and Electro-Thermal Elements.....	111
4.1 Introduction	112
4.2 The Theoretical and Practical Background	115
4.2.1 The Theoretical and Practical Background of the Ice Tracking Process.....	116
4.2.2 The Theoretical and Practical Background of the De-Icing Process.....	120
4.2.3 The Theoretical and Practical Background of the Relaxation Process.....	124
4.3 The Experimental Setup and Method.....	125
4.3.1 The Requirements of the Integrated System.....	126
4.3.2 The Experimental Setup	130
4.3.3 The Experimental Method	135
4.4 Processing and Analyzing the Thermal and Optical Images.....	136
4.4.1 The Image Processing Method for Tracking Ice Accumulation.....	136
4.4.2 The Image Processing Method for Tracking Ice Removal.....	139
4.4.3 The Validation Method.....	140
4.5 Results and Discussion.....	143
4.5.1 Ice Tracking Cycle.....	143
4.5.2 De-icing Cycle.....	149
4.5.3 Relaxation Cycle.....	155
4.5.4 The Integrated System	156
4.6 Conclusions	170
4.7 References	172

Chapter 5: A New Method to Limit Thermal Energy Required to De-Ice the Leading Edge of A Cylindrical Surface	176
5.1 Introduction	177
5.2 The Theoretical Background.....	179
5.3 Experimental Method.....	185
5.4 Results and Discussion.....	191
5.4.1 Ice Accretion.....	191
5.4.2 De-icing	197
5.5 Conclusions	209
5.6 References	210
Chapter 6: Conclusions and Recommendation	213
6.1 Summary and Conclusions.....	213
6.2 Recommendations for Future Studies	215
6.3 A List of Publications and Co-Authorship Statement.....	216
. Appendix A: Measurements and Uncertainty Analysis.....	217
Ice Thickness Along the Heater Edge (h_e)	217
Spatial Calibration Factor (SCF)	218
Ice Thickness Along the Stagnation Line (h_{SL})	220
Computing Ice Thickness Along the Heater Edge (h_e)	221
Computing Ice Mass (m_{ice})	223
Heater Power (P_{heater})	225
Heat Energy (Q).....	227

List of Symbols & Abbreviations

V_{sc}	Spherical cap volume in m^3
V	Droplet volume in m^3
$V_{droplet}$	Droplet volume in m^3
γ_{SA}	Gas-solid interfacial surface tension
γ_{SL}	Solid-liquid interfacial surface tension
γ_{LA}	Gas-liquid interfacial surface tension
CA, θ	Contact angle in ($^\circ$)
CA_{est}	Estimated contact angle in ($^\circ$)
CA_{mrd}	Measured contact angle in ($^\circ$)
h	Droplet height in mm
BM	Binary image
ROI	Image Region of Interest
ROI_{image}	Actual Region of Interest
ROI_{actual}	Actual Region of Interest
$ROI_{thermal}$	Thermal region of interest
$ROI_{optical}$	Optical region of interest
$ROI_{surface}$	Surface temperature ROI
T_{thr}	Threshold value
$Thresh$	Global threshold
SE	Constructing element
OS	Object Segmentation
SCF	Spatial calibration factor in ($pixel / mm^2$)
$CLAHE$	Contrast-limited adaptive histogram equalization method
$I(x, y)$	Input image
$Z(a, b)$	Output image
N	Number of objects
d_{eqv}	Equivalent diameter in mm

d_{mrd}	Measured base diameter in mm
$Area_{Object(i)}$	Area of object (i) in pixels
Ra	Surface roughness
CPT	Center point of tendency
IR	Infrared
GS	Droplet group size
LWC	Liquid water content
MVD	Median volumetric diameter
SP	Stagnation point
SZ	Stagnation zone
SL	Stagnation line
LE	Leading edge
T_{ref}	Reference temperature
$t_{respond}$	Time to respond
T_{avg}	Average surface temperature
T_{min}	Minimum Temperature
m_{ice}	Ice mass
L_{SL}	Length of SL
A_{ice}	Ice area at SP
Q	Heat energy
h_{SL}	Ice thickness at SL
h_e	Ice thickness at heater edge
ρ_{ice}	Ice density
P_{heater}	Heater power
t_{ice}	Icing duration
t_{de-ice}	De-icing duration
θ	Heating angle
R	Cylinder radius
V	Electric Voltage
R	Resistance

List of Figures

Figure 2.1 The principle of blade vibration ice sensing technique (modified from [11])	14
Figure 2.2 The schematic of Acoustic wave ice sensing technique (modified from [18])	16
Figure 2.3 A sketch of ultrasonic experimental set-up (modified from [20]).....	17
Figure 2.4 Microwave ice detector (modified from [26]).....	19
Figure 2.5 The principle of ice detector using OFDR (modified from [32]).....	20
Figure 2.6 Infrared ice sensing technique setup (modified from [39]).....	22
Figure 2.7 Capacitive ice sensing technique (modified from [42])	24
Figure 2.8 A sketch of impedance ice sensing technique, (modified from [48]).....	25
Figure 2.9 Heat resistance de-icing of wind turbine blades (modified from [51])	30
Figure 2.10 Hot air de-icing of wind turbine blades (modified from [57,60])	32
Figure 2.11 Schematic of a microwave ice remover for wind turbine blades (modified from [65])	33
Figure 2.12 The principle of flexible rubber boots de-icing technique (modified from [30]).....	35
Figure 2.13 A 3-D model of ultrasonic transducer in wind turbine blade (modified from [69,71])	36
Figure 3.1 A diagram of a droplet shape.....	56
Figure 3.2 A diagram of a spherical cap as part of a complete sphere.	57
Figure 3.3 Schematic representing a water droplet on a solid flat surface.	58
Figure 3.4 Droplet CAs on S.S-304 with different surface roughness- modified from [20].	60
Figure 3.5 The effect of base diameter of the droplet on the volume with fixed CA.	61
Figure 3.6 The effect of CA on the volume for various droplets' sizes.....	62
Figure 3.7 Illustration of the impact of the overall arithmetic mean of CAs on droplets' volume	63
Figure 3.8 The distribution of raindrops' frequency according to their group size. [37].	64
Figure 3.9 The distribution of CAs and droplet group sizes.....	65
Figure 3.10 A comparison of volume obtained by the group CAs and the overall mean.....	65
Figure 3.11 Wettability chart representing the relation of droplet shape and CA	67
Figure 3.12 The principle of latent heat energy released from deposited supercooled water droplets.....	68
Figure 3.13 A flowchart sketch of the involved image processing stages.....	69

Figure 3.14 A diagram for the actual ROI _{actual} plane and its corresponding ROI _{image} image plane	70
Figure 3.15 An illustration of the stages of a processed thermographic image.....	72
Figure 3.16 Calculating the equivalent diameter from a droplet's object.....	73
Figure 3.17 Thermal imaging experiment of droplets deposition on a cold surface	75
Figure 3.18 A photograph of a side view of a deposited droplet with a measuring tool	76
Figure 3.19 A comparison of actual droplet shapes with known shapes from surface wettability chart.....	76
Figure 3.20 Thermographic image and its image converted to greyscale, representing ROI.....	78
Figure 3.21 B/W image contains droplet's objects and its equivalent circle's images.....	78
Figure 3.22 Side view image for a droplet.....	79
Figure 3.23 Measured and estimated droplet profile diagrams.....	85
Figure 3.24 A comparison of measured volume and volume obtained by group CAs & d_{mrd}	86
Figure 3.25 A comparison of measured volume and volume obtained by group CAs & d_{eqv}	86
Figure 3.26 The thermal distribution map for a droplet deposited on a cold surface	87
Figure 3.27 Temperature versus time at two points of a droplet during its freezing process.....	88
Figure 3.28 The effect of thermal conductivity of the droplet's CA	89
Figure 3.29 Illustration of the effect of wind speed on droplet's CA	91
Figure 3.30 Experimental results of droplet shapes affected by different wind speeds	91
Figure 3.31 Illustration of the effect of inclined angle and gravity on droplet shape.....	93
Figure 3.32 Experimental example illustrating deposited frozen droplets with $\angle 90^\circ$ inclined angle.....	93
Figure 3.33 Most common droplet shapes formed on a surface.....	94
Figure 3.34 Converting elliptical shape to equivalent spherical shape.....	95
Figure 3.35 The equivalent shapes of the most common droplet shapes.....	96
Figure 3.36 Image processing stages of separating overlapped droplets from thermal image	98
Figure 3.37 The stages of estimating the average volume of rime/mixed iced droplet	100
Figure 3.38 Illustration of the work principle of the proposed method	103
Figure 3.39 Using the proposed method in an integrated system.....	104
Figure 4.1 Airflow around circular and airfoil objects	115
Figure 4.2 An illustration of ice profile shape around SP increments over time.....	116

Figure 4.3 Thermal distribution along A-B section	117
Figure 4.4 Thermal images show ice accumulation over time	118
Figure 4.5 The concept of the actual and image region of interests for an ice layer	119
Figure 4.6 Calculating the average ice thickness in pixels	120
Figure 4.7 An illustration of ice accumulation around SZ, A-thin layer, and B-thick ice layer. 120	
Figure 4.8 The changes of ice and warm regions over time at SL surface during de-icing	122
Figure 4.9 An illustration of the simplest morphological transformation method	123
Figure 4.10 Estimating the remaining ice region using morphological method.....	124
Figure 4.11 ROI _{surface} definition (A) and T _{avg} versus time during relaxation cycle (B).....	125
Figure 4.12 A block diagram of the hardware configuration of the integrated system	127
Figure 4.13 Schematic diagram of integrating IR ice sensing and electro-thermal ice mitigation	128
Figure 4.14 Flowchart of the process flow of the integrated system	129
Figure 4.15 Defining both regions ROI _{thermal} and ROI _{surface}	132
Figure 4.16 The experiment setup for the integrated system for ice tracking and mitigation	134
Figure 4.17 The steps of image processing algorithms used for processing thermal images.....	138
Figure 4.18 The steps of morphological transformation used for processing ice thermal images	140
Figure 4.19 The optical region of interest ROI _{optical} without ice (A), and with ice (B)	142
Figure 4.20 Measuring the average ice thickness within ROI _{optical} along with SL in Pixels	142
Figure 4.21 The average ice thicknesses measured from optical ice images versus time	143
Figure 4.22 The ice thickness increment over time (A).....	146
Figure 4.23 The ice thickness increment over time (B).....	147
Figure 4.24 Measured and estimated average ice thickness over time	148
Figure 4.25 The average ice thickness and average surface temperature versus time.....	149
Figure 4.26 Measured and estimated average ice thickness over time during de-icing	152
Figure 4.27 The average ice thickness and average surface temperature during de-icing	153
Figure 4.28 The decrement of ice thickness over time for both thermal and optical images	154
Figure 4.29 Tracking average surface temperature during relaxation	155
Figure 4.30 The complete system response for ice thick. 20 mm & ambient temp. -15 °C	158
Figure 4.31 The complete system response for ice thick. 8 mm and ambient temp. -5 °C	159

Figure 5.1 An illustration of ice profile shape increments with time	180
Figure 5.2 The effect of the ice thickness at heater's edge on de-icing process.....	181
Figure 5.3 The relation of the ice thicknesses at SP and heater's edge	183
Figure 5.4: Measuring average ice thicknesses along SL and at heater's edge	184
Figure 5.5: The experiment setup of managing heat energy needed for de-icing, top view.....	187
Figure 5.6: The experiment setup of managing heat energy needed for de-icing, side view	188
Figure 5.7: The hardware configuration required for ice buildup and de-icing.....	188
Figure 5.8: Measuring average ice thickness along SL using ROI (A) and at the heater edge (B)	190
Figure 5.9: Ice samples on leading edge of cylinder	192
Figure 5.10: Ice thicknesses at SL and heater's edge over time	196
Figure 5.11: The effect of ice thickness at heater's edge on the ratio of (R).....	200
Figure 5.12: Thermal and optical images describe the de-icing process using thermal elements	203
Figure 5.13: Ice thicknesses at both SL and heater's edge and the ratio of Q/m_{ice}	205
Figure 5.14: An example to predict the heat energy using the computed ice thickness at heater edge.....	206
Figure 5.15: The effect of the heating angle on the heating area above the LE surface.....	208

List of Tables

Table 2.1 The capabilities of ice sensors for WT blades	25
Table 2.2 Environmental impacts and installation consideration of ice sensors for WT blades ..	26
Table 2.3 A technical comparison for the studied ice mitigation techniques	37
Table 2.4 The applicability of Hot air ice mitigation technique with the studied ice sensing techniques	39
Table 2.5 The applicability of Thermal resistors ice mitigation technique with the studied ice sensing techniques	40
Table 2.6 The applicability of Microwave ice mitigation technique with the studied ice sensing techniques	41
Table 2.7 The applicability of Ultrasonic ice mitigation technique with the studied ice sensing techniques	42
Table 2.8 The applicability of Flexible boot ice mitigation technique with the studied ice sensing techniques	43
Table 3.1 A comparison between infrared ice detectors published in the literature.....	55
Table 3.2 The data of each group size	64
Table 3.3 A general comparison for the properties of material surface wettability	66
Table 3.4 The operating conditions of the experiment	74
Table 3.5 The droplet data of each group size	77
Table 3.6 Droplet volume based on image analysis of equivalent diameter and observed CA....	78
Table 3.7 Droplet volume based on measured droplet CA and diameter	80
Table 3.8 Droplet dimension uncertainties based on avera. of measured and estimated d & θ° ..	81
Table 3.9 Droplet volume uncertainties based on averaging of measured and estimated d & h ..	82

Table 3.10 The capabilities and limitations of the proposed method	102
Table 4.1 The setting of thermal camera FLIR E60	132
Table 4.2 The position and dimension of the ROI _{thermal} and ROI _{surface} in pixels.....	132
Table 4.3 The predefined setpoint and operating conditions values used in the experiments....	133
Table 4.4 The position and dimension of the optical region (ROI _{optical}) in pixels	141
Table 4.5 Ice thickness uncertainties based on averaging of optical and thermal values	148
Table 4.6 Ice thickness uncertainties based on averaging of optical and thermal values	152
Table 4.7 The system response comparison according to the two experiments' results	161
Table 4.8 The applicability of the proposed integrated system based on two studies	165
Table 5.1: Measured values of accreted ice samples	191
Table 5.2: A comparison between measured and computed values of h_e and their %error	194
Table 5.3: The ice sample data and the results of de-icing experiments	198
Table 5.4: The effect of the heating angle on the ice thickness near the heater's edge.....	208
Table 5.5: The effect of the ice thickness at heater edge on the de-icing efficiency	208
Table A.1: Measurements of ice thickness at heater edge (h_e) and its uncertainty (Δh_e).....	218
Table A.2: Samples of measuring average SCF and ΔSCF	220
Table A.3: Measurements of average ice thickness (h_{SL}) along SL and its uncertainty (Δh_{SL})...221	
Table A.4: The computed h_e and its uncertainty Δh_e based on the propagation of error.....	223
Table A.5: Ice mass (m_{ice}) and uncertainties for each ice sample.....	224
Table A.6: Measurements of V, I, and calculated P and ΔP for each sample.....	227
Table A.7: Heat energy (Q) and uncertainties for each sample.....	228

Chapter 1: Introduction and Overview

1.1 Introduction and Motivations

Ice formation on structures in cold regions can pose serious dangers [1, 2], especially on the leading edge (LE) of curved surfaces such as cylinder and airfoil surfaces [1, 2]. Wind turbines, for example, are one of the most common structures used to generate electricity from wind energy in cold regions. The front edge of the airfoil surface is particularly vulnerable to icing [3, 4]. Any slight change in the surface roughness of the airfoil will have a detrimental impact on the turbine's aerodynamic properties, and the aerodynamic characteristics of the airfoil's surface are extremely susceptible to ice buildup, which can cause serious damage [1].

To address this issue, an ice sensor associated with an ice mitigation system is necessary to prevent ice growth on the LE surface of the airfoil. Currently available airfoil ice sensors can only detect a few icing properties, such as the presence, type, mass, and rate of the icing event. Ice detection techniques are classified as indirect or direct. Indirect ice detection systems collect fresh data and compare it to previously recorded data to determine the quantity of ice accreted on the airfoil surface. These techniques are based on measuring the meteorological conditions that cause icing, such as air temperature, humidity, and wind speed, or on detecting the effects of icing. Direct ice sensing techniques, on the other hand, measure the change in properties caused by ice deposition on surfaces, such as mass, signal reflection, dielectric constants, inductance, and conductivities. In a study of 24 direct measuring methods, the most promising technologies were capacitance, ultrasonic signal, resonance, microwave signal, impedance, infrared, axial load, and hybrid measurement [5].

In the wind turbine industry, ice mitigation techniques are used to prevent ice buildup on the blades of the turbine. These techniques can be broadly categorized as active or passive. Active ice mitigation techniques are used to either prevent ice accumulation during icing occurrences or to eliminate accumulated ice following ice accretion. Active anti-icing techniques are energy-intensive, while de-icing devices are activated after ice is detected and remain active until the blade surfaces are clear of ice. Two types of de-icing methods are available: thermal and mechanical. Thermal techniques maintain the surface temperature above freezing using electrical heating elements, hot air blowing, or microwave electromagnetic energy. In contrast, mechanical ice mitigation techniques use mechanical energy from vibrations or mechanical motions of the surface, such as ultrasonic waves and flexible boots, to break up accumulated ice.

Several commercial ice mitigation methods and technologies are currently available in the wind turbine industry. The Vestas Anti-Icing System is a widely used commercial solution that uses a combination of passive heating and aerodynamic design to prevent ice buildup on the blades. LM Wind Power's Blade Heater uses a resistive heating element embedded within the blade to prevent ice buildup. De-icing coatings offered by several companies, including PPG Industries and NEI Corporation, can be applied to the blades to prevent ice buildup. GRT Genesis Icephobic Coatings is another ice-phobic coating technology that uses a proprietary blend of materials to prevent ice buildup on the blades. These commercial ice mitigation solutions offer a range of options for wind turbine operators to prevent ice buildup on the blades and ensure reliable performance in cold weather conditions.

One of the challenges in the field of ice sensing and mitigation is the identification of a suitable ice sensing technology compatible with a de-icing technology with comparable features that complement each other, such that the two can be integrated into a cohesive system. In [2], the ice

detection and deicing techniques are reviewed and, in order to develop an integrated system, each ice detection approach is compared to all de-icing methods. As a result, the infrared sensing approach has been deemed a promising technique because it is a non-destructive technology for remote ice detection and can be integrated with ice mitigation using thermal elements in the workplace without physical contact [2]. This finding motivated our interest in combining an infrared ice sensor with a thermal de-icing system.

It is generally known that an infrared camera can detect the heat signature produced by the deposition of supercooled water droplets on a cold surface. However, improving the capabilities of the infrared (IR) approach from only detecting ice to estimating its amount is another challenge, which motivated our interest in developing a new method based on two factors: the droplet's contact angle and the droplet base's diameter [7]. The proposed method can recognize and calculate the volume of a single droplet or group of frozen droplets as soon as they are deposited on a cold solid surface. The contact angle is determined beforehand, and the equivalent diameter is extracted from the thermal image of the droplet via image processing. The volume of the frozen droplet can then be predicted using information on the contact angle and diameter of the deposited frozen droplet. Evaluations suggest that droplet volumes are overestimated by approximately 19% on average.

Several studies have reported that the LE of the airfoil is the part most prone to ice buildup [3, 4]. The process of ice accumulation often occurs around the stagnation zone (SZ), where the maximum amount of accumulated ice mass is located [8-11]. This means that the ice profile shape will roughly resemble the shape of the airfoil's curved surface. Over time, the ice profile turns into an elliptical shape on the LE of an airfoil surface [12-14].

Multiple studies have demonstrated that the temperature distribution and accreted ice along the leading edge (LE) surface evolve over time as ice accumulates [15, 16]. This evidence inspired our desire to expand upon previous research [7] and develop a method for tracking and measuring the thickness of ice accumulation on the stagnation line (SL) of a round surface using processed thermal images.

While our previous study indicated that the integration of an infrared ice sensor with thermal resistance as a de-icing technology is a promising approach [2], a significant challenge is the development of an integrated system that can track and measure ice not only during its accumulation process, but also during its removal process. During the de-icing process, the thermal resistance generates heat that diffuses into the ice, causing it to break, loosen, and fall off in thin areas, leaving a warm region behind [17]. As time passes, more heat diffuses into thick ice regions, causing the ice to disintegrate and shed [17], and the warm region expands while the ice region shrinks. From the perspective of image processing, the warm region is the bright region where the surface becomes ice-free. The cold region is the dark region, along the SL, where ice still exists. The warm region (bright region) gradually spreads across the SL surface, and the entire surface becomes ice-free. This means that the current ice region (dark region) complements the current warm region (bright region), and warm region information can be used to estimate the present dark ice region. This motivated our interest in developing an integrated technique based on processed thermal images to measure ice decrement during ice mitigation on the SL surface.

In previous research [18], it was found that as the thickness and area of the ice layer on the leading edge (LE) surface increase, the adhesion strength of the ice to the LE surface also increases, requiring more heat energy to weaken and remove it. The thicknesses of the ice at both the stagnation line (SL) and the heater edge are correlated, such that an increase in the ice thickness at

the heater edge leads to an increase in the amount of heat energy required for de-icing. This finding motivated our interest in developing a geometric correlation between the elliptical shape of the ice accumulation on a cylinder surface and the circular shape of the cylinder surface, which may be used to calculate the unknown value of ice thickness at the edge of the heater using the known value of ice thickness at the stagnation line (SL). The aim of the study is to investigate the effect of ice thickness at the heater's edge on the amount of heat energy needed to remove the ice and verify that the correlation between the ice thickness at the stagnation line and ice thickness at the heater's edge can assist in managing the ice thickness at the stagnation line within the confines of ice thickness at the heater's edge, thereby regulating the accumulation of ice mass and modifying the heat energy required for de-icing.

1.2 Research Objectives

The primary goal of this thesis is to design and implement an integrated system for detecting and mitigating ice. In order to fulfill this overarching objective, the following specific objectives have been identified:

1. Investigate and compare various ice sensing and de-icing approaches on airfoil surfaces in order to identify an ice sensor and deicer with the necessary characteristics for integration into a system for interactive ice detection and mitigation, with the aim of improving their performance and efficiency.
2. Develop a thermal imaging technique that goes beyond simply detecting the presence of ice to quantifying its amount and demonstrating this experimentally.
3. Create image processing algorithms to track ice accumulation on the airfoil surface using sequential thermal imaging of the ice accumulation process, in order to measure the thickness of the ice on the surface.

4. Use image processing and the bitwise image transformation approach to track the removal of accumulated ice on an airfoil surface during the thermal de-icing process.
5. Construct an integrated system based on an infrared thermal camera, electro-thermal elements, data acquisition, and MATLAB code, in order to track and measure the thickness of accumulated ice on an airfoil surface's stagnation line for both ice buildup and ice removal.
6. Develop a technique to be used in conjunction with the integrated system for managing the accumulated ice mass on the surface of the stagnation zone, in order to reduce the amount of electricity required for the de-icing process.

1.3 Research Contributions

The aim of this thesis is to investigate and develop an integrated method for monitoring ice accumulation and de-icing operations using thermal imaging, image processing, and thermal components. This method will be implemented through a series of experiments and analysis to demonstrate its effectiveness and practicality. The findings of this research will significantly contribute to the development of advanced techniques for the effective management of ice accumulation on surfaces, a pressing concern within the realm of the power industry utilizing wind turbines in cold climates. The primary focus of this research is to achieve the following research contributions:

1. Review the literature on integrating ice detection and mitigation based on their conceptual functional design, with the goal of adding value to existing ice detection and mitigation technologies.
2. Expand the capabilities of the IR technique from simply detecting ice to quantifying its amount, making a contribution to remote ice sensing methods.

3. Use experimental investigation to demonstrate the effectiveness of thermal imaging in detecting the presence of ice and extracting relevant information, as well as the ability of image processing to assess, compare, and track variations across sequential thermal images.
4. Adapt the IR camera and heat elements to operate in an integrated ice sensing and mitigation system that can track and control ice loads, providing a novel contribution to ice detection and mitigation methods.
5. Explore the integration of infrared thermography with heat elements for accurate, direct detection and mitigation of ice on a surface, and develop a computational technique for this purpose.
6. Investigate the performance of the integrated system without human interference and examine its ability to control de-icing using temperature and thermographic images.
7. Investigate the experimental and computational methodologies utilized for developing a closed system that integrates heat elements, IR camera, and image processing techniques.
8. Develop a method to be used with the integrated system to manage the accumulated ice mass on the surface of the stagnation zone in order to reduce the consumption of electric power required for the deicing process.

1.4 Thesis Structure

Chapter 1 provides an introduction to the research, including the objectives of the study and the research motivation. The chapter also outlines the structure of the dissertation.

Chapter 2 is a review of the current approaches for detecting and mitigating ice on wind turbine airfoil surfaces. The chapter presents a comparison of the various techniques, including

their benefits and drawbacks, as well as a discussion of the conceptual design of integrating ice detection and mitigation approaches.

Chapter 3 presents a novel method for estimating the volume of a frozen water droplet on a cold solid surface using the contact angle and thermal imaging. The chapter also discusses the variables that can affect the contact angle, such as temperature, surface roughness, and droplet size, and describes a thermal image processing method for tracking and calculating the equivalent diameters of a group of frozen droplets on a cold surface.

Chapter 4 focuses on the development and implementation of an integrated ice tracking and mitigation system based on thermal imaging and heat elements along a cylindrical surface's stagnation line. The chapter describes the techniques for tracking and measuring ice buildup during an ice event, as well as ice decrement during de-icing, using sequential thermal images and image processing algorithms. The chapter also includes a validation method for the optical camera.

Chapter 5 presents an investigation and design of a strategy for managing ice mass accumulation on a cylindrical surface's stagnation zone in order to reduce the heat energy required for de-icing. The chapter discusses the relationship between ice thickness at the stagnation line and ice thickness at the heater edge, using the geometry of the cylinder's circular form and the elliptical shape of the ice developed above the cylinder surface. The chapter also includes a method for tracking the increase in ice thickness at the heater edge in relation to the increase in ice thickness at the stagnation line, as well as an experimental technique for applying the derived strategy.

Chapter 6 concludes the research with a summary of the findings and contributions, as well as suggestions for future work. The chapter also reflects on the learning and contributions of this research towards improving the design of ice detection and mitigation systems.

1.5 References

- [1] Technical Research Centre of Finland (VTT). Wind energy growing strong in cold climates. Clean Technica, <https://cleantechnica.com/2013/05/30/wind-energy-growing-strong-in-cold-climates/> ; 2013 [accessed 10 Dec. 2017].
- [2] E. Madi, K. Pope, and W. Huang, T. Iqbal. A review of integrating ice detection and mitigation for wind turbine blades. *Renew. Sust. Energ. Rev*; 2019; 103:269-281.
- [3] Thomas, S. K., Cassoni, R. P., & MacArthur, C. D. Aircraft anti-icing and de-icing techniques and modeling. *Journal of Aircraft*; 1996; 33(5), 841-854.
- [4] Kibler, Elijah Mendoza. Determination of adhesive strength and freezing rate of ice on aircraft structures at subcooled temperatures. 2013. Theses. 297.
- [5] Homola M, Nicklasson P, Sundsbo P. Ice sensors for wind turbines. *Cold reg sci technol* 2006; 46:125-131.
- [6] Andersen E, et al. Report: Wind power in cold climate. *Nordic energy research*; 2011.
- [7] E. Madi, K. Pope, and W. Huang. Estimating the volume of frozen water droplets on a cold surface during the phase change with thermal image processing. *Measurement*; 2021;183:109907.
- [8] Pierre Lavoie. Modeling of thin water films on swept wings in icing condition. 2017; Thesis. Université de Montréal.
- [9] Anderson, John D. *Fundamentals of aerodynamics*. 4th Edition. New York: McGrawHill, 2007.
- [10] A. Ebrahimi. Atmospheric icing effects of S816 airfoil on a 600 kW wind turbine's performance. *Scientia Iranica B*; 2018; 25(5), 2693-2705.
- [11] Fortin, G. and Perron, J. Wind turbine icing and deicing. AIAA 2009-274, Orlando, Florida: 47th AIAA. Aerospace Sciences Meeting; 2009
- [12] M. Bragg, A. Broeren, H. Addy, M. Potapczuk, D. Guffond, and E. ontreuil. Airfoil ice-accretion aerodynamic simulation. in 45th AIAA Aerospace Sciences Meeting and Exhibit, p. 85, 2007.
- [13] D. Switchenko, W. G. Habashi, G. Baruzzi, and I. Ozcer. Fensap-ice simulation of complex wind turbine icing events, and comparison to observed performance data. in 32nd ASME Wind Energy Symposium; p. 1399, 2014.
- [14] Pedersen, M. C. *Modelling Icing on Structures for Wind Power Applications*. Ph.D. thesis. Aalborg University, Denmark; 2018
- [15] Liu, Yang & Waldman, Rye & Hu, Hui. An experimental investigation on the unsteady heat transfer process over an ice accreting NACA 0012 Airfoil; 2015; 10.2514/6.2015-0035.
- [16] Virk, Muhammad & Ghani, Rizwan. Experimental study of atmospheric ice detection on wind turbine blade using thermal infrared technique. *Wind Engineering*. 2013; 7: 71-78.
- [17] Peter Suke, B.Eng. Analysis of heating systems to mitigate ice accretion on wind turbine blades. Master thesis. McMaster University. 2014.
- [18] E. Madi, K. Pope, and W. Huang. An integrated ice tracking and mitigation system on the stagnation line of a cylindrical surface based on thermal imaging and electro-thermal elements. *Journal of Measurement*; 2022; 199: 111539, 2022.

Chapter 2: A Review of Integrating Ice Detection and Mitigation for Wind Turbine Blades*

* *The materials in this chapter were published in Renewable and Sustainable Energy. Rev; 2019; 103:269-281. Authors Ezieddin Madi, Dr. Kevin Pope, Dr. Weimin Huang, and Dr. Tariq Iqbal all contributed significantly to the paper. Madi led the research process, while Pope and Huang played a pivotal role in the research and provided supervision and editing support. Iqbal provided general guidance and support to the team.*

2.1 Introduction

The demand for wind energy is rising dramatically in cold climate regions of the world. According to a study, 323 GW of power will be extracted from wind energy in Europe by 2030 [1]. Also, it is expected that a total of 23 GW of cumulative wind energy capacity will be generated by wind turbines in Canada by 2035 [2]. The sparse population and favorable wind conditions of cold climates provide a strong potential for wind power development. These regions are exposed to very strong winds and high cold air density, and these can be considered as advantages to extract a greater capacity of energy [3]. Canada's northern regions are considered one of the greatest resources of wind energy in the world, especially in sites with harsh cold weather. Canada has a target of more than 10 GW of wind power production before 2020, with 90% of new installations designated for cold climate regions [4]. Many wind turbine manufactures state on their turbine specifications that operating temperature thresholds can go as low as $-20\text{ }^{\circ}\text{C}$, while other manufactures state the range of operating temperature thresholds can go as low as $-30\text{ }^{\circ}\text{C}$, and structural ranges as low as $-40\text{ }^{\circ}\text{C}$ [4].

Turbine blades are highly susceptible to icing [5]. Any small change in the blade surface roughness will negatively affect the turbine's aerodynamic characteristics, even slight icing. A heavy icing event can cause a complete turbine shutdown. Furthermore, the period for which ice remains on the turbine can last longer than the period of ice accumulation if the air temperature stays below the freezing point of water. A research project [6] analyzed 517 wind turbines which produced 682 MW and discovered that in 29 months there was a loss of 18,966 MWh of the total produced power because of turbine blades icing. Conversely, ice accretion can cause overproduction of power output by changing the blades' profile. Excessive operation beyond the design limits puts the wind turbine at a risk of collapse and can reduce the lifespan of generators, bearings and gear boxes. Furthermore, the irregular detachment of ice from blades' surfaces can

result in uneven loads on the wind turbine as a result of mass imbalances. Additionally, falling ice from the blades can threaten public safety, especially when the turbines are installed in populated areas [5].

To reduce aerodynamic degradation, an ice removal system integrated with an early ice detection device is needed to effectively operate wind turbines in cold climates. However, ice detection techniques currently available in the market tend to be inefficient and unreliable for wind turbines [6, 7]. Typical ice sensors can detect only a few icing parameters, such as the presence, type, mass and rate of the icing event. The ice detection techniques can be divided into indirect and direct techniques.

The principle of indirect techniques for ice detection involves gathering new measurements and comparing them with previously recorded measurements. The compared result determines the amount of accumulated ice on a blade surface. These techniques are based on the measurement of weather condition parameters that lead to icing, which include air temperature, humidity and wind speed; or recognizing the impacts of icing. Indirect techniques include the difference between produced and designed power, the difference in measurements of heated and unheated anemometers, ambient temperature and dew point, as well as the direct measurement of liquid water content and mean volume droplets [7].

The direct techniques of ice-sensing depend on measuring the change in properties resulting from ice deposition on surfaces, such as mass, signal reflection, and the constants of dielectric substances, inductance and conductivities. In an investigation of twenty-four direct measurement methods, the most promising techniques were capacitance, ultrasonic signal, resonance, microwave signal, impedance, infrared, axial load and hybrid measurement [7]. Direct ice measurement techniques for wind turbines are categorized into two types: nacelle-based and

blade-based [8]. Ice measurements which are performed on the nacelle produce faulty results, due to an uneven amount of deposited ice along the blade surface and across other blades' surfaces. These measurements provide overestimated values [9].

Relying on blade measurement for ice sensing is necessary to maintain the efficiency of wind turbines in icing conditions [7, 8]. Nacelle-based methods measure instrumental icing, which represents a single point measurement and does not accurately represent the blade surface conditions. Therefore, these measurements have a high degree of uncertainty compared to the operational requirements of the turbine. The blade's tip rotates much higher than the height of the nacelle, which makes the blade more likely to come into contact with clouds and icing conditions. The blade's tip has a different structural design and during operation, unlike the other stationary parts of the turbine, it faces stresses and vibrations from the environment.

2.2 Sensing of Ice Accretion on Wind Turbine Blades

In this chapter, direct techniques to detect / monitor ice on the blade surface are reviewed. The techniques are categorized in the following way: based on their reactions to ice, including (i) reaction of the wind turbine blade to ice, (ii) reaction of a signal to ice, and (iii) reaction of an electric field to ice.

2.2.1 Sensing Techniques Based on Reaction of Blade to Ice

Wind turbine blades are airfoil structures that typically vibrate within the limits of their *natural frequencies* and should not exceed specified limits [14]. Ice accumulation and its distribution on blades is not uniform, due to the varied blade surfaces and the different stages of icing events. Ice mass on the blade reduces natural frequencies of the blade and raises the risk of resonance. This deviation in natural frequencies can be used to monitor ice growth on a blade surface [10, 11]. Typically, when blade vibration surpasses the normal rate, the changes in

frequencies are analyzed and the amount of mass added to the blade surface is calculated; then, a control system takes over the turbine stoppage and triggers the de-icer to remove ice from the blade surface [14]. The principle of this technique is illustrated in Figure (2.1).

The advantages of this technique are that it can detect the change of ice mass on the blade surface and that the sensor device is protected against lightning because it is installed inside the blade. However, disadvantages such as blade vibration during heavy icing events that can cause a loud noise might cause interference with measured data [13]. The sensor does not work properly when the wind turbine is stalled or when the wind is absent or below wind turbine cut-in speed. Also, wind turbulence might disturb the measurement data of the sensor and give incorrect readings and its sensitivity is very low, because it does not activate until an ice layer reaches a preset value [7, 12]. Moreover, the sensor does not sense the presence of ice, but changes of a substance's mass, which means the substance could be absorbed water or a leaked liquid from the turbine to blade surface [15]. The applications of this sensing technique have two statuses (ice, no ice) which make their reaction to heavy ice events very slow [14]. For these reasons, this technique might not work properly in applications that require fast interactions and integrated systems. Tables (2.1) and (2.2) present an overview of ice sensing techniques for wind turbine blades.

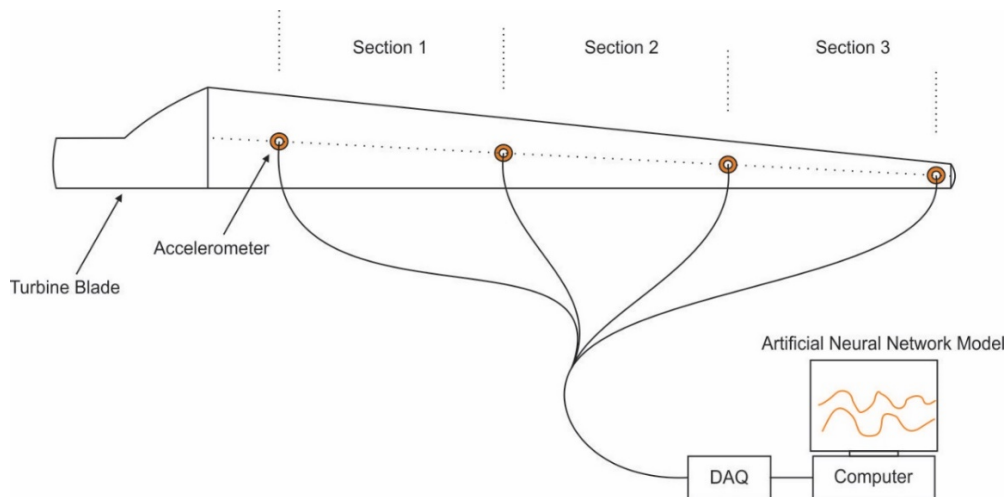


Figure 2.1 The principle of blade vibration ice sensing technique (modified from [11])

2.2.2 Sensing Techniques Based on Reaction of a Signal to Ice

Transmitting or propagating a signal into an ice layer on the blade surface will cause some of the signal to be absorbed by ice or attenuate into ice, and the rest of the signal will reflect. Therefore, by using this signal reaction to ice, the sensor can detect ice presence, thickness and type of ice on a blade surface. This technique will be highlighted through the study of some signal cases done with an iced blade, such as acoustic waves ice sensing, ultrasonic waves ice sensing, microwave ice sensing, optical ice sensing and thermal infrared ice sensing.

The second studied ice sensing technique uses an *acoustic wave* as a mechanism for ice detection. Typically, *acoustic waves* are generated by piezoelectric devices and propagated through the blade surface. The propagated acoustic waves are measured by accelerometers attached along the blade surface. As ice accumulates on the blade surface, the velocity of propagated waves and the amplitude are changed. By measuring the amplitude attenuation and phase shift of the propagated waves and then applying frequency analysis and algorithms, both ice and water can be detected, as well as distinguished [16, 18]. The principle of this technique is illustrated in Figure (2.2).

This technique has a high sensitivity to mass accretion, and might be an applicable sensor for onset ice [7]. It has wide applications in the telecommunications industry, which means it may be used for further investigation in wind turbine applications [16]. However, the compressional waves, which are created by liquids, have excessive influence on the attenuation of the acoustic waves, which could affect the system's sensitivity [16]. Attenuation and propagation velocity are affected by the piezoelectric substrate material; thus, it is carefully selected [16]. Furthermore, the detection operation is very complicated, maintenance and accessibility are extremely difficult [17] and the system response is negatively affected by the flickers caused by water [17]. The airfoil

shape of the blade structure limits the capability of the technique to be used in such applications. A final disadvantage is the complicated process required to calibrate the sensitivity of the sensor [17].

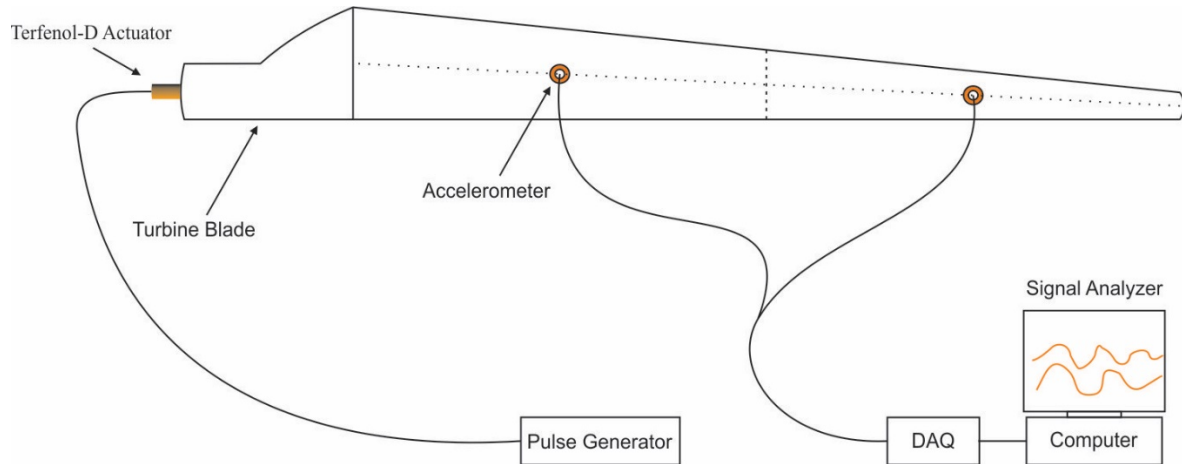


Figure 2.2 The schematic of Acoustic wave ice sensing technique (modified from [18])

In principle, propagation and reflection of *ultrasonic waves* into different mediums have different time delays due to the fact that the amplitude attenuation and phase shift of the ultrasonic waves are affected differently in different materials [22]. Ultrasonic waves propagated to and reflected from ice layers can be used to detect icing by measuring the attenuated amplitude of the reflected waves [19]. The technique, shown in Figure (2.3), consists of two ultrasonic transducers, a signal generator, a signal receiver and a discriminator. The measured amplitude is analyzed by the discriminator to determine the presence of ice. The ice sensor is not sensitive to dry air or water [20]. The desired sense accuracy of the detector to the thickness of the ice is determined by selecting and tuning the appropriate frequency range of the ultrasonic waves [20].

One advantage of an ultrasonic technique is that the ice thickness can be measured accurately [19]. Another advantage is that it can be adapted to the blade surface [23]. This

technique has several disadvantages, such as that the difference in mass between blade layer and ice layer might lead to low sensitivity of ice sensing [7]. The sensor mounting method could affect blade structure negatively. The technique has a low limit of sensing coverage due to the difference between its local sensing ability compared with the large area of the blade surface [21]. The thin accreted ice layers may cause a saturated status in the sensor which then gives continuous false signals that could negatively affect the system's reliability [19]. Furthermore, the surrounding noise which is produced by internal turbine equipment might lead to false measurement readings which could lower the system's sensitivity and reliability [22]. The temperature has some influence on wave propagation velocity and this relation is subject to frequency ranges, where temperature has a less significant effect on the low frequencies' range than the high frequencies' range [23]. High frequencies vanish quickly in long blades and adding other sensing devices to cover the whole blade surface could lead to a blade overweight [24]. Turbulent wind speeds and harsh climates have effects on surface smoothness which can scatter ultrasonic waves [25]. Also, the presence of the gas bubbles in the water or ice can scatter the waves [25].

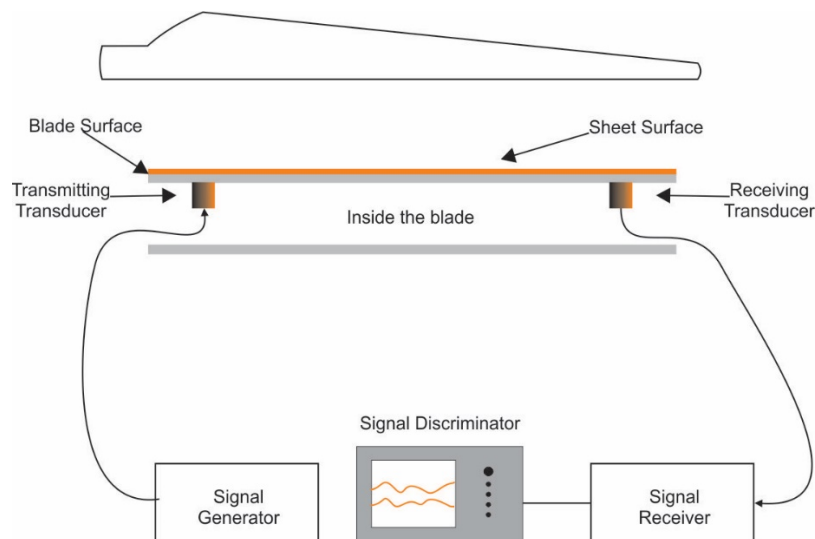


Figure 2.3 A sketch of ultrasonic experimental set-up (modified from [20])

The principle of the *microwave ice detection technique* is that the impedance and reflection parameters of the waveguide are affected by the change of ice accumulation on the waveguide surface [30, 31]. Secondly, the coefficients of reflected microwave signals are not the same for water and ice and can be differentiated [27]. The measurement of ice parameters, including type, rate and thickness, can be performed by applying the appropriate spectroscopy range of microwave signals [28]. Therefore, by applying specific algorithms to the measured data, the result will be a discrimination between water and ice, as well the identification of the ice type [29, 30]. In general, microwave electromagnetic energy which is transmitted into an ice layer and the characteristics of the returned signal are used to monitor and measure the presence and mass of accumulated ice. The apparatus of this technique, illustrated in Figure (4.4), includes a microwave electromagnetic energy generator, a coupling for propagating the microwave energy into a surface layer of ice and a reflectometer for monitoring the microwave energy transmitted to and reflected from the ice layer [26].

The benefits of this technique are that its sensitivity of detection is high [7]; it can also detect ice presence on the blade surface [29] and the sensor can be mounted or embedded inside the blade surface, which can increase its protection against lightning [29]. The disadvantages of this technique are that it is difficult to mount on a non-flattened shape, such as a wind turbine blade surface, so its suitability for wind turbines is not clear [7]. The airfoil shape is a drawback to the internal reflection performance and mounting the device and its elements, especially the waveguide, presents another challenge [31]. Other drawbacks are that its coverage area along the wind turbine blade surface is limited, due to its principal structure and that its weight may affect the airfoil structure of the blade [31]. The surrounding signals can cause faulty measurements. Accessibility and maintenance requirements could also lead to an unsuccessful system [30].

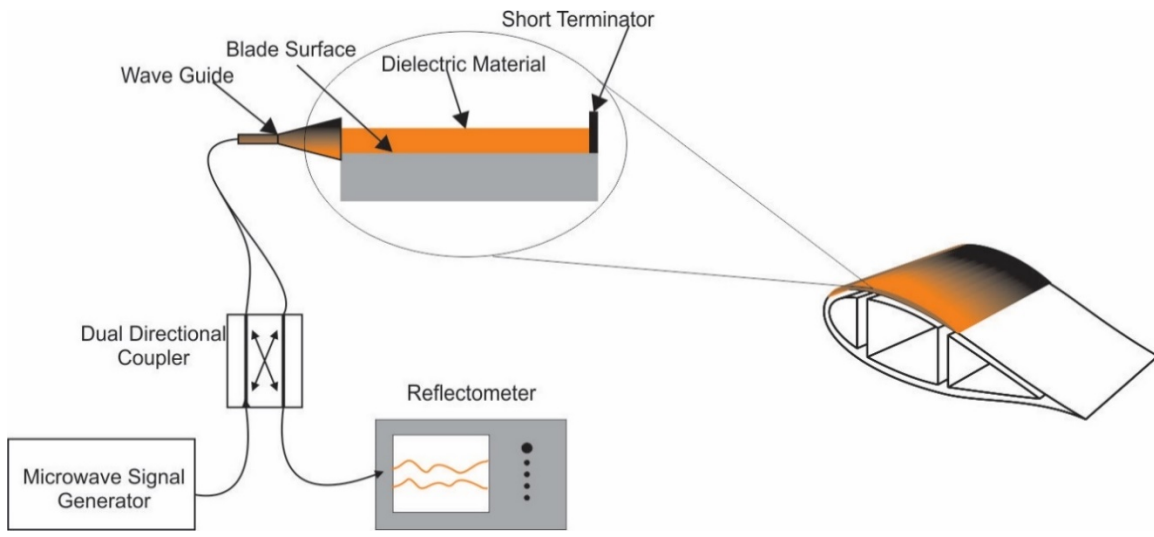


Figure 2.4 Microwave ice detector (modified from [26])

The principle of the *optical frequency-domain reflectometry* technique can be expressed as the interaction between photons of light and the phases of water molecules [36]. This property can be used to measure ice accretion on a wind turbine blade surface by applying an optical signal normal to the surface where its reflection shows the ice presence, thickness and type. The design, as illustrated in Figure (2.5), shows the system configuration [32]. In this technique, a continuous laser light with a swept frequency from a tunable laser is applied through optical fibers to optical sensors, which are mounted and distributed on the blade surface. Accreted ice on the blade surface will reflect a specific quantity of light that interferes with a reference tool. The interference edges of the laser signal which sweeps the blade surface are measured and then the delay of the signal's journey and the amplitude are calculated. Different ice types and thicknesses are deduced using the refractive index and scattering of the ice, which results in distinctive reflectivity profiles with ice depth. The detector in this technique can differentiate between air, water, rime ice and glaze ice [32].

The main feature of this technique is its accuracy of detecting the presence of ice within the sensing element location. Other features include an ability to distinguish ice type and the capability of measuring ice thickness [32, 34]. The sensing element also has a low weight, a small size and modern technology [33]. It has a high sensitivity, a fast response, a high resolution, and can cover long distances without signal loss. It is not affected by surrounding signals or by lightning and has a low power consumption [35, 37]. Furthermore, the technique's durability makes the sensor less subject to failure [34, 35]. With this technique, many sensors can be embedded in a single array, multiplexed on a single fiber, and can read the output signals using a single pulse [34, 35]. The drawbacks of this technique are its high cost and commercial unavailability [34, 35]. The technique can be adapted for the blade of a wind turbine and offers an acceptable capability to measure some properties of ice accumulation, such as detection of the presence, type, thickness, location and rate of accumulation of ice on a blade surface.

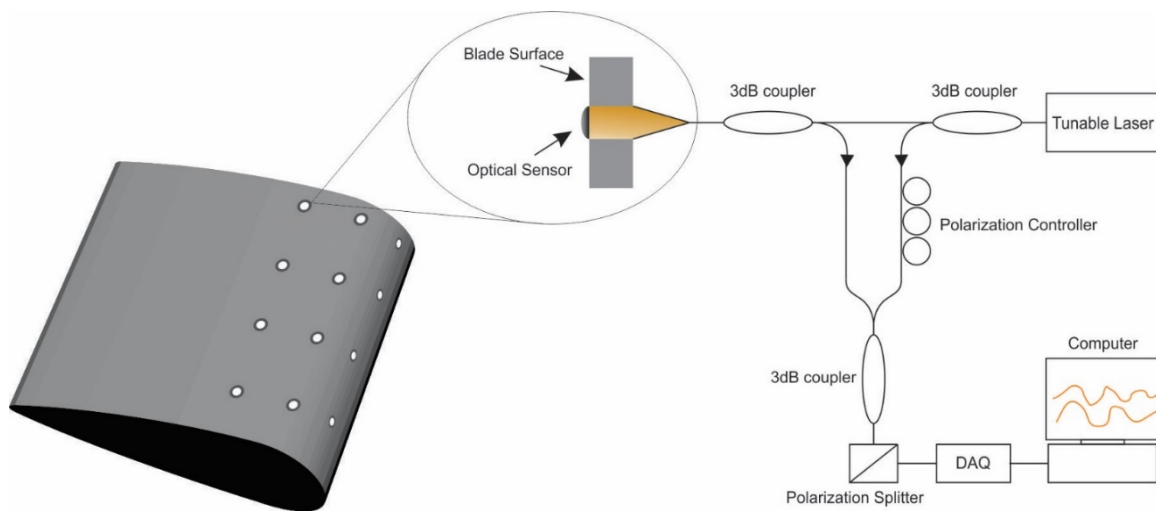


Figure 2.5 The principle of ice detector using OFDR (modified from [32])

The working principle of the *infrared thermography ice sensing technique* is that an electromagnetic wave signal, which is emitted or reflected by the blade surface, is received and then analyzed by the sensor device [39]. Measurements gathered by sensing elements form a map of temperature variations. Each pixel is analyzed by imaging software and converted to temperature [40]. The thermal infrared sensor, illustrated in Figure (2.6), which is mounted at a circular field view of 22° with the white blade surface, detects the emitted radiometric temperature from the white surface of the turbine blade. This technique has non-invasive measurements and can be used to instantaneously examine the situation of the blade surface. The emissivity change occurs on a surface and when ice is present, the emissivity value becomes low [39]. The technique has several benefits, including remote sensing, fast response, high resolution, wide range, high sensitivity, high accuracy, no physical contact and the ability to measure many points within a covered area simultaneously [38, 40]. Also, it can detect ice presence and differentiate between types and conditions of ice [39]. The disadvantages include the accuracy of the measured temperature, which might be affected by ambient temperature, the surface material, which has a very low emissivity that is able to reflect the radiation of the nearby objects, daylight and weather conditions, which might cause major effects on the emissivity [38]. Furthermore, wind speed and blade movement could have significant impacts on the measured data and its accuracy. To sum up, the thermal infrared sensor can only detect ice presence and its location with limited surface coverage, due to the limitation of its angle view with respect to the blade surface area. Also, it is considered the simplest technique for installation and retrofitting, compared to other techniques.

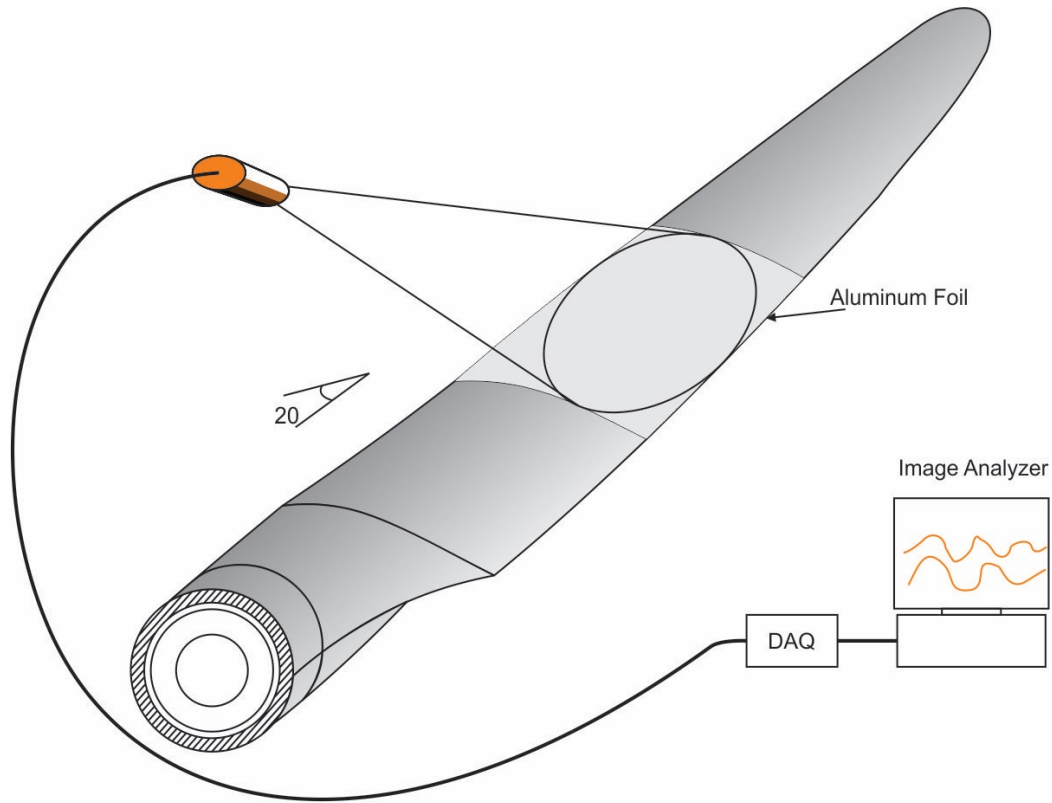


Figure 2.6 Infrared ice sensing technique setup (modified from [39])

2.2.3 Sensing Techniques Based on Reaction of Electric Field Towards Ice

The electrical properties of ice have been used to measure the presence and thickness of ice on a surface. Capacitive ice sensing elements produce an electrical field to measure the presence of dielectric substances. The sensor's element is surrounded by electrical field radiations and when a dielectric substance approaches and interrupts the field, the capacitive value of the sensor's element changes, a property that allows measurements without physical contact. The impedance sensing technique and capacitive sensing technique are very similar to one another, but the former technique is designed for current measurement, while the latter is designed for voltage measurement [41]. In this chapter, capacitive ice sensing and impedance ice sensing are reviewed.

A *capacitive sensor* generates an electrical field, which is used to sense the presence of dielectric substances that enter the field region. Change in dielectric material will cause a change

in capacitance. This property is used to determine ice presence, thickness and location [42]. The design in Figure (2.7) represents the basic configuration of the capacitive sensing technique. It consists of two capacitive sensors, a temperature sensor, two capacitive measuring circuits, a temperature measuring circuit, dividing circuit, dual timer and low pass filter [42]. Multiple capacitive sensors can be configured within an array of sensors and each sensing element has its own unique address, which means each sensor can be monitored individually. By scanning the addressable sensors within the array of sensors and using signal processing algorithms to analyze the measured signals, the ice presence, type and thickness can be determined [21, 43].

Advantageously, the capacitive technique has a high sensitivity, a light weight, and the sensor can be mounted close to the blade tip [7]. Other features, such as ice presence and thickness, can be determined within an area and in real time [21]. Embedded arrays of sensors can cover and fit large areas of the blade surface. It also has a very low power consumption [7]. The fringe-effect caused by the edge of the sensing element has a negative impact on the electrical field, which may reduce the sensor capacitance. Also, a limitation of using high frequencies is that they can reduce the efficiency of the sensor [44]. It is not known whether freezing temperatures have any effect on the performance of the sensing elements. However, the changes in air gaps between sensing elements can affect the capacitive measurement [45]. Furthermore, the ambient temperature could change the dielectric constant of the medium material, which might lead to inaccurate measurement. The sensing element geometry can affect its electric field [46]. The capacitive sensor is one of the ice detection techniques that can be adapted for the blade of a wind turbine. Capacitive sensors are promising techniques that are capable of measuring the main parameters of ice accumulation, such as detection of the presence, type, thickness, location and rate of accumulation ice on the blade surface. Also, the capacitive technique is commercially available.

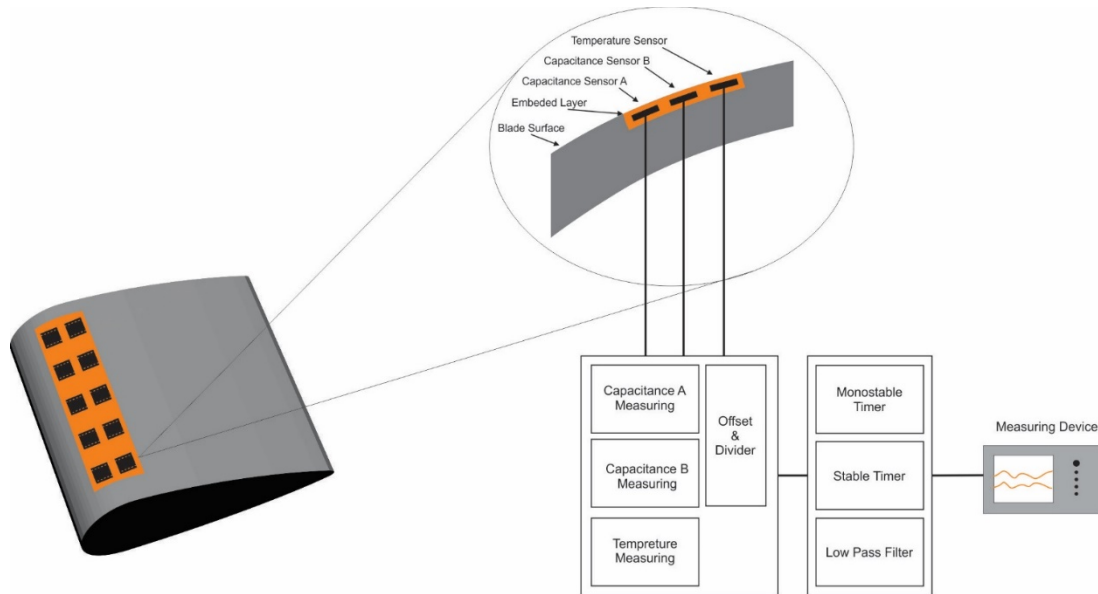


Figure 2.7 Capacitive ice sensing technique (modified from [42])

In the *impedance ice sensing technique*, an excitation signal is generated by the frequency generator and delivered to the inductive electrodes. When water or ice approaches the electrodes, the impedance of the electrodes changes. By measuring these changes using a voltage detector, some ice properties can be detected, such as ice presence, ice thickness and the ice load between the spaced electrodes. The basic design, illustrated in Figure (2.8), consists of inductive ice-sensing elements, temperature detectors, a signal generator, a voltmeter, a resistance's bridge, and a micro processing unit [48]. The performance of this technique is determined by the shape, dimensions and gap between the sensing electrodes and the inductive sensitivity to the ice in the region of the spaced electrodes. The inductive sensors can be distributed and embedded on the blade surface. The electrodes should be insulated to avoid a misreading that could be caused by conductive substances or electrolytes. There is lack of references related to this technique. The advantages of this technique are that it can deliver some parameters, such as ice thickness and ice load [47] and that it can also detect ice formation along the blade's leading edge. Moreover, the sensing electrodes can be adapted to the blade surface. Other features are that the technique structure is

retrofitable to existing wind turbines and it also has a very low power consumption [7]. This technique has no commercial applications because of its structure, which makes it unsuitable [47]. It does cover the leading edge, but it does not detect ice location or ice type. Finally, this technique might be inapplicable to use with the studied ice mitigations due to its structure and its limited capability.

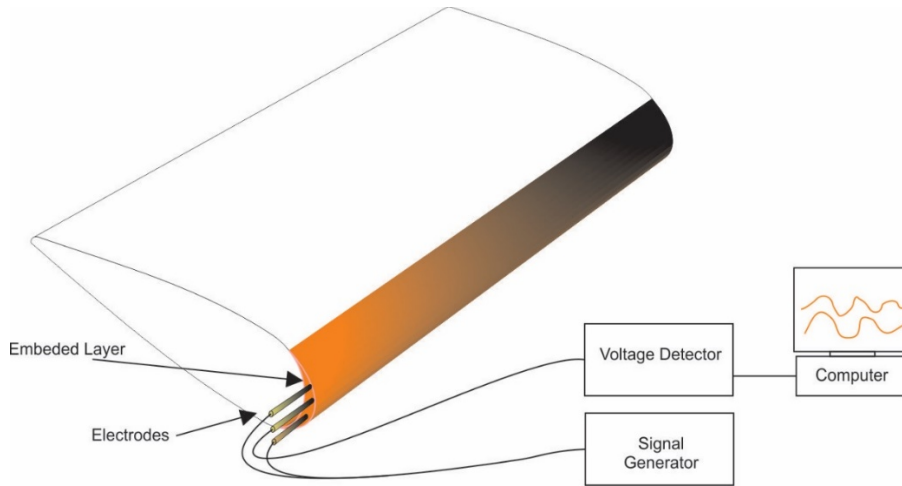


Figure 2.8 A sketch of impedance ice sensing technique, (modified from [48])

Table 2.1 The capabilities of ice sensors for WT blades

Detection Technique	Measurements					
	Ice Presence	Ice Type	Ice Thickness	Ice Mass	Ice Location	Ice Rate
Reaction of WT Blade Towards Ice						
Blade Vibration Techniques	No	No	No	Yes	Yes	N/A
Reaction of a Signal Towards Ice						
Acoustic Wave Techniques	No	No	No	Yes	Yes	N/A
Ultrasonic Waves Techniques	Yes	No	No	No	No	N/A
Microwave Techniques	Yes	No	No	Yes	No	N/A
Optical Techniques	Yes	Yes	Yes	No	Yes	Yes
Infrared Thermo. Techniques	Yes	No	No	No	Yes	N/A
Reaction of Electric Field Towards Ice						
Capacitive Techniques	Yes	Yes	Yes	No	Yes	Yes
Impedance Techniques	Yes	No	Yes	No	No	N/A

Table 2.2 Environmental impacts and installation consideration of ice sensors for WT blades

Detection Technique	Environment Impacts			Installation		
	Heavy Event	Dust	Noise	Mount Type	Accessibility	Surface Coverage
Reaction of WT Blade Towards Ice						
Blade Vibration Techniques	N/A	N/A	Negative	Blade Outside	Simple	Unlimited
Reaction of a Signal Towards Ice						
Acoustic Wave Techniques	N/A	N/A	Negative	Blade Outside	Simple	Unlimited
Ultrasonic Waves Techniques	N/A	N/A	Negative	Blade Inside	Difficult	Limited
Microwave Techniques	N/A	N/A	Negative	Blade Outside	Difficult	Limited
Optical Techniques	N/A	N/A	N/A	Blade Outside	Difficult	Unlimited
Infrared Thermo. Techniques	N/A	Negative	N/A	Remote	Simple	Limited
Reaction of Electric Field Towards Ice						
Capacitive Techniques	N/A	N/A	N/A	Blade Outside	Difficult	Unlimited
Impedance Techniques	N/A	N/A	N/A	Blade Outside	Difficult	Limited

2.3 Ice Mitigation for Wind Turbine Blades

Icing mitigation techniques are divided into passive or active. Passive techniques typically employ hydrophobic or icephobic paint for the surface. Recent researchers have stated that using a coating on the blade surface reduces the strength of ice adhesion. However, leading edge erosion and pitting may result in damage to all blade coatings that currently exist, which has a negative impact on the effectiveness of the coatings and contributes to an increase in roughness on the blade's surface. Ice repellent coatings must either be durable or at least re-applicable in order to be successful [49]. The coatings that are specifically designed to work with heated surfaces can help to extend the life of the turbine blades and improve their overall performance. The effect of

heating on the coating of turbine blades will depend on various factors, including the type of coating, the temperature of operation, and the duration of exposure to heat.

Active techniques are used for removing ice from turbine blades and are either anti-icing or de-icing. An anti-icing technique averts ice accumulation during icing events while a de-icing technique removes accumulated ice after ice accretion events. There are many techniques of de-icing and anti-icing; most of them are still under development. A de-icing system is typically initiated after the deposited ice has been recognized and stays active until the surfaces of the blades are free of ice. As little as 5% or less of the turbine's capacity should be used for de-icing, and an active anti-icing technique usually withdraws a high amount of power from the rated power of the turbine output [50]. There are many different techniques for de-icing; however, none have overcome the higher costs associated with the increased power demand [50]. This chapter shall focus solely on active de-icing techniques that remove accumulated ice following ice accretion events. Furthermore, the techniques must be readily integrated with ice detectors and controllable through a closed system. They are divided into two categories, including thermal ice mitigation techniques and mechanical ice mitigation techniques.

2.3.1 Thermal Ice Mitigation Techniques

To avoid ice buildup on the wind turbine blade surface, the temperature of that surface has to be maintained above the freezing point, which requires an energy source. The available techniques that are considered in this study include electrical heating elements, blowing hot air and microwave electromagnetic energy. A technical comparison of ice mitigation techniques for wind turbine blades is presented in Table (2.3).

One of the thermal de-icing techniques uses *electrical heating elements* to develop a thin layer of water between the blade surface and the ice to enable gravity and centrifugal forces to shed ice from the blade surface [51, 53, 55]. In this technique, an electrical resistance element is embedded inside a coated material on the surface [51, 52]. As illustrated in Figure (2.9), the configuration of this technique includes a power supply, controller and heating elements [51]. To make the technique more effective, numerous heating elements are connected in a grid and attached to the blade surface. When ice thickness reaches a certain preset value in a particular region on the blade surface, the heating elements in that region are activated. Once a water film is created at the surface interface, the heat elements are deactivated [51, 55]. The duration and amount of heat is calibrated and controlled based on parameters that include blade surface temperature, ice type, ice thickness and the thermal property of embedded material [54]. The control process in this technique can conserve energy by de-icing the entire area section by section. Finally, the air-drag force and gravity play a major role in ice removal [51, 55]. However, the time needed to keep the most significant portions of the blade surface ice free, such as the leading edge and tip portion, may increase the average power consumption [51]. Also, the amount of thermal energy needed to melt ice at the tip is larger than at the hub. [56, 71], because the outer ends of the blades are more exposed to icing than the hub portion. There are several reasons for this, including that they are close to low clouds, sweep a larger area, which can lead to collecting more ice from the larger volume, and that the tip has the highest relative velocity, which can increase the rate of ice accretion [7].

The advantages of a heat resistance ice mitigation technique are a capability of retrofit on preinstalled turbine blades, a high thermal efficiency, because of direct heat transfer, which increases its effectiveness and response, and that it can be distributed on the blade surface [54, 55,

56, 58]. The heating cycle and its duration depend on surface temperature, ambient temperature and the difference between the two [54, 58]. Better performance can be achieved by using higher intensity pulse signals for de-icing the blade surface [13]. Other features, such as embedded heat elements, are available on the market and can be used in the wind turbine industry [54, 57, 58]. However, the technique has some disadvantages. It may increase blade surface roughness and can cause a run-back water effect [13, 55, 57]. Another issue involves the fact that ice is removed by rotational centrifugal force, which is affected by wind speeds. Therefore, as wind speeds slow down, removing the melted ice through this force becomes difficult. Another disadvantage is that heavy icing events might reduce the technique's effectiveness [54, 56, 58]. In cases of failure, any heat element could cause a major imbalance in the wind turbine's performance [55, 56, 58]. Heating elements can be damaged by lightning if not embedded into an appropriate material. [54, 58]. Furthermore, with inappropriate attaching properties, the glue material can cause detachment of the heat elements, which leads to large losses in energy production [57]. The continuous overheating may induce permanent damage to the blade surface if not considered in the design [58]. Moreover, a large number of heat elements that cover the blade surface require a complex network of wiring, which might cause a problem in the heating system; this needs to be considered during design [13]. Even though there are commercial products available, none of them are widely used [54, 55, 56].

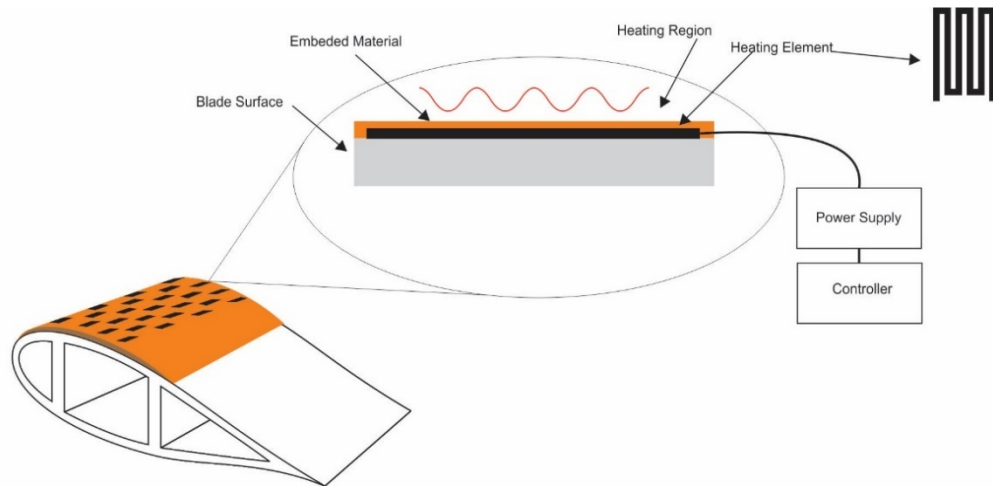


Figure 2.9 Heat resistance de-icing of wind turbine blades (modified from [51])

In *hot air de-icing*, hot air is injected inside the blade to develop a thin layer of water between the blade surface and the ice [54, 52]. A blower consists of a centrifugal fan and an electrical heater blowing hot air inside the rotor blade. Blow devices are mounted internally in the hub or in each blade and close to the root. The thermal energy is conducted to the blade surface which prevents the blade from icing [52]. The internal volume of the blade, which is close to the leading edge, is divided into two sections by special ducts. Hot air is injected in the section close to the leading edge. The cold air, which is received through the other duct section, is reheated at the desired temperature and recirculates [54]. Figure (2.10) illustrates a hot air circuit inside a wind turbine blade. In particular, the factors that affect the efficiency of the technique are blade wall thickness, thermal conductivity of the blade material, focusing on the outer part close to the blade tip rather than the hub portion, the scale size of the blade, and the temperature and volume of hot air [11, 49, 52, 54, 59]. In addition, the power consumption for heating can be greatly reduced by using a closed system instead of an open system, and by considering the external ambient temperature, the air can be heated to the required temperature. The waste heat produced by the turbine equipment can be used to enhance the system's performance [60].

The hot air ice mitigation technique has advantages, including that it can effectively melt ice [60] and that its efficiency can be increased when the waste heat, which is already generated by turbine equipment, is used to remove ice on the blade surface [60]. It has no effect on the environment, and is not affected by lightning [11, 54]. However, this technique has a low thermal efficiency because of its poor heat distribution, which might lead to run-back water being frozen again on some areas of the blade surface, leading to blade mass imbalance. The highest heat transfer should be at the tip of the blade, while the heat source is mounted at the hub, which is a critical problem, especially in large scale turbines [49, 54, 60]. Other issues include that it is ineffective if used at a standstill or at low wind speeds after icing events because of the cost of the large amount of heat energy to melt the ice without power production [11]. During low temperature events, the forced convection requires a large amount of heating power to remove the ice, which makes the technique inapplicable. [13, 61]. In this technique, the turbine is shut down and blade heating is activated whenever ice on the blade surface is detected, which makes the technique inconvenient for closed systems and integrated systems [52]. The thermal resistance increases as a result of increased material thickness in large turbine blades, and this can cause the temperature to decrease on the blade surface [49, 52]. Furthermore, few commercial applications are available [49].

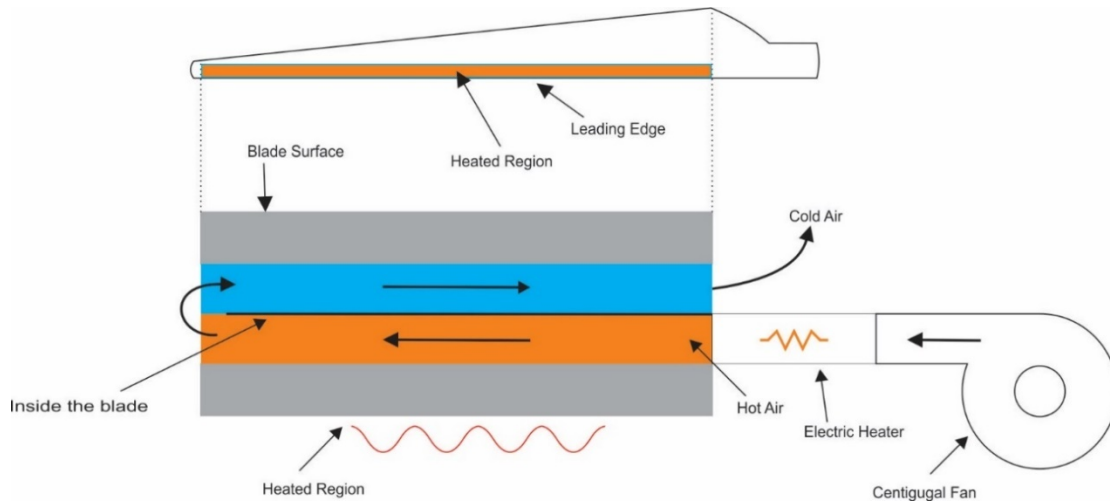


Figure 2.10 Hot air de-icing of wind turbine blades (modified from [57,60])

Another technique is based on generating heat by transmitting *microwave electromagnetic energy* to the blade surface to prevent ice formation [54, 56, 65]. To increase effectiveness, the blade surface is covered by a dielectric coating that increases the reflection of the microwave energy [54, 56, 58]. Once a supercooled water droplet collides with the blade surface, the heat which is generated by microwave energy weakens the ice adhesion and thereby prevents ice formation [58, 65]. This technique is presented in Figure (2.11). The distribution of transmitted microwave electromagnetic energy into the dielectric material is designed to provide suitable heating time. It is also designed to provide the necessary amount of thermal energy to heat supercooled water droplets to above the freezing point before they collide with the blade surface [54, 65]. The appropriate selection of both the microwave frequency and the thickness of the dielectric coating play significant roles in improving the technique's performance [58, 65].

The technique can be modified; instead of applying microwave energy to heat ice droplets directly, which is poorly absorbed by ice, it can be used indirectly inside the blade and conduct heat energy through the wall blade to melt the ice, making this technique more efficient [66]. Other features include that it has low power consumption, no lightning issues, and even heat distribution [4]; it also has no effect on blade surface roughness. However, the drawbacks of this technique

include the weak ability of pure water and ice to absorb microwave energy; this reduces the effectiveness of heat transfer [67]. The blade shape could influence the microwave propagation negatively, which will reduce its efficiency [4, 62, 64, 66]. The technique has a low thermal efficiency [62, 64]. It has a minimal effect during heavy icing events due to its low thermal efficiency and its effect on bigger water droplets is low [64]. It has a limited surface coverage because of its technical structure, which needs to be implemented inside the turbine blade, and this might affect blade weight and balance. Furthermore, it has no successful implementation [54, 56, 58, 63], and needs further investigation regarding safety [4, 67].

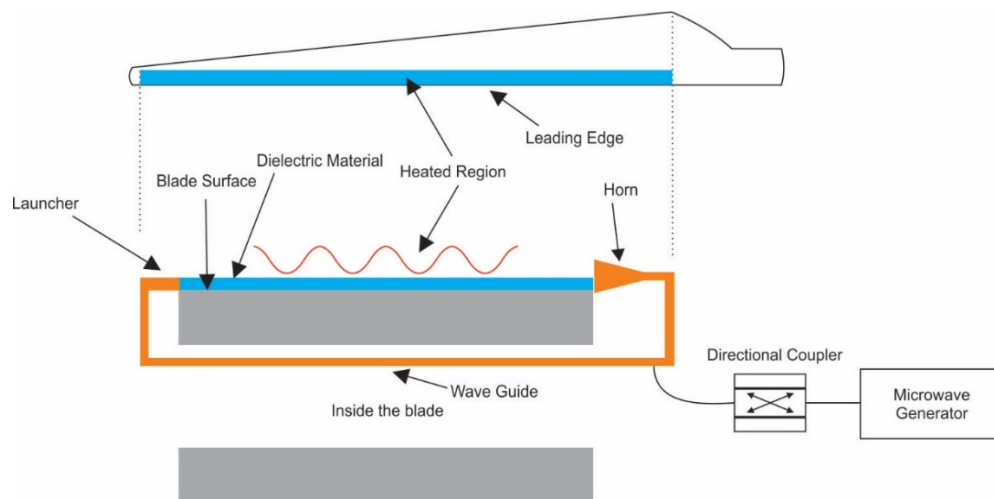


Figure 2.11 Schematic of a microwave ice remover for wind turbine blades (modified from [65])

2.3.2 Mechanical Ice Mitigation Techniques

The mechanical ice mitigation technique is a mechanical process to break the accumulated ice and accelerate its separation using the energy produced by vibrations or mechanical movement of a structure. Both ultrasonic waves and flexible boots techniques are considered in this chapter.

Flexible boots de-icing uses tubes on the leading edge of the blade surface. Once the ice is accumulated on the blade surface, the device is inflated with compressed air to break ice from the surface [30]. Originally, the technique was invented to be used in aircrafts. It is typically made of layers of rubber, with one or more air chambers between the layers and shaped as stripes aligned with the long direction of the boot, as shown in Figure (2.12). The technique has a fast mechanism of inflation and deflation of chambers, either at once, or in specific groups. The duration cycle of the inflation and deflation operations are a few seconds to accomplish an optimal ice removal cycle. After the ice has cracked, its adhesive strength to the surface is broken and then it is thrown by gravity and centrifugal forces. The chambers are deflated, and a vacuum is applied to ensure the surface is deflated completely and the boot comes back to the original position [30, 67]. Usually in this technique, ice is not removed completely on the first attempt, but it could be after additional attempts. Moreover, boot performance can be enhanced by painting the boot surface with ice phobic coatings [30].

The positive features of flexible boot ice mitigation technique are that it has a low energy consumption and fast response [67, 68]. It is also simple to build and operate and is easily installed [68]. However, the drawbacks of this technique are that it cannot operate at very low temperatures due to the rubber becoming brittle [30]. Also, there needs to be a significant amount of ice on the boot surface to operate because a thin ice layer cannot peel off [30]. It may also increase the surface roughness, and this can impact the aerodynamics of the blade negatively by increasing drag force [30, 67]. It cannot be easily mounted on complex surfaces such as wind turbine shapes [30]. In

addition, it has a shorter life span due to its mechanical operation [30, 67]. Accordingly, this technique still needs to be investigated in laboratories before use in wind turbine installations [67].

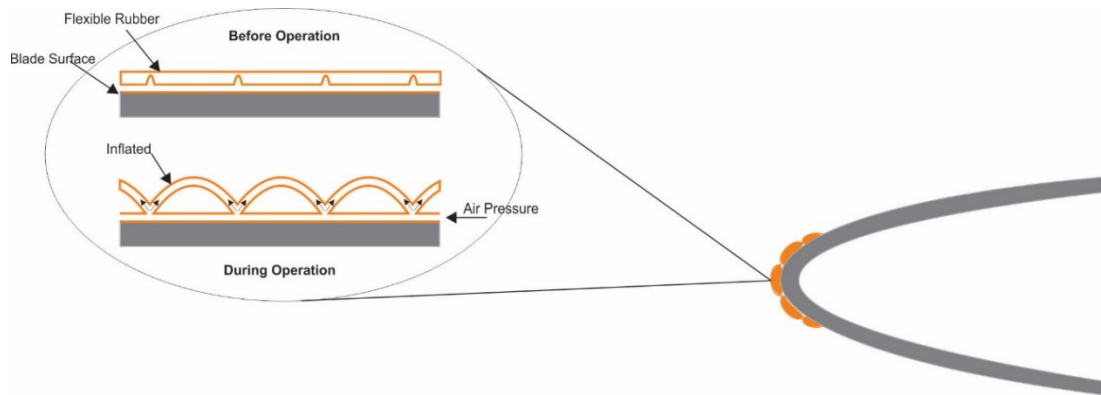


Figure 2.12 The principle of flexible rubber boots de-icing technique (modified from [30])

In the *ultrasonic de-icing technique*, piezoelectric actuators are used to produce local shear stresses at positions where ice has accumulated to weaken and break the interfaced ice layer with the blade surface [69, 70]. The difference in the existing physical properties of the ice and blade surface makes the speed of the propagated waves behave differently, which produce shear stresses [70]. To achieve the best performance for an ultrasonic de-icing technique, many factors must be chosen carefully, such as the ultrasonic frequency, the thickness of the laminated composite material, and the distance between ultrasonic transducers. The ultrasonic transducers are distributed and fixed on the inner surface of the wind turbine blade to have a direct contact with blade surface, shown in Figure (2.13). An ultrasonic de-icer can remove the accumulated ice attached to the leading edge of the blade within a few seconds [69]. The technique has notable positive features such as its strong record of quickly and easily removing the ice layer on the blade surface within the operated region, its low energy consumption and its lack of effect on blade

surface roughness or turbine aerodynamics [69, 70]. In addition, it has a reasonable performance in low temperature environments [71]. However, installing the devices of this ice mitigation technique inside the blades will definitely increase the total weight of wind turbine blades so that the whole performance of the wind turbine is inevitably affected [71]. The technique still needs to be developed [69, 70].

The ultrasonic de-icing technique has a low effect on heavy icing events due to its low output capability and its effectiveness on the bigger water droplets is unknown. It also has a limited surface coverage compared to the length of blade because of its technical structure which needs to be implemented inside the turbine blade and therefore could affect blade weight, material, and balance.

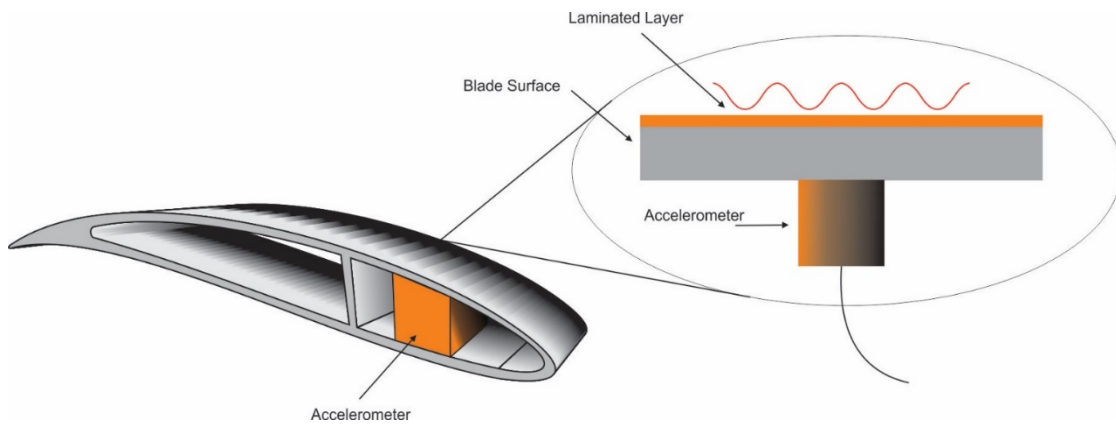


Figure 2.13 A 3-D model of ultrasonic transducer in wind turbine blade (modified from [69,71])

Table 2.3 A technical comparison for the studied ice mitigation techniques

Parameter	Used Technique					
	Microwave	Resistance	Hot air	Ultrasonic	Boot	
General Specification	Active type	Anti-icing	De-icing	De-icing	Anti-icing	De-icing
	Mitigation Type	Prevention	Removal	Removal	Prevention	Removal
	Technique Concept	Droplet Heating	Create Water Film	Create Water Film	Vibrational Cracking	Mechanical Cracking
	Energy consumption	Low	Medium	High	Low	Low
	Thermal efficiency	Low	High	Low	Low	None
	Response	Not Available	Fast	Slow	Not Available	Fast
	Surface Coverage	Limited	Unlimited	Unlimited	Limited	Limited
	Heat distribution	Good	Moderate	Poor	Not Available	Poor
Mechanical Impacts	Blade bend stress effect	Not Available	Negative	Not Available	Not Available	Not Available
	Surface roughness Increased	No	Yes	No	No	Yes
	Mass imbalance	Not Available	No	Yes	Not Available	Not Available
	Effect on turbine aerodynamic	Good	Good	Medium	Not Available	Poor
	Rotational centrifugal force effect	Positive	Positive	Positive	Positive	Negative
Environmental Impacts	Run-back water	No	Yes	Yes	No	No
	Noise Effect	Low	Low	Low	Low	High
	Attract lightning	No	Yes	No	No	No
	Icing conditions Effect at low wind speed	Not Available	Negative	Not Available	Not Available	Not Available
	Effective for different icing events	Low	High	High	Not Available	High
Availability & Accessibility	Retrofitting	No	Yes	No	No	No
	Maintenance Complicity	Moderate	Moderate	Difficult	Moderate	Intensive
	Used Application	None	Few	Few	None	None
	Application Type	Prototype	Commercial	Commercial	Prototype	Prototype

2.4 Integrated Ice Sensing and De-icing Systems for Wind Turbine Blades

2.4.1 Integrated Systems Based on Hot Air Ice Mitigation Techniques:

In this integration, the quantity of thermal energy that is transferred by conduction to the blade surface varies and depends on the shape, thickness, length and material of blade. All these dependent factors play a significant role in the distribution of heat, which can cause uneven temperature distribution along the blade surface. Adding to these factors, the source of heating is a single source and is required for heating the entire blade in different icing conditions, which causes de-icing a single ice spot on the blade surface to be impossible without heating the entire blade. Furthermore, its thermal input to ice takes a long period of time from receiving an activation signal from the ice sensor, which means it has a slow response to the control signal and that will increase the length of the heat activation intervals which lead to more energy consumption. Most ice sensing techniques, when integrated with this ice mitigation technique and are mounted or wired from inside the blade, will be damaged by the internal high temperature of blade. Table (2.4) presents the comparison of the conceptual functions analysis between the studied techniques. Integrated systems based on infrared ice sensing technique might be more applicable than the other integrated techniques. The limitation of its applicability depends on its limited coverage area over the blade surface and its limited sensing vision during different ice events.

Table 2.4 The applicability of Hot air ice mitigation technique with the studied ice sensing techniques

Deicing Technique	Hot air							
Sensing Technique	Blade vibration	Acoustic Wave	Ultrasonic	Microwave	Optical	Infrared Thermo.	Capacitive	Impedance
System Response	Slow	Slow	Slow	Slow	Slow	Slow	Slow	Slow
Physical Integration at Workplace	Applicable	Applicable	Inapplicable	Inapplicable	Inapplicable	Applicable	Inapplicable	Inapplicable
Closed Loop System	Yes	Yes	No	No	Yes	Yes	Yes	Yes
MIMO System	No	No	No	No	No	No	No	No
Coverage Area	Unlimited	Unlimited	Limited	Limited	Unlimited	Limited	Unlimited	Unlimited
Ex. Disturbances	Yes	Yes	Yes	Yes	No	Yes	Yes	Yes
Used Application	N/A	N/A	N/A	N/A	N/A	N/A	N/A	N/A
System Complicity	High	High	High	High	High	Medium	High	High
System Resolution	Low	Low	Low	Low	Low	Low	Low	Low
Energy Consumption	High	High	High	High	High	High	High	High
Analyzing System	Logarithm	D-Signal	D-Signal	D-Signal	Logarithm	Image	N/A	N/A
System Concept	Inapplicable	Inapplicable	Inapplicable	Inapplicable	Inapplicable	Applicable	Inapplicable	Inapplicable
System Interaction	Weak	Weak	Weak	Weak	Weak	Acceptable	Weak	Weak

2.4.2 Integrated Systems Based on Thermal Resistors Ice Mitigation

Techniques:

This integration technique utilizes thermal resistors for direct heating of ice accumulated on the blade surface. They are attached in grids and each heat element in these grids can be addressed and controlled individually through the ice sensor. However, this integration technique still has some minor defects that affect performance and interactions within its integrated system with the various ice sensing techniques in Table (2.5). Comparison of the conceptual design in the table shows that only four combination techniques are promising. There are applicable combinations that each can result in an integrated system, however, all combinations have shortcomings that require more investigation and development. In particular, the integration based on an ice sensing technique of optical, infrared, capacitance, and impedance with thermal resistance as a de-icer are promising techniques but need more investigation.

Table 2.5 The applicability of Thermal resistors ice mitigation technique with the studied ice sensing techniques

Deicing Technique	Thermal Resistance							
	Blade Vibration	Acoustic Wave	Ultrasonic	Microwave	Optical	Infrared Thermo.	Capacitive	Impedance
System Response	Slow	N/A	N/A	N/A	Fast	Fast	Fast	N/A
Physical Integration at Workplace	Applicable	Applicable	Inapplicable	Inapplicable	Applicable	Applicable	Applicable	Applicable
Closed Loop System	Yes	Yes	No	No	Yes	Yes	Yes	Yes
MIMO System	Yes	No	No	No	Yes	Yes	Yes	Yes
Coverage Area	Unlimited	Unlimited	Limited	Limited	Unlimited	Limited	Unlimited	Unlimited
Ex. Disturbances	Yes	Yes	Yes	Yes	No	Yes	Yes	Yes
Used Application	N/A	N/A	N/A	N/A	Exp.	Exp.	Exp.	N/A
System Complicity	Medium	Medium	High	High	High	Medium	High	High
System Resolution	Medium	Low	N/A	N/A	High	High	High	High
Energy Consumption	Medium	High	N/A	N/A	Low	Low	Low	Low
Analyzing System	Logarithm	D-Signal	D-Signal	D-Signal	Logarithm	Image	N/A	N/A
System Concept	Inapplicable	Inapplicable	Inapplicable	Inapplicable	Applicable	Applicable	Applicable	Applicable
System Interaction	Weak	Weak	Weak	Weak	Acceptable	Acceptable	Acceptable	Acceptable

2.4.3 Integrated Systems Based on Microwave Ice Mitigation Techniques:

Table (2.6) shows that most of the integrated systems based on microwave ice mitigation techniques are inapplicable for several reasons. Microwave ice mitigation techniques affect the blade weight which is undesirable. Also, it cannot be integrated in a MIMO system, it can be affected by environmental disturbances, and it has low resolution. Furthermore, it has a weak effect on larger water droplets. Consequently, these reasons are weakening its integrated system sensitivity, response, and performance. However, the only integrated system that might be applicable is based on an infrared ice sensing technique because of the feature of remote sensing which means it can detect ice on the blade surface directly without affecting the blade by any means. The shortcomings of this technique are evident in its limited coverage area and its limited sensing vision during heavy icing events.

Table 2.6 The applicability of Microwave ice mitigation technique with the studied ice sensing techniques

Deicing Technique	Microwave							
Sensing Technique	Blade Vibration	Acoustic Wave	Ultrasonic	Microwave	Optical	Infrared Thermo.	Capacitive	Impedance
System Response	N/A	N/A	N/A	N/A	Fast	Fast	N/A	N/A
Physical Integration at Workplace	N/A	N/A	Inapplicable	Inapplicable	Inapplicable	Applicable	Inapplicable	Inapplicable
Closed Loop System	N/A	N/A	No	No	No	Yes	No	No
MIMO System	N/A	N/A	No	No	No	No	No	No
Coverage Area	Unlimited	Unlimited	Limited	Limited	Unlimited	Limited	Unlimited	Unlimited
Ex. Disturbances	Yes	Yes	Yes	Yes	No	Yes	No	No
Used Application	N/A	N/A	N/A	N/A	N/A	N/A	N/A	N/A
System Complicity	Medium	Medium	Medium	Medium	High	Medium	High	High
System Resolution	Low	Low	Low	Low	N/A	High	N/A	N/A
Energy Consumption	Low	Low	Low	Low	Low	Low	Low	Low
Analyzing System	Logarithm	D-Signal	D-Signal	D-Signal	Logarithm	Image	N/A	N/A
System Concept	Inapplicable	Inapplicable	Inapplicable	Inapplicable	Inapplicable	Applicable	Inapplicable	Inapplicable
System Interaction	Weak	Weak	Weak	Weak	Weak	Weak	Weak	Weak

2.4.4 Integrated Systems Based on Ultrasonic Ice Mitigation Techniques:

This integration technique uses several ultrasonic devices as ice mitigation in each blade and adds additional weight to the wind turbine blades, negatively affecting the aerodynamic performance of the blades. The use of ultrasonic local shear stresses in the ice cracking process on the surface of the blades causes damage to ice sensors. Even if this damage does not happen in the near term, it certainly affects them negatively in the long term. Also, the vibration produced by this ice mitigation may disturb the measured signals of the ice sensors. Therefore, the only integration that might be applicable is that with remote ice sensing, as presented in Table (2.7).

Table 2.7 The applicability of Ultrasonic ice mitigation technique with the studied ice sensing techniques

Deicing Technique	Ultrasonic							
Sensing Technique	Blade Vibration	Acoustic Wave	Ultrasonic	Microwave	Optical	Infrared Thermo.	Capacitive	Impedance
System Response	N/A	N/A	N/A	N/A	Fast	Fast	N/A	N/A
Physical Integration at Workplace	N/A	N/A	Inapplicable	Inapplicable	Inapplicable	Applicable	Inapplicable	Inapplicable
Closed Loop System	N/A	N/A	No	No	No	Yes	No	No
MIMO System	N/A	N/A	No	No	No	No	No	No
Coverage Area	Unlimited	Unlimited	Limited	Limited	Unlimited	Limited	Unlimited	Unlimited
Ex. Disturbances	Yes	Yes	Yes	Yes	No	Yes	No	No
Used Application	N/A	N/A	N/A	N/A	N/A	N/A	N/A	N/A
System Complicity	Medium	Medium	Medium	Medium	High	Medium	High	High
System Resolution	Low	Low	Low	Low	N/A	High	N/A	N/A
Energy Consumption	Low	Low	Low	Low	Low	Low	Low	Low
Analyzing System	Logarithm	D-Signal	D-Signal	D-Signal	Logarithm	Image	N/A	N/A
System Concept	Inapplicable	Inapplicable	Inapplicable	Inapplicable	Inapplicable	Applicable	Inapplicable	Inapplicable
System Interaction	Weak	Weak	Weak	Weak	Weak	Weak	Weak	Weak

2.4.5 Integrated Systems Based on Flexible Boot Ice Mitigation Technique:

The leading-edge of the blade is the vital place where the flexible boot ice mitigation technique is mounted, and where ice is adheres. However, the limited work area of the de-icer and the mechanical operation of the de-icer make the necessity of achieving the requirement of physical integration with the ice sensor in the same place infeasible. This ice mitigation technique produces a loud noise during its operation which may reduce the measurement efficiency of the ice sensor if one is present. This de-icer also cannot remove ice on the ice sensors due to its mechanism of work. For these reasons, this kind of integration is inapplicable and the only ice sensor that might be integrated with this ice mitigation is the remote ice sensor which is the infrared ice sensor, as presented in Table (2.8). However, this integration has also minor issues, such as sensing vision limitation and coverage area limitation and that need further investigation.

Table 2.8 The applicability of Flexible boot ice mitigation technique with the studied ice sensing techniques

Deicing Technique	Flexible Boot							
Sensing Technique	Blade vibration	Acoustic Wave	Ultrasonic	Microwave	Optical	Infrared Thermo.	Capacitive	Impedance
System Response	N/A	N/A	N/A	N/A	N/A	Fast	N/A	N/A
Physical Integration at Workplace	Inapplicable	Inapplicable	Inapplicable	Inapplicable	Inapplicable	Applicable	Inapplicable	Inapplicable
Closed Loop System	N/A	N/A	N/A	N/A	Yes	Yes	Yes	Yes
MIMO System	N/A	N/A	N/A	N/A	Yes	Yes	Yes	Yes
Coverage Area	Limited	Limited	Limited	Limited	Limited	Limited	Limited	Limited
Ex. Disturbances	Yes	Yes	Yes	Yes	Yes	Yes	Yes	Yes
Used Application	N/A	N/A	N/A	N/A	N/A	N/A	N/A	N/A
System Complicity	High	High	High	High	High	Medium	High	High
System Resolution	Low	Low	Low	Low	Low	Low	Low	Low
Energy Consumption	Low	Low	Low	Low	Low	Low	Low	Low
Analyzing System	Logarithm	D-Signal	D-Signal	D-Signal	Logarithm	Image	N/A	N/A
System Concept	Inapplicable	Inapplicable	Inapplicable	Inapplicable	Inapplicable	Applicable	Inapplicable	Inapplicable
System Interaction	Weak	Weak	Weak	Weak	Weak	Acceptable	Weak	Weak

2.5 Conclusions

From this review of design and working principles of ice detection techniques that can be adapted for the blades of wind turbines, it is found that sensors based on optical and capacitive techniques offer reasonable potential to detect some important parameters pertaining to ice accretion such as detection of presence, type, thickness, location and rate of the ice on blade surface. The thermal infrared sensor can also detect ice presence and location. Also, the ultrasonic waves technique and microwave technique can detect ice directly due to signal reflection / attenuation. Also, some of ice mitigation techniques are reviewed regarding the performance, effect of the turbine structure, effect of the environment, and accessibility. It has been concluded that both microwave and ultrasonic ice mitigation techniques have a low energy consumption, fast response, and no effect on blade surface roughness. In addition to these techniques is the heat

resistance technique, which has a high thermal efficiency, fast response and can be distributed on the blade surface. Even though these ice sensors and ice mitigations have reasonable accepted advantages, they still have critical drawbacks that make them inapplicable when combined in integrated systems. Therefore, they need further investigation to improve their properties and capabilities regarding their interactions with each other to achieve optimum integration.

2.6 References

- [1] Wind Europe, Wind energy in Europe: scenarios for 2030, Report, Sep. 2017.
- [2] National Energy Board, Canada's energy future: energy supply and demand projections to 2035, an energy market assessment, Report no. NE23-15/2011E-PDF ISBN 978-1-100-19464-6, Nov. 2011.
- [3] Technical Research Centre of Finland (VTT), Cold climate wind energy showing huge potential, ScienceDaily, 2013.
- [4] L. Battisti, Optimising wind turbine design for operation in cold climates, In: John Dalsgaard Sørensen, Jens N Sørense (Ed.), Wind Energy Systems, Woodhead Publishing, 2011, p.388.
- [5] Technical Research Centre of Finland (VTT), Wind energy growing strong in cold climates, Clean Technica, May 2013.
- [6] Jesús María Pinar Perez, Fausto Pedro García Marquez, Diego Ruiz Hernandez, Economic viability analysis for icing blades detection in wind turbines, Journal of Cleaner Production, 2016, Vol.135, 1150-1160.
- [7] Homola, M., Nicklasson, P., Sundsbo, P., Ice sensors for wind turbines. Cold Regions Science and Technology, 2006 (46), 125-131. doi:10.1016/j.coldregions.2006.06.005
- [8] Rene Cattin, Ulla Heikkilä, Evaluation of ice detection systems for wind turbines: Final Report, VGB Research Project no. 392, METEOTEST, Weather Forecasts Renewable Energies Air and Climate Environmental IT, Bern, Feb 2016.
- [9] Shervin Shajjee, Lucy Y. Pao, Robert R. McLeod, Monitoring ice accumulation and active de-icing control of wind turbine blades, In: Ningsu Luo, Yolanda Vidal, Leonardo Acho (Ed.), Wind turbine control and monitoring, Published by Springer, 2014, p.193, doi: 10.1007/978-3-319-08413-8
- [10] Brenner, D., Determination of the actual ice mass on wind turbine blades, Winterwind, Sweden: Bosch Group., 2016.
- [11] Gantasala, S., Luneno, J. C., Aidanpää, J. O., Detection of ice mass based on the natural frequencies of wind turbine blade, Wind Energy Science, 2016 (17), doi:0.5194/wes-2016-30
- [12] Laakso T., Baring I., Durstewitz M., Horbaty R., Lacroix A., Peltola E., Wallenius T., State-of-the-art of wind energy in cold climates, Technical Research Centre of Finland (VTT), 2010.

- [13] Seifert, H.; Technical Requirements for Rotor Blades Operating in Cold Climate; BOREAS VI, 2003, p. 13, Pyhä, Finland.
- [14] D. J. Lekou, Probabilistic design of wind turbine blades, Centre for Renewable Energy Sources and Saving (CRESS), Greece, 2013.
- [15] Tesauro, A., Pavese, C., & Branner, K., Rotor blade online monitoring and fault diagnosis technology research, DTU Wind Energy, 2014.
- [16] Drafts B., Acoustic wave technology sensors, Sensors Magazine, Oct. 2000, Available from <https://www.sensormag.com/components/acoustic-wave-technology-sensors>
- [17] Knowles T., Kalmus C., Acoustic wave ice and water detector, USA Patent No. 7,026,943 B2., 2006.
- [18] Berbyuk, V., Peterson, B., & Möller, J., Towards early ice detection on wind turbine blades using acoustic waves. SPIE, Gothenburg, Sweden, 2014, doi:10.1117/12.2046362.
- [19] David K. Hsu, Frank J. Margetan, Samuel J. Wormley, Jeffrey A. Simpson, Apparatus and method for detection of icing onset and ice thickness, USA Patent No. 5,095,754., 1992.
- [20] Roger D. Watkins, Arthur B. Gillespie, Michael O. Deighton, Roger B. Pike, Colin B. Scott-Kestin, Ice detector, USA Patent No. 4,604,612., 1986.
- [21] Gerardi J. J., Hickman G. A., Khatkhate A. A., Pruzan D. A., Apparatus and method for determining the existence of ice or water on a surface from the capacitance between electrodes on said surface , USA Patent No. 5,874,672., 1999.
- [22] Chamue J. R., Mass F., Ultrasonic aircraft ice detector using flexural waves, USA Patent No. 4,461,178., 1984.
- [23] Gómez C., Arcos A., García Márquez FP, Wavelet transforms and pattern recognition on ultrasonic guides waves for frozen surface state diagnosis, Renewable Energy, 2017, 1-13, doi: 10.1016/j.renene.2017.03.052.
- [24] Tcherniak, D., & Gaard, M., Vibration-based SHM system: application to wind turbine blades. DAMAS. 628. Lyngby, Denmark: Journal of Physics, 2015, doi:10.1088/1742-6596/628/1/012072
- [25] Canbolat, H., A novel level measurement technique using three capacitive sensors for liquids. IEEE Transactions on Instrumentation and Measurement, 2009, Vol. 58(10).
- [26] Magenheim B., Microwave ice detector, USA Patent No. 4,054,255., 1977.
- [27] Meindl T., Moniaci W., Pasero E., Riccardi M., An embedded hardware-software system to detect and foresee road ice formation, Int. joint conference on neural networks, 2006, Vancouver, Canada: IEEE. doi:0-7803-9490-9/06
- [28] Mughal U., Virk M. S., Mustafa M., Electromagnetism based atmospheric ice sensing technique - A conceptual review. Int. Jnl. of Multiphysics, 2012, Vol.6(4).
- [29] Rennó N. O., Arbor A., Aircraft icing detector, USA. Patent No. 9,302,777 B2., 2016.
- [30] Ryerson, Charles C., Assessment of superstructure ice protection as applied to offshore oil operations safety, 2009, US Army - Research. 49, available from: <http://digitalcommons.unl.edu/usarmyresearch/49>
- [31] MacKenzie I. K., Method and apparatus for measuring ice thickness on substrates using backscattering of gamma rays, USA Patent No. 5,821,862., 1998.

- [32] Shervin Shajiee, Lucy Y. Pao, Patrick N. Wagner, Eric D. Moore, and Robert R., Direct ice sensing and localized closed loop heating for active de-icing of wind turbines blades, American Control Conference (ACC), June 2013: 634-639.
- [33] Ikiades A. A., Spasopoulos D., Amoiropoulos K., Richards T., Howard G., Pfeil M., Detection and rate of growth of ice on aerodynamic surfaces using its optical characteristics using its optical characteristics, Aircraft Engineering and Aerospace Technology, 2013, Vol.85(6), 443–452. doi:10.1108/AEAT-11-2012-0219
- [34] Luo N., Vidal Y., Acho L., Advances in Industrial Control: Wind Turbine Control and Monitoring. Springer International Publishing, 2014, doi:10.1007/978-3-319-08413-8
- [35] Chao F., Papachristou C., Grey-model based ice prediction sensor system on wind turbine system. IEEE, 2012, doi:978-1-4673-2792-3/12/\$31.00
- [36] Hackmeister R. L., Optical ice sensors for wind turbine – nacelles, Wind systems magazine, 2010, available from windsystemsmag.com
- [37] Oberson P., Huttner B., Guinnard O., Guinnard L., Ribordy G., Gisin N., Optical frequency domain reflectometry with a narrow linewidth fiber laser. IEEE Photonics Technology, 2000, Vol.12(7).
- [38] Clark M., McCann D., Forde M., Application of infrared thermography to the non-destructive testing of concrete and masonry bridges. NDT&E Int., 2003, Vol. 36, 265–275.
- [39] Quiterio Gómez Muñoz C., Pedro García Márquez F., Sánchez Tomás J., Ice detection using thermal infrared radiometry on wind turbine blades. Measurement, 2016, Vol.93, 157-163.
- [40] Pappalardo G., Mineo S., Perriello Zampelli S., Cubito A., Calcaterra D., Infrared thermography proposed for the estimation of the cooling rate index in the remote survey of rock masses, International journal of rock mechanics & mining sciences, 2016, Vol.83, 182-196.
- [41] Umair N. Mughal, Muhammad S. Virk, Atmospheric icing sensors - an insight, SENSORCOMM : The seventh international conference on sensor technologies and applications, 2013 , p. 191-199, ISBN: 978-1-61208-296-7.
- [42] Weinstein L., Ice sensor, USA Patent No. 4,766,369, 1988.
- [43] Gerardi J. J., Hickman G. A., Khatkhate, A. A., Pruzan D. A., Apparatus for measuring ice distribution profiles, USA Patent No. 5,398,547, 1995.
- [44] Roggen A., An overview of dielectric measurements, IEEE transactions on electrical insulation, 1990, Vol.25(1). doi:0018-9367/90/0200-95.
- [45] Ikechukwu C., Marine icing sensor design using capacitive techniques, a master thesis, Memorial University of Newfoundland, 2017.
- [46] Terzic, E., Nagarajah, R., Alamgir, M., & Terzic, J., Capacitive sensing technology, In: A neural network approach to fluid quantity measurement in dynamic environments, published by Springer, 2012, doi:10.1007/978-1-4471-4060-3.
- [47] Mughal U., Virk M., Mustafa M., State of the art review of atmospheric icing sensors. Sensors & Transducers, 2016, Vol.198(3), 2-15.
- [48] Seegmillar H., Ice detector and deicing fluid effectiveness monitoring system, USA Patent No. 5,523,959; 1996.

- [49] Suke P., Analysis of heating systems to mitigate ice accretion on wind turbine blades, a master thesis, McMaster University, January 2014.
- [50] Andersen, E. et al.; Report: Wind power in cold climate, Nordic energy research, 23 August 2011.
- [51] Petrenko V., Methods for modifying friction between an object and ice or snow, US Patent 7,034,257 B2, 2006.
- [52] Laakso, T., Peltola, E., Review on blade heating technology and future prospects. BOREAS VII, 2005, p.12, FMI, Saariselkä, Finland.
- [53] Battisti, L., et al., Warm-air intermittent de-icing system for wind turbines. *Wind Engineering* 2006, 30 (5), 361–374.
- [54] Adrian Ilinca., Analysis and mitigation of icing effects on wind turbines, In: Dr. Ibrahim Al-Bahadly (Ed.), *Wind Turbines*, InTech, 2011, doi: 10.5772/15484
- [55] J.G. Pallarol, B. Sunden & Zan Wu, On ice accretion for wind turbines and influence of some parameters, *WIT Transactions on State of the Art in Science and Engineering*, 2014, Vol. 81,129-159, doi:10.2495/978-1-78466-004-8/006.
- [56] Md Abu S Shohag, Emily C Hammel, David O Olawale and Okenwa I Okoli, Damage mitigation techniques in wind turbine blades: A review, *Wind Engineering*, 2017, 41(3):185–210, doi: 10.1177/0309524X17706862.
- [57] Reza Barati-Boldaji, Mohammad Komareji, Techniques of identifying icing and de-icing of wind turbines, *Journal of Electrical Engineering Science*, December 2017, ISSN: 2008-9864.
- [58] Olivier Parent, Adrian Ilinca, Anti-icing and de-icing techniques for wind turbines: Critical review, *Cold Regions Science and Technology*, 2011, 65: 88–96.
- [59] Battisti, L., Fedrizzi, R., 2D numerical simulation of a wind turbine de-icing system, using cycled heating. *Wind Engineering* 2007, 31 (1): 33–42.
- [60] Teng Xie, Jiankai Dong, Haowen Chen, Yiqiang Jiang, Yang Yao, Experimental investigation of deicing characteristics using hot air as heat source, *Applied Thermal Engineering* 2016, Vol.107, 681–688.
- [61] Shervin Shajiee, Lucy Y. Pao and Robert R. McLeod, Optimizing the layout of heaters for distributed active de-icing of wind turbine blades, *Wind Engineering*, 2014, Vol. 38(6): 587- 600.
- [62] J.D. Sørensen, J.N. Sørensen, *Wind energy systems: optimising design and construction for safe and reliable operation*, Woodhead Publishing Ltd., UK, 2011.
- [63] Jasinski WJ, Noe SC, Selig MC, Bragg MB., Wind turbine performance under icing conditions, *Trans ASME J Sol Energy Eng*, 1998, Vol.120: 60–5.
- [64] Oloufemi Fakorede, Zoé Feger, Hussein Ibrahim, Adrian Ilinca, Jean Perron, Christian Masson, Ice protection systems for wind turbines in cold climate: characteristics, comparisons and analysis, *Renewable and Sustainable Energy Reviews*, 2016, Vol. 65 : 662- 675.
- [65] Robert J., Hansman, Jr., Microwave ice prevention system, US Patent 4,365,131, 1982.
- [66] Elin Andersen, Elin Börjesson, Wind power in cold climate: A report, WSP Environment & Energy, 23 August 2011, Sweden.

- [67] Raul Ruiz de la Hermosa Gonzalez-Carrato, Fausto Pedro García Márquez, Jesús María Pinar, Maintenance management of icing blades in wind turbines, The Tenth International Conference on Condition Monitoring and Machinery Failure Prevention Technologies, CM 2013 and MFPT 2013, Kraków, Poland
- [68] Charles C. Ryerson, Ice protection of offshore platforms, Cold Regions Science and Technology 2011, Vol. 65: 97–110.
- [69] Zhenjun Wang, Recent progress on ultrasonic de-icing technique used for wind power generation, high-voltage transmission line and aircraft, Energy and Buildings, 2017, Vol.140 : 42–49.
- [70] Congbo Yin, Zhendong Zhang, Zhenjun Wang, Hui Guo, Numerical simulation and experimental validation of ultrasonic de-icing system for wind turbine blade, Applied Acoustics 2016, Vol.114 : 19–26.
- [71] Jared T. Soltis, Dr. Jose Palacios and Dr. Douglas E. Wolfe, Design and testing of an erosion resistant ultrasonic de-icing system for rotorcraft blades, Applied Research Laboratory, Pennsylvania State University, Technical report TR 14-007, Aug. 2013.

Chapter 3: Estimating the Volume of Frozen Water Droplets on A Cold Surface During the Phase Change With Thermal Image Processing[†]

[†] *The materials in this chapter were published in Measurement; 2021;183:109907. Authors include Ezieddin Madi, Dr. Kevin Pope, and Dr. Weimin Huang. Madi served as the primary author, contributing to conceptualization, methodology, software development, data curation, and drafting. Dr. Pope as a co-author provided valuable conceptual insights and expertise throughout the entire process, while Huang provided supervision, review, and editing as the primary supervisor.*

3.1 Introduction

In cold climates, supercooled water droplets can hit and freeze on structures' surfaces, leading to serious hazards [1]. Detecting and measuring ice accumulation on structures is a challenge that has been investigated for many years and attracted many researchers to test and examine different techniques and methods to obtain an effective method that can detect and measure a structure's ice load [1-12]. In our previous study, both ice sensing and de-icing methods were reviewed. The ice detection techniques included in the study were acoustic waves ice sensing, ultrasonic waves ice sensing, microwave ice sensing, optical ice sensing, thermal infrared ice sensing, capacitive ice sensing, and impedance ice sensing techniques. Each ice sensing technique was compared with all de-icing techniques to form an integrated system for ice detection and de-icing. The result of this comparison considered the infrared sensing method a promising technique. It can contribute to the ice sensing field because it is the only method that is a non-destructive method for remote ice sensing and can be integrated with an ice mitigation system in the workplace without physical contact [1]. This result was the first motivation for our interest in using the IR ice sensing technique in this study. The importance of the integrated system of ice detection and mitigation must not be limited to detecting ice but evaluating its amount as well so that the de-icing process can be activated in a controlled manner according to the amount of ice. Thus, the de-icing process cycle's duration time can be reduced and controlled, and the overall energy consumption and cost required for removing ice are reduced.

Expanding the IR technique's capability from just detecting ice to evaluating its amount was the second motivation for our interest in this study. The integrated system of ice detection and mitigation consists of three stages: detecting and extracting each deposited frozen droplet's data, tracking and controlling ice accumulation based on the received data, and using a de-icing unit to

remove the accumulated ice. The current study is focused on the first stage, while the other two stages will be the subject of our future work.

Infrared remote sensing techniques are based on the reception and analysis of the electromagnetic energy reflected, absorbed, or emitted by a surface. Data obtained by remote sensors can be used to retrieve features and parameters of the observed surface without physical contact. The use of infrared techniques for ice sensing goes back several decades. There are several infrared-based ice sensing methods published in the literature. For ease of comparison between them, Table (3.1) has been prepared, representing the functions they perform. The evaluation includes the necessary functions that the ice sensor should provide. The functions required for ice detection are remote sensing, wide area detection, detection of onset ice, ice measurement, and real time tracking.

Table (3.1) shows that all listed techniques have the feature of detecting ice presence remotely. The advantage of techniques [9- 12] is that they use cameras for wide vision detection and consider multiple point detectors. Only methods [2, 6, 12] can measure ice thickness, but they have shortcomings. Methods [2, 6] need an external light source above and close to the thin ice layer to measure the ice thickness that makes the method limited to close contact measurement and unsuitable for far distance measurements, and the disadvantages of method [12] are that it can only be used after the icing event to measure the accumulated ice on tower structures. Secondly, it needs to capture the images from three view angles, which makes the method complex. Most of the techniques use predefined information in the system to compute or predict a third variable such as wavelength data, to distinguish between ice and water. Another example, method [12], uses the dimensions of the tower structure as predefined information to measure the ice thickness. Predefined information can be considered a feature to predict a third variable. Techniques [2-7]

use a single point IR-detector and are not useful for wide area detection. Only methods [3, 9, 10] are considered as real time detectors because they track the change in surface temperature during an icing event, while method [11] tracks the ice surface temperature compared to the heated bed surface which is under the ice droplets. Even though techniques [9-12] offer some of the required functions for an ice detector, methods [9, 10, 11] cannot perform any kind of ice measurement and method [12] is not a real time tracking method. Based on this comparison, none of the studied methods can offer the complete requirement of ice detection functions simultaneously. It is imperative to continually innovate and develop methods that can concurrently detect, track, and perform ice load measurements.

Ice that accumulates on the outer surface of a structure is often caused by frozen supercooled water droplets of different sizes. Detecting multiple deposited iced droplets on a wide surface requires a visual technique, because it has a wide vision and can simultaneously track various water droplets. A thermal infrared camera can capture the latent heat energy released by water droplets when they collide with a cold surface. The thermal images can show high thermal radiation areas, which help locate deposited iced droplet locations on cold surfaces [3, 10]. Thus, the equivalent diameters of the deposited iced droplets can be extracted from the captured thermal image using image processing.

Several researchers noted that when a water droplet is deposited and freezes on a cold surface, its shape tends to be a spherical cap [13-16]. Once the contact angle and the droplet diameter are known, the droplet's volume can be calculated [17]. Furthermore, the droplet shape is affected by the solid's surface characteristics, droplet size, surface temperature, and ambient temperature [18-22]. The effects of these factors will be highlighted in detail in this study.

Since the freezing and solidification of a water droplet is a rapid process [23], measuring the contact angle and the iced droplet's base diameter during the freezing process is not a simple task using conventional methods. However, this task becomes more difficult and complicated when measuring many iced water droplets' contact angles simultaneously, considering the effects of temperature, droplet size, and surface roughness on each droplet's contact angle measurement. Frozen water droplets are countable elements and have properties such as contact angles with values that vary within a close range that statistical methods can handle. Therefore, using the arithmetic mean of contact angles and droplet group size method to obtain iced droplets' volumes can give good results with some acceptable uncertainty.

Currently there are two other remote methods to monitor ice. The satellite technique uses reflected microwave signals to track the changes of ice dimensions and often works at a very large distance to monitor a wide area in cold climate regions. The radar technique uses reflected microwave signals and works at a medium distance; it is commonly used in the marine field to track floating icebergs. However, the suggested IR ice sensing is a remote technique, works at a short distance with wide vision, and has some advantages compared to the mentioned remote sensing techniques. It can detect the iced droplet itself during phase change, not the medium that obstructs the signal. Also, it can offer the required functions of an ice detector. It can predict the onset icing represented by the first frozen droplet on a wide area of a cold surface. Also, it can detect the heat signature that is released from the deposition of supercooled water droplets on a cold surface and estimate the volume of a single iced droplet, a group of iced droplets, or the first layer of iced droplets covering the surface. It can also be adapted to work in an integrated ice sensing and mitigating system to track and control the ice load. Hence, the suggested method can be considered as a new contribution to the ice sensing techniques based on processed thermal

images and predefined information of CAs of the iced droplets deposited on a cold hydrophilic surface.

This chapter investigates and develops a detection technique and volume estimation of initially deposited iced droplets on a cold surface. It also includes an investigation of the effect of temperature and surface roughness on the shape of the droplet and a numerical analysis of a droplet size's effect on the contact angle. Also, the effect of substance thermal conductivity, wind speed, impact angle, and droplets' overlapping on the droplet behavior and geometry will be highlighted in the discussion section. In this study, the droplet diameter, droplet contact angle, and the droplet volume refers to the diameter, the contact angle, and the volume of a frozen droplet.

Table 3.1 A comparison between infrared ice detectors published in the literature

Reference no.	[2]	[3]	[4]	[5]	[6]	[7]	[8]	[9]	[10]	[11]	[12]
Published year	1989	1991	1998	2011	2012	2013	2016	2012	2013	2016	2017
Detector	Thermal	Thermal	Thermal	Thermal	Thermal	Thermal	Thermal	Thermal	Thermal Camera	Thermal Camera	Camera
No. Of detectors	1	1	1	3	1	1	1	1	1	1	3
Ice detector type	Single point	Single point	Single point	Single point	Single point	Single point	Single point	Multiple points	Multiple points	Multiple points	Multiple points
Ice detection	Yes	Yes	Yes	Yes	Yes	Yes	Yes	Yes	Yes	Yes	Yes
Wide area detection	No	No	No	No	No	No	No	Yes	Yes	Yes	Yes
Ice thickness	Yes (thin layer)	No	No	No	Yes (thin layer)	No	No	No	No	No	Yes
Real time track	No	Yes	No	No	No	No	No	Yes	Yes (interval)	Yes	No
Use predefined information	Wavelength data	—	Wavelength data	Wavelength data	Wavelength data	Wavelength data	Emissivity data	Historical data	Emissivity data	—	Structure dimensions
Sensing concept	IR absorb. diff.	latent heat emission	IR absorb. difference	IR absorb. difference	IR absorb. difference	Reflected & diffused near IR	Emissivity changes	Temp. distribut	Emissivity & temp. distribut.	Temp. distribut.	Predefined dimensions change
Workplace	Transparent flat surface	Blade surface	Road surface	Road surface	Transparent flat surface	Road surface	Blade surface	Lakes & rivers	Blade leading edge	Hot flat surface	Tower structure surface
Need external device	Light source	No	No	No	IR light source	No	Metallic surface	No	No	Heat bed	Dark background
Surface rotation	No	Unknown	No	No	No	No	Unknown	No	No	No	No
Position to target surface	Perpendicular	In front with angle	In front with angle	In front with angle	Perpendicular	In front with angle	In front with angle	Parallel	Parallel	Perpendicular	Perpendicular
Image process.	No	No	No	No	No	No	No	Yes	No	No	Yes
Simplicity	No	Yes	Yes	Yes	No	Yes	No	Yes	Yes	No	No

3.2 The Relation of The Droplet Shape and its Contact Angle

When a small supercooled droplet falls and is deposited on a cold surface, heat energy is released, due to the phase change's latent heat [27]. The deposited water droplet has a spherical shape, and when frozen, its tip tends to become a conical shape, as shown in Figure (3.1) [13, 14, 15, 16, 28, 29]. Since the droplet shape tends to be spherical, the volume of a droplet deposited on a surface can be calculated with the contact angle θ and radius r [17, 30].

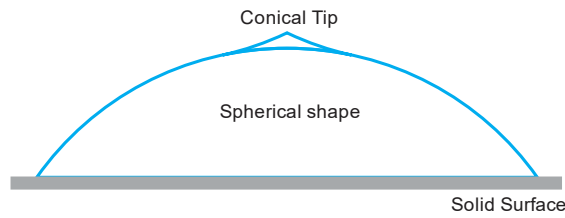


Figure 3.1 A diagram of a droplet shape.

It is possible to obtain the spherical cap volume if the cap is part of a complete sphere, as shown in Figure (3.2). The base radius of the spherical cap is r , while R is the radius of the full sphere, and h is the height from the center of the sphere to the base of the cap. By considering a circular slice πr^2 at the center of the sphere with a thickness dz , where z is the height of the circular slice above the center of the sphere with radius R , and r is the radial distance from the sphere's center at z [30], such that:

$$r^2 = R^2 - z^2 \quad (3.1)$$

By integrating the circular slice over the height of the spherical cap dh , as in Eq. (3.2), where $z = h$ and $z = R$ are the distances from the center of the sphere to the base of the cap and the top of the sphere respectively, which yields Eq. (3.3):

$$V_{sc} = \int_h^R \pi(R^2 - z^2) dz \quad (3.2)$$

$$V_{sc} = \pi \left(R^3 - \frac{1}{3}R^3 - R^2h + \frac{1}{3}h^3 \right) \quad (3.3)$$

The correlations below are used in Eq. (3.3) to eliminate h and R and create a volume equation that is dependent on the cap base radius r and contact angle θ . Therefore, this yields Eq. (3.7) for calculating the volume of a droplet [19], where r is the base radius of the deposited droplet and θ is the contact angle between the droplet base and the surface.

$$r^2 = R^2 - h^2 \quad (3.4)$$

$$h = R \cos(\theta) \quad (3.5)$$

$$R = \frac{r}{\sin(\theta)} \quad (3.6)$$

$$V_{droplet} = \frac{\pi r^3}{3} \left(\frac{2 - 3 \cos(\theta) + \cos^3(\theta)}{\sin^3(\theta)} \right) \quad (3.7)$$

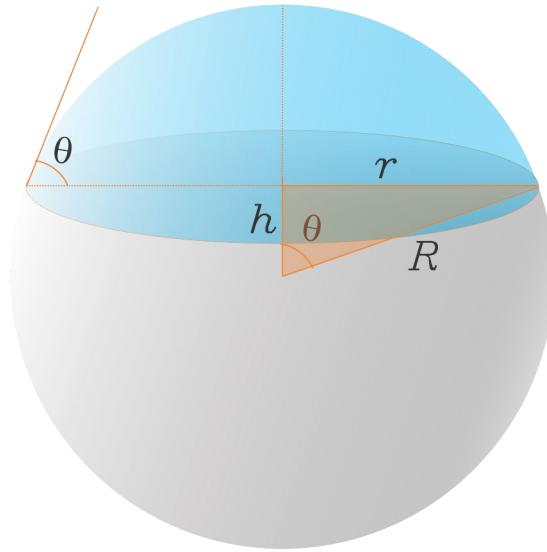


Figure 3.2 A diagram of a spherical cap as part of a complete sphere.

The droplet contact angle is defined as the angle formed between the tangent line of the spherical cap and the flat surface, as illustrated in Figure (3.3). Young's relation defined the contact angle by the formula:

$$\cos(\theta) = \frac{\gamma_{SA} - \gamma_{SL}}{\gamma_{LA}} \quad (3.8)$$

where γ_{SA} , γ_{SL} and γ_{LA} are gas-solid, solid-liquid and gas-liquid interfacial surface tension[20].

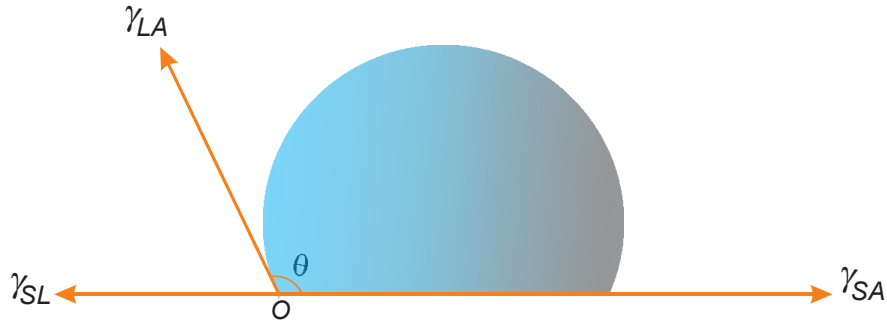


Figure 3.3 Schematic representing a water droplet on a solid flat surface.

However, the droplet shape is dependent on CA, and several factors are affecting this relation. Many studies stated that the factors that affect the droplet shape are surface characteristics, droplet size, cold surface temperature, and ambient temperature [18-22].

During the freezing process, a liquid-solid interface is formed at the bottom of the water droplet. The contact surface with the water droplet's solid surface keeps its initial shape and size [22, 31]. As time passes, water gradually turns into ice, and the liquid-solid interface moves upward. After the entire droplet is frozen, one small protrusion appears on the top of the ice bead. [32]. Most researchers agree that the water droplet shape is slightly affected by the solidification process caused by water and ice density differences [22].

Experimental results show that lowering the environmental and surface temperatures below the freezing point speed up the process of solidification and increase the adhesion strength [15,19]. However, as the temperature rises and approaches the freezing point, both the adhesion strength and the droplet's solidification time decrease [19], which slightly affects the contact angle. Therefore, keeping the ambient and surface temperatures low keeps the droplet solidified and preserves its shape and contact angle with the surface. Once the droplet entirely freezes, changing

the temperature within negative values has no significant impact on droplet shape if the droplet remains frozen.

As shown in Figure (3.4), the surface texture's roughening is considered the main factor that directly influences the droplet shape and, accordingly, the droplet's CA [19, 20]. Experiments have shown that the larger the surface roughness is, the more flattened shape the water droplet presents on the surface [23, 24], and accordingly, less CA with the surface [20]. Also, the freezing time of supercooled droplets increases on hydrophilic surfaces, compared to plain surfaces, due to the decrease of the droplet's contacted area with the surface [19, 33]. Also, the surface texture plays a vital role in the adhesion of droplets to the surface; the rougher the surface texture, the greater the area of adhesion of the droplet [26].

However, the surface texture of a material is not perfectly homogeneous [34, 35]. It seems to be a random process that depends on the manufacturing method and has the effect of an input parameter on the determination of parameters. This means the parameter itself is an unavoidable random variable that needs to be considered for tolerancing the surface texture. When tolerating rough surfaces, the parameter Ra is often used. It defines the arithmetic mean variation of the roughness profile, defined by Eq. (3.9) [36].

$$Ra = \frac{1}{n} \sum_{k=1}^n |r_k| \quad (3.9)$$

The relation of surface roughness and the CA, as shown in Figure (3.4), proves that the surface roughness is a vital factor and affects the shape and the CA of the droplet [26]. An illustrative example, as in Figure (3.4), shows that an uncertain surface texture of value ($\pm \delta Ra$) can lead to uncertainty in a droplet's CA of value ($\pm \delta CA$). This means that if a group of droplets of equal size are deposited on a surface, then their CA with the surface is the arithmetic mean of

their CAs. However, if the droplets are not similar in size, then the droplet sizes' effects on CA have to be considered.

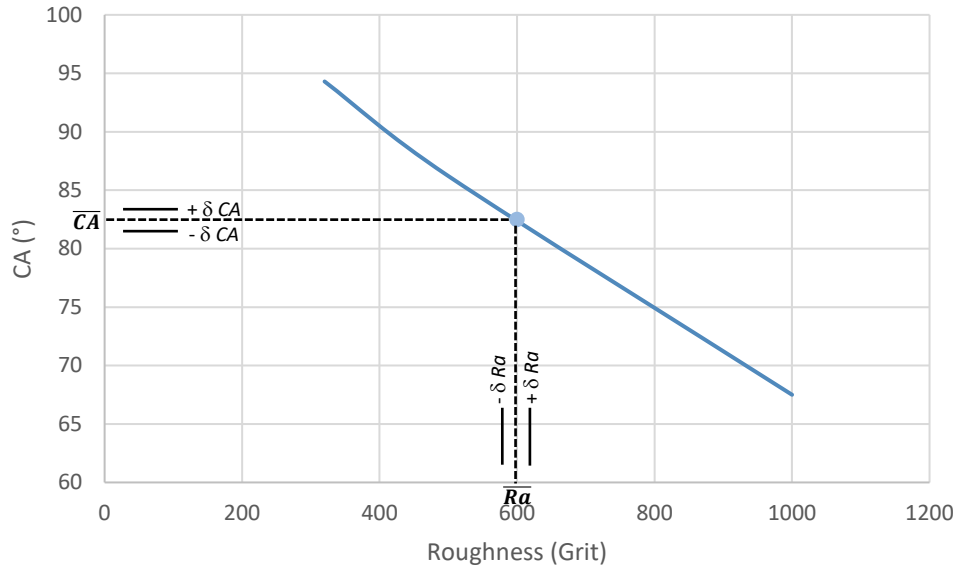


Figure 3.4 Droplet CAs on S.S-304 with different surface roughness- modified from [20].

The droplet size is another factor that affects the CA of the droplet. An experimental investigation of the impact of the droplet size on the CA concluded that as the droplet size increases, the CA decreases slightly [25], and the adhesion area to the surface increases. Other researchers stated that the water droplet's spherical shape appears more on the surface when the contact angle becomes large, and the base diameter becomes small. [23, 24]. Also, examination of the contact angle as a function of drop size has shown that the contact angle measured for 2- to 5-mm drops can differ significantly [21], but the cause it is not mentioned.

Fundamentally, as the droplet size increases, its volume increases as well. Using the relation of contact angle and the droplet's base diameter, represented in Eq. (3.7), a numerical analysis is performed to investigate the effect of droplet size on the CA and the base diameter. In this investigation, five droplets of various sizes are chosen, and their base diameters are 1mm,

1.5mm, 2mm, 2.5mm, and 3mm. It is assumed that they have been deposited on a perfectly homogeneous surface, to neglect the effect of the surface roughness uncertainty on their CAs, and their CAs with the surface range between $\angle 80^\circ$ and $\angle 70^\circ$ from the smallest droplet to the largest droplet. In the beginning, the base diameter is varied, while the CA is kept fixed at $\angle 75^\circ$. The relation of the base diameter to the volume is shown in Figure (3.5). Then the effect of varying the CA on the volume of each droplet's size is investigated, as shown in Figure (3.6). It is evident in Figure (3.5) that the base diameter has more influence on the volume, compared to the effect of the CA in Figure (3.6). As the base diameter slightly increases, the volume exponentially increases. Figure (3.6) shows that CA's effect on the small droplets' volume is almost negligible. The CA begins to affect the volume when the droplet size becomes large, as shown in Figure (3.6), for droplets of 2.5mm and 3mm. As the droplet size increases, the volume increases gradually by a small amount. It is concluded that the CA has an insignificant impact on small droplets, a slight impact on medium size droplets, and a considerable impact on large droplets.

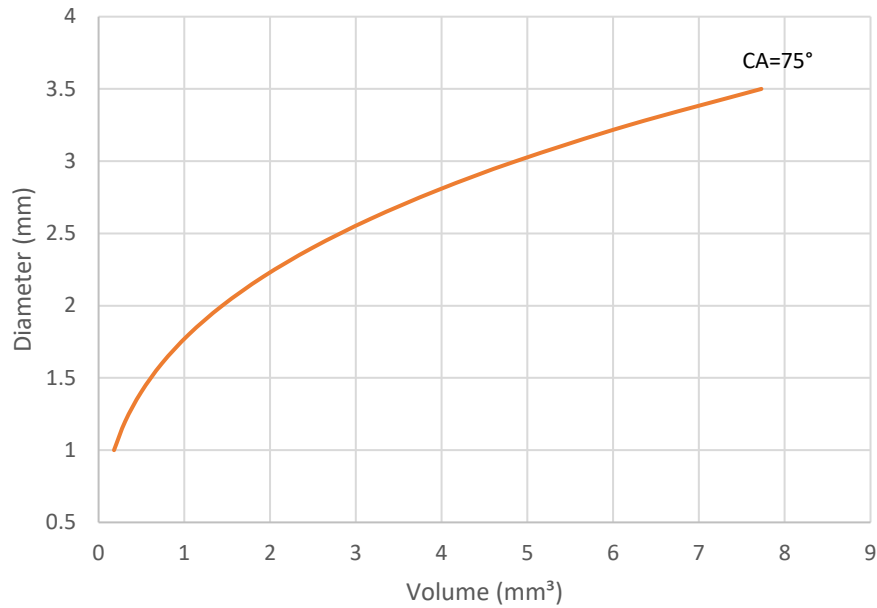


Figure 3.5 The effect of base diameter of the droplet on the volume with fixed CA.

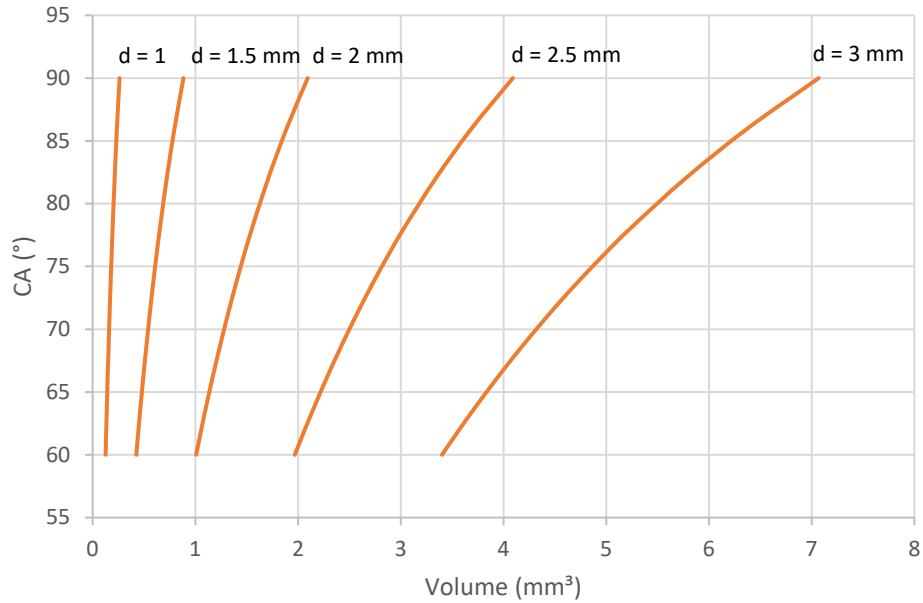


Figure 3.6 The effect of CA on the volume for various droplets' sizes.

To study the impact of the overall arithmetic mean of CAs on the droplets' volume, a numerical analysis based on Figure (3.6) is performed, and the result is as shown in Figure (3.7). According to the previous conclusion, as the droplet size increases, its CA slightly decreases. The slope line represents the relation of droplet size and its CA. Therefore, the smallest droplet has the maximum CA_{max} , the largest droplet has the minimum CA_{min} , and all CAs of other droplets must lie inside the shadow area between the mean line and the slope line. The diagram shows that when the droplet size is close to the center point of the tendency (CPT), its volume deviation value becomes very small. When the droplet's size is on the right side and far from the CPT point, its volume deviation value increases gradually. The results prove the previous conclusion and support the use of the arithmetic mean of CAs. The volume uncertainty in the large droplet, $d_{base} = 3\text{mm}$, is $\delta V = \pm 0.28\text{mm}^3$ and can be accepted if it is for a single droplet. If the quantity of water droplets of

the large size increases, then the large droplet's volume uncertainty is considered a substantial value that can magnify the total volume.

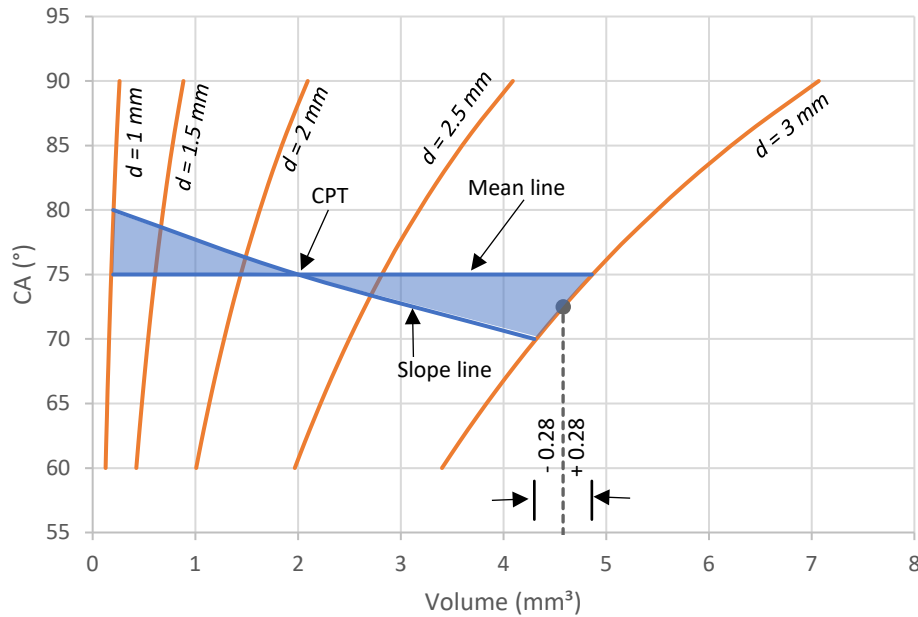


Figure 3.7 Illustration of the impact of the overall arithmetic mean of CAs on droplets' volume

In nature, water droplets are deposited onto surfaces in large numbers and different sizes. In Figure (3.8), which represents the distribution frequency of water droplets [37], the droplets are combined in groups based on their sizes. The medium-sized droplets, representing the major quantity, are in the middle, while the smallest and largest droplets, representing the minor quantities, are at the edges.

The uncertainty value of the large droplet's volume increases as the number of large droplets increases. Therefore, using a single estimated CA_{est} for all the droplets' sizes leads to a massive overestimation in the large droplets' volume, due to the accumulation of their uncertainty values, even if they are the minority. Thus, the droplet quantity has to be considered when obtaining the volume, especially for large droplets.

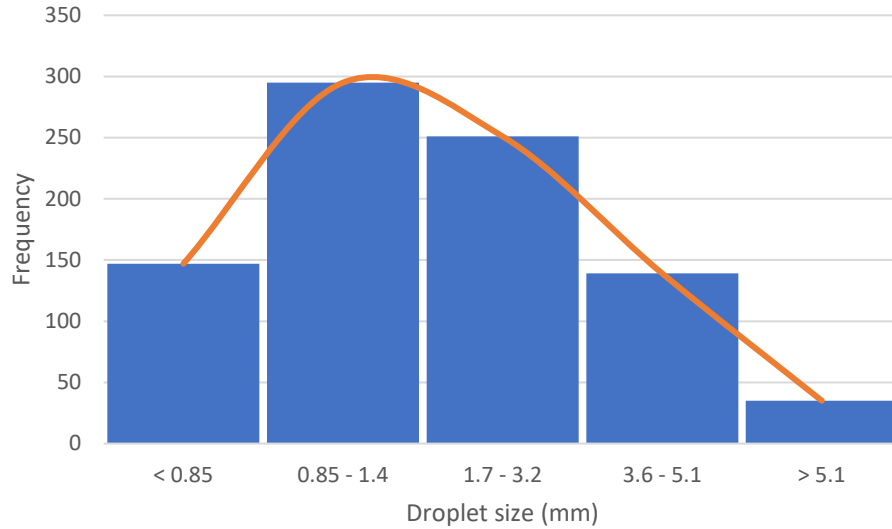


Figure 3.8 The distribution of raindrops' frequency according to their group size. [37].

A numerical analysis investigates the droplet quantity's effect on the volume and assumes the droplets' data, as listed in Table (3.2). The droplets are combined into groups and classified based on the droplets' sizes, as shown in Figure (3.9). The angles' range, which is the length between CA_{max} and CA_{min} , is divided into equal spacing angles. The smallest group size, GS-1, takes the largest CA_{max} , and the CAs of the rest of the GSs are obtained using Eq. (3.10). It is assumed that each GS has a quantity, as listed in Table (3.2).

$$CA_{current\ GS} = CA_{previous\ GS} - \frac{CA_{max} - CA_{min}}{No.\ of\ droplet\ groups - 1} \quad (3.10)$$

Table 3.2 The data of each group size

Group size	GS-1	GS-2	GS-3	GS-4	GS-5
Droplet size range (mm)	<1	1-1.5	1.5-2	2-2.5	2.5-3
CA_{est}	80°	77.5°	75°	72.5°	70°
Droplet quantity	40	20	12	8	5

By comparing the volume obtained by the overall mean CA method with the volume obtained by the estimated group CA method, as shown in Figure (3.10), it is found that there is a

slight increase in the small GSs' volumes obtained by group CA compared to the volume of the same GSs obtained by the overall mean CA, and that there is a significant decrease in the volume of the large GSs compared to the volume obtained by the overall mean method. This leads to the conclusion that the estimated group CA can reduce the overestimation volume of the large droplets. Thus, using the estimated group CA method can correct the volume and minimize the volume uncertainty.

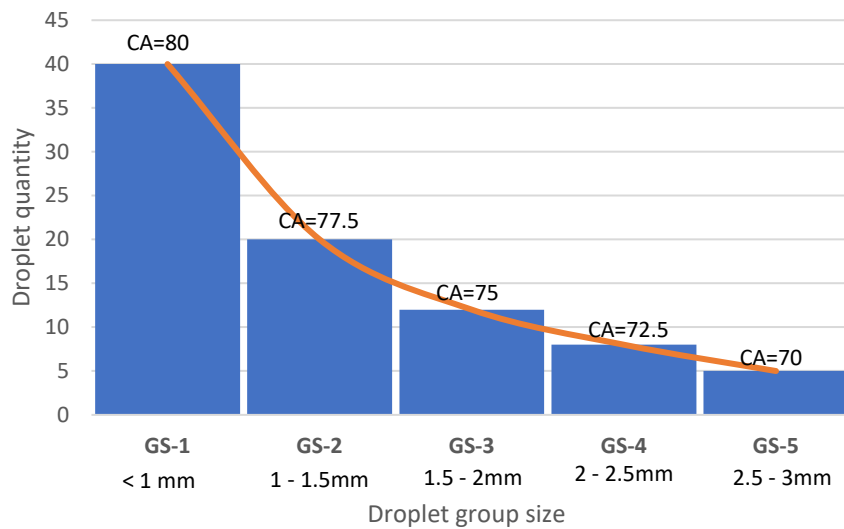


Figure 3.9 The distribution of CAs and droplet group sizes

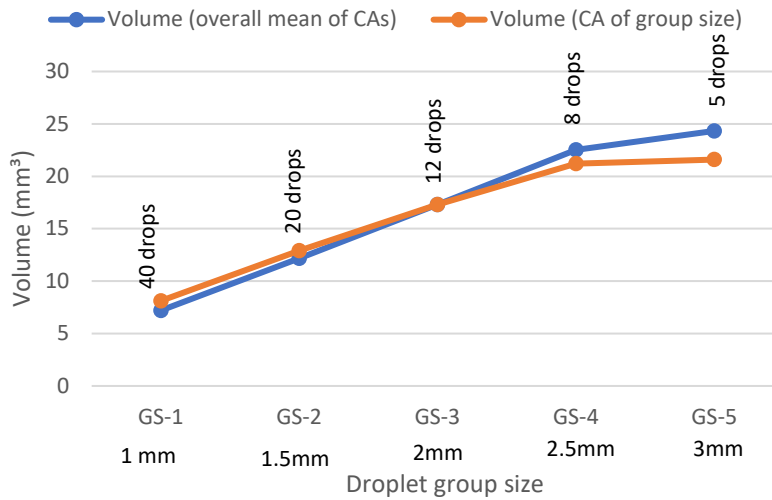


Figure 3.10 A comparison of volume obtained by the group CAs and the overall mean

Usually, contact angles are measured using the goniometer method, which is considered a simple method with some uncertainty [26, 38, 39]. However, several factors make it a difficult task. The first is that the deposition of water droplets on surfaces is often in large numbers and different sizes; this makes measuring the contact angles using the traditional method more difficult. Another factor is that exposing the surface to a dynamic environment may alter the surface texture's roughness. Thus, the contact angles of the droplets on site must be re-measured from time to time.

A visual estimation method is introduced, based on the correlation of the surface wettability type, droplet contact angle, and droplet shape, as shown in Table (3.3) [40- 43]. It also demonstrates that the larger the contact angle is, the more spherical the water droplet becomes on the surface [23, 24], and vice versa. The chart in Figure (3.11) represents the correlation of droplet shape and CA, and this can be used as a visual method to estimate a droplet contact angle according to its shape. The following sections provide an application example illustrating the use of the proposed method.

Table 3.3 A general comparison for the properties of material surface wettability

Surface type	Hydrophilic	Hydrophobic	Superhydrophobic
Contact angle range	0° - 90°	90° - 150°	150° - 180°
Surface energy	High -to-Moderate	Low	Weak
Surface finishing	Rough -to-Moderate	Fine	Very fine
Min. droplet shape	Flatten disk	Cap	High cap
Max. droplet shape	Cap	High cap	Sphere

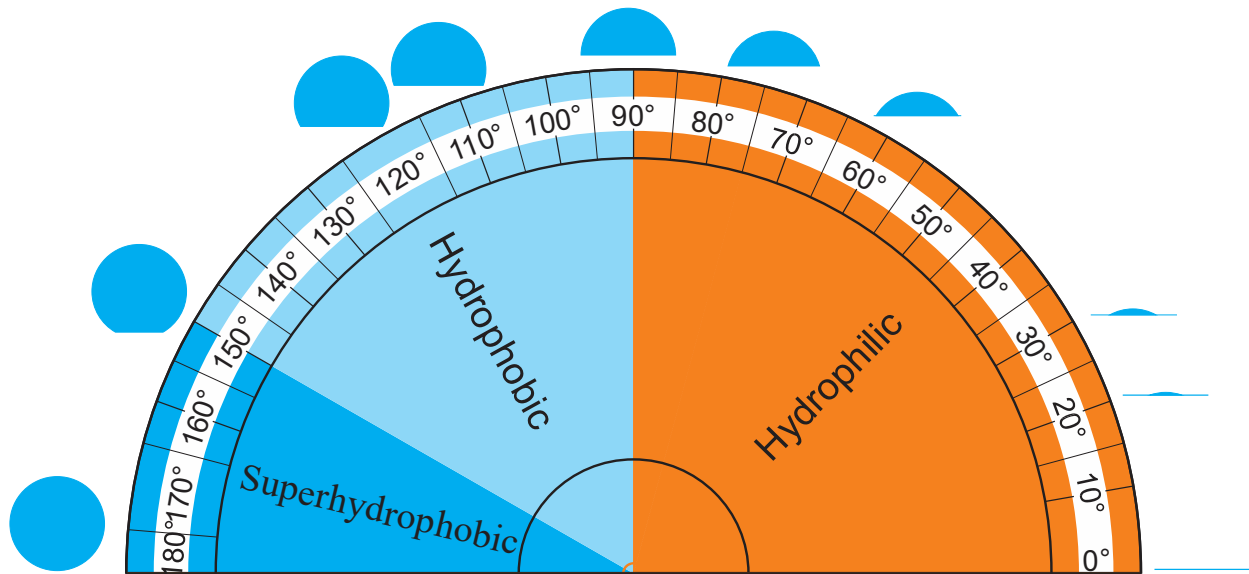


Figure 3.11 Wettability chart representing the relation of droplet shape and CA

3.3 Analyzing the Thermal Image of An Object

Infrared cameras detect and measure infrared radiation emitted by objects, which is related to their temperature and physical properties. The detector in the camera is typically made of materials such as indium antimonide, mercury cadmium telluride, or microbolometers that are sensitive to different wavelengths of infrared radiation. When an object emits infrared radiation, the camera lens focuses it onto the detector, which converts it into an electrical signal that is processed by the camera's electronics to produce an image of the object's temperature distribution. To detect thermal radiation from ice and cold surfaces, the camera should be sensitive to wavelengths in the long-wave infrared (LWIR) region of the electromagnetic spectrum, which corresponds to the peak wavelength of the radiation emitted by objects at temperatures between -40°C and +100°C.

Infrared cameras are capable of detecting heat transfer from droplets to surfaces and the heat released into the surrounding air. These cameras operate by detecting the thermal radiation emitted by objects with temperatures above absolute zero. The emitted thermal radiation is directly

proportional to the temperature of the object, enabling infrared cameras to measure the temperature of the droplet and the surface. Subsequently, image processing methods play a crucial role in isolating the droplet object from the background surface. Thus, the heat that is emitted from objects can be detected by thermal imaging. Moreover, the thermal energy released from the droplets deposited on a cold surface can be recorded using an infrared camera, as shown in Figure (3.12). The deposited droplets have sufficient contrast to be distinguished from the background [10].

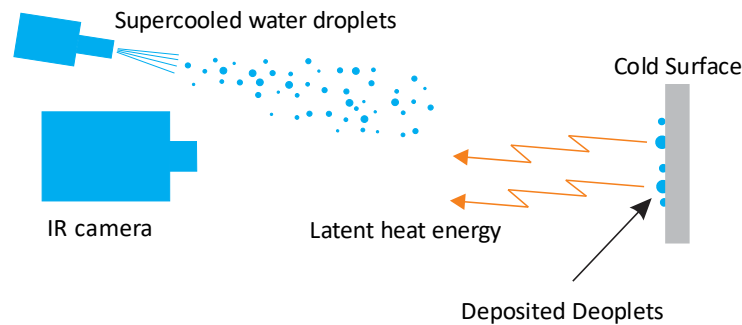


Figure 3.12 The principle of latent heat energy released from deposited supercooled water droplets

Thermographic images contain information about the target object, and also about the surroundings. Thus, to determine the target object's temperature, it needs to be identified in the image. The thermographic images need to be analyzed using image processing, and the relevant theory is divided into three stages, as shown in Figure (3.13).

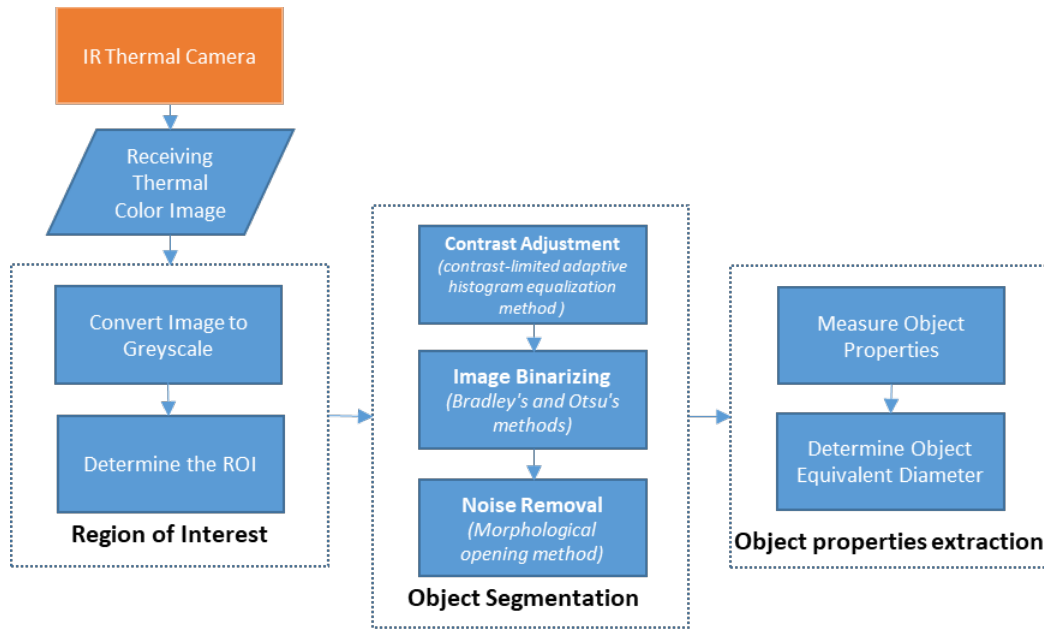


Figure 3.13 A flowchart sketch of the involved image processing stages

Once the thermal image is captured, a greyscale conversion is performed to obtain a greyscale image. The advantages of the greyscale image are that it has an appropriate focus and higher contrast, making objects more clearly visible [44].

Figure (3.14) shows the coordinates (x, y) and (x', y') , which are associated with the actual region of interest (ROI_{actual}) plane and the image's region of interest (ROI_{image}) plane, respectively. The axis z , perpendicular to the planes (x, y) and (x', y') , is the optical axis of the imaging setup [39]. The actual ROI_{actual} defines the true area's borders on the cold surface under consideration, and its dimensions are known. However, the image ROI_{image} area corresponds to the actual ROI_{actual} area; its area in pixels is known, and it is analyzed by image processing. The image ROI_{image} area must be defined according to the actual ROI_{actual} area before any other process is performed. Finally, the ROI_{image} area is cropped from the full captured image to speed image processing operations and monitor the changes that occur only in the ROI_{actual} area.

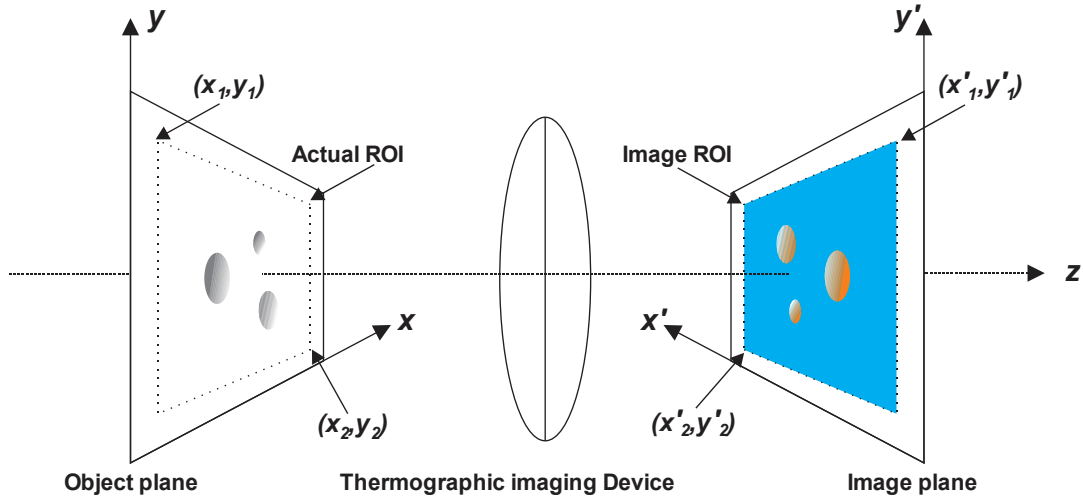


Figure 3.14 A diagram for the actual ROI_{actual} plane and its corresponding ROI_{image} image plane

The image properties that affect image quality are spatial image resolution and its quantization. Spatial resolution is the density of pixels in the image. The spatial calibration factor (SCF) is defined as the ratio of dimensions in millimeters to pixel dimensions [44, 47]. The spatial calibration factor can be calculated by Eq. (3.11).

$$SCF (mm^2/pixel) = \frac{\text{Actual area of ROI (mm}^2\text{)}}{\text{Image area of ROI (pixel)}} \quad (3.11)$$

Image segmentation aims to separate a digital image into independent partitions or regions that are more significant, to recognize the objects in an image. Segmentation occupies a very important role in image processing because it is often the vital first step that must be successfully taken before the next tasks, such as feature extraction and classification [39, 40]. Furthermore, contrast adjustment is performed to remap image intensity values to the full display range of the data type. An image with good contrast shows sharp differences between black and white. Here, the contrast-limited adaptive histogram equalization method (CLAHE) is performed, enhancing the contrast of each region of connected pixels representing a droplet. After performing the equalization, neighboring grouped pixels are combined using bilinear interpolation to eliminate artificially induced boundaries [47, 50, 51].

The enhanced image needs to be binarized using Bradley's [52] and Otsu's [53] techniques to extract the droplets' pixels. In Bradley's method, a locally adaptive threshold is applied to the image, which calculates a threshold for each pixel using the local mean intensity around the pixel neighborhood. Then a binary image is created by replacing all values above the determined threshold with 1s and setting all other values to 0s, as in Eq. (3.12). Otsu's method is performed to obtain the threshold value, which minimizes the thresholded black and white pixels' intraclass variance. Now, the returned image is black and white and is represented by a logical matrix with the same size as the original ROI image. A droplet image is a higher contrast spot in the binarized image than are the rest of other background areas. This spot is represented in the binarized image by a group of pixels attached to each other, or in other words, they are connected pixels to comprise an object figure [47, 50].

$$Z(a, b) = \begin{cases} 1, & I(x, y) > T_{thr} \\ 0, & I(x, y) < T_{thr} \end{cases} \quad (3.12)$$

where $I(x, y)$ is the input image, $Z(a, b)$ is the output image, and T_{thr} is the threshold value.

Unfortunately, the binarized image still has some noise; it is necessary to remove this noise from the image, and some noise sizes are close to small droplets, which are tiny droplets and can be neglected. In this step, the small objects with sizes of less than 10 pixels are considered neglected objects and removed from the binarized image, using the morphological opening method. The objects which have a larger size are preserved. The open morphological operation is an erosion followed by a dilation. All connected pixels representing a droplet object are kept if the number of the object's pixels is greater than 10. However, all foreground pixels that cannot be reached by the object's structure will be eroded away [47, 50]. Figure (3.15) shows the mentioned stages of image processing.

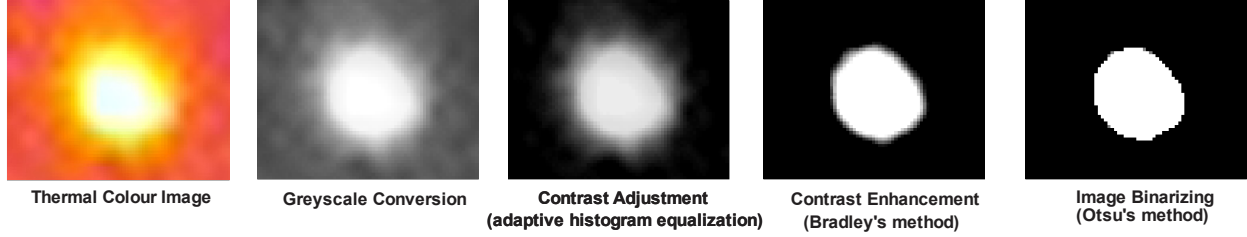


Figure 3.15 An illustration of the stages of a processed thermographic image

Finally, the image is in black and white, and it is possible to measure the objects' properties and features in the image. Using Matlab, all objects in the ROI area are labeled, as in Eq, (12) [46], where N is the number of objects representing the number of droplets in the image.

$$Object (1), Object (2), \dots, Object (N) \quad (3.13)$$

A structure array is then created by MATLAB to hold the values of the objects' extracted properties. The object properties can be obtained directly by MATLAB code. The main properties that are considered in our study and which can be extracted from the black and white image are as follows:

One property is the *object centroid*. It is the center of the object (x,y) where each object's center is located in the ROI image.

$$(x, y)_{Object(1)}, (x, y)_{Object(2)}, \dots, (x, y)_{Object(N)} \quad (3.14)$$

The second property is the *object area*, which is the number of white pixels (n) attached and forms the object (i); the area is represented by Eq.(3.15).

$$Area_{Object(i)} = \sum_{k=1}^{k=n} Pixel(k)_{Object(i)} \quad (3.15)$$

The equivalent diameter (d_{eqv}) of an irregular circular shape is the diameter of a circle, the area of which is the same as that of this irregular circular shape, as shown in Figure (3.16). Also, it represents the diameter of a regular circuit. The diameter based on the equivalent circular area can be expressed by Eq. (3.16).

$$d_{eqv}(i) = \sqrt{\frac{4 \times Area_{Object(i)}}{\pi}} \times SCF \quad (3.16)$$

where the equivalent diameter of Object(*i*) is d_{eqv} in *mm*, the area of Object(*i*) is $Area_{Object(i)}$ in pixels, and the spatial calibration factor is SCF in ($mm^2/pixels$).

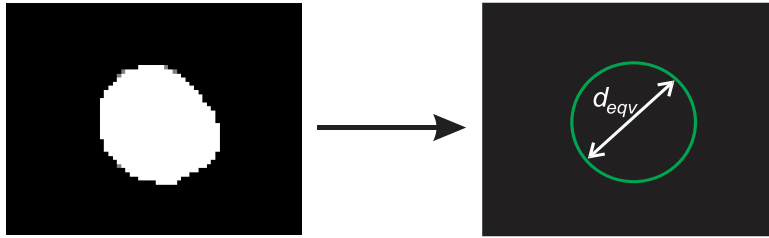


Figure 3.16 Calculating the equivalent diameter from a droplet's object

3.4 Experimental Method

An experiment was conducted to verify the estimated CAs obtained by the group CA method and the droplet's base diameter obtained by the thermal image analyzing method to find the droplet volume. The upper and the lower CAs are estimated visually from the proposed surface wettability chart, and the equivalent diameter is extracted from the droplet thermal image using image processing techniques. Figure (3.17) illustrates the experiment, conducted inside a cold room. The experiment's apparatus consists of a solid surface, a thermal infrared camera (Flir E60), a spray bottle, a camera (Canon 7D), a laptop, a T-type thermocouple, Matlab software, and Flir sdk.

The solid surface is made from fiberglass covered by fiberglass tape, with a hydrophilic surface to make the deposited droplets on the surface form a shape close to spherical cap shape. The water inside the bottle is sprayed through a nozzle by pushing a finger trigger. The nozzle's opening is adjusted left or right to allow the desired amount of water to spray. The camera (Canon 7D) is used to capture a side view photograph for each deposited droplet.

The solid surface is fixed to a pole that stands on the floor in front of the fan. The infrared camera is placed inside an insulated box with a transparent window on one side, facing the solid surface. The experiment's configuration was set up according to Figure (3.17).

Table 3.4 The operating conditions of the experiment

ROI W x H (mm)	Water Temp	Cold Room Temp	Surface Temp	Camera Distance (m)	Camera Emissivity	Wind Speed (m/s)
70 x 50	2°	-15°	-12°	1	0.95	4

There are some requirements for the experiment which must be addressed before beginning the experiment. The IR camera parameters that affect image quality and measurement accuracy, have to be set and adjusted and they are emissivity, focal length, target distance, and surrounding temperature. The actual ROI_{actual} on the surface is defined, along with its dimension (70mm X 50mm). However, the image ROI_{image} is set according to the rectangle that appears in the active camera's view. This rectangle is adjusted to match the area of the actual ROI_{actual} that appears during the adjustment, and then the adjusted region is saved in the camera's memory. The water in the bottle has been cooled to slightly above the freezing point. The nozzle's opening has been adjusted to generate a single spurt of different sizes of water droplets that have a sufficient acceleration force to reach the solid surface. A T-type thermocouple is buried beneath the thin tape covering the solid surface. It is used to measure the temperature of the cold surface throughout the experiment's period.

When the experiment's operating conditions are achieved and become stable, as demonstrated in Table (3.4), the IR camera is activated, and the events on the solid surface are recorded on the laptop. A few water droplets are then sprayed toward the solid surface by pressing the bottle's finger trigger. It is observed that the time for water droplets to reach the cold surface and collide with it is less than 2 seconds. During this trip, the water droplets have been exposed to

both a very low room temperature and cold wind, which play roles in reducing the cold droplets' temperature before they collide with the cold surface. Only a few of the droplets hit and are deposited on the solid surface, while the rest remain outside the target surface. The freezing and impact behavior of the droplets on the target surface is observed and recorded. When the droplets are entirely frozen, the experiment is stopped.

To capture photographs for the droplets, the solid surface is removed from the stand where the frozen droplets are deposited; then, a photo is taken of each deposited droplet to measure its base diameter and its contact angle in a further procedure. The photographed objects, as shown in Figure (3.18), include the side view of the droplet and a measuring tool on the millimeter scale. Both objects are at the same distance from the camera's lens to find the dimensional measurements of both objects more accurately.

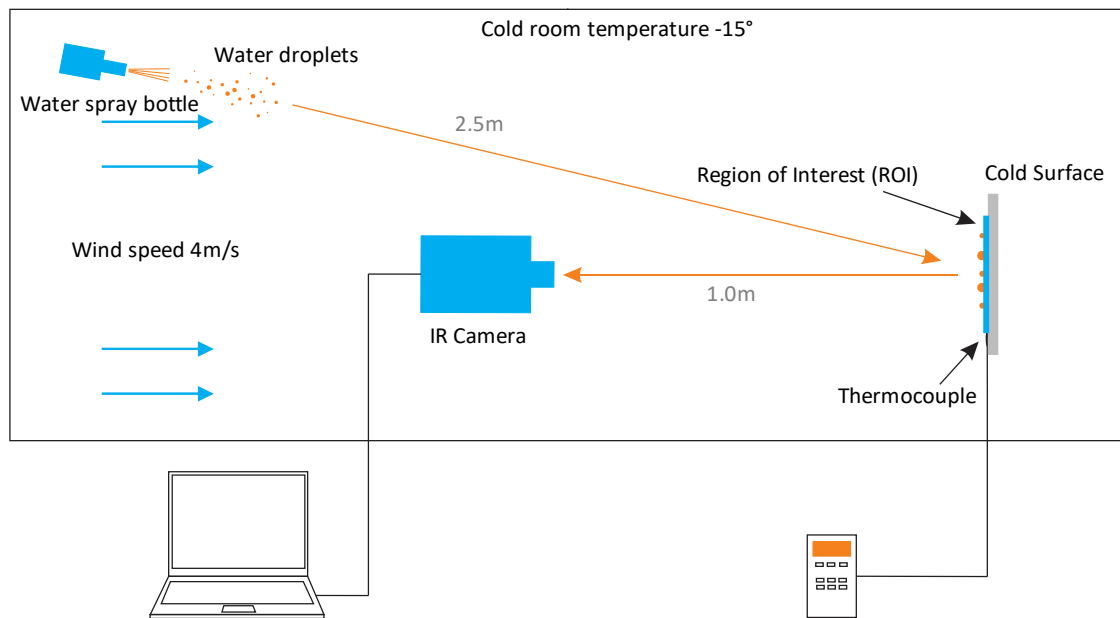


Figure 3.17 Thermal imaging experiment of droplets deposition on a cold surface

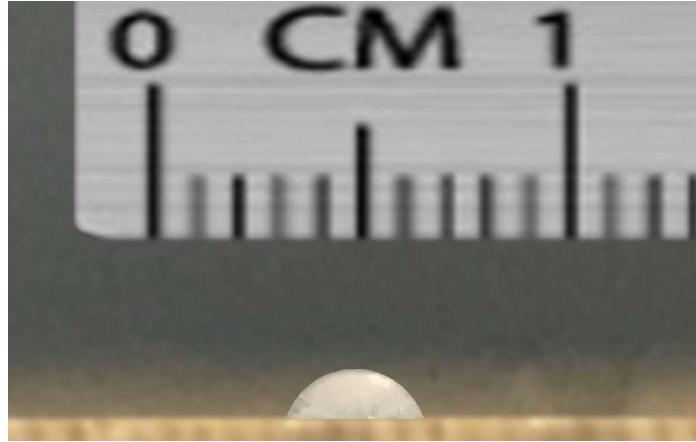


Figure 3.18 A photograph of a side view of a deposited droplet with a measuring tool

3.4.1 Contact Angle Estimation and Equivalent Diameter Extraction Methods

The images of the actual droplet profile shapes are arranged, as shown in Figure (3.19), and are visually compared to known droplet profile shapes of the Figure (3.11) chart. It is clear that all image profile shapes are not even close to the shape of $\angle 90^\circ$ and are not less than the shape of $\angle 60^\circ$. All image profile shapes are greater than the shape of $\angle 60^\circ$, and mostly are close to the shape of $\angle 75^\circ$. Therefore, it seems that all contact angles of the deposited droplets lie between $\angle 65^\circ$ and $\angle 75^\circ$. This means the surface's wettability is in the upper range of the hydrophilic type in the chart shown in Figure (3.11).

Droplet	7	6	5	4	3	2	1
Image							
Shape							
CA	90°		75°				60°

Figure 3.19 A comparison of actual droplet shapes with known shapes from surface wettability chart

All the droplets are clear water deposited on the same surface material and subjected to the same experimental conditions, so that their shapes and CAs must be close if they have the same size. The CA value varies according to the droplet's size. As droplet size increases, the droplet

base diameter increases, and the CA decreases. According to this principle, the smallest droplet, which is group size GS-1, takes the upper contact angle CA_{max} , and the rest of the CAs are obtained by Eq. (3.10). Table (3.5) lists the distribution of CAs according to their group sizes.

Table 3.5 The droplet data of each group size

Group size	GS-1	GS-2	GS-3	GS-4	GS-5
Droplet size range (mm)	>1.25	1.25-1.75	1.75-2.25	2.25-2.75	2.75-3.25
CA_{est}	75°	72.5°	70°	67.5°	65°
Droplet quantity	1	2	2	1	1

The thermal image of each deposited droplet captured by the IR camera is analyzed individually using the previously mentioned image processing methods, by MATLAB code. The image ROI_{image} is determined and cropped from the entire image, and the spatial calibration factor (SCF) is calculated using Eq. (3.11) and it is found $0.0592mm^2/pixel$. Then the thermal image is converted to greyscale, as shown in Figure (3.20). The next step consists of an image normalization to enhance the image's contrast using a predetermined threshold algorithm. The image is then binarized by replacing all values above the predetermined adaptive and Otsu thresholds with 1s and setting all other values to 0s, as shown in Figure (3.21).

The binarized image is a logical matrix of 1s and 0s and has the same size as the original ROI image. In the binarized image, each droplet spot is represented by a group of connected white pixels. The next step is noise removal. The binarized image still has some noise, and some noise size is close to small droplets. Any tiny droplets/ particles droplets with a size of less than 10 pixels are neglected and removed from the binarized image using morphological opening methods. That means the minimum diameter of a deposited droplet that can be extracted is around 0.6mm, which is 10 pixels. Any particles less than this limit will be considered as noise, and they are eliminated. This feature can be adjusted, and it depends on the IR camera resolution.

In contrast, the objects which have a larger size are preserved. The final step is the object properties extraction. The pixels inside the contour of each droplet are computed. The equivalent diameter d_{eqv} for each droplet is extracted and listed in Table (3.6).

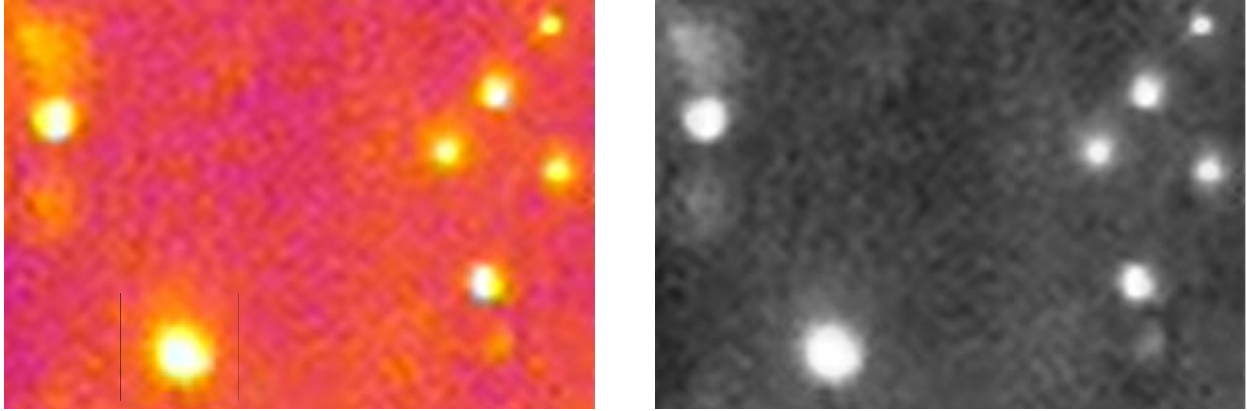


Figure 3.20 Thermographic image and its image converted to greyscale, representing ROI

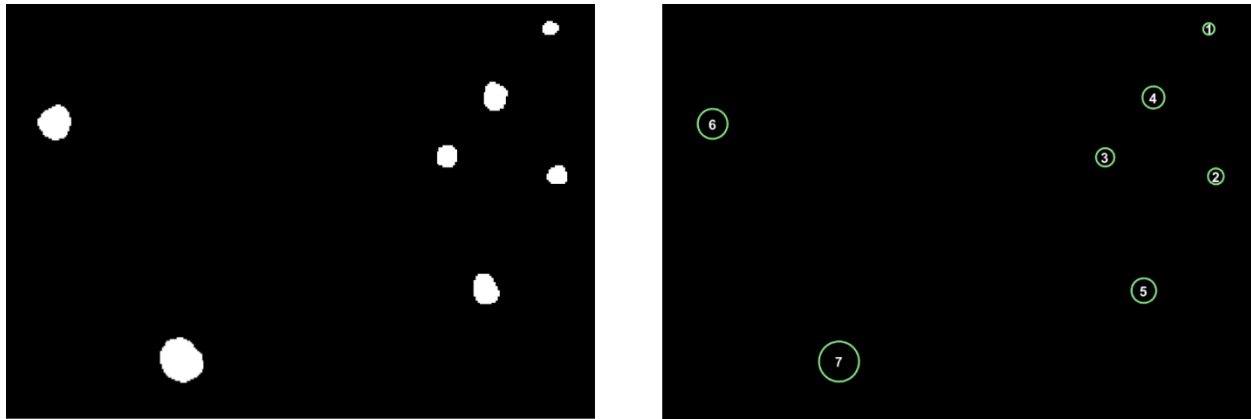


Figure 3.21 B/W image contains droplet's objects and its equivalent circle's images

Table 3.6 Droplet volume based on image analysis of equivalent diameter and observed CA

Droplet	Group size	CA_{est} (Deg)	d_{eqv} (mm)	V (mm ³)
1	GS-1	75	1.13	0.260
2	GS-2	72.5	1.46	0.528
3	GS-2	72.5	1.66	0.777
4	GS-3	70	1.93	1.150
5	GS-3	70	2.10	1.481
6	GS-4	67.5	2.81	3.344
7	GS-5	65	3.37	5.435

3.4.2 Validation of the Estimated Results

The numerical results obtained by the estimated method need to be validated. An experiment is conducted to measure the contact angle and diameter for each deposited droplet. A side view photograph for each deposited droplet is used in this experiment, and CorelPaint software is employed to measure the dimension in pixels.

On each droplet image, shown in Figure (3.22), a tangent line is drawn starting from the base of the droplet's spherical shape to where it touches a point around the droplet's circumference. The contact angle CA_{mrd} between the base and the tangent line is measured. The readings of the measurements are listed in Table (3.7).

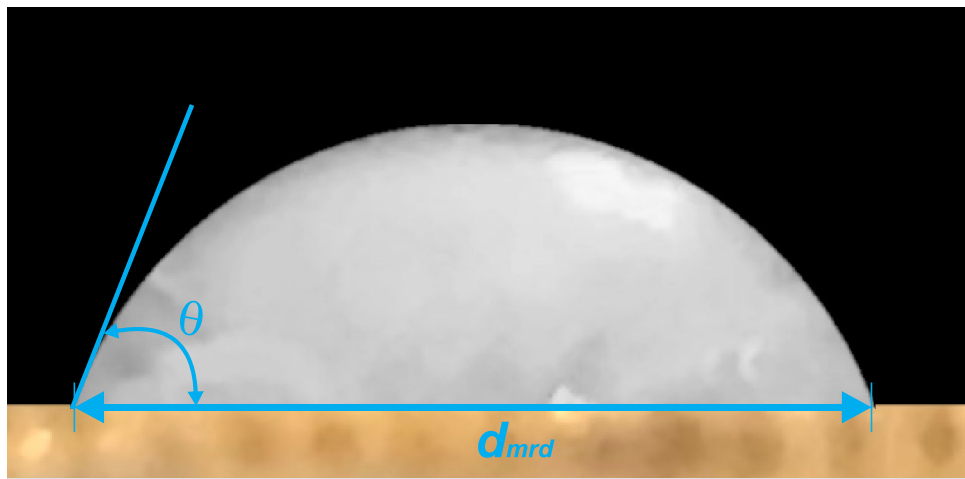


Figure 3.22 Side view image for a droplet

Furthermore, for each droplet image, a straight line is drawn to highlight the droplet base d_{mrd} , as shown in Figure (3.22). The number of pixels is used to count the diameter of the droplet base. Then, the droplet base diameter is calculated in millimeters according to an object of known dimension in the image, using Eq. (3.17) below, and the results are listed in Table (3.7).

$$d_{mrd}(mm) = \frac{d_{mrd}(\text{pixels}) \times \text{Known object dimension (mm)}}{\text{known object dimension (pixels)}} \quad (3.17)$$

Table 3.7 Droplet volume based on measured droplet CA and diameter

Droplet	Group size	CA _{mrd} (Deg)	d _{mrd} (mm)	V (mm ³)
1	GS-1	70.55	1.08	0.204
2	GS-2	71.27	1.35	0.406
3	GS-2	76.83	1.47	0.598
4	GS-3	74.57	1.73	0.924
5	GS-3	69.16	1.96	1.181
6	GS-4	68.24	2.63	2.791
7	GS-5	69.14	3.15	4.898

3.5 Results and Discussion

Figure (3.20) shows the droplets' distribution on the target surface and reveals large droplets in the lower part, and small ones in the upper part of the target. Droplets' sprays are typically characterized by statistical quantities obtained from size and velocity measurements of many individual droplets [54]. The forces acting on a small droplet moving in the steady flow of air include droplet drag, weight, and buoyancy. The predominant force exerted on a droplet is the fluid dynamic drag resulting from the relative velocity of air with respect to the droplet [55]. In dense sprays, when the droplet spacings are small, the drag coefficient of each drop is significantly altered. The droplet interaction has a leading order effect on the dynamics [56]. Collisions of this type have an influence on the droplet size spectrum in a spray, since they make droplets of given sizes disappear and produce larger droplets [56]. The larger the droplets, the greater their inertia becomes, which leads to a significant difference between the velocity of larger and smaller drops [56]. So, the droplet motion can no longer be evaluated without taking into account the crossing trajectories 'effect. The trajectory path of the large droplet becomes lower than the trajectory path of the small droplets. The large droplets attempt to fall on a nearby wall while small droplets attempt to take a higher path and fall further away [57].

The readings resulting from the experiment shown in Tables (3.6, 3.7) are used to obtain the uncertainties of each droplet's diameter and contact angle. The results are listed in Table (3.8).

Table 3.8 Droplet dimension uncertainties based on averaging of measured and estimated values d & θ°

Droplet	\bar{d} (mm)	δd (mm)	$\bar{\theta}^\circ$	$\delta\theta^\circ$
1	1.11	± 0.02	72.78	± 2.23
2	1.41	± 0.05	71.89	± 0.62
3	1.57	± 0.10	74.67	± 2.17
4	1.83	± 0.10	72.29	± 2.29
5	2.03	± 0.07	69.58	± 0.42
6	2.72	± 0.09	67.87	± 0.37
7	3.26	± 0.11	67.07	± 2.07

For simplicity, to calculate the volume uncertainties, the geometric correlations between the droplet radius and droplet height in Eq. (3.18) and Eq. (3.19) are used to obtain the average volume and derive the volume uncertainty formulas.

$$h = \frac{r}{\tan(\theta)} - \frac{r}{\sin(\theta)} \quad (3.18)$$

$$V = \frac{\pi h}{6}(3r^2 + h^2) \quad (3.19)$$

where r , θ and h are radius, contact angle, and height of the deposited droplet, respectively, and the volume uncertainty δV is calculated using Eqs. (3.20), (3.21), and (3.22):

$$\frac{\delta V}{V} = \sqrt{\left(\frac{\delta A}{A}\right)^2 + \left(\frac{\delta B}{B}\right)^2} \quad (3.20)$$

$$\frac{\delta A}{A} = \sqrt{\left(\frac{2\delta r}{r}\right)^2 + \left(\frac{\delta h}{h}\right)^2} \quad (3.21)$$

$$\frac{\delta B}{B} = \frac{3\delta h}{h} \quad (3.22)$$

Table 3.9 Droplet volume uncertainties based on averaging of measured and estimated values d & h

Droplet	\bar{d} (mm)	δd (mm)	\bar{h} (mm)	δh (mm)	\bar{V} (mm ³)	δV (mm ³)
1	1.11	± 0.02	0.41	± 0.026	0.23	± 0.05
2	1.41	± 0.05	0.51	± 0.026	0.47	± 0.10
3	1.57	± 0.10	0.60	± 0.013	0.69	± 0.18
4	1.83	± 0.10	0.67	± 0.009	1.04	± 0.23
5	2.03	± 0.07	0.71	± 0.030	1.34	± 0.25
6	2.72	± 0.09	0.91	± 0.024	3.04	± 0.49
7	3.26	± 0.11	1.08	± 0.006	5.17	± 0.72

Table (3.9) lists the average and the uncertainty of the droplet diameter, height, and volume, respectively. The results show that droplets 1, 3, 4, and 7 have the highest CA uncertainty, $\pm 2.23^\circ$, $\pm 2.17^\circ$, $\pm 2.29^\circ$, and $\pm 2.07^\circ$ respectively, and the rest of the CAs' uncertainties are low. The droplet height, as shown in Table (3.9), increases as droplet size increases. This leads to the conclusion that the CA has a role of forming the curve shape of the droplet, but has a slight impact on the droplet height, compared to the effect of diameter. This finding is also confirmed in most of the droplet profile shapes shown in Figure (3.23), where the tip of the estimated profile is higher than the tip of the measured profile, due to the effect of the d_{eqv} .

Table (3.9) shows that the droplets' volumes increase as the droplet sizes increase. Also, the volume uncertainty increases as the droplet size increases, and Figures (3.23) and (3.24) confirm this result caused by the uncertainty of the base diameter d_{eqv} .

Although the droplets of groups GS-2 and GS-3 in Figures (3.24) and (3.25) have a double quantity and the droplets of groups GS-4 and GS-5 have a single quantity, the volumes of the large size groups, GS-4 and GS-5, are much greater than the volumes of small size groups, GS-2 and GS-3.

Figure (3.24) illustrates the validity of the volume results obtained by the estimated group CA and actual diameter d_{mrd} , compared to the actual volume results. The droplets are classified and combined into groups based on the diameter size. This shows that the volume deviation between the two curves is almost negligible for the small size droplets of groups GS-1, GS-2, and GS-3. The estimated volume starts to be underestimated gradually, starting from group GS-4, and becomes $\pm 0.23\text{mm}^3$ at group GS-5. This reduction in the volume of the large droplets, as shown in Figure (3.25), can play a role in reducing the overestimation of volume caused by the uncertainty of the d_{eqv} extracted from the thermal image.

Figure (3.25) shows that the volume deviation between two curves increases slightly from group GS-1 to GS-2. It is noted that the diameter uncertainty plays the primary role in the uncertainty of the droplets' volumes, whereas the uncertainty of the CA_{est} plays an insignificant role. It can be concluded that using both the visual estimated CAs obtained by the wettability chart and the estimated group CAs methods can help to obtain the volumes of a group of droplets of different sizes with minimal uncertainties.

Note, from both droplet profiles in Figure (3.23) and the volume curves in Figure (3.24), that the equivalent diameter d_{eqv} in all estimated profiles is always slightly higher than the measured diameter d_{mrd} . This overestimation is also noted in Table (3.9), which shows that diameter uncertainty δd increases as the droplet's base diameter increases. It is clear that there is an overestimation in the estimated volume, by an average of 19%. The repetition and the convergence of this overestimation in all readings are caused by the extracted equivalent diameter from the thermal image, which is always greater than the measured diameter. It is a systematic error caused by several factors that can be explained.

Fundamentally, the droplet thermal image does not represent the droplet's actual image, but rather the thermal distribution map for both the deposited droplet and the cold surface. The illustrative example in Figure (3.26) shows the droplet's thermal distribution in four regions to understand the thermal interference between the droplet's outer edge and surface. The ranges of brightness intensity in these regions are read using image processing tools of MATLAB. In region (A and B) this is 255-225, and in region (C and D), 140-225. The highest temperatures are at the center of each droplet, and are represented in the image by the highest brightness intensity, as shown in regions (A, B). In contrast, the lowest temperatures are at the edge of the droplet, and are represented in the image by the lowest brightness intensity, regions (C, D). The brightness intensity fades gradually, according to the amount of heat energy transferred from the water droplet to the solid surface. The amount of this transferred heat depends on the size of the deposited water droplet.

Region (D), as shown in Figure (3.26), surrounds the outer edge of droplet region (C), and has a brightness close to the intensity of the outer edge of region (C), due to the similarity of temperature degrees in this area. This similarity causes the droplet diameter from the thermal image to be measured incorrectly and enlarges the diameter length. This effect is reduced by applying the mean intensity thresholding value to the image. However, it cannot delete it completely, and it still has a slight effect on the accuracy of measuring the equivalent diameter d_{eqv} when extracted from the thermal image.

Another factor is the noises in the image where some noise pixels are attached or close to the actual droplet pixels, and there is no such method to eliminate them. The undesirable noises become part of the pixels that form the droplet image, which increases the length of the equivalent diameter d_{eqv} when extracted from the thermal image.

Image resolution is another factor that can cause inaccurate measurement. Usually, images of objects are represented by the number of pixels that form the object's shape in the image. Clearly, when more pixels represent the object in the image, the object's image quality increases and becomes more explicit, and vice versa. Low-resolution images can cause inaccurate measurements due to image blurring, and when the scale of the pixel unit's spatial representation is low.

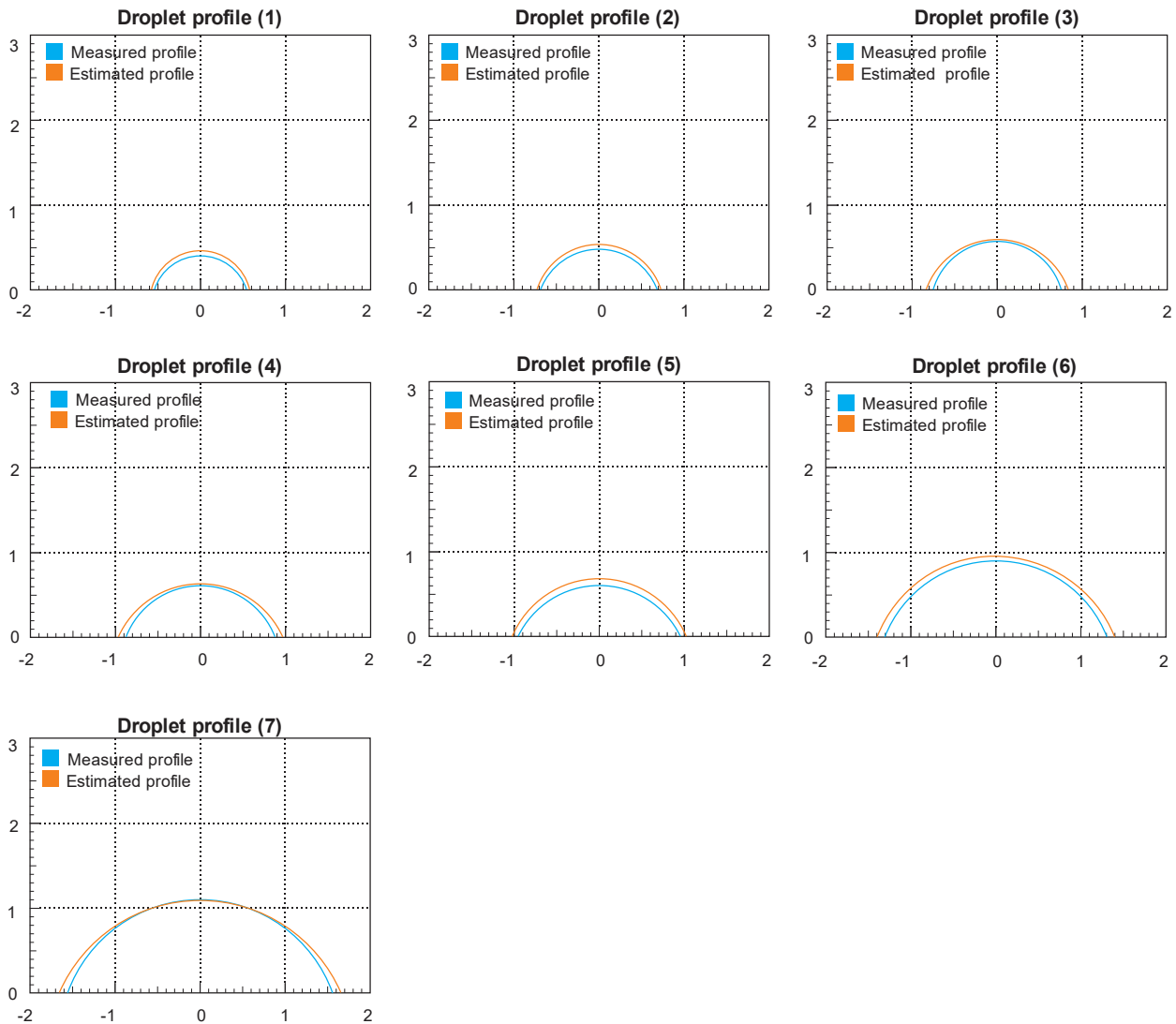


Figure 3.23 Measured and estimated droplet profile diagrams

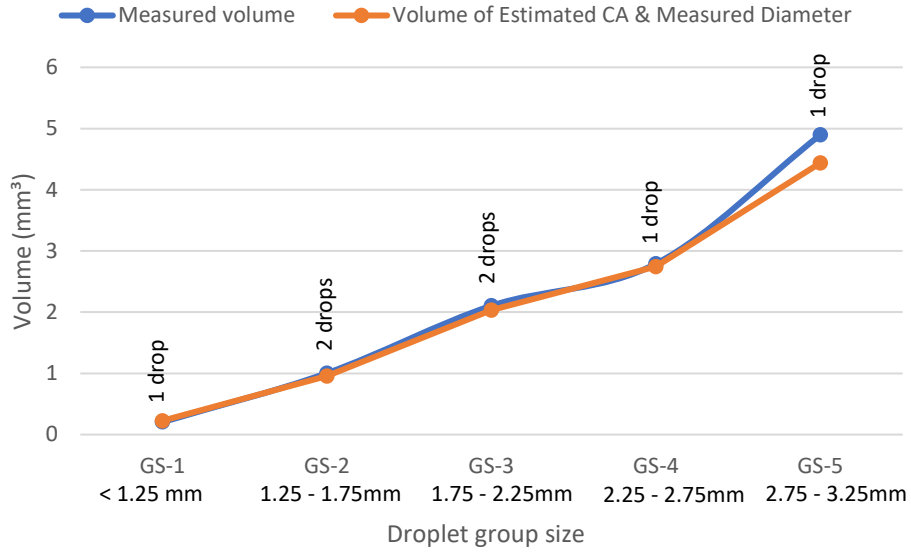


Figure 3.24 A comparison of measured volume and volume obtained by group CAs & d_{mrd}

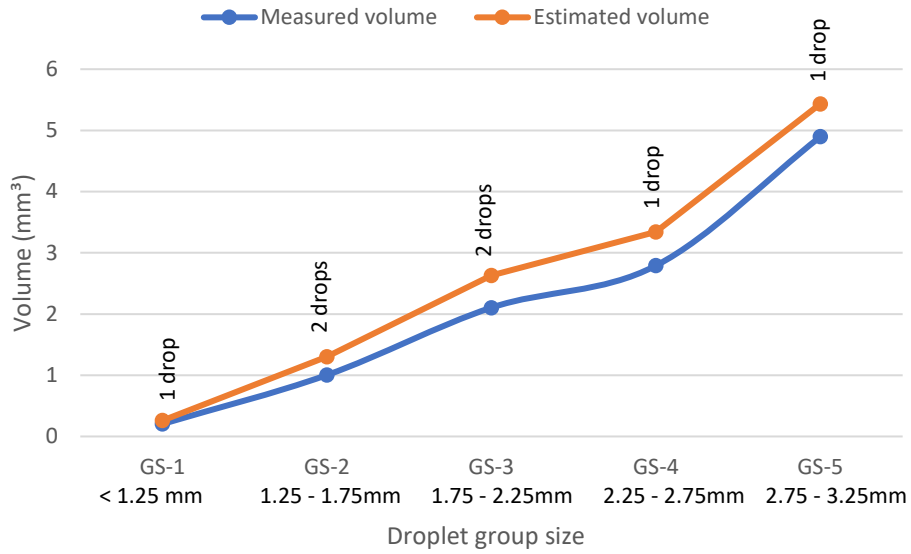


Figure 3.25 A comparison of measured volume and volume obtained by group CAs & d_{eqv}

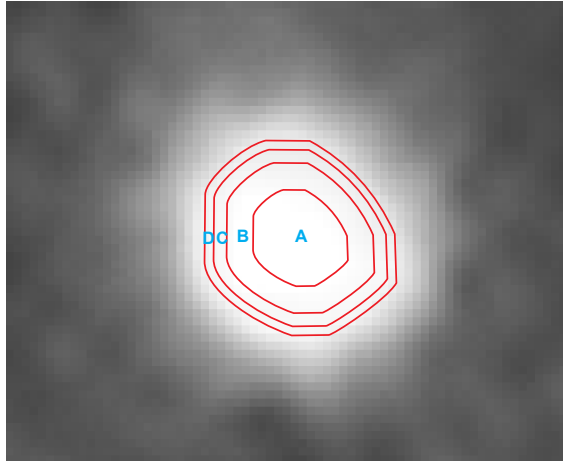


Figure 3.26 The thermal distribution map for a droplet deposited on a cold surface

Figure (3.27) shows the dynamic thermal changes at two points of a droplet during its freezing process versus time. Curve (A) represents the temperature of a point at the center of the droplet, and curve (B) represents the temperature of a point at the outer edge of the droplet. It shows that when a water droplet collides a cold surface, its molecules start to crystallize and the freezing process speeds up, which leads to a sudden increase in the released heat energy. Because of this increasing heat flux, the temperature rises and becomes 0 °C or close to 0 °C. During the crystallization period, the temperature starts to decrease until all the water molecules turn into ice [25, 26]. Capturing the droplet image at time range t_1 to t_2 creates the opportunity to obtain a better measurement accuracy because the brightness intensity at this range is at the highest value which an IR camera can distinguish, even for a tiny droplet. Secondly, the freezing process at the droplet's outer edge is faster than the center, which causes the emitted heat energy to fade gradually and fast from the outer edge to the center of the droplet. In the same manner, the brightness intensity fades, and vanishes at the center. Since the droplet diameter keeps its size during and after the freezing process, it should be extracted at range t_1 to t_2 , which is the time after the collision process period, to obtain better accuracy.

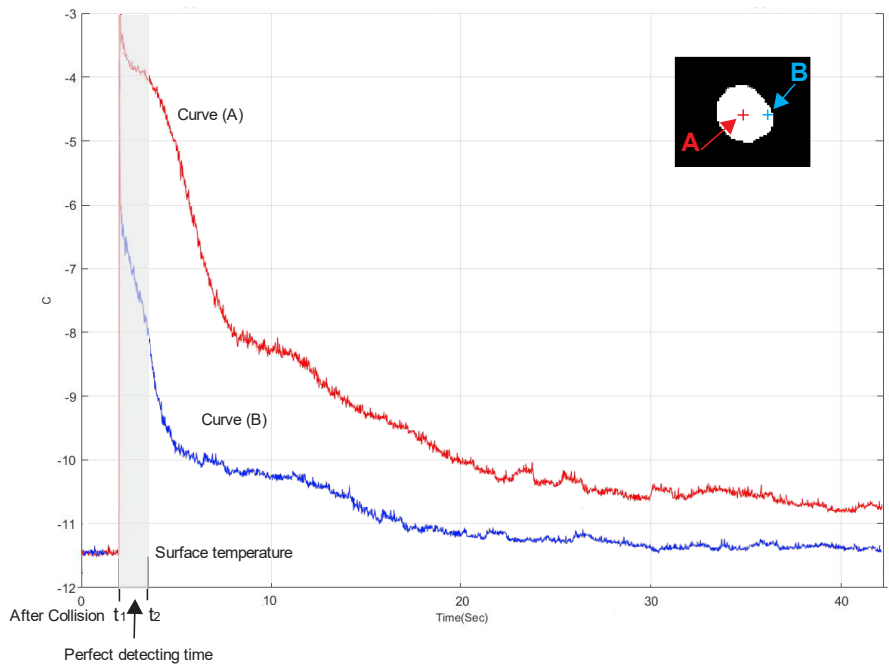


Figure 3.27 Temperature versus time at two points of a droplet during its freezing process

The numerical analysis conducted in this study at an early stage indicates that an increase in the static contact angle of a droplet has a negligible impact on the droplet size in comparison to a small increase in the droplet diameter. Based on this finding, the proposed method utilizes pre-estimated static contact angle values that are representative of a surface with a specific wetting property. The experimental results demonstrate that utilizing pre-estimated contact angles of frozen droplets yields acceptable results in the calculation of droplet volume. Given that the contact angles utilized in this investigation are pre-estimated from frozen droplets, they represent static contact angles rather than dynamic contact angles. Consequently, the term "contact angle" (CA) exclusively refers to static contact angles in this study.

The impact process of a droplet on a surface expands the spreading diameter and promotes the retraction to an extent, but at a lower surface temperature the droplet is quickly frozen with a smaller change in diameter on the stainless-steel surface than on a Teflon plate, due to the difference in their thermal conductivities [57]. It has been found that the CA and freezing time are

dependent on the size of the contact area and the thermal conductivity of the surface [58, 59, 60]. Figure (3.28) shows that at lower surface temperatures, the droplet is flatter in the case of a substance with high thermal conductivity (A), while in the case of a substance with a lower thermal conductivity (B) it is more spherical. The target surface used in this experiment was made from fiberglass, and the thermal conductivity of fiberglass is $0.045 \text{ W}\cdot\text{m}^{-1}\cdot\text{k}^{-1}$, which is considered a low thermal conductivity substance. Therefore, the thermal conductivity of the substance must be considered when estimating the CAs of different droplets' sizes, and this procedure should be performed under the same operating conditions and on the same substance in the experiment.

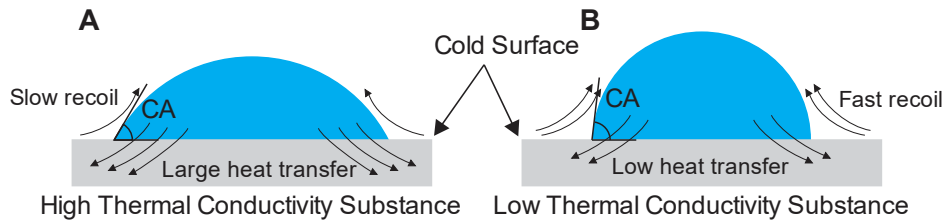


Figure 3.28 The effect of thermal conductivity of the droplet's CA

Wind speed carries the droplets with the same speed and high wind speed can cause the droplet to collide with the surface with a high impact speed, as shown in Figure (3.29-A). The droplet spreads to the maximum diameter and often the droplet does not preserve its individual state, but rather splits into small droplets. During the spreading stage, the drop changes from a sphere to a disc-like shape and is increasingly subject to viscous forces and, to a lesser extent, influenced by surface tension, and surface roughness.

Higher wind speed greatly accelerates the cooling rate of the droplet in a low temperature environment. That implies that the droplet will freeze faster because of the supercooling effect [61, 62]. Figure (3.29-B) illustrates the high impact speed of the supercooled water droplet under the effects of a low temperature environment and cold wind. Because of the effect of these operating

conditions, the impact spreading diameter is reduced from the maximum, compared to the previous case. The recoil stage is strong enough to counterbalance a fixed diameter so that the final shape becomes a spherical cap, as shown in Figure (3.29-B) [61, 62].

Lowering both surface and ambient temperatures below freezing point can make the droplet behave differently. An experiment is conducted to investigate the effect of the droplet impact speed on the droplet shape and CA under an operating condition of negative temperature. The experiment is conducted with different wind speeds 0m/s, 4m/s, 8m/s, 10m/s, and 12m/s. To investigate the droplets' shapes and their CAs, the droplets which are close in size, are selected and presented in Figure (3.30). It is noted that the droplets' shapes for wind speed 0m/s, 4m/s, 8m/s, and 10m/s are similar in their spherical shapes and the visual estimation of their CAs ranges from 70° to 75° , according to the wettability chart of Figure (3.11). This small difference in the range of CAs is due to the little differences in the sizes of the droplets. This leads to the conclusion that the CA of a droplet which is estimated at any wind speed below 12m/s can be used for the same droplet's size for a wind speed range from 0m/s to 10m/s.

The droplet shape of wind speed 12m/s, as shown in Figure (3.30), is less spherical than the other droplet shapes and its visually estimated CA is approximately within 65° to 67° . It should be noted that a high speed droplet can increase the inaccuracy of the measurement due to high uncertainty in the estimated CA's value. That means the CA should be estimated according to the operating conditions prior to the experiment in order to avoid any errors due to the effect of wind speed.

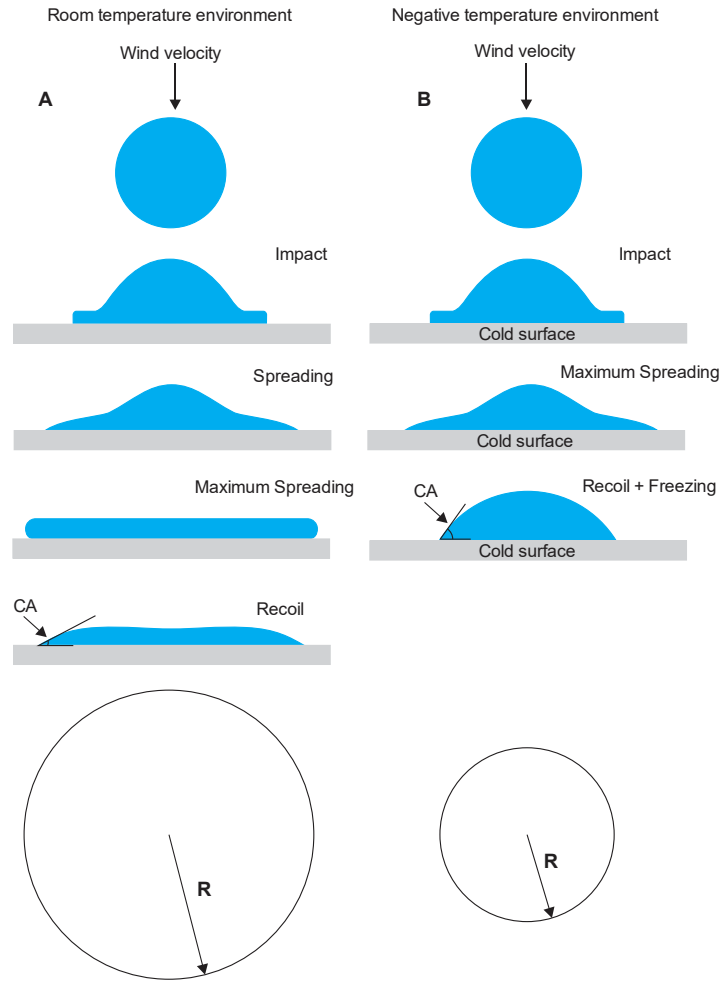


Figure 3.29 Illustration of the effect of wind speed on droplet's CA

Surface temperature: - 8°		Ambient temperature: - 10°			Surface type: Hydrophilic (fiberglass texture)	
Wind speed:	0 m/s	4 m/s	8 m/s	10 m/s	12 m/s	
Top view						
Side view						
Estimated CAs range: 65° - 75°						

Figure 3.30 Experimental results of droplet shapes affected by different wind speeds

The effects of impact angle and gravity on a droplet shape at room temperature are illustrated in the Figure (3.31). The higher impact angle allows the water droplet to spread with a larger momentum in the tangent direction at the early stage of the impact process. Once the water droplet's leading point stops moving, the surface tension causes the water droplet to recoil. As the droplet settles and stops moving, the final shape of the stationary droplet is formed [63]. The gliding stage lasts for a long period of time, until the droplet stops and settles.

As declared earlier, lowering both surface and ambient temperatures below freezing point can interrupt the gliding process early due to the rapid freezing of the droplet surface in contact with the cold surface [64]. That means the negative temperatures of both surface and ambient areas have a significant effect on the behavior and equilibrium state of a droplet [64, 65].

The inclined angle in the conducted experiment was $\angle 90^\circ$, as shown in Figure (3.32). It is evident that the deposited droplets do not have sufficient momentum to spread. The effects of the surface tension and low temperature of both the surface and the environment slow the glide stage and give enough time for the droplet to freeze. It is noted in Figure (3.30) that under operating conditions of a temperature below freezing of both surface and environment, and an inclined angle of $\angle 90^\circ$, the spherical shape of the deposited droplet does not deform, and it keeps its shape and CA as long as the operating conditions do not change.

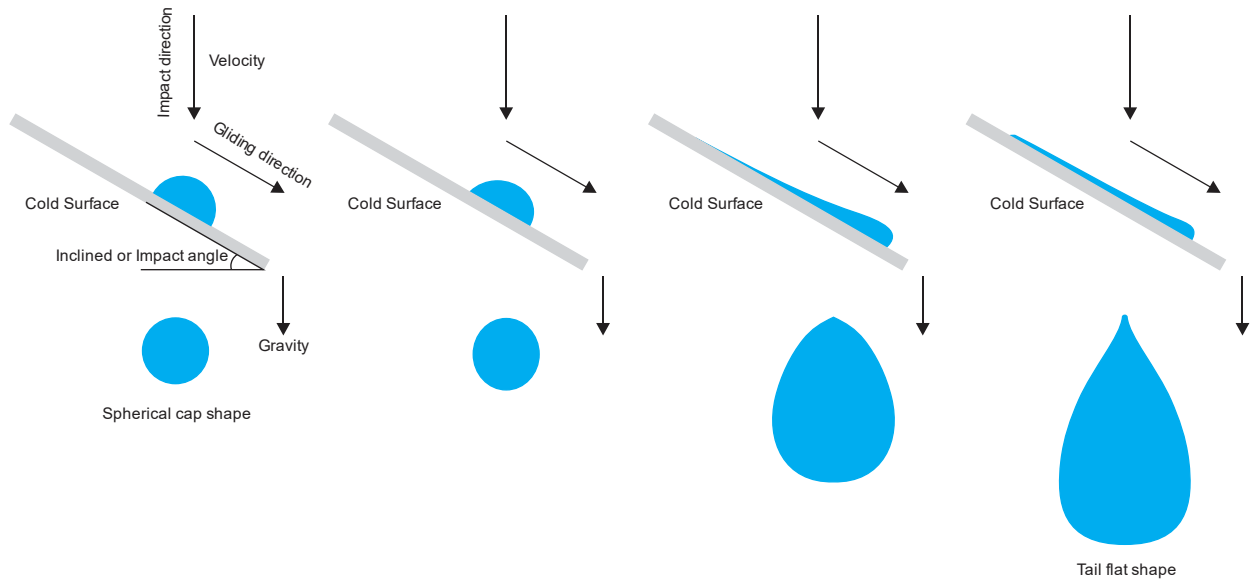


Figure 3.31 Illustration of the effect of inclined angle and gravity on droplet shape

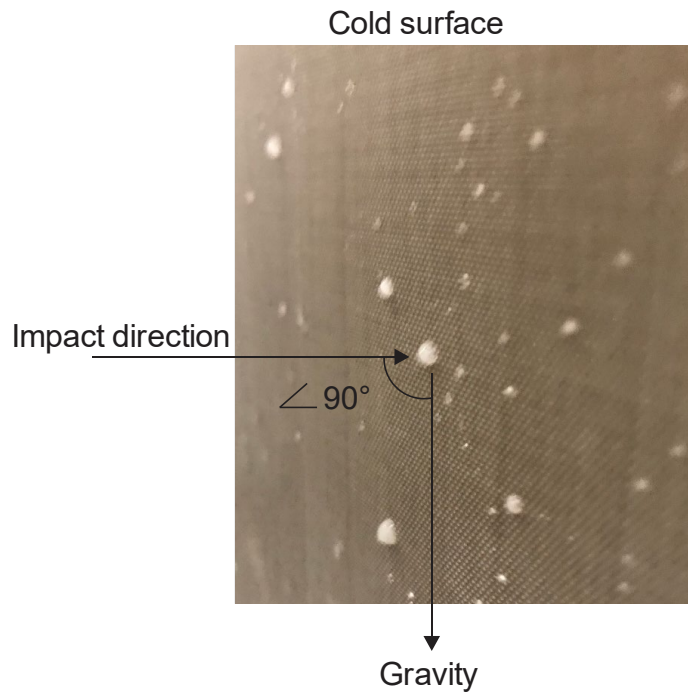


Figure 3.32 Experimental example illustrating deposited frozen droplets with $\angle 90^\circ$ inclined angle

Often the droplet shape when deposited tends to be spherical. The shape is treated by base area and angle of contact, using the two formulas (3.17) and (3.7) to find volume. This typical

shape can be deformed by changing the operating conditions as well as by the two characteristics of thermal conductivity and surface roughness of the substance used in the experiment. Figure (3.33) shows most of the regular shapes that can be formed on the surface due to deposition and freezing of water droplets.













Shape number	1	2	3	4	5	6
Shape name	Spherical cap	Elegonted	Sephoroide	Flattened	Disc	Tail
Sectional view						
Top view						

Figure 3.33 Most common droplet shapes formed on a surface

Geometrically, these shapes can be described as belonging to the family of round shapes, characterized by having one center or two centers, as in shapes 2, 4, and 6 with two centers as shown in Figure (3.33). There are nondimensional morphological parameters which can qualify the object shapes. These parameters also define a morphological space in which different shape families can be identified. To test whether the object belongs to the round shape family, the definition of the roundness parameter is employed for this purpose, using Eq. (3.23). This parameter measures the roundness of the mass distribution around the center, and it increases from 0 to ∞ as the object shape becomes less and less uniform. This parameter is equal to 1 only for a circle and it is less than one for any other shape.

$$roundness = \sqrt{\frac{4\pi \times Area}{Perimeter^2}} \quad (3.23)$$

$$ellipticity = \frac{L_{min}}{L_{max}} \quad (3.24)$$

The ellipticity parameter measures the stretching of the droplet using Eq.(3.24). It corresponds to the ratio of the width to the length of the rectangle that most closely encompasses the droplet image, shown in Figure (3.34). Since elliptical and tail shapes are stretched from a circular shape, each elliptical shape in Figure (3.33) is converted to a circular shape using the equivalent area method, as shown in Figure (3.34). This means that the number of pixels in a stretched shape can be expressed by the same number of pixels in a circular shape. Then the equivalent diameter of the new circular shape is calculated. The equivalent shapes are listed in Figure (3.35).

By comparing each shape in the sectional view with the wettability chart of Figure (3.11), the approximate range of the CAs for each shape is identified, as listed in Figure (3.35). It must be considered that these estimated ranges do not reflect the true estimation: but the real estimation of CAs is made during and at the workplace, and under operating conditions at that moment.

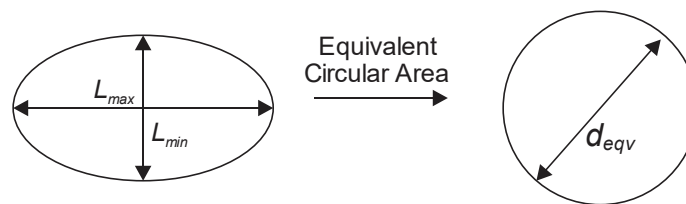


Figure 3.34 Converting elliptical shape to equivalent spherical shape



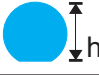









Shape number	1	2	3	4	5	6
Shape name	Spherical cap	Elegonted	Sephoroid	Flattened	Disc	Tail
Equivalent Sectional view						
Equivalent Top view						
Radius	$R \geq h$	$R \geq h$	$R < h$	$R \gg h$	$R \gg \gg h$	$R \gg \gg h$
CA	$30^\circ - 90^\circ$	$30^\circ - 90^\circ$	$> 90^\circ$	$10^\circ - 30^\circ$	$< 10^\circ$	$< 10^\circ$

Figure 3.35 The equivalent shapes of the most common droplet shapes

However, this study has shown that the operating conditions as well as the surface texture roughness and the thermal conductivity of the substance used in the experiment are essential factors in the formation of the droplet's shape. For example, shape no. 3 in Figure (3.33) will form on hydrophobic surfaces that are not wettable at low temperatures and does not form on hydrophilic surfaces. Shape no. 5 is formed on the surface of a substance with high thermal conductivity and at a high wind speed and low temperature. Also, Shape no. 1 which is represented in the current study, is formed as a result of low temperature, a low wind speed, low thermal conductivity substance, and a hydrophilic surface. Thus, the study of the effect of these factors on the formation of the shape of the droplet could help in developing a method for predicting the shape of the droplets that could form under certain operating conditions.

Several studies have been developed to solve overlapped objects in the literature, and some focus on the boundary curvature or the convex-hull detection [66, 67]. Other works are based on the Hough Transformation method [68,69]. Recently some algorithms support multidimensional image processing. The watershed segmentation to separate touching objects in an image and the

watershed transform find catchment basins and watershed ridgelines. The key to using the watershed transform for segmentation of touched and overlapped objects is that the image is converted into another image, the catchment basins of which are the objects that need to be identified. More details can be found in references [70, 71].

The main issue in the overlapped droplets' image is identifying the center of each droplet. Once the center of the object is identified, its equivalent diameter can be found through the relation between the center and the perimeter. The grey image that is derived from a thermal image is unlike the grey image taken by a normal camera. The latter represents the reflected light from the actual overlapped droplets, and identifying the droplets' centers is a complicated procedure. The thermal image represents the temperature distribution from the center of the droplet to the droplet's edge. The region A in Figure (3.26) shows the highest temperature, and it can be identified since its pixels are connected to each other. This region's mass center represents the mass center of the droplet and image tools of MATLAB can identify it.

Figure (3.36) shows an illustrative example of the stages of image processing, analyzing, and segmenting three overlapped droplets from a thermal grey image. The image of the overlapped droplets is cropped from the entire image to speed up the process of the analysis. The first step as indicated in Figure (3.36); the warmest regions are segmented from the corresponding gray image using a threshold of intensities ranging between (250 - 255). The segmented hot spots image indicates that there are three overlapped objects, and they are labeled (A, B, and C). The center of each hot spot is determined using MATLAB image processing tools. The binary image of the overlapped object is extracted, as shown in step (3). The output binary image shown in step (2) is used as a mask in the binary image of the overlapped objects in step (4) to extract each overlapped

object's center. Starting from the center location of the first labeled object (A) as shown in step (5), the pixels are counted in several directions (4, 6, or 8) towards the last pixel on the contour of the overlapped objects. The number of counted pixels in each direction represents the length from the center to the contour in that direction. The lengths of the directions that have similar or close lengths are selected. Then the equivalent droplet diameter is the average of the selected lengths. All other droplets are treated in the same way to obtain their equivalent circle, as shown in step (6).

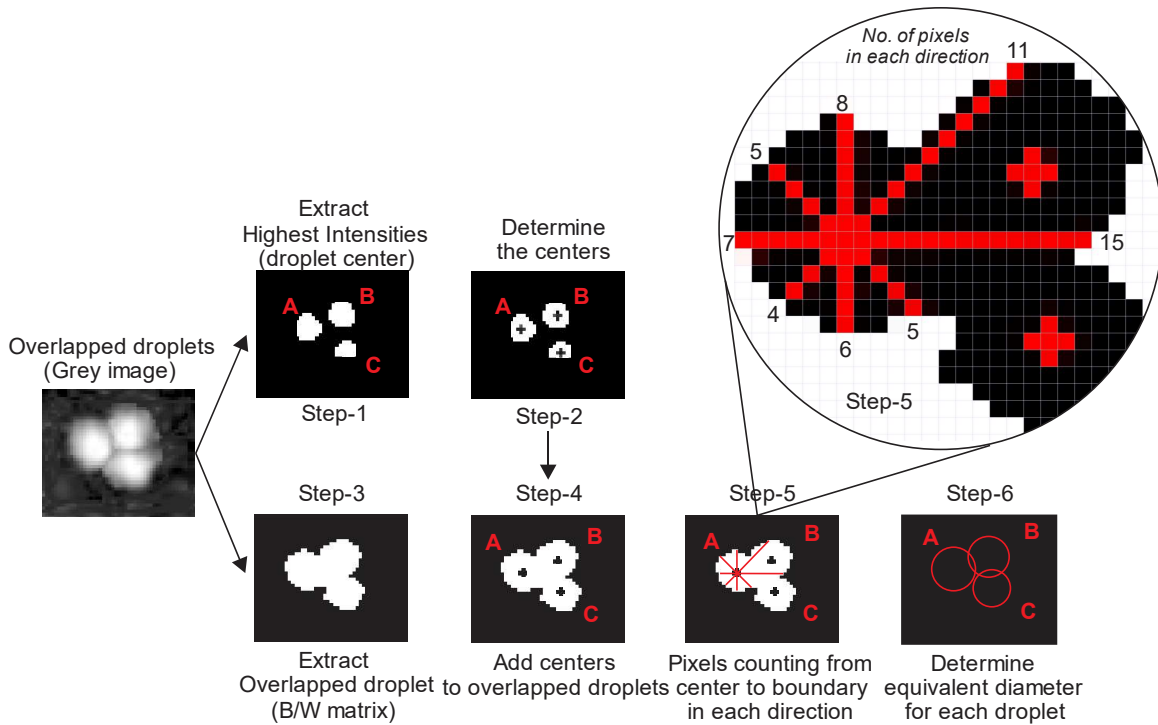


Figure 3.36 Image processing stages of separating overlapped droplets from thermal image

Ice particles in a cloud of liquid droplets are in a favorable environment to grow by diffusion because the environment is supersaturated with respect to ice. If supercooled droplets exist with ice particles, the latter grow at the expense of the liquid droplets [72]. We believe that

if the droplet contains some liquid that can emit heat energy when it hits a cold surface and starts freezing, then its temperature signature can be detected by the proposed method.

There are three icing regimes that can form on a cold surface a when water droplet freezes: glaze, mixed, and rime. Predicting what ice regime will form is a difficult task because the regime has a complex dependency on temperature, the liquid water content (LWC) and the median volume diameter (MVD). The glaze ice regime is normally encountered at relatively warm temperatures, large MVDs, and high LWCs. Rime ice is typically encountered at cold temperatures, small MVDs, and low LWCs. The transition between glaze ice and rime ice is the mixed ice regime [73, 74]. The temperature, LWC, and MVD, which represent the environmental conditions, are essential input parameter to predict or model icing. Many existing instruments rely on these parameters to distinguish between ice regimes [74]. LWC and MVD are statical parameters used to estimate the ice accumulation. Likewise, by knowing the environmental conditions, the ice regime can be predicted. When water droplets freeze, they can form one of the three ice regimes, which depends on the specific climatic conditions. During the freezing process, thermal energy is released regardless of the resulting ice regime. This released heat can be detected by an IR camera and the equivalent diameter of each droplet can be extracted by thermal image processing. However, the volume calculation for rime and mixed ice cannot be performed due to the different pattern of ice formed. It can be assumed that the average volume of the group size (GS) in the case of glaze ice is the same for the similar GS of the rime ice case. Figure (3.37) illustrates the concept. For the rime ice regime, the extracted equivalent diameter of an iced droplet is assigned to its GS and then the estimated droplet volume will be the average volume of that GS.

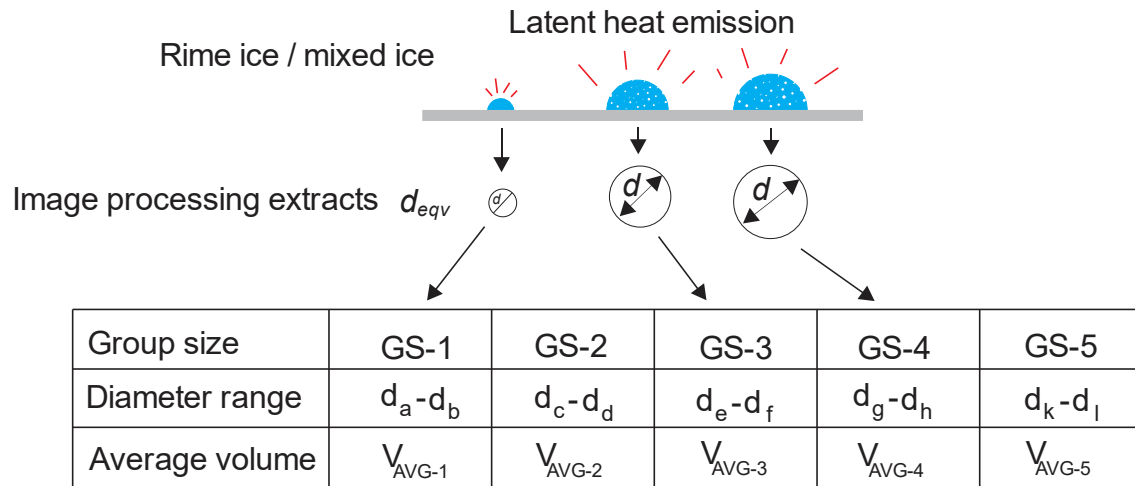


Figure 3.37 The stages of estimating the average volume of rime/mixed iced droplet

Table (3.10) presents the capabilities and limitations of the proposed method. The table lists six categories. The first category is the droplet and describes the droplet type, size and contact angle. The second category describes the limit of the substance parameters that affect the method's capability. This shows that the method can work effectively using the assumptions which follow: the surface is hydrophilic, the deposited droplets are clear water, and environmental and surface temperatures are below freezing point to allow the deposited water droplets to freeze immediately. Moreover, the proposed method, as shown in Table (3.10), can work on any opaque and solid hydrophilic surface, and the surface texture has a roughness that allows the water droplet to remain on the surface and does not absorb it, provided that a contact angle is formed between the surface and the water droplet and does not exceed $\angle 90^\circ$. Still, it is limited to the substances that have hydrophilic surfaces, for two reasons, which are:

Hydrophobic surfaces are repellent to water droplets, due to the droplets' small adhesion area to the surface, making them unstable and easy to expel from the surface. While hydrophilic

surfaces attract water droplets and allow the surface to wet, their adhesion force to the surface is high, due to the large area of the droplets' adhesion, keeping them attached to the surface, which makes it easy to track them with an IR camera. Secondly, the volume formula is derived for a spherical cap shape, and is useful for CAs up to $\angle 90^\circ$, which is a full cap shape. This range of CAs represents the wettability region of the hydrophilic surfaces. The CAs of the hydrophobic surfaces are beyond this range and obtain the volume needed to modify the current formula.

This study shows that the operating conditions of the experiment such as surface and ambient temperatures, and wind speed, as shown in Table (3.10), must be considered and the pre-estimated CAs of the droplets must be taken prior to the experiment for better measurement accuracy.

Table 3.10 The capabilities and limitations of the proposed method

Item	Item Name	Item Type	Limit	Details	
Droplet	Liquid type		Clear water	Tested on clear water.	
	Diameter(mm)		0.6 - (Raindrop size)	0.6mm is min. due to nearness to noise and max. is raindrop max. size.	
	Shape		Flat - full spherical cap	Regular shapes can be converted to their equivalent spherical shapes.	
	CA		$\angle 1^\circ - 90^\circ$	Depends on the visual estimation accuracy of CA.	
Substance	Hydrophilic surface	High roughness	Less Spherical shape (flat)	The shape should appear above the surface.	
		Low roughness	High Spherical shape	Can obtain better spherical shape.	
	Hydrophobic surface	Not applicable	Not applicable	Due to formula limitation and slow freezing.	
	Thermal conductivity	Low conductivity	$> 0.045 \text{ W.m}^{-1}.\text{k}^{-1}$	Tested on fiberglass substance and gets good results.	
High conductivity		-	Can obtain better results.		
Operating Condition	Temperature	Surface	Negative	The lower temperature can obtain better results.	
		Ambient	Cold Climate	The lower temperature can obtain better results.	
	Wind Speed	Low	$\leq 10\text{m/s}$	Can obtain better results.	
		High	$> 10\text{m/s}$	Increases the uncertainty due to shape is deformed. (not recommended).	
IR Camera	Resolution		$\geq (320 \times 240)$	Flir E-60 (76,800 (320 x 240)) is used in this study (use near distances).	
	Distance		$< 4\text{m}$	Larger distance needs zooming and high resolution.	
	Emissivity		-	0.96 is used in this study and must be calibrated to operating conditions.	
Visual estimation	Error CA %		0.5% - 6.5%	Error in CA visual estimation with measured, according to this study.	
Image processing	Detection	Ice	Glaze/Rime/Mixed	All regimes can release heat energy when water droplet freezes	
	Image extract	Round object	Eqv. Diameter	All detected objects have images which are used to extract d_{eqv} .	
	Compute	Volume	Flat - full spherical cap	Formula limitation, rime and mixed match d_{eqv} with group size.	
	Overlapping	Touched boundary		-	Can be extracted with reasonable results.
		Inside boundary		-	If the centers can be extracted. It can lead to high uncertainty.
	Noise	Min. droplet		≥ 10 pixels	Less than 10 pixels considered as noise and depends on image quality.
	Err. d_{eqv} %			2.3% - 6.1%	Error in d_{eqv} extracted with measured, according to this study.

The working principle of the proposed method can be simplified in two stages, as shown in block diagram in Figure (3.38). The stages include the image processing stage and the computing stage, and their functions can be summarized as follows.

The image processing stage's work is to define the image ROI in the IR camera according to the actual area ROI before the start of imaging. After capturing the image, it is processed according to the previously described method. Then, a binary matrix is obtained from the processed image, and finally, the data for each droplet are extracted from the binary matrix, including (x, y) location, area, and equivalent diameter d_{eqv} .

The computing stage's contribution is to enter the droplet group sizes (GS-1, GS-2, etc) and the droplet CAs range (CA_{Max} and CA_{Min}) into the system. Then, CAs are assigned to each group size according to the previously described group size method of CAs. After receiving the droplets' data, each droplet's data are classified into its GS according to size. Finally, the volume for each droplet is obtained and the final data are registered as the following:

Droplet (1), (x, y) Location, Diameter, CA. Area, Volume

Droplet (2), (x, y) Location, Diameter, CA. Area, Volume

Droplet (3), (x, y) Location, Diameter, CA. Area, Volume

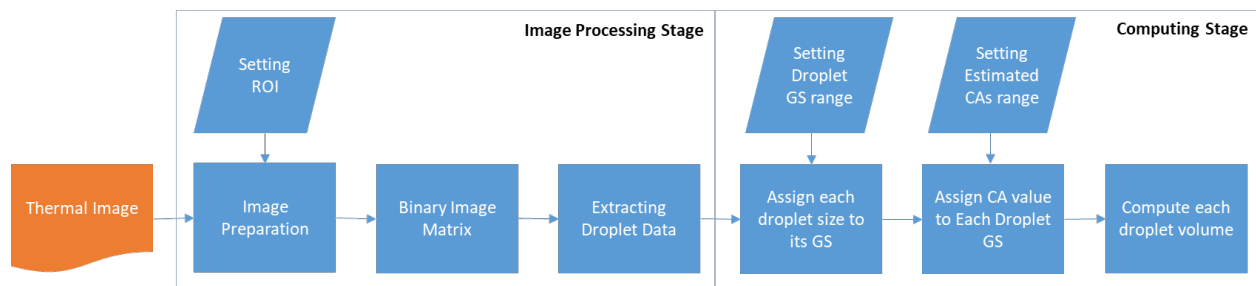


Figure 3.38 Illustration of the work principle of the proposed method

The proposed method can be used in many applications. One application is that the proposed method can be adapted to work in an integrated ice sensing and mitigating system, as shown in Figure (3.39). The configuration of the integrated system consists of three stages. The imaging frame rate of the IR camera is 24 frames/second. To increase the speed of the system's process, the captured image frame rate is reduced to 3 – 6 frames /second. Then, each captured image frame is processed to obtain a binarized matrix using the proposed method. Each binarized matrix frame extracted from sequenced captured images is sent to the next stage. The tracking and controlling stage's role is to track the change in each binarized matrix frame by comparing it to the previous binarized matrix frame, which checks whether the ROI is covered with ice. Ice layers are tracked by calculating the droplet location and area. The new droplet that overlapped with an old droplet in the same position is counted within the layer it belongs to. When the volume or average thickness of the accumulated ice layers reaches a predefined value, then a message is sent to activate the de-icing unit to clean the surface.

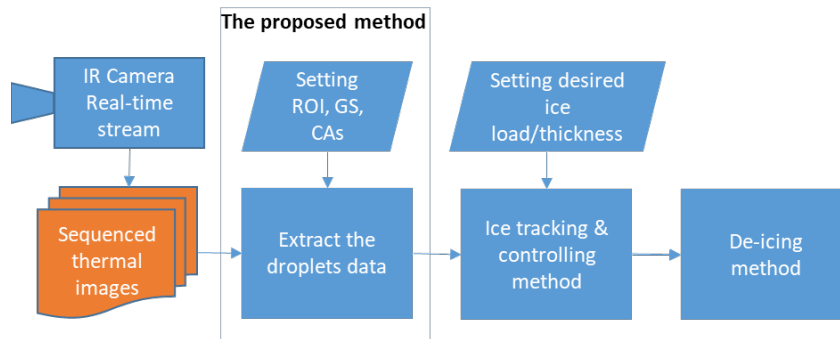


Figure 3.39 Using the proposed method in an integrated system

Another application for the suggested method is for use in the field of droplet morphology to study and analyze droplet behavior in cold climate, as described earlier in this study. Additionally, many existing instruments rely on MVD as a parameter to predict ice load. The suggested method can be used to obtain this parameter through using the method in cold operating conditions. Then,

using the droplet group size method, the MVD for a particular droplet size will be the average volume of that group size GS.

3.6 Conclusions

This study investigates a deposited frozen droplet's geometry, and a volume equation is devised. A literature review of both the temperature and the surface roughness effects on the CA concludes that the effect of temperature has an insignificant impact on CA as long as the frozen droplet is kept frozen. However, the surface roughness shows a significant impact on CA, due to the roughness uncertainty, which causes the difference in the CAs of the droplets of similar size, and the arithmetic mean of the CAs can solve the problem.

The relation of droplet size and CA is numerically analyzed and shows that the CA's effect on the small size droplet volume is almost negligible. At the same time, it contributes a considerable volume uncertainty to the large size droplets. The droplet's quantity effect on the volume is investigated as well, and it is demonstrated that the estimated group CAs method can minimize the volume uncertainty, especially for large droplets.

Furthermore, the proposed methods of the estimated group CA_{est} and the extracted equivalent diameter d_{eqv} are examined and considered as valid methods for hydrophilic surfaces. They can give good results with some uncertainties. The estimated CAs obtained visually from the wettability chart show a good agreement in the volume results obtained by the measured CAs.

The uncertainty evaluations show there is an average overestimation in droplets' volumes of about 19%. It is concluded that the estimated droplet volume provides acceptable agreement for numerous applications when there is no need for accuracy of the measurement. In high-risk applications, the average error value can be considered corrective, because it is a systematic error

and almost fixed and repetitive. Finally, the suggested method for estimating a droplet volume is new and merits further future studies to improve it.

Acknowledgements

The financial support of the Libyan Ministry of Higher Education and Scientific Research and the Natural Sciences and Engineering Research Council of Canada (NSERC) are gratefully acknowledged. We thank D H Prajitno [20] for providing the data of Figure (3.4).

3.7 References

- [1] Madi E, Pope K, Huang W, Iqbal T. A review of integrating ice detection and mitigation for wind turbine blades. *Renew. Sust. Energ. Rev*; 2019; 103:269-281. 10.1016/j.rser.2018.12.019.
- [2] Sinner A.M. Compositional state detection system and method. US Patent 4,808,824; 1989.
- [3] Adam Dershowitz, R. John Hansman Jr. Experimental investigation of passive infrared ice detection for helicopter applications. Massachusetts institute of technology. USA;1991. 10.2514/6.1991-667.
- [4] James A. Misener. Investigation of an optical method to determine the presence of ice on road surfaces. Institute of transportation studies. university of California, Berkeley. MOU 285 final report: ucb-its-pwp-98-17; 1998.
- [5] Jonsson P. Remote sensor for winter road surface status detection. *Proceedings of IEEE Sensors*; 2011; 1285-1288. 10.1109/ICSENS.2011.6127089.
- [6] Zhao Yong, Peng You-xin, Zhang Bo, Zhang Kai. Icing rate sensor based on infrared spectrum absorption. *AASRI procedia*; 2012. 1: 244 – 247.
- [7] L. Colace, F. Santoni, G. Assanto. A near-infrared optoelectronic approach to detection of road conditions. *Optics and Lasers in Engineering*; 2013; 51: 633–636
- [8] Carlos Quiterio Gómez Muñoz, Fausto Pedro García Márquez, Juan Manuel Sánchez Tomás. Ice detection using thermal infrared radiometry on wind turbine blades. *Measurement*; 2016; 93:157–163
- [9] Janet Light, Subashini Parthasarathy, William McIver. Monitoring winter ice conditions using thermal imaging cameras equipped with infrared microbolometer sensors. *Procedia Computer Science*; 2012; 10:1158 – 1165.
- [10] Rizwan Ghani and Muhammad S. Virk. Experimental study of atmospheric ice detection on wind turbine blade using thermal infrared technique. *J. Wind. Eng*; 2013; 37:71-78. 10.1260/0309-524X.37.1.71.
- [11] Taimur Rashid, Hassan A. Khawaja and K. Edvardsen. Ice detection of pure and saline ice using infrared signature. *sensors & transducers*; 2016; 206; 11: 82-87

- [12] Azam Fazelpour, Saeed R. Dehghani, Vlastimil Masek, Yuri S. Muzychka. Ice load measurements on known structures using image processing methods. *international journal of electrical and computer engineering*; 2017; 11:8.
- [13] Xuan Z, Xin L, Xiaomin W. Impacting-freezing dynamics of a supercooled water droplet on a cold surface: Rebound and adhesion. *Int J Heat Mass Tran*; 2020;158. 119997. 10.1016/j.ijheatmasstransfer.2020.119997.
- [14] Walford M, Hargreaves D, Stuart-Smith S, Lowson M. Freezing of water drops on a cold surface. *J. Glaciol*; 1991; 37. 10.1017/S0022143000042787.
- [15] Xuan Z, Xiaomin W, Xin L. Modelling of sessile water droplet shape evolution during freezing with consideration of supercooling effect. *Appl. Therm. Eng*; 2017; 125: 644-651. 10.1016/j.applthermaleng.2017:07.017.
- [16] Bin D, Hong W, Xun Z, Rong C, Qiang L. How supercooled superhydrophobic surfaces affect dynamic behaviors of impacting water droplets. *Int. J. Heat Mass Transf*; 2019;124:1025-1032. 10.1016/j.ijheatmasstransfer.2018.03.112.
- [17] Song M, Dang C, Higashi T, Hihara E. Review of experimental data associated with the solidification characteristics of water droplets on a cold plate surface at the early frosting stage, *Energy & Buildings*; 2020; 223:110103
- [18] Lingyan H, Zhongliang L, Yaomin L, Yujun G, Li W. Effect of contact angle on water droplet freezing process on a cold flat surface. *Exp. Therm Fluid Sci.*; 2012; 40. 74–80. 10.1016/j.expthermflusci.2012.02.002.
- [19] Emelyanenko K, Emelyanenko A, Boinovich L. Water and ice adhesion to solid surfaces: common and specific, the impact of temperature and surface wettability. *Coatings*; 2020; 10. 648. 10.3390/coatings10070648.
- [20] Prajitno D, Maulana A, Syarif D. Effect of surface roughness on contact angle measurement of nanofluid on surface of stainless steel 304 by sessile drop method. *Journal of physics: conference series*; 2016; 739. 012029. 10.1088/1742-6596/739/1/012029.
- [21] Jaroslaw D, Miller J, Hupka J. The effect of drop size on contact angle over a wide range of drop volumes. *J. Colloid Interface Sci.*; 1993; 155, 379-385
- [22] Zhang H, Yugang Z, Lv R, Yang C. Freezing of sessile water droplet for various contact angles. *Int. J. Therm. Sci.*; 2016; 101. 59-67. 10.1016/j.ijthermalsci.2015.10.027.
- [23] Huang L, Liu Z, Liu Y, Gou Y, Wang L. Effect of contact angle on water droplet freezing process on a cold flat surface. *Exp. Therm Fluid Sci.*; 2012; 40. 74–80. 10.1016/j.expthermflusci.2012.02.002.
- [24] Sterl S. Dynamics of supercooled droplets: Impacts, jets, explosions and more. *Mater thesis*. 2015; University of Twente.
- [25] Schuster J, Schvezov C, Rosenberger M. Influence of experimental variables on the measure of contact angle in metals using the sessile drop method. *Procedia Mater. Sci.*; 2015; 8. 742-751. 10.1016/j.mspro.2015.04.131.

- [26] Yuan Y, T. Randall Lee. Contact angle and wetting properties. Springer series in surface sciences;2013; 51, doi 10.1007/978-3-642-34243-1_1
- [27] Fazelpour A. Image analysis methods in the measurement of ice loads on structures. Master thesis; 2017; Memorial University of Newfoundland.
- [28] Truong V, Gretar T, Shunji H, Wells J. Numerical investigations of drop solidification on a cold plate in the presence of volume change. *Int. J. Multiph. Flow*; 2015; 76:73-85.
- [29] Malot H, Blaisot J. Droplet size distribution and sphericity measurement of low density sprays through image analysis. *Part Part Syst Char*; 2000; 17:146-158. 10.1002/1521-4117(200012)17:43.0.CO;2-4.
- [30] Bonomo M E. Analyzing the singularities of freezing sessile water droplets. Honor thesis; 2013; Dickinson College.
- [31] Jieteng W, Zhongliang L, Yujun G, Xinhua Z, Shuiyuan C. Deformation of freezing water droplets on a cold copper surface. *Science in china series E: Technological sciences* 2006 vol.49 No.5 590—600. DOI: 10.1007/s11431-006-2017-y
- [32] Zhang H, Jin Z, Jiao M, Yang Z. Experimental investigation of the impact and freezing processes of a water droplet on different cold concave surfaces. *Int. J. Therm. Sci.*; 2018; 132; 498–508
- [33] S. Jung, M. Dorrestijn, D. Raps, A. Das, C. M. Megaridis, and D. Poulikakos. Are superhydrophobic surfaces best for icephobicity?. *Langmuir*; 2011;27: 6. 3059–3066.
- [34] Brandon S, Haimovich N, Yeager E, Marmur A. Partial wetting of chemically patterned surfaces: The effect of drop size. *J. Colloid Interface Sci.*; 2003; 263. 237-43. 10.1016/S0021-9797(03)00285-6.
- [35] Letellier P, Mayaffre A, Turmine M. Drop size effect on contact angle explained by nonextensive thermodynamics. Young's equation revisited. *J. Colloid Interface Sci.*; 2007; 314. 604-14. 10.1016/j.jcis.2007.05.085.
- [36] Seewig J. The Uncertainty of Roughness Parameters. *AMA Conferences – Sensor*; 2013. DOI 10.5162/sensor2013/B6.2
- [37] Heidorn C, Wilson B. The raindrop. In *man, too. The weather doctor*. 2000. <http://www.heidorn.info/keith/weather/history/rdbentley.htm> (accessed 15/10/2020).
- [38] Neumann A W, Good R J. In *Surface and colloid science: experimental methods*, vol. 11, ed. by R.J. Good, R.R. Stromberg (Plenum Publishing, New York, 1979), p. 31
- [39] Hunter R J. *Foundations of colloid science*, 2nd ed. Clarendon press, Oxford, 2001.
- [40] Majeed M H. Static contact angle and large water droplet thickness measurements with the change of water temperature; *Journal (NUCEJ)*; 2014;17:1;114-128
- [41] Chang S, Zhou S, Zheng H. Freezing characteristics of water drop on different wettability surface. *5th International Conference on Experimental Fluid Mechanics – ICEFM*; 2018.
- [42] Yuntao P, Kewei S, Xili D, Greg N. Experimental investigation of water droplet impact and freezing on micropatterned stainless steel surfaces with varying wettabilities. *Int. J. Heat Mass Transf*; 2019;129:953-964.

- [43] Yuntao P. Experimental investigation of water droplet impact and icing on hydrophobic surfaces with varying wettabilities. Master thesis. 2018; Memorial University of Newfoundland.
- [44] Zivcak J, Hudak R, Madarász L, Rudas I. Methodology, models and algorithms in thermographic diagnostics. Springer; 2013; 10.1007/978-3-642-38379-3.
- [45] Blaisot J B, Yon J. Droplet size and morphology characterization for dense sprays by image processing: Application to the Diesel spray. *Exp Fluids*; 2005; 39: 977-994. 10.1007/s00348-005-0026-4.
- [46] McAndrew A. An introduction to digital image processing with Matlab; 2004.
- [47] MATLAB 2018a. The MathWorks, Inc., Natick, Massachusetts, United States.
- [48] J S Jakati, S S Matad. PCB defect detection based on pattern matching and segmentation algorithm. *IJARCCCE*; 2014; 3: 9; 8007–8011.
- [49] Agrawal P, Shriwastava S K, Limaye S S. Matlab implementation of image segmentation algorithms. 3rd IEEE International Conference on Computer Science and Information Technology- Chengdu (ICCSIT); 2010; 427–431.
- [50] Al-Obaidy F. IC testing using thermal image based on intelligent classification methods. Master thesis; 1996; University of Technology, Baghdad, Iraq.
- [51] Zuiderveld K. Contrast limited adaptive histogram equalization. *Graphic Gems IV*. San Diego: Academic Press Professional; 1994; 474–485.
- [52] Bradley D, Roth G. Adapting Thresholding Using the Integral Image. *JGT*; 2007;12:2,13-21.
- [53] Otsu N. A threshold selection method from gray-level histograms. *IEEE T Syst Man Cy C*; 1979; 9:1, 62-66.
- [54] Masoud Darbandi, Mohammad Fard, and Gerry E. Schneider. Developing FVBF method to perform the droplet catching efficiency sensitivity analysis in tentative ice accretion circumstances
- [55] Xavier Loyseau. Numerical simulation of droplet dispersion and deposition in pipes. PhD thesis. Cranfield University; United Kingdom. 2016.
- [56] N. Ashgriz. Handbook of atomization and sprays. Springer publishing. 2011.
- [57] Qing Xu, Zhanyong Li, Jin Wang, and Ruifang Wang. Characteristics of single droplet impact on cold plate surfaces. *Drying technology*, 30: 1756–1762, 2012
- [58] Kaniz Ronak Sultana. Investigation of transient phase change phenomena of water droplets for marine icing applications. PhD thesis. Memorial University of Newfoundland. 2019
- [59] Linn Karlsson. A Numerical and experimental investigation of the internal flow of a freezing water droplet. Luleå University of Technology; 2015.
- [60] Lam, L., Sultana, K., Pope, K., Muzychka, Y.S. (2020) Effect of thermal transport on solidification of high impact salt and freshwater water droplets on marine surfaces. *International Journal of Heat and Mass Transfer* 153: 119452.

- [61] Ke Xu, Jianlin Hu, Lichun Shu, Xingliang Jiang, and Zhengyong Huang. Influence of hydrophobicity on ice accumulation process under sleet and wind conditions. *AIP advances* 8, 035113 (2018)
- [62] Sultana, K.R., Pope, K., and Muzychka, Y.S. (2017) Phase change and droplet dynamics for a free falling water droplet. *International Journal of Heat and Mass Transfer* 115: 461-470.
- [63] Zheyang Jin, Huanhuan Zhang, Zhigang Yang. The impact and freezing processes of a water droplet on a cold surface with different inclined angles. *International Journal of Heat and Mass Transfer*. 2016; 103: 886-893.
<https://doi.org/10.1016/j.ijheatmasstransfer.2016.08.012>.
- [64] Zheyang Jin, Dongyu Sui, Zhigang Yang. The impact, freezing, and melting processes of a water droplet on an inclined cold surface. *International Journal of Heat and Mass Transfer* 90 (2015) 439–453
- [65] Yina Yao, Cong Li, Zhenxiang Tao, Rui Yang, Hui Zhang. Experimental and numerical study on the impact and freezing process of a water droplet on a cold surface. *Applied Thermal Engineering* 137 (2018) 83–92
- [66] Kim, J.Y., Chu, J.H. and Lee, S.Y., 1999, Improvement of pattern recognition algorithm for drop size measurement. *Atomization and sprays*, Vol. 9, No. 3, pp. 313--329.
- [67] Kim, Y.D., Lee, S.Y. and Chu, J.H., 2001. Separation of overlapped particles using boundary curvature information. *Proceedings of the 6th annual conference on liquid atomization and spray systems (ILASS-Asia 2001)*, pp. 259-264.
- [68] Sang Yong Lee, Yu Dong Kim. Sizing of Spray particles using image processing technique. *KSME International Journal*; 2004; 18: 6; 879-894.
- [69] Kim, Y. D. and Lee, S. Y., 2002, Application of Hough transform to image processing of heavily overlapped particles with spherical shape. *Atomization and Sprays*, Vol. 12, No. 4, pp. 451 --461.
- [70] Steve Eddins. The Watershed Transform: strategies for image segmentation. *MathWorks* <https://www.mathworks.com/company/newsletters/articles/the-watershed-transform-strategies-for-image-segmentation.html>
- [71] Help Center. marker-controlled watershed segmentation. *Mathworks* <https://www.mathworks.com/help/images/marker-controlled-watershed-segmentation.html>
- [72] National Weather Service. Icing. Retrieved from https://www.weather.gov/source/zhu/ZHU_Training_Page/icing_stuff/icing/icing.htm [Accessed 2 April 2021].
- [73] Jared Soltis, Jose Palacios, Douglas Wolfe. Design and testing of an erosion resistant ultrasonic de-icing system for rotorcraft blades. Pennsylvania state university. technical report No. TR 14-007. 2013
- [74] Staffan Rydholm, Benny Thörnberg. Liquid Water Content and Droplet Sizing Shadowgraph Measuring System for Wind Turbine Icing Detection. *IEEE SENSORS JOURNAL*. 2016; 16: 8.

Chapter 4: An integrated Ice Tracking and Mitigation System on the Stagnation Line of A Cylindrical Surface Based on Thermal Imaging and Electro-Thermal Elements*

* *The materials in this chapter were published in. Measurement; 2022; 199:. 111539, 2022. Authors are Ezieddin Madi, Dr. Kevin Pope, and Dr. Weimin Huang. Madi was the primary author, responsible for conceptualization, methodology, software development, data curation, and drafting. Dr. Kevin Pope, an esteemed co-author and expert in the field, contributed his conceptual insights and valuable expertise to the paper, while Dr. Huang offered general guidance and support as the primary supervisor.*

4.1 Introduction

In cold climates, ice accumulation on structures may lead to severe hazards [1], particularly on the leading edge (LE) of curved surfaces such as cylinder and airfoil surfaces. An ice sensor integrated with an ice mitigation system is required to prevent ice formation on an LE surface. However, the current sensing and de-icing technologies are inefficient, and integrated systems need appreciable improvement [1]. The present study will focus on finding an appropriate integrated technique to detect, track, measure, and remove ice on the LE of a circular surface.

Several direct techniques to detect / monitor ice on airfoil surfaces were reviewed in our previous study [1]. The reviewed ice detection techniques included in the study were acoustic wave, ultrasonic wave, microwave, optical, thermal infrared, capacitive, and impedance ice sensing techniques. Each ice sensing technique was compared with all de-icing techniques to decide on an integrated ice detection and de-icing system. The result of this comparison showed the infrared sensing method to be a promising technique. It can contribute to the ice sensing field because it is a non-destructive method for remote ice sensing and can be integrated with an ice mitigation system without physical contact [1]. This factor was the first motivation for our interest in using the IR ice sensing technique in the study.

In the second previous study [2], several infrared-based ice sensing techniques were evaluated based on the ice sensor's necessary functions. The functions required for ice detection are remote sensing, wide area detection, detection of onset ice, ice measurement, and real-time tracking. The comparison showed that the evaluated methods could not simultaneously offer the complete required functions for accurate ice detection. The second study aimed to expand the IR technique's capability to detect ice to measure its amount. The method was based on two factors. The first factor is the droplet's contact angle, only estimated once and used for all droplets. The

second factor is the droplet base's diameter, extracted from each droplet's thermal image using the image processing algorithms [2].

The previous study proved that thermal images can be used to sense the presence of ice and extract valuable information that can be used in later stages. It also showed that image processing helps analyze, compare, and track differences among sequenced thermal images and shows promising results. It was stated that the proposed method could be modified and adapted to work in an integrated ice sensing and mitigating system [2]. This was the second motivation of our interest in developing a technique based on the previous study to track and measure the thickness of ice accumulation on an LE surface, using sequenced thermal images processed and analyzed by image processing algorithms.

Several studies reported that the front edge of the airfoil (LE) is the part most prone to ice buildup [3, 4]. The process of ice accumulation often occurs around the stagnation zone (SZ), where the maximum amount of accumulated ice mass is located. [5, 6, 7, 8]. This means that the ice profile shape will roughly resemble the shape of the airfoil's curved surface. Over time, the ice profile turns into an elliptical shape on an airfoil's LE if it has a large diameter and tends to approximate a triangular form (tooth-shaped) on an LE with a short diameter [9-12].

Several experiments indicated that the temperature distribution and accreted ice along the LE surface keep changing over time as the ice builds up [13, 14]. This evidence was the third motivation of our interest in developing a method from our previous study to track and measure the thickness of ice accumulation on the SL surface using processed thermal images.

To avoid ice buildup on the LE surface, the temperature of that surface has to be maintained above the freezing point, which requires an energy source. Our previous study stated that the

integration based on an ice sensing technique of using infrared with thermal resistance as a de-icer is a promising technique [1]. The thermal resistance generates heat, which diffuses into the ice. Ice begins to break, loosen, and fall in places where the ice is thin, leaving a warm region [15]. As time passes, more heat diffuses into the thick ice regions, causing ice to disintegrate and shed [15], and the warm region expands while the ice region shrinks. From the perspective of image processing, the warm region is the bright region where the surface becomes ice-free. The cold region is the dark region, along the SL, where ice still exists. The warm region (bright region) gradually spreads across the SL surface, and the entire surface becomes ice-free. This means that the present ice region (dark region) complements the present warm region (bright region), and warm region information can be used to estimate the dark ice region present. This was the fourth reason for our interest in developing an integrated technique based on processed thermal images to measure ice decrement during ice mitigation on the stagnation line (SL) surface.

This research aims to experimentally investigate and develop an integrated technique to track, measure, and remove accumulated ice within a region of interest (ROI), along a small-scale SL of a cylinder's LE surface. What is innovative in this research is the use of sequenced thermal images and heat elements to track both ice buildup during icing events and ice decrement during ice mitigation of the SL, indicating the presence of ice or the absence of ice, in order to operate or stop the ice mitigation process directly and remotely. The integrated technique is composed of three main cycles. The first is the tracking component, which tracks the changes in accumulated ice throughout an icing event using thermal images and image processing techniques. The second is the de-icing cycle, which also employs thermal imaging and image processing algorithms to track the decrease in average ice thickness as the ice mitigation process progresses. The relaxation is the third cycle, which involves monitoring the average surface temperature as it approaches the

freezing point before the experiment is ended. The experiment uses visual (optical) images to validate the result obtained by thermal images. The IR camera and heat elements can be adapted to work in an integrated ice sensing and mitigating system to track and control the ice load. For these reasons, it is believed that the suggested integrated technique can add a new contribution to ice sensing and mitigation techniques.

4.2 The Theoretical and Practical Background

An aerodynamic study describes the behaviour of airflow around circular and airfoil objects, as shown in Figure (4.1). The airflow is separated at the front of the leading edge (LE) in both objects. The streamlines in the LE region show sudden upward and downward deflections [6]. The point where the flow velocity is null represents the stagnation point (SP) of the flow, and at this point, a positive pressure peak is present [5, 6, 12]. Although the aerodynamic properties of an airfoil object differ from those of a circular object, they both share the location of the stagnation zone, where ice buildup occurs often and the maximum amount of accumulated ice mass is located [3, 4]. As a result, for tracking ice accumulation and de-icing processes, this study adopts a small-scale circular shape of a cylinder to conduct the necessary experiments around the stagnation zone.

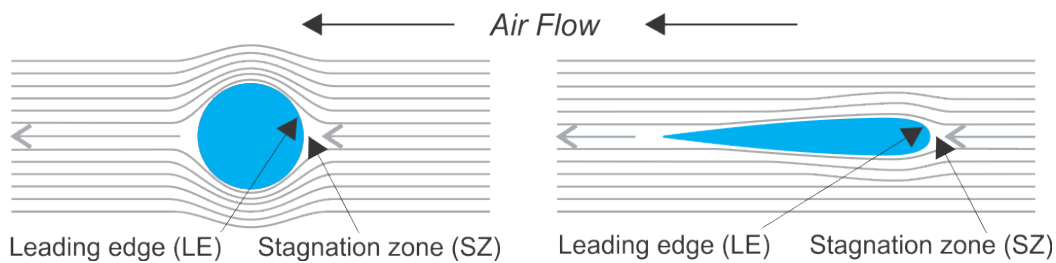


Figure 4.1 Airflow around circular and airfoil objects

Since the SZ in front of the LE is the most vital part exposed to the ice where the maximum ice thickness is located [1,3, 4], the tracking location of both ice accumulation and removal should be around the SZ of the LE. Ice detection and mitigation techniques must be designed to form an

integrated system [1]. The role of the integrated system is to detect and evaluate the ice amount around the SZ, activate the de-icing process in a controlled manner according to the amount of ice [2], and then deactivate the de-icing process when the ice is removed. The suggested integrated system is comprised of three interlinked stages: the ice tracking cycle, the de-icing cycle, and the relaxation cycle. Each of these components has its own theoretical basis as well as a set of characteristics developed from earlier experimental work. In this chapter, the theoretical foundation and practical backdrop of each component of the integrated system will be discussed individually as a basis for carrying out the current study experiments. This section covers the theoretical and practical background of ice tracking, de-icing, and relaxation stages.

4.2.1 The Theoretical and Practical Background of the Ice Tracking Process

In nature, ice often accumulates on an LE surface and takes its shape. Ice grows around the stagnation point (SP) of the LE surface, as shown in Figure (4.2). The ice mass collection distribution has a peak near the SP and decreases to zero at the lower and upper surfaces [7, 8, 16]. The greater ice accumulation causes a significant effect on the ice load, and the maximum accumulated ice thickness is at the SP [16].

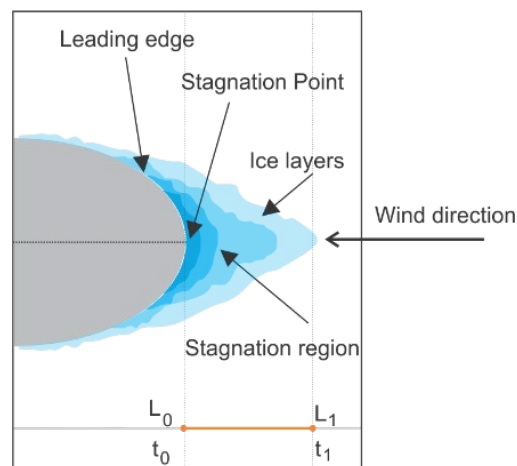


Figure 4.2 An illustration of ice profile shape around SP increments over time

When ice accumulates on the LE of a circular surface, the region where the accumulation occurs becomes warmer than the surrounding surface, due to the release of the latent heat of fusion as the impinging supercooled water droplets freeze [14, 17-21]. Figure (4.3) illustrates a surface temperature distribution at a section of a cylindrical surface during ice buildup. The graph indicates that the maximum temperature is at the surface's front, A point (A) where the maximum accumulated ice thickness is located, and then the surface temperature gradually decreases as the measurement spot moves towards point (B), where the minimum accumulated ice thickness is located. This example proves the concept that as more ice accumulates, the front part of the LE surface becomes warmer than the surrounding surface. The surface's temperature distribution changes over time as ice builds up on the surface [13, 14]. The images in Figure (4.4) illustrate the process of ice accumulation along the LE captured by an IR thermal camera. The images were taken at different times during the icing event. It is clear that as the ice grows on the LE surface, both the ice surface and the location of heat emission advance by the same amount and direction. This demonstrates that ice accumulation can be tracked using the temperature signature emitted during the freezing process, and average ice thickness can be obtained along the SL surface using the image processing method described in our previous study [2].

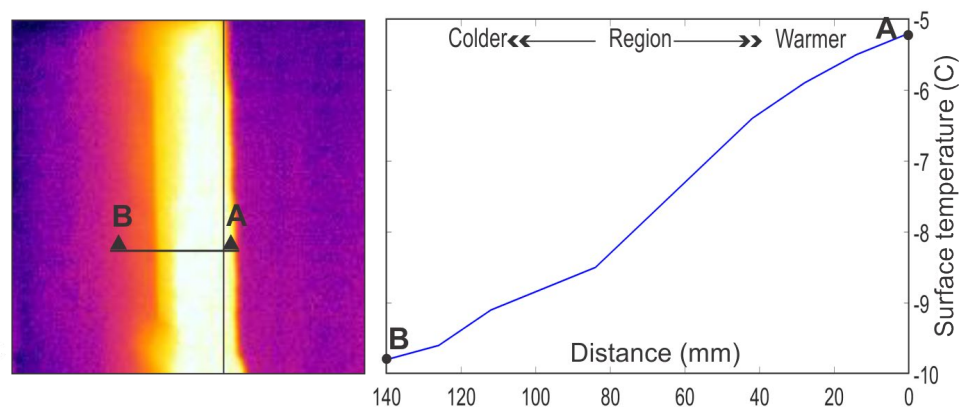


Figure 4.3 Thermal distribution along A-B section

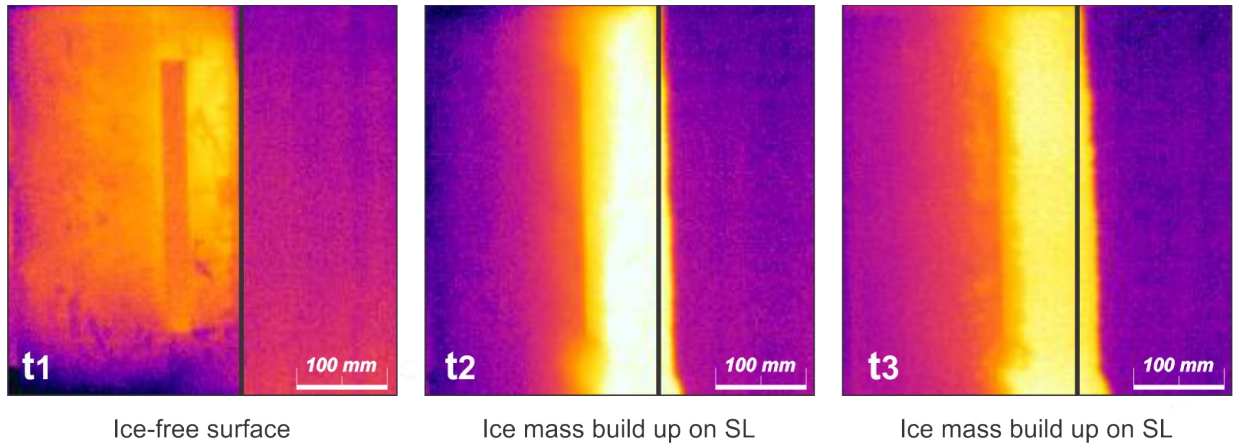


Figure 4.4 Thermal images show ice accumulation over time

To track the changes of ice accumulation within a certain area on the SL surface during an icing event, a region of interest in front of the SL surface where ice is accumulated has to be defined. Figure (4.5) illustrates the concept of the region of interest. The coordinates (x, y) and (x', y') , heights h, h' , and widths w, w' are associated with the actual region of interest (ROI_{actual}) plane and the image's region of interest (ROI_{image}) plane, respectively. The center line is the optical axis of the imaging setup [2]. The actual ROI_{actual} defines the true area's borders on the target surface under consideration (region of interest), and its dimensions are known. However, the image ROI_{image} area corresponds to the actual ROI_{actual} area of the region of interest; its area in pixels is known. The image ROI_{image} area must be defined according to the actual ROI_{actual} area before any other process is performed. To know the real width of (A) from its image width (A') within the ROI_{image} , it has to be calibrated with a Spatial Calibration Factor (SCF) [2] in the X-axis direction. SCF is defined as the ratio of dimensions in millimeters to pixel dimensions within the ROI_{image} and is obtained using Eq. (4.1). Here, the term ROI_{thermal} is used instead of ROI_{image} throughout the manuscript for the ROI of the thermal images taken by the IR camera Flir E-60.

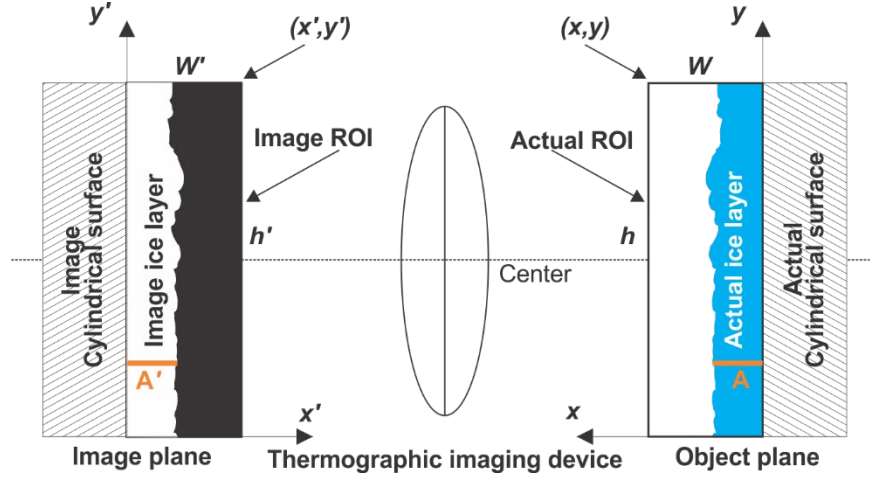


Figure 4.5 The concept of the actual and image region of interests for an ice layer

$$SCF \text{ in } X - \text{axis} = \frac{\text{Image } (w') \text{ dimension (pixel)}}{\text{Actual } (w) \text{ dimension (mm)}} \quad (4.1)$$

To extract the accumulated ice information from a thermal image, object segmentation is applied to the captured thermal image of the accumulated ice. The image segmentation aims to separate a digital image into independent partitions or regions that are more significant, to recognize the objects in an image [2, 20, 22]. Several image processing algorithms are applied to prepare the thermal image for object segmentation. The last step is to calculate the average thickness of the ice, as shown in Figure (4.6). The thermal region ROI_{thermal} has known dimensions, and its width represents the thickness. The average thickness of the accumulated ice is obtained in millimeters using Eq. (4.2), where $Row \ length(i)$ is the number of pixels in the row (i), (n) is the number of rows within the thermal region, ROI_{thermal} , and SCF_{thermal} is the spatial calibration factor of the thermal region of interest, ROI_{thermal} .

$$\overline{Thickness}_{\text{Thermal}} \text{ (mm)} = \frac{1}{n} \left(\sum_{i=1}^{i=n} Row \ length(i) \right) \times SCF_{\text{Thm}} \quad (4.2)$$

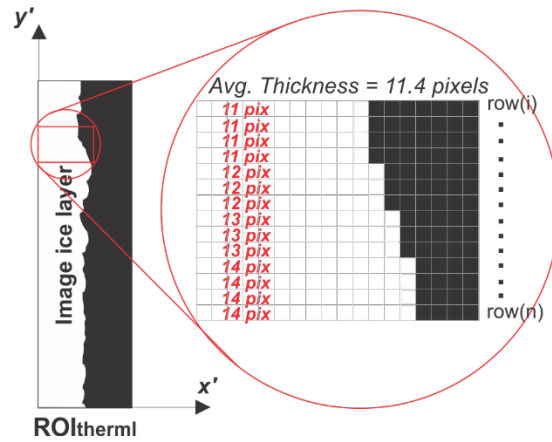


Figure 4.6 Calculating the average ice thickness in pixels

4.2.2 The Theoretical and Practical Background of the De-Icing Process

It is stated that as ice accumulates and thickens in the SZ region where the maximum collection efficiency is found, the deflection of droplets increases, increasing the ice thickness in the regions surrounding the SZ [11], as shown in Figure (4.7-B). Also, as the ice layer area increases, the adhesion area to the surface increases, increasing the adhesion strength of the ice to the surface [23]. Figures (4.7-A and B) show that the heaters underneath the ice layer provide a relatively constant heat [15], which means that the time to de-ice thick ice in Figure (4.7-B) is much more than in the case of the thin ice in Figure (4.7-A). In the latter, the generated heat takes less than a minute to melt the ice interfaced layer, and gravity sheds the ice [15]. As seen in Figure (4.7-B), the de-icing behaviour in thick ice can be explained empirically as follows.

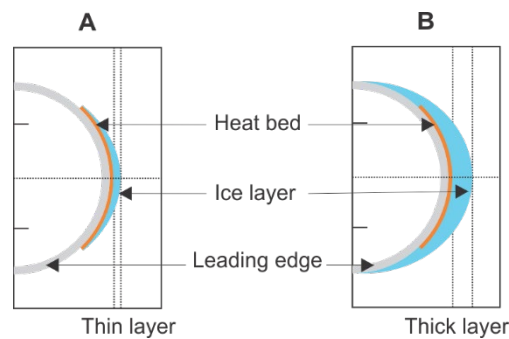


Figure 4.7 An illustration of ice accumulation around SZ, A-thin layer, and B-thick ice layer

Figure (4.8) illustrates thermal, binary, and visible images of the ice removal process employing heat elements under the ice layer at various times to help study the behaviour of ice throughout the de-icing process. The images A1, B1, C1, and D1 in Figure (4.8) are the thermal images. The images A2, B2, C2, and D2 in Figure (4.8) are the binary images of the corresponding thermal images. The images A3, B3, C3, and D3 in Figure (4.8) represent the actual visible images of the remaining ice at the corresponding time of the thermal images A1, B1, C1, and D1. During the de-icing process, as seen in image A1 of Figure (4.8), most heat energy produced by the heaters diffuses into the ice above the heaters [15]. In contrast, it diffuses weakly into the LE surface substance, due to fiberglass's low thermal conductivity [23]. If the heaters run long enough, the heat will cause joint failures in the thinner ice areas, and ice cracking occurs due to the difference in the thermal expansion coefficients of the ice and the substrate material [23]. The heat penetrates the outer surface of the ice [15], and when the ice breaks and falls, a warm region appears [15], as shown in image B1 of Figure (4.8). As time passes, the warm region gradually grows along the SL surface and replaces the ice region, as shown in image C1 in Figure (4.8). The heat over time reaches the surface skin of the regions surrounding the heaters' zone, and the rest of the ice loses its adhesion strength and is shed, as shown in image D1 of Figure (4.8).

The sequenced thermal images in Figure (4.8) show that as the warm region grows along the SL, as seen in images B2 and C2, the cold region where the ice region is located decreases, as seen in images B3 and C3. When the warm region covers the entire SL, as shown in image D2, the cold region vanishes, which means the surface became ice-free, as shown in visible image D3. Monitoring the growth of the warm region within the ROI_{thermal} and along the SL using thermal imaging helps estimate the remaining ice region along the SL because the two regions complement

each other. By knowing both the previous ice region and the present warm region, the remainder of the current ice region can be calculated.

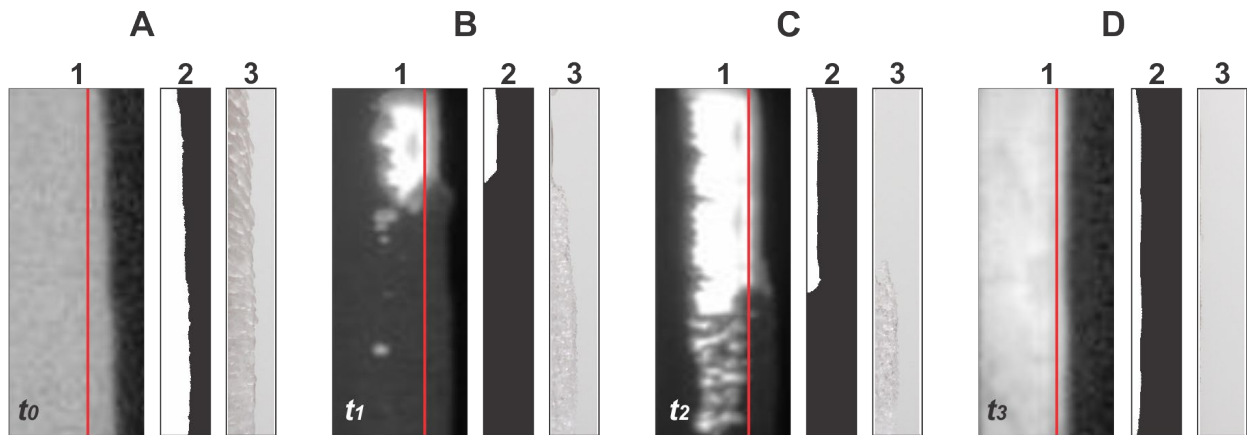


Figure 4.8 The changes of ice and warm regions over time at SL surface during de-icing

The de-icing process is a decremental process of the accumulated ice and can be described as in the illustrative example shown in Figure (4.9). Here, object (A) represents the previous event, object (B) represents the current event that affects the previous event of object (A). Object (C) represents the outcome of the arithmetic operation and is the remainder of the previous event of object (A). This example demonstrates the simplest technique of morphological transformation based on a subtraction operation [24]. It describes how object (C) can be obtained if both objects (A) and (B) are known. The concept of image transformation is that it generates a new image from two or more sources (historical data) to estimate the present situation. It has been used for many fields, such as mapping the changes in urban development around cities with satellite images, identifying areas where deforestation is occurring, and to identify areas of unhealthy or stressed vegetation. Another use for satellite images is tracking ice dimensions' changes in cold climate regions [24]. More details about image transformation methods can be found in references [25, 26].

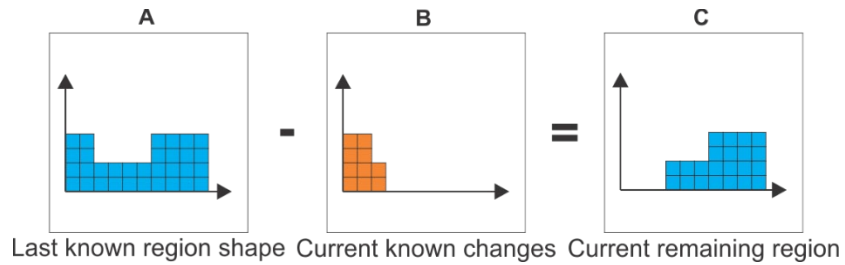


Figure 4.9 An illustration of the simplest morphological transformation method

The IR camera sees the cold region (ice layer) as a dark region next to the warm region. To estimate the size of the cold region of the current event, applying the concept of the described morphological transformation method to the last historical data on ice layer size can help estimate the ice region size of the current remaining ice layer. The binary images in Figure (4.10) are the exact binary images used in Figure (4.8). It illustrates the outcome of applying the method to historical ice data. The second column is the last historical binary image of the ice region, the fourth column is the binary image of the warm region of the current event, and the fifth column is the estimated binary image of the remaining ice region for the current event using image processing morphological subtraction. The obtained binary image in the fifth column is used as the last known historical data for the next event for estimating the next remaining ice region, as shown in B and C. This operation is repeated till the surface becomes completely warm, indicating that the surface is ice-free, as shown in D. The average thickness of the estimated ice layer is obtained in millimeters using Eq. (4.2).

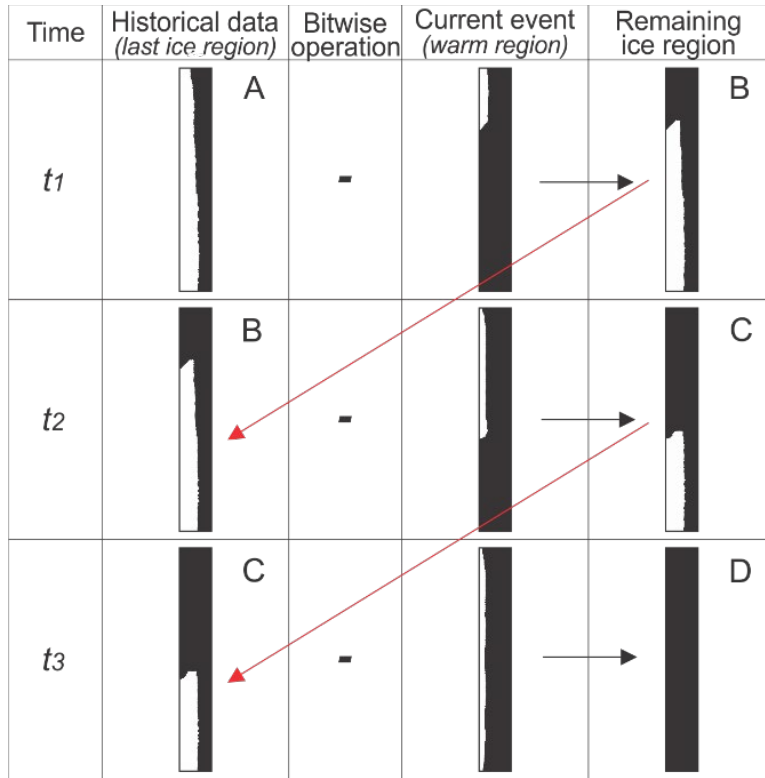


Figure 4.10 Estimating the remaining ice region using morphological method

4.2.3 The Theoretical and Practical Background of the Relaxation Process

Fundamentally, an IR camera captures the thermal distribution over a target surface. If any object is placed on a surface, the IR camera sees the thermal distribution of the top surfaces of both objects. The time required to melt the ice increases as the thickness of the ice grows [27, 28]. Because the accumulated ice on the SL is the thickest region, it is the last point to melt before the surface becomes ice-free. As a result, in order to track the average temperature on the LE surface, it must be at the SL, where the ice thickness is greatest. The term average surface temperature (T_{avg}) is defined as the arithmetic mean of all pixels' temperatures of the surface inside a narrow region of interest ($ROI_{surface}$) at the SL and adjacent to the $ROI_{thermal}$, as shown in Figure (4.11-A). The integrated system uses the $ROI_{surface}$ to track the average surface temperature, T_{avg} , throughout

the experiment. The T_{avg} can be obtained using Eq. (4.3) where $Temperature(i)$ is the surface temperature at pixel (i) and (N) is the number of pixels within the surface temperature region, $ROI_{surface}$.

$$\overline{Surface\ Temperature} (T_{avg}) = \frac{1}{N} \sum_{i=1}^{i=N} Temperature (i) \quad (4.3)$$

The de-icing process is deactivated when the system detects that the ice along the SL is removed. At this point, the surface temperature behaviour over time can be demonstrated, as shown in Figure (4.11-B). The average surface temperature T_{avg} , of the SL, starts to decrease until it reaches the freezing point within period t_l . During this period ice does not form on the surface, because the surface temperature is above the freezing point, which is the reason it is called a relaxation cycle. The surface temperature value T_{min} , is predefined and has to be entered into the system during the system setup. Once the tracked value of T_{avg} meets the condition of the minimum temperature of T_{min} , the system terminates the experiment.

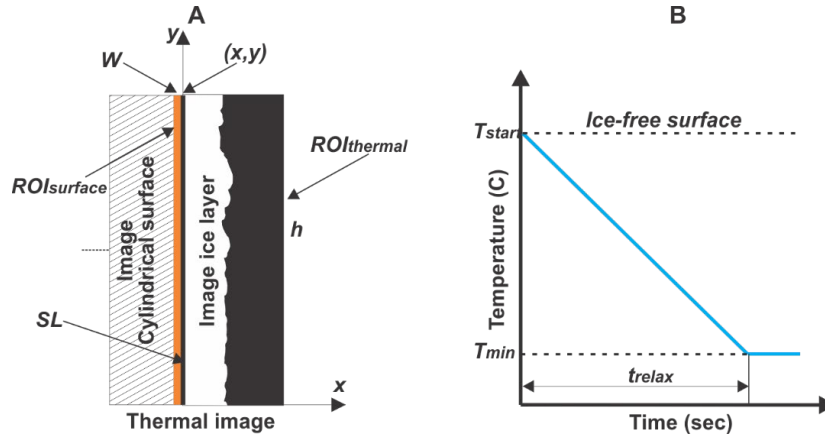


Figure 4.11 $ROI_{surface}$ definition (A) and T_{avg} versus time during relaxation cycle (B)

4.3 The Experimental Setup and Method

The methodology section is divided into three sub-sections. The first sub-section focuses on the requirements of the integrated system, such as hardware and software, for developing the

proposed system model. The experimental setup is covered in the second sub-section. The experimental method is in the third sub-section.

4.3.1 The Requirements of the Integrated System

As illustrated in Figures (4.12 and 4.13), a hardware control unit with customized circuitry is built. The hardware consists of a data acquisition module, namely NI9375, installed in a compact cDAQ-9171 chassis made by National Instruments. The NI 9375 provides 16 digital output channels [29, 30]. 12 of these channels are used in the experiment. Each channel is connected to a single switching relay to activate or deactivate a single electro-thermal element. Another component is a latch circuit, Model OME-DB-24R from Omega, which consists of 24 electromechanical relays. The contact of each relay can control 0.5 A /110 V. The relay is energized by applying a 5 V signal to the appropriate relay channel [31]. 12 of these electromechanical relays are connected to 12 pieces of silicone rubber fiberglass insulated flexible heaters, Model SHS80300, from Process Heaters Inc. [32]. The flexible heaters are placed in front of the target surface, as shown in Figure (4.12). The data acquisition module controls both the latch circuit and the heating elements. By setting the digital output of the data acquisition module NI9375 to 1 or 0, the heating elements turn on or off whenever the computer sends a corresponding operational signal.

An IR camera Flir E-60 is used in this study to capture sequential thermal images which received by a laptop. The Flir E-60 thermal camera offers several color palettes, including IRON and Grayscale palettes. The grayscale thermal image is the source of information in this study because it is a scaled indexed image and can be easily optimized, filtered, and binarized to extract ice thickness data using image processing algorithms. The IRON color image (false-color image)

is displayed directly on the computer screen because it is a multi-spectral image that helps the user observe and distinguish the temperature change during ice accumulation. The Flir Atlas SDK interface software is used in this study to extract IRON and grayscale images from the streaming images received directly from the IR camera by calling the palette manager using (`pal = thrmfile.PaletteManager;`) then assigning the name of the desired palette using (`thrmfile.Palette = pal.Iron;`) for IRON palette and (`thrmfile.Palette = pal.Grey;`) for grayscale palette [34].

The proposed integrated hardware is connected to a laptop and operates using customized software developed using a MATLAB platform [33] and FLIR SDK [34]. Altogether, this forms an integrated system of ice tracking and de-icing. The software user interface provides communication protocols to the hardware control unit and the IR camera. The flowchart map in Figure (4.14) describes the process flow of the customized software.

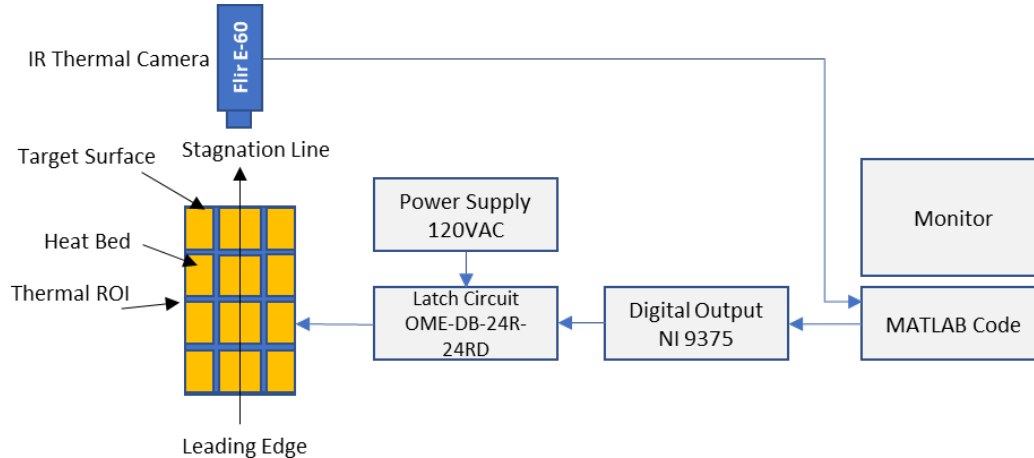


Figure 4.12 A block diagram of the hardware configuration of the integrated system

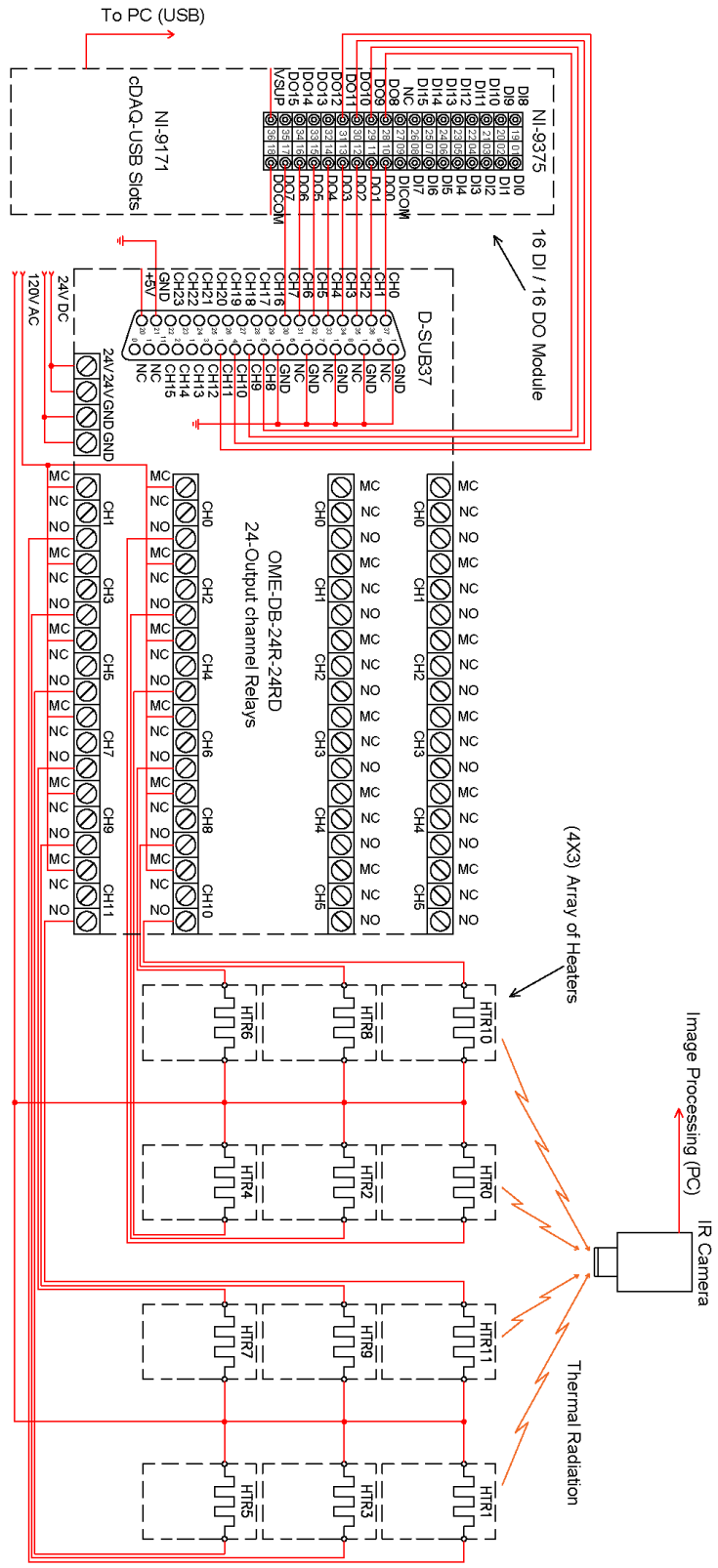


Figure 4.13 Schematic diagram of integrating IR ice sensing and electro-thermal ice mitigation

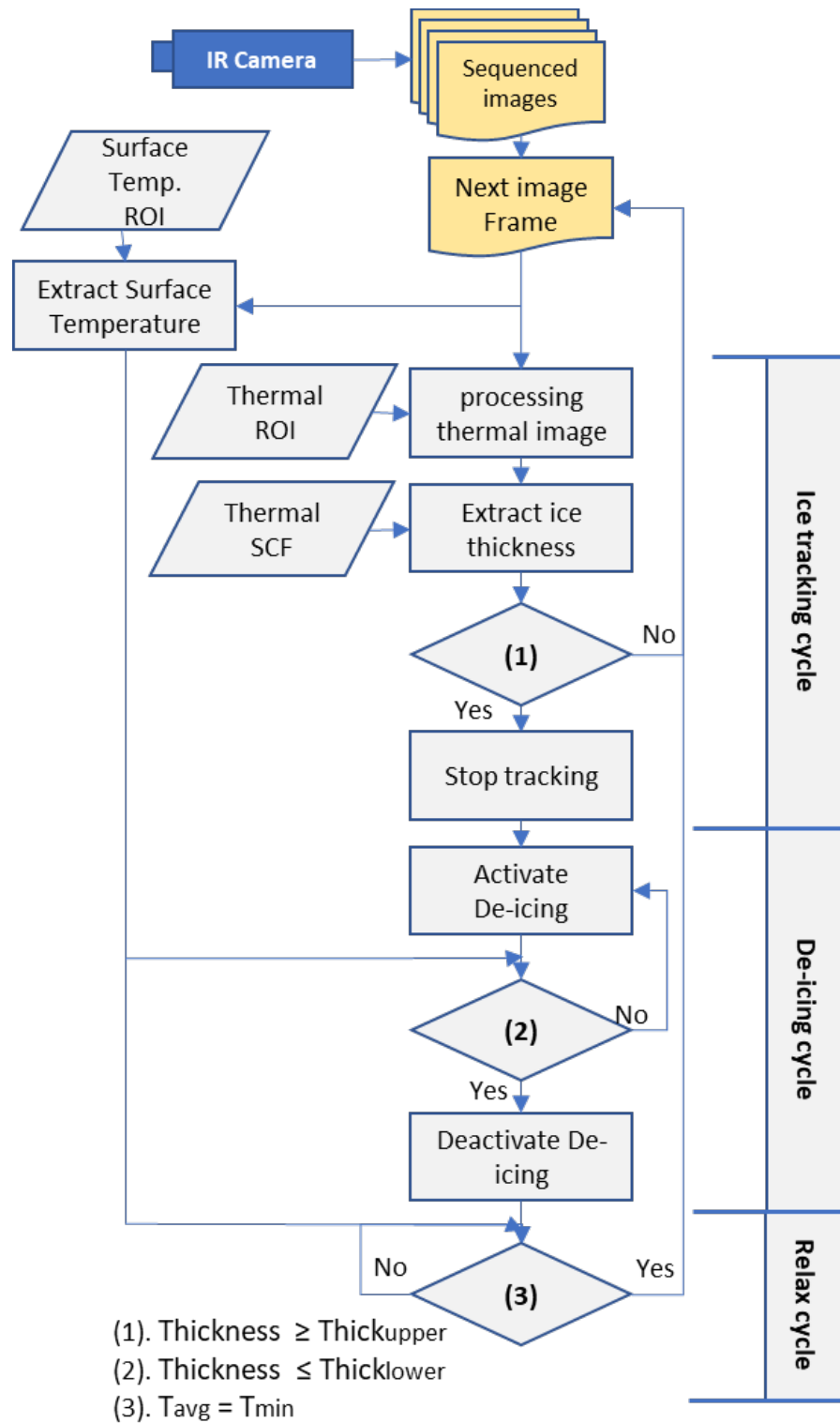


Figure 4.14 Flowchart of the process flow of the integrated system

4.3.2 The Experimental Setup

The purpose of the experiment is to verify that the integrated system of IR ice sensing and electrical heating elements can track the average thickness of ice accumulation on an SL of a cylindrical surface, trigger the heat elements when the thickness of accumulated ice reaches a predefined value of $Thick_{Upper}$, deactivate the heat elements once the remaining accumulated ice reaches the predefined value of $Thick_{Lower}$, at which time the target surface is ice-free, and observe the average surface temperature, T_{avg} , until it reaches the predefined value, T_{min} . Then the experiment is terminated.

Figure (4.16) illustrates the configuration of the experiment. The experiment's apparatus consists of a fiberglass cylinder with dimensions of a 24-inch length and 10-inch diameter, and a wall thickness of $\frac{1}{4}$ inch. The LE is the half part of the cylinder that faces the wind direction. The experiment's apparatus also includes a thermal infrared camera (FLIR E60) [35], an optical camera (Canon 7D), a laptop, MATLAB code, and a FLIR SDK. 12 heat beds cover the front region where the SZ of the LE surface of the cylinder is located. The heat beds are covered by fiberglass tape to protect the heat elements of the heat beds from damage by the running water during icing events and when the ice melts. Both cameras (FLIR E-60 and CANON 7D) are placed inside an insulated box made from styrofoam to protect the cameras from being damaged by low temperatures. The box has a window on one side facing the target surface. Both camera lenses are adjusted to focus on the SL of the surface target, as shown in Figure (4.16).

The experiment is conducted in a cold room. The cold room's visual environment is outfitted with light fixtures that create suitable light levels and uniform light distribution, as seen in Figure (4.16). The floor paint is a dark grey which plays a role in reducing the effect of reflection from the floor. The environmental temperature inside the cold room can be maintained in the range of -25°C to $+10^{\circ}\text{C}$. An axial fan is used to drive the airflow cycling inside the cooler. The wind

velocity is provided by a variable frequency drive which has the maximum rotor frequency of 59 Hz, and by varying the rotor frequency, different wind velocities can be obtained.

Pneumatic atomizing spray nozzles (Full Jet G and H nozzles), along with pressure regulators, are installed; the nozzles are in front of the fan to inject micro-sized water droplets into the airflow. The nozzles produce uniform spray distribution from 0.07 to 25 gpm (0.29 to 92 lpm). By manipulating the pressure regulators on the air and water lines of the spray nozzles, the mass flow rate of water injected into the airflow, and thereby, the liquid water content (LWC) of the airflow inside the cooler, can be adjusted. The liquid water content (LWC) is 0.6 and the mean volume diameter of the spray is 50 μm . The sprayed cloud is exposed to the low temperature of the cold airflow and its temperature drops during its journey towards the target surface, which helps in the formation of the icing condition.

There are some requirements for the experiment which must be addressed before beginning the experiment. The reflectivity is one of the parameters that must be calibrated in the IR camera. The reflected temperature feature will compensate for the error source provided that it has been measured properly. The measuring and compensating steps for reflected temperature require an IR camera and a diffuse infrared reflector. A diffuse reflector made from a crumpled and re-flattened sheet of aluminum foil has been wrapped around a piece of cardboard. The reflector is placed in front of the SL of the cylindrical surface. The IR camera emissivity control is set to 1.0, then the apparent temperature of the diffuse reflector is measured. The measured value of the reflected temperature is found to be $-5\text{ }^{\circ}\text{C}$ and is set in the IR camera E-60. Also, the emissivity parameter in the IR camera E-60 is set to value 0.95 which is the emissivity of ice [35]. The settings' configuration of the FLIR E60 camera is listed in Table (4.1).

Table 4.1 The setting of thermal camera FLIR E60

Image Type	Image Resolution (pixels)	Focus type	Camera Distance (m)	Emissivity	Reflectivity
IR Flir E-60	320 x 240	Manual	1.5	0.95	-5 °C

In addition, the ROIs are defined; the first region is a thermal ROI_{thermal} where the ice has to be tracked by an IR camera, as shown in Figure (4.15). Another region of interest is the surface temperature region, ROI_{surface}, which is used to track the average temperature, T_{avg} , within the narrow white region next to the SL throughout the experiment, as shown in Figure (4.15). Both the ROIs' size and location data are listed in Table (4.2). The SCF_{thermal} is calibrated within the ROI_{thermal} in the X-axis of the thermal image using Eq. (4.1) and is found to be (0.3861 Pixel/mm).

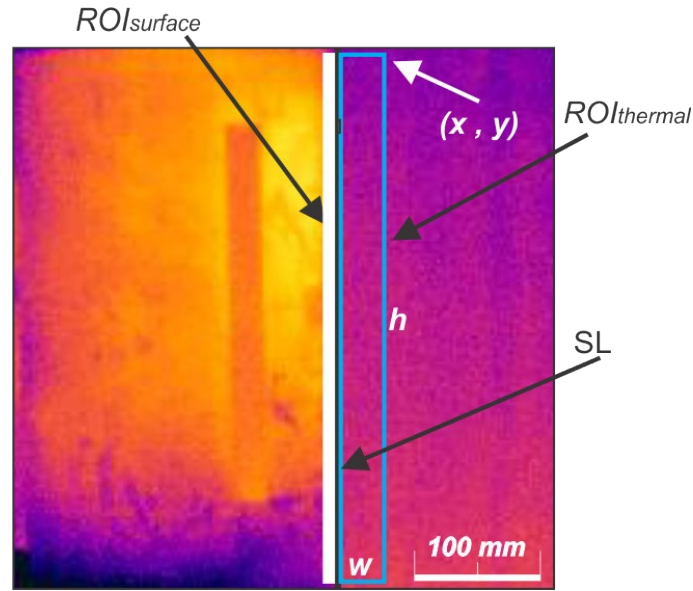


Figure 4.15 Defining both regions ROI_{thermal} and ROI_{surface}

Table 4.2 The position and dimension of the ROI_{thermal} and ROI_{surface} in pixels

Item	Top Position	Width	Bottom Position	Height
Thermal ROI _{thermal}	121.4	75.8	15.6	118.0
Surface Temperature ROI _{surface}	136.9	4	15.6	118.0

Moreover, the operation of the system components is controlled by providing the system with the necessary operational setpoints. These setpoints constitute the operating conditions of the system. Each subsystem of the integrated system works by checking the tracked variable with a predefined conditional value. When the condition is met, the operation of the subsystem is terminated and then the next subsystem is brought into operation. These setpoints include the value of the thickness of the ice at which the tracking process of ice accumulation stops, $Thick_{Upper}$, the value of the lower average ice thickness at which the de-icing process stops, $Thick_{Lower}$, and the value of the temperature at which the relaxation process stops, T_{min} , when the experiment is terminated. These values are entered into the system before starting the experiment. The experiment is conducted under two scenarios. The setpoints and the operating conditions of the two scenarios are listed in Table (4.3).

Table 4.3 The predefined setpoint and operating conditions values used in the experiments

Scenario	$Thick_{Upper}$ (mm)	$Thick_{Lower}$ (mm)	T_{min} (°C)	Cold Room Temp (°C)	Start Surface Temp (°C)	Wind Speed (m/s)
Scenario-1	20	< 1	0	-15°	-15° to -11°	4
Scenario-2	8	< 1	0	-5°	-5° to -4°	4

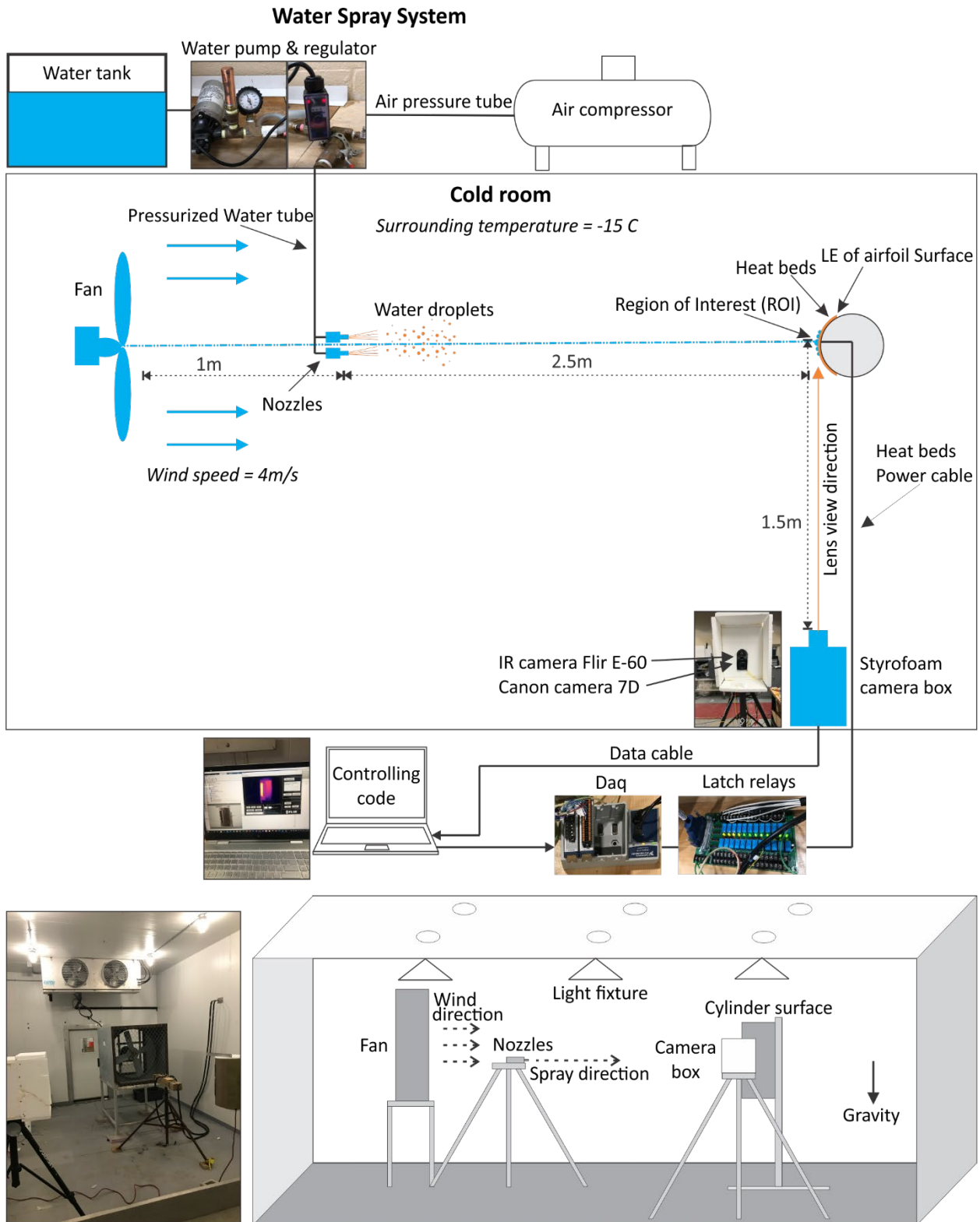


Figure 4.16 The experiment setup for the integrated system for ice tracking and mitigation

4.3.3 The Experimental Method

As shown in Table (4.3), the predefined Scenario-1 values for $Thick_{Upper}$, $Thick_{Lower}$, and T_{min} are utilized to configure the integrated system. The temperature in the cold room is $-15\text{ }^{\circ}\text{C}$, and the wind speed is 4 m/s . The IR camera is triggered once the operating requirements of Scenario-1 have been reached and stabilized inside the cold room. The water spray system is then triggered, and droplets begin to fly from the jet nozzles towards the cold surface, colliding with it. The deposited droplets freeze on the target surface. The freezing and impact behaviour of the droplets on the target surface are observed and recorded using the IR thermal camera. The customized software of the integrated system extracts a single thermal image frame every second from the received sequential thermal images. The image processing subroutines, discussed earlier, start tracking ice accumulation. As time passes, a MATLAB code monitors the extracted average thickness of the ice from the analyzed thermal images. Once the tracked average thickness becomes equal or close to the predefined setpoint value of $Thick_{Upper} \geq 20\text{ mm}$, the system stops the process cycle of ice tracking, and at the same time activates the de-icing cycle by sending a digital pulse to data acquisition to trigger the heat elements.

When the de-icing cycle is activated, the system starts monitoring the average ice thickness of the accumulated ice along with the SL and within the $ROI_{thermal}$. The system continues tracking the decrease of the average ice thickness, and when it reaches the lower predefined value of ice thickness, $Thick_{Lower} \leq 1\text{ mm}$, which indicates that the surface has become almost ice-free, a signal is sent to the data acquisition unit to turn off the heating elements. During the relaxation cycle, the system tracks the decrease of the surface temperature, T_{avg} , within the $ROI_{surface}$. Both wind and environmental temperature play roles in lowering the target surface's temperature. When the

tracked temperature becomes close to the setpoint's value of $T_{min} = 0^{\circ}\text{C}$, the system stops tracking the average surface temperature, and the experiment is terminated.

Throughout the experiment, all icing and de-icing events that occur on the LE's surface were recorded using the IR camera, saved on the laptop's hard drive, and displayed on the laptop's monitor to ensure that the system is functioning as intended. The next section will go through how to process and analyze the sequenced thermal images that were captured.

4.4 Processing and Analyzing the Thermal and Optical Images

The sequenced thermal images recorded throughout the experiment are subjected to several image processing algorithms before yielding the findings. This section is divided into three subsections, the first of which is concerned with the analysis of thermal images of the ice formation process. The second sub-section addresses the analysis of thermal images taken while tracking the de-icing process. The third sub-section deals with the optical images that were acquired to validate the thermal imaging data.

4.4.1 The Image Processing Method for Tracking Ice Accumulation

To extract the accumulated ice information from a thermal image, object segmentation is applied to the processed thermal image of the accumulated ice. The image segmentation aims to separate a digital image into independent partitions or regions that are more significant, to recognize the objects in an image [2, 20, 22]. Several image processing algorithms are applied to prepare the thermal image for object segmentation.

Figure (4.17) shows the successive steps of image processing algorithms that is used to process and analyze all grayscale thermal images. To speed up the process of analyzing the images and to focus only on the $\text{ROI}_{\text{thermal}}$, the captured sequenced thermal image is cropped according to

the position and dimensions specified in the thermal region, ROI_{thermal} , which includes all pixels in the input image, and then a contrast adjustment is performed to remap image intensity values to the full display range of the data type. An image with good contrast shows sharp differences between black and white. Here, the contrast-limited adaptive histogram equalization method (CLAHE) enhances the contrast of the white region of connected pixels representing the ice layer. After performing the equalization, neighbouring grouped pixels are combined using bilinear interpolation to eliminate artificially induced boundaries [33, 36, 37]. The enhanced image needs to be binarized using Bradley's [38] and Otsu's [39] techniques to extract the droplets' pixels. For Bradley's method, a locally adaptive threshold is applied to the image, which calculates a threshold for each pixel using the local mean intensity around the pixel neighbourhood. Then a binary image is created by replacing all values above the determined threshold with 1s and setting all other values to 0s, as in Eq. (4.4). Otsu's method is performed to obtain the threshold value, which minimizes the thresholded black and white pixels' intraclass variance. The noise in the image can be a very thin noisy layer in front of the actual ice layer. The noise causes are the thermal radiation of the active ice layer and the tiny droplets that are still flying and have not hit the ice surface yet. Also, the noise can be holes inside the ice layer. Usually, the noise is defined as the separated connected pixels that are not part of the main object. To reduce the effect of the noise, morphological reconstruction algorithms [2, 33, 40] are used to fill any hole in the white object by replacing 0 with 1 and to remove undesired tiny white connected pixels in the black background area by replacing 1 with 0.

$$Z(a, b) = \begin{cases} 1, & I(x, y) > T_{thr} \\ 0, & I(x, y) < T_{thr} \end{cases} \quad (4.4)$$

where $I(x, y)$ is the input image, $Z(a, b)$ is the output image, and T_{thr} is the threshold value.

In nature, ice accumulates on a surface in layers. To simulate this procedure, a logic operator OR in Eq. (4.5) is used to add the new event in the current binary matrix (current layer), $BM_{current}$, to the previous events in the last binary matrix (the previous layer), $BM_{previous}$, as shown in Figure (4.17- E, F). The output image of the updated ice layer, $BM_{updated}$, is as shown in Figure (4.17- G). The pixels' details in the final segmented binary image, as shown in Figure (4.17-G), represent the updated accumulated ice layer at the moment of the process. The next step is to compute the average ice thickness from the ice region indicated in Figure (4.17-G). Both the spatial calibration factor ($SCF_{thermal}$) and the formula in Eq. (4.6), are used to calculate the average thickness of the present ice layer in millimeters.

$$BM_{updated} = BM_{Current} \Phi BM_{Previous} \quad (4.5)$$

$$\overline{Thickness}_{Thermal} (mm) = \frac{1}{n} \left(\sum_{i=1}^{i=n} Row\ length(i) \right) \times SCF_{Thm} \quad (4.6)$$

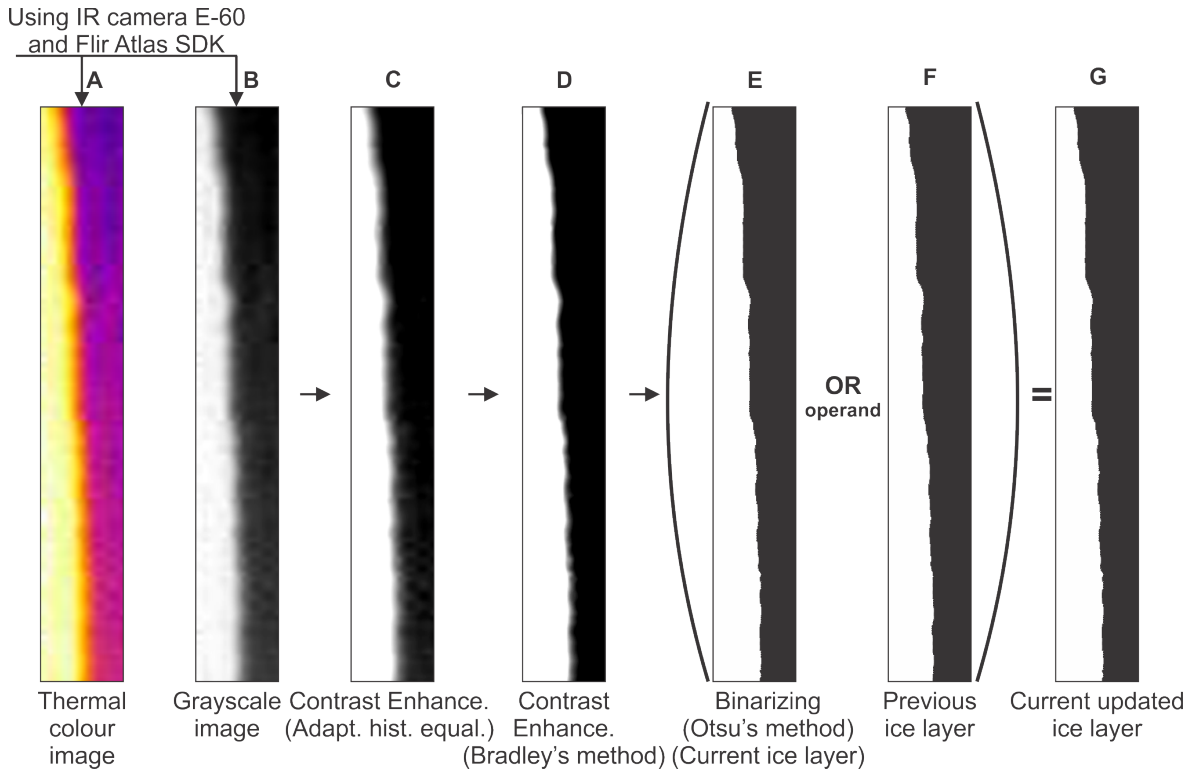


Figure 4.17 The steps of image processing algorithms used for processing thermal images

4.4.2 The Image Processing Method for Tracking Ice Removal

To track the decrement of the ice layer caused by de-icing process, a customized morphological transformation technique is developed using MATLAB code. First, the thermal image of the current ice layer, as shown in Figure (4.18-A), is processed using the image processing algorithms described at the early stage. Then the binary images of both the previous ice layer and the segmented object of the warm region, as shown in Figure (4.18-C), are exposed to a customized morphological transformation. The coding technique consists of three sequenced steps. First, a bitwise logical operation of ‘AND’ is applied to the binary matrices (BM) of both the current and previous thermal images’ objects to obtain the intersected portion of both objects. Then the output is used as a subtrahend in Eq. (4.7) to eliminate the intersected portion from the previous object and obtain the $BM_{uncleaned\ ice\ region}$. Subsequently, the warm region's area has to be set to zero. To achieve that, the average length, L , of the white columns of the current object (warm region) is obtained by Eq. (4.8). Then both the length, L , and the obtained object, $BM_{uncleaned\ ice\ region}$, are applied in Eq. (4.9) for replacing all undesired white pixels where the warm region is located with zeros. Figure (4.18-D) shows the estimated current ice layer's output binary matrix (BM). Both the dimensions of the thermal region $ROI_{thermal}$ and $SCF_{thermal}$, which are described at an early stage, are known. The formula in Eq. (4.2) is used to measure the average thickness of the current ice layer in millimeters.

$$BM_{uncleaned\ ice\ region} = BM_{prev.\ ice\ region} - (BM_{prev.\ ice\ region} \text{ AND } BM_{warm\ region}) \quad (4.7)$$

$$\bar{L} (pixel) = \frac{1}{N} \sum_{i=1}^{i=N} BM(i)_{warm\ region} \quad (4.8)$$

$$BM_{current\ ice\ region} = BM_{uncleaned\ ice\ region} \begin{pmatrix} 1,1 = 0 & 1,n = 0 \\ \cdot & \cdot \\ \bar{L}, 1 = 0 & \bar{L}, n = 0 \end{pmatrix} \quad (4.9)$$

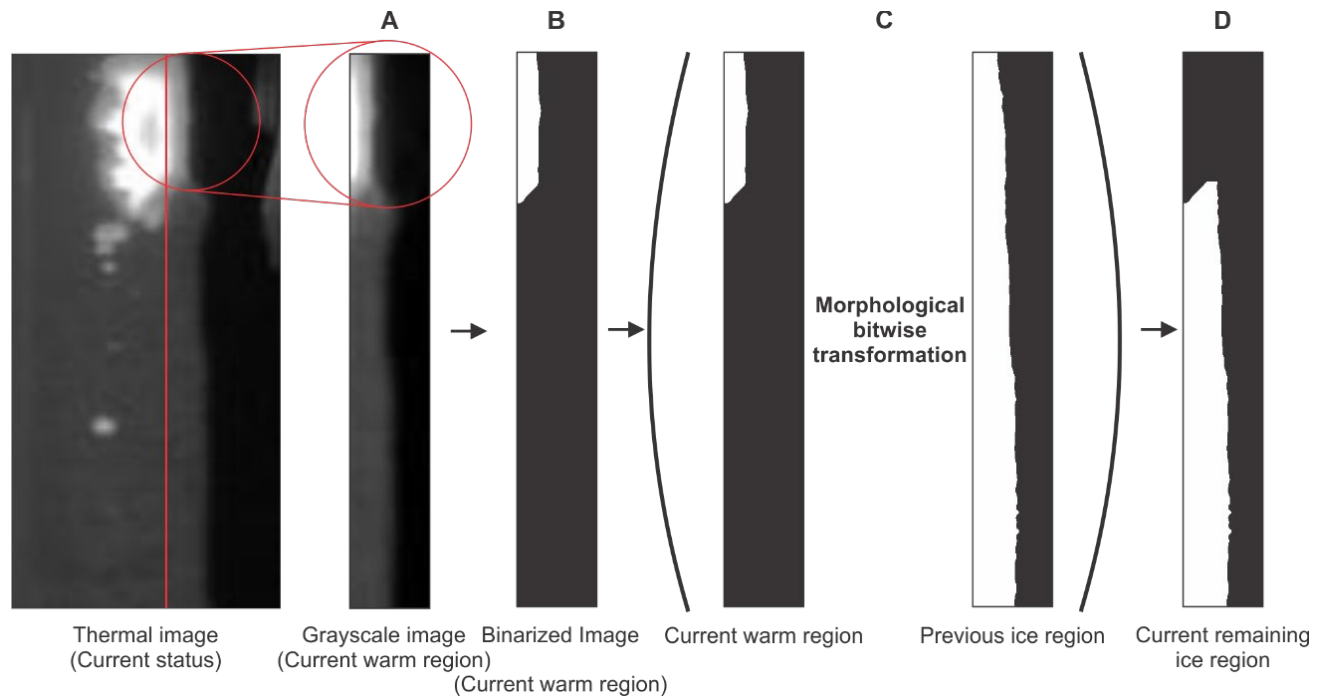


Figure 4.18 The steps of morphological transformation used for processing ice thermal images

All thermal image processing and analysis techniques discussed in the ice accumulation and de-icing sub-sections are iterative cycles. In each cycle, a single thermal image is extracted from the sequenced images and processed in fractions of a second. The IR camera FLIR-E60 uses 30 f/s for capturing sequenced images. Processing the images using this rate is unproductive. For this reason, it has been found that a frame rate of 1 f/s is sufficient to extract a single thermal image from the sequenced images to detect, track, and measure the changes in the ice layer thickness while recording the events of icing and de-icing.

4.4.3 The Validation Method

To check the validity of the results extracted from the thermal images, visible images corresponding to the thermal images are taken in the same region of interest. An optical region, $ROI_{optical}$, is used by an optical camera to obtain sequenced visible images. It corresponds to the thermal $ROI_{thermal}$ in location and size, as shown in Figure (4.19-A) and Table (4.4). Here, the term

optical image is used throughout the manuscript for the visual photos taken by the Canon 7D camera. The real dimension of an object can be obtained from its optical image using the Spatial Calibration Factor (SCF) [2] described earlier. The $SCF_{optical}$ is calibrated within the $ROI_{optical}$ in the X-axis of the optical image using Eq. (4.1) and is found to be (6.5426 Pixel/mm).

An optical image is captured using the CANON 7D approximately every 5 minutes during the tracking of ice accumulation cycle, and approximately every 1 minute during the de-icing cycle, as shown in Figure (4.19-B). For each captured optical image, the average ice thickness is obtained by using a MATLAB tool called “imtool”. First, the $ROI_{optical}$ is divided into a number of lines (n) of equal spacing, as shown in Figure (4.20) and then ice thickness at each individual line is measured in pixels, as shown in Figure (4.20). Finally, the optical region $ROI_{optical}$ dimension is known. The formula in Eq. (4.10) is used to measure the average thickness of the accumulated ice in millimeters, where *Thickness at line(i)* is the number of pixels at line (i), (n) is the number of lines within the $ROI_{optical}$ region, and $SCF_{optical}$ is the spatial calibration factor of the optical region of interest, $ROI_{optical}$. The measured average ice thickness results from the optical images are used to draw the graph in Figure (4.21). The time of capturing each optical image is used by MATLAB coding to look at the sequenced thermal images to extract the corresponding thermal image that is captured at a time equal or close to the captured time of the optical image. The results of both matched thermal and optical images are saved and used later in the results and discussion section.

$$\overline{Thickness}_{optical} (mm) = \frac{1}{n} \left(\sum_{i=1}^{i=n} Thickness \text{ at line } (i) \right) \times SCF_{optical} \quad (4.10)$$

Table 4.4 The position and dimension of the optical region ($ROI_{optical}$) in pixels

Item	Top Position	Width	Bottom Position	Height
Optical $ROI_{optical}$	2985	709.7	264.4	1981.9

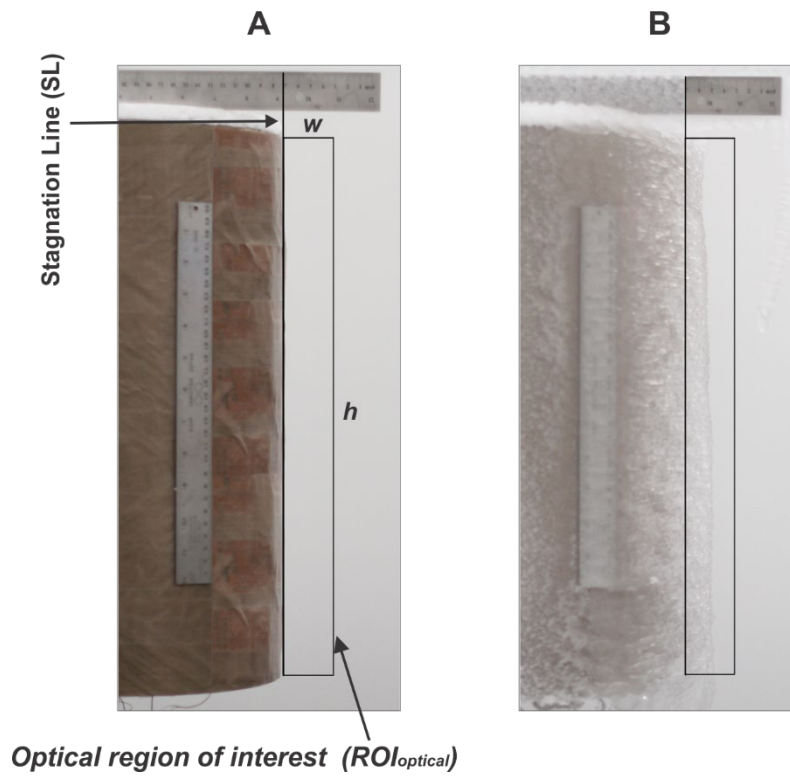


Figure 4.19 The optical region of interest $ROI_{optical}$ without ice (A), and with ice (B)

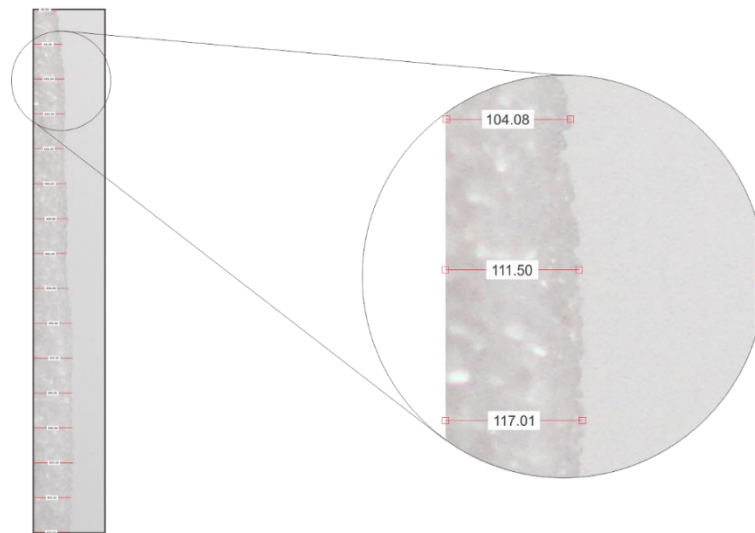


Figure 4.20 Measuring the average ice thickness within $ROI_{optical}$ along with SL in Pixels

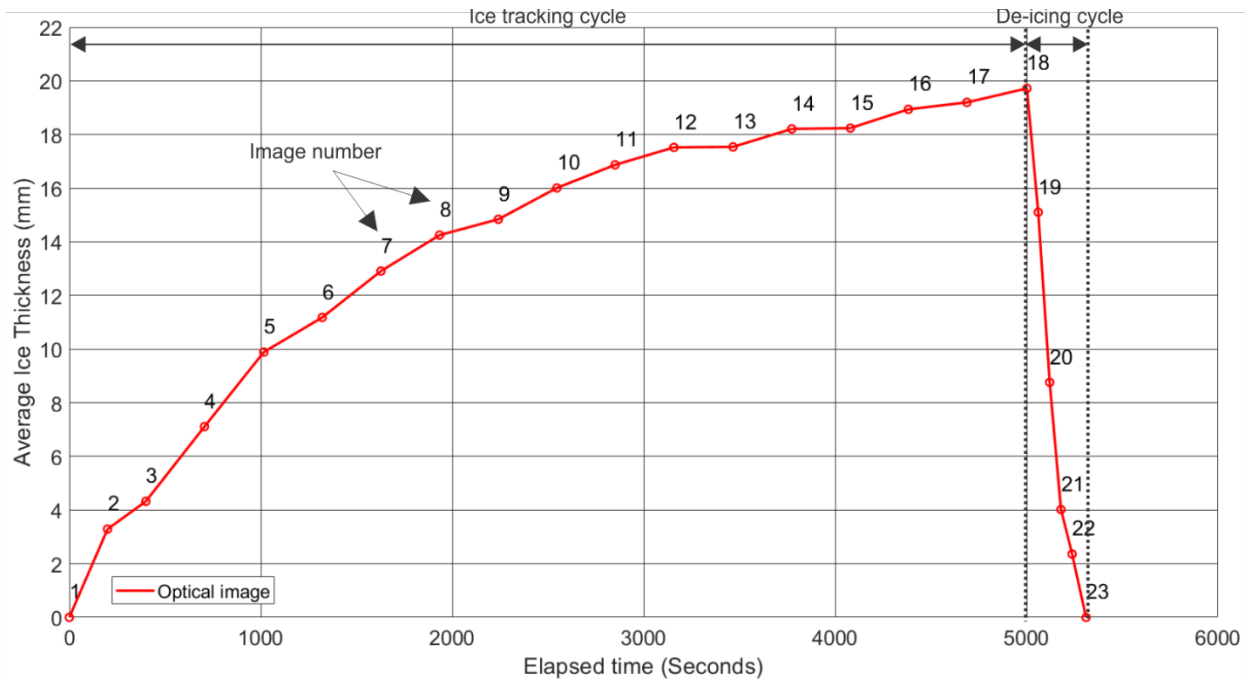


Figure 4.21 The average ice thicknesses measured from optical ice images versus time

4.5 Results and Discussion

The results and the discussion of the experiment are divided into four sections: ice tracking, de-icing, relaxation, and the integrated system.

4.5.1 Ice Tracking Cycle

Figures (4.22 and 4.23) show visual extracted results for the sequential thermal images. Each image has two cells. The left cell shows the actual thermal image before it is subjected to image processing, and the right cell is its binary image processed using image processing methods. The images are arranged according to their chronological order, starting from left to right and then from top to bottom. The extracted readings include the capturing time in minutes and the average ice thickness in millimeters. Successive images show the accumulation of ice over time.

The diagram in Figure (4.24) illustrates two curves representing the average ice thickness readings versus the time for the ice tracking process. The curve of the readings extracted from the

thermal images is based on an image frame rate of 1f/s, which means the ice thickness is measured every second. The data obtained by the validation method is used to generate the average ice thickness curve of optical images in Figure (4.24). The capturing time of the optical images is matched with the capturing time of the corresponded thermal images. Both curves show an increase in the average thickness of the accumulated ice as time passes.

The values of average (\bar{x}) and uncertainty (δx) of the measurements are obtained using Eq. (4.11) and Eq. (4.12), where x_1 is the optical ice thickness and x_2 is the thermal ice thickness. The average uncertainty ($\delta \bar{x}$) is obtained by summing the uncertainties values over the number of readings (N) using Eq. (4.13), and the standard deviation (s) is obtained by Eq. (4.14).

$$\bar{x} \text{ (mm)} = \frac{x_1 + x_2}{2} \quad (4.11)$$

$$\delta x \text{ (mm)} = \frac{|x_1 - x_2|}{2} \quad (4.12)$$

$$\delta \bar{x} \text{ (mm)} = \frac{|\delta x_1 + \delta x_2 + \delta x_3 + \dots + \delta x_n|}{n} \quad (4.13)$$

$$s = \sqrt{\frac{\sum \delta x_i^2}{(n - 1)}} \quad (4.14)$$

Table (4.5) lists the average and the uncertainty of the ice thicknesses extracted from both thermal and optical images. The results show that the accumulated ice in images 13, 15, and 17 have the highest thickness uncertainty, ± 0.33 mm, ± 0.35 mm, and ± 0.27 mm respectively, and the rest of the average thickness uncertainties are low. The reason for the increase in uncertainty at these points is that as more droplets hit the surface, the released heat radiation remains for a longer time and forms a thin layer in front of the ice layer. This layer is not part of the ice layer; it is a heat radiation layer. The heat radiation layer can cause noise, affecting the accuracy of the

readings extracted from the thermal images. This effect is called a systematic error [2], and can be reduced by applying the mean intensity thresholding value to the image. However, this cannot delete it completely, and it still has a slight effect on the accuracy of the number of pixels that represent the ice thicknesses, along with the SL, when extracted from the thermal image. The total average uncertainty value is found to be ± 0.16 mm with a standard deviation of 0.034 mm.

The plot in Figure (4.25) shows two curves. One curve is the average ice thickness within the ROI_{thermal} and the other represents the average surface temperature of the ROI_{surface} . Both results are extracted from the thermal sequenced images. The diagram consists of two zones (Zone-A and Zone-B). At the beginning of Zone-A, there is a significant fluctuation in the average surface temperature, ranging between -15 °C and -4 °C. The surface temperature is still far from the zero point. The reason for the high fluctuation in the surface temperature is that the water droplets freeze immediately, resulting in a rapid loss of the released heat due to fast freezing. As more droplets hit the surface and immediately freeze, the curve of ice accumulation rises exponentially. This rise decreases with the stability of the surface temperature as it approaches -2 °C at the time of 2700 s.

The average ice thickness curve at the beginning of Zone-B shows an insignificant increase and as time passes it does not increase; the average ice thickness curve is almost a horizontal line at the time of 4600 s and afterward. The reason for this is clearly shown in the average temperature curve at Zone-B. Once the surface temperature becomes close to zero, it becomes more stable and fluctuates less than in the previous zone, ranging between -1.6 °C and -1.2 °C. The water runback increases much more, stopping any ice thickness increase, as shown in Zone-B of Figure (4.25).

It was noted that when the average ice thickness reached 20 mm, the tracked value met the setpoint condition defined in the system. At this point, the system stopped the process of ice tracking and sent a signal to activate the heat elements of the de-icing process cycle. The ice

tracking cycle was terminated at 5002 s. The average surface temperature was $-1.2\text{ }^{\circ}\text{C}$, and the average ice thickness was 20.16 mm.

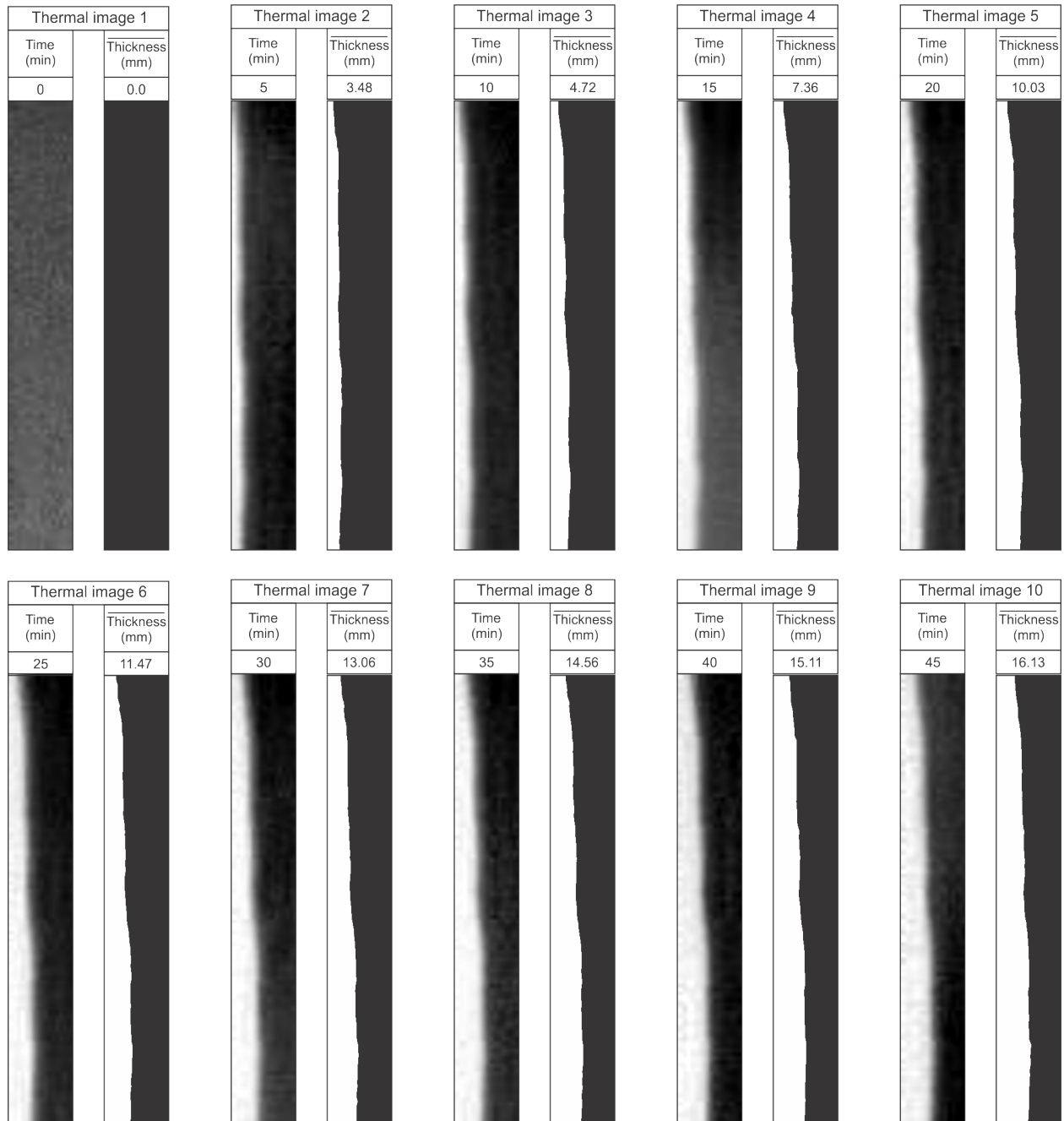


Figure 4.22 The ice thickness increment over time (A)

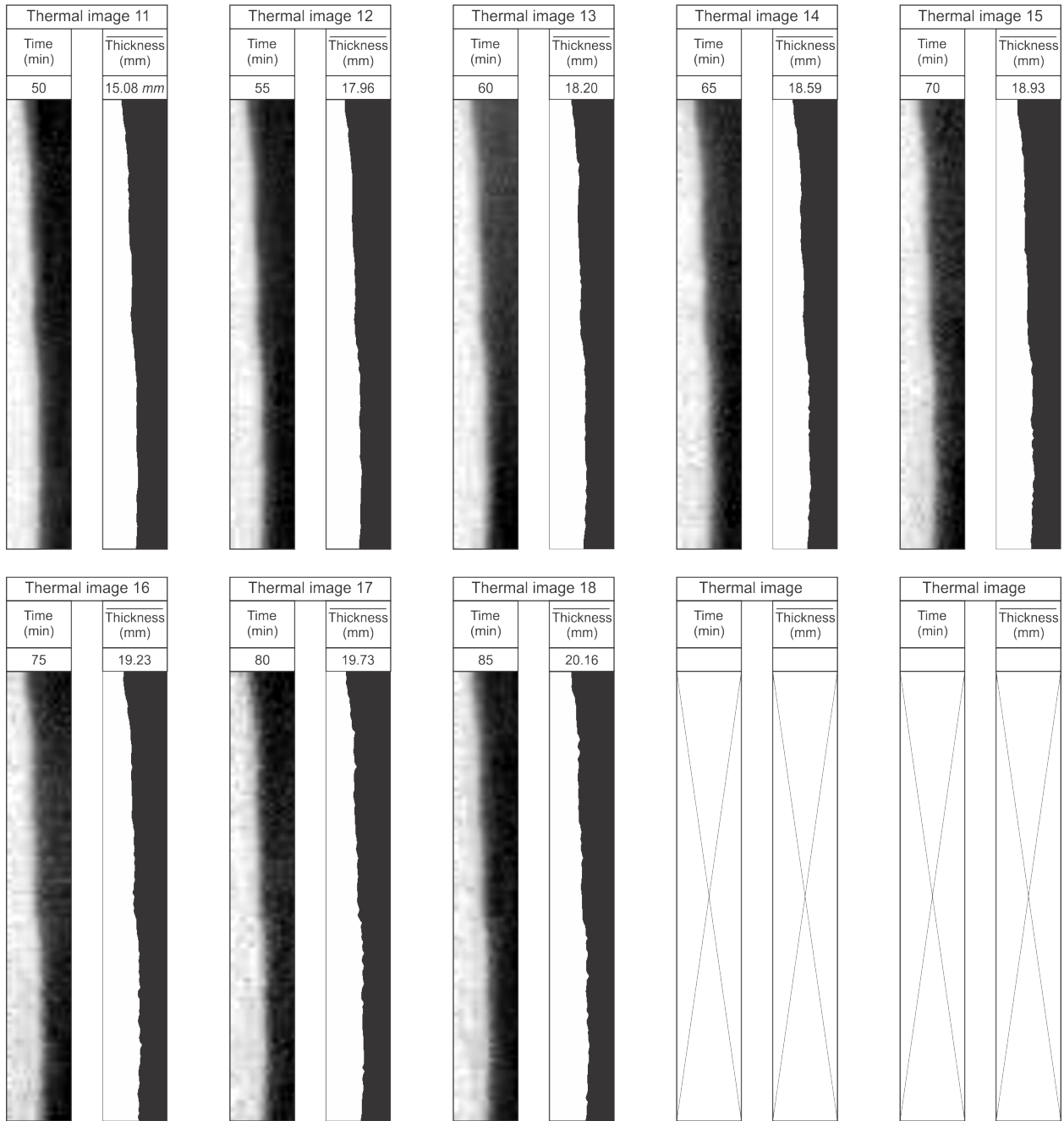


Figure 4.23 The ice thickness increment over time (B)

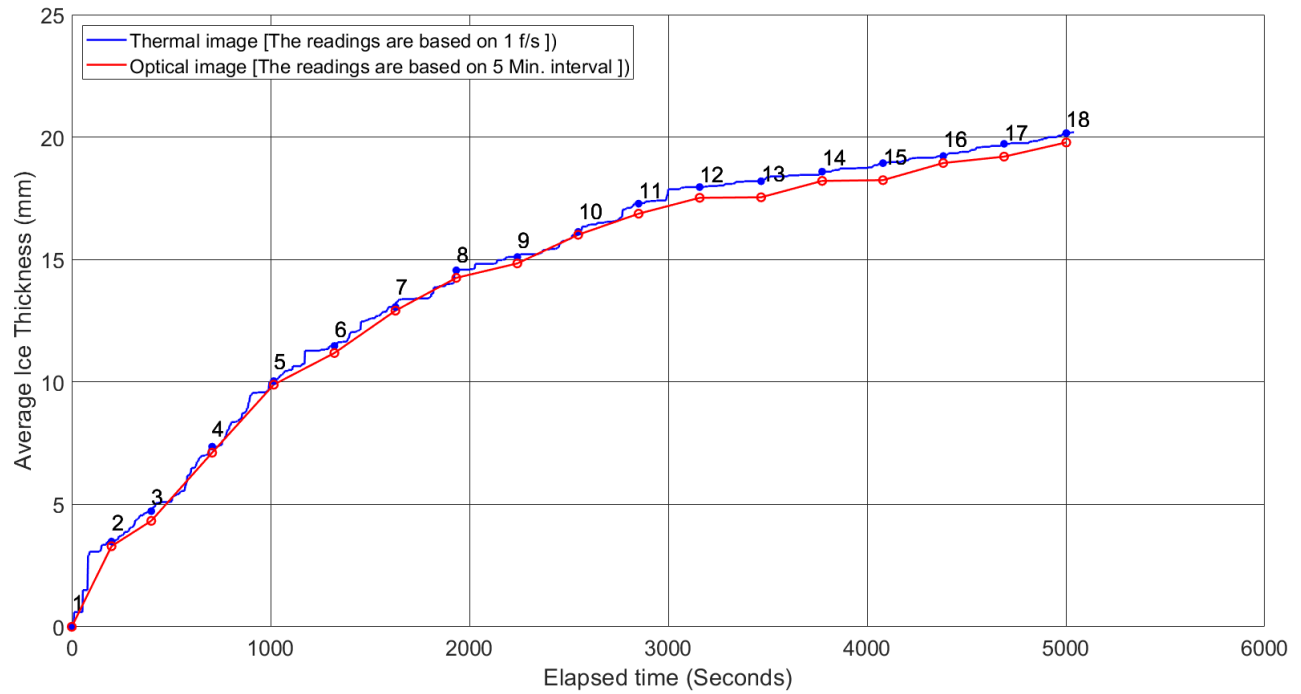


Figure 4.24 Measured and estimated average ice thickness over time

Table 4.5 Ice thickness uncertainties based on averaging of optical and thermal values

Image No.	Time (Min)	$\overline{Thick} (mm)$	$\overline{\partial Thick} (mm)$
1	0	0.00	0.00
2	5	3.39	± 0.10
3	10	4.53	± 0.20
4	15	7.24	± 0.13
5	20	9.96	± 0.07
6	25	11.33	± 0.15
7	30	12.97	± 0.10
8	35	14.41	± 0.16
9	40	14.98	± 0.14
10	45	16.07	± 0.10
11	50	17.08	± 0.21
12	55	17.74	± 0.22
13	60	17.87	± 0.33
14	65	18.40	± 0.20
15	70	18.59	± 0.35
16	75	19.09	± 0.15
17	80	19.47	± 0.27
18	85	19.94	± 0.22

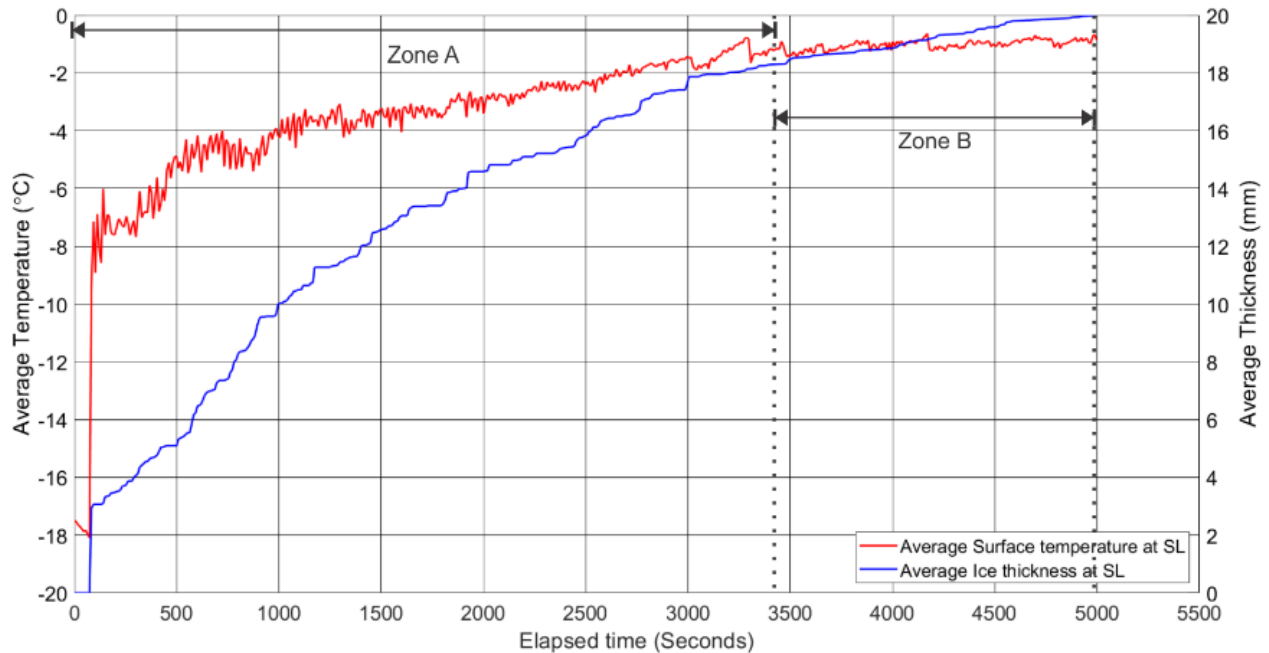


Figure 4.25 The average ice thickness and average surface temperature versus time

4.5.2 De-icing Cycle

The diagram in Figure (4.26) illustrates two curves representing the average thickness readings versus the time for the de-icing process. The curve of the results extracted from the thermal images is based on an image frame rate of 1f/s, which means the reading rate is a single reading per second. The data obtained by the validation method is used to generate the average ice thickness curve of optical images in Figure (4.26). A one-minute gap separates each pair of average ice thickness values retrieved from optical images. Both optical and thermal imaging measurements are used to plot the average ice thickness curves. Note that the graph only compares the readings of the thermal images that correspond to the time they were taken with the time the readings of the optical images were taken. This means that the curve of the optical images shows only the average ice thickness readings that are synchronized with the average ice thickness readings extracted from the thermal images with 60 second intervals. Both curves show a decrease in the ice thickness layer as time passes.

Table (4.6) lists the average and the uncertainty of the ice thicknesses extracted from both thermal and optical images. The results show that the accumulated ice extracted from images 18 and 21 have the highest thickness uncertainty, ± 0.22 mm and ± 0.14 , respectively, and the rest of the average thickness uncertainties are low. The following explains why these points have the most significant thickness uncertainties: the thermal radiation variations over the heated region vary continuously because of ice disintegrating and dropping. These changes can generate a perception of a halo (noise) encircling the actual warm region and an apparent increase in the size of the warm region. When the complementary cold zone (the remaining ice region) is computed, this noise can lead to an erroneous estimation. By applying the mean intensity thresholding value to the image, the noise influence is decreased, and the inaccuracy of the extracted reading from the thermal image is minimized. The average uncertainty as an outcome is 0.1 mm, with a standard deviation of 0.018 mm. The majority of the measured average thickness values from thermal images are close to the measured average thickness values from optical images, as shown at the measured points in Figure (4.26). The two curves in Figure (4.26) show the smooth operation of the de-icer, and it is turned off by the system when the surface becomes ice-free at $Thick_{lower}$ value.

The plot in Figure (4.27) shows two curves of the results obtained from the de-icing process. One curve is the average ice thickness within the $ROI_{thermal}$ and the other represents the average surface temperature, T_{avg} , of the $ROI_{surface}$. Both results are extracted from the thermal sequenced images. At the beginning of the de-icing stage, the average ice thickness curve shows a slight decrease of about 1.2 mm, as shown in Figure (4.27), due to the melting of the bottom of the ice layer interfaced with the heated region. During the same period, the T_{avg} curve in Figure (4.27) shows no change; it is very close to zero, because the IR camera detects only the average temperature of the accumulated ice layer's outer surface (the cold region). Heat transfer from the

warmest region (under the ice layer) to the coldest region of the outer ice layer surface takes about 36 s to respond [27, 28]. Several factors affect the length of this period. The first is that the period increases with the increase of both the thickness of the accumulated ice and its area at the SL [27, 28] because heat diffuses in thin ice faster than in thick ice. Secondly, the heat exchange process between the outer surface of the ice, and both the low temperature and the wind inside the cooling chamber, contribute to increasing the time required for the ice surface to respond to the heat transferred from the bottom of the ice layer.

As time passes, the ice at the SL starts to disintegrate and fall at the time of 5041 s and the system shows the average thickness value decreases from 18.96 mm to 15.21 mm, as shown in Figure (4.27); the corresponding image is image-19 in Figure (4.28). In Figure (4.27), the T_{avg} curve shows a sharp increase in T_{avg} as a result of an ice-free surface, where ice has disintegrated and falls to the floor. The average thickness of accumulated ice on the SL surface continues to decrease from the time of 5041 s to 5319 s, as shown in Figure (4.27). In the same period, the temperature curve of T_{avg} shows a large increase in the average surface temperature at the SL surface, as shown in Figure (4.27). This means that as the ice cracks and falls, the warm ice-free region expands, and thus the measured average surface temperature, T_{avg} , increases within the $ROI_{surface}$ along with the SL. It can be concluded that the average ice thickness of the remaining ice decreases as T_{avg} increases, as shown in Figure (4.27) and in the sequenced thermal images in Figure (4.28). When average ice thickness reaches a value below 1 mm, as shown in Figure (4.27), the system deactivates the heat elements.

It was observed that the de-icing process stopped at 5319 s, while the monitoring of the average surface temperature, T_{avg} , continued during the cooling process of the relaxation cycle within the region of the $ROI_{surface}$. The experiment shows a gradual decrement in the readings of

the ice thickness during ice removal. This can be considered a good result, since it can be used to de-activate the heat elements when the surface becomes ice-free.

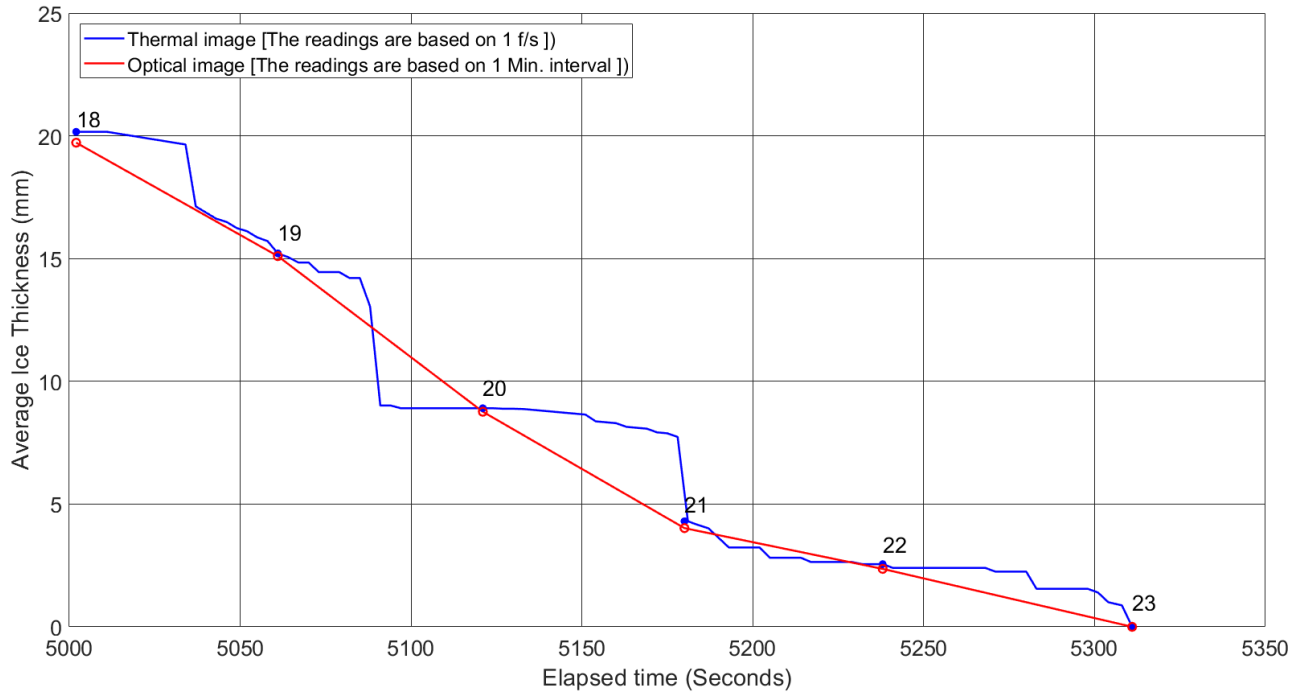


Figure 4.26 Measured and estimated average ice thickness over time during de-icing

Table 4.6 Ice thickness uncertainties based on averaging of optical and thermal values

Image No.	Time (Min)	$\overline{\text{Thick}}$ (mm)	$\bar{\partial}$ $\overline{\text{Thick}}$ (mm)
18	85	19.94	± 0.22
19	86	15.16	± 0.06
20	87	8.83	± 0.07
21	88	4.16	± 0.14
22	89	2.46	± 0.01
23	90	0.00	0.00

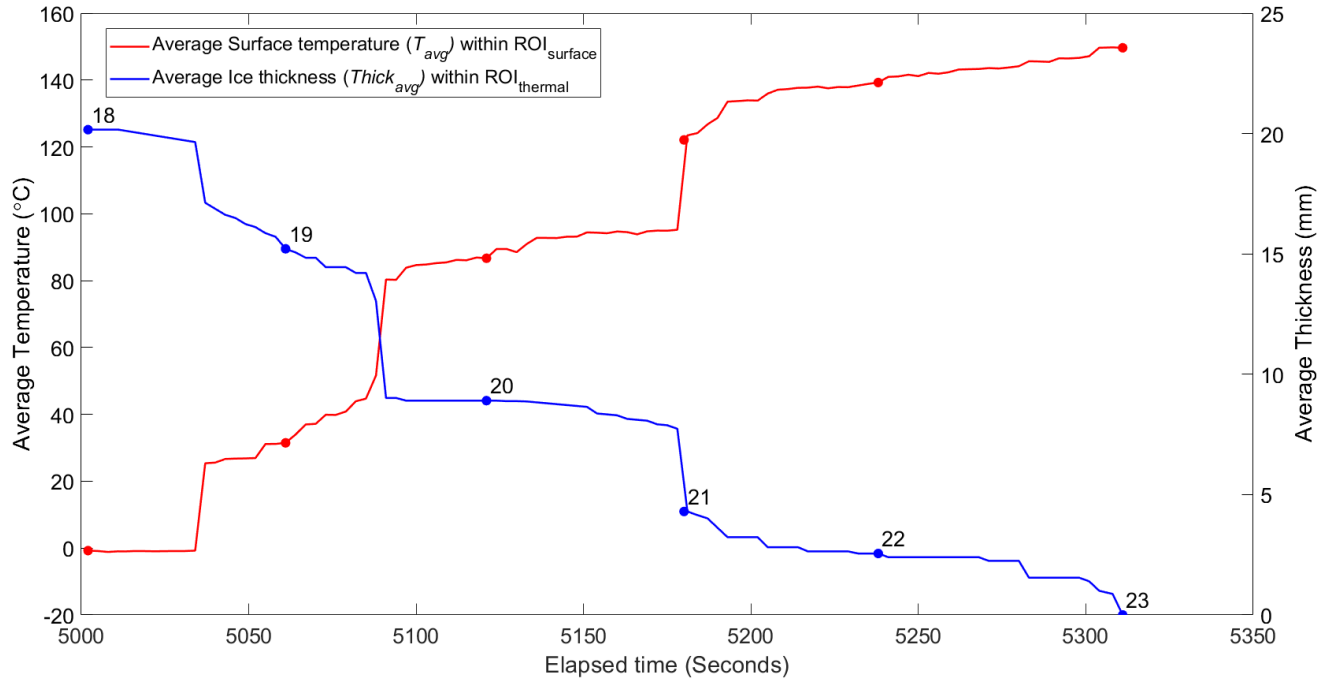


Figure 4.27 The average ice thickness and average surface temperature during de-icing

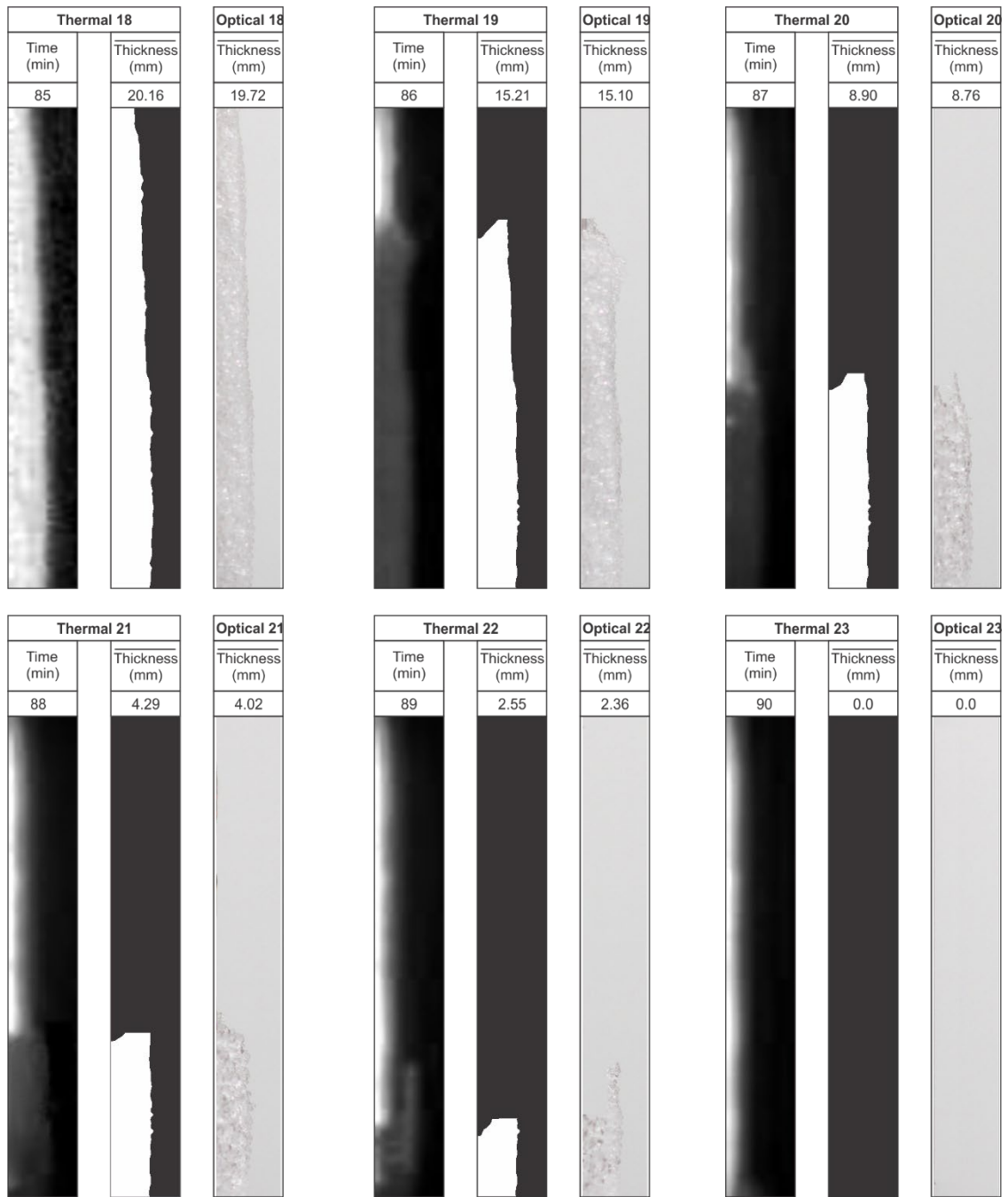


Figure 4.28 The decrement of ice thickness over time for both thermal and optical images

4.5.3 Relaxation Cycle

The relaxation cycle begins immediately after the de-icing cycle is completed and the system turns off the heat elements. The diagram in Figure (4.29) describes the process of the relaxation cycle. The system starts monitoring the surface temperature T_{avg} within the $ROI_{surface}$. The curve shows an exponential decrease in the T_{avg} , from 149 °C to 10 °C, at the time of 5319 s, for a period of 614 s. At this period, the average temperature of the surface T_{avg} is still high enough to continue melting the rest of the remaining ice adhering to the surface. As time passes, the curve shows a gradual decrease in T_{avg} . The system detects the freezing point at the time of 6294 s, which meets the condition of the setpoint of the average surface temperature. At this point, the system stops the relaxation cycle, and the experiment is terminated. The relaxation cycle takes 983 s to reach the freezing point, which is the setpoint temperature, T_{min} , defined in the system.

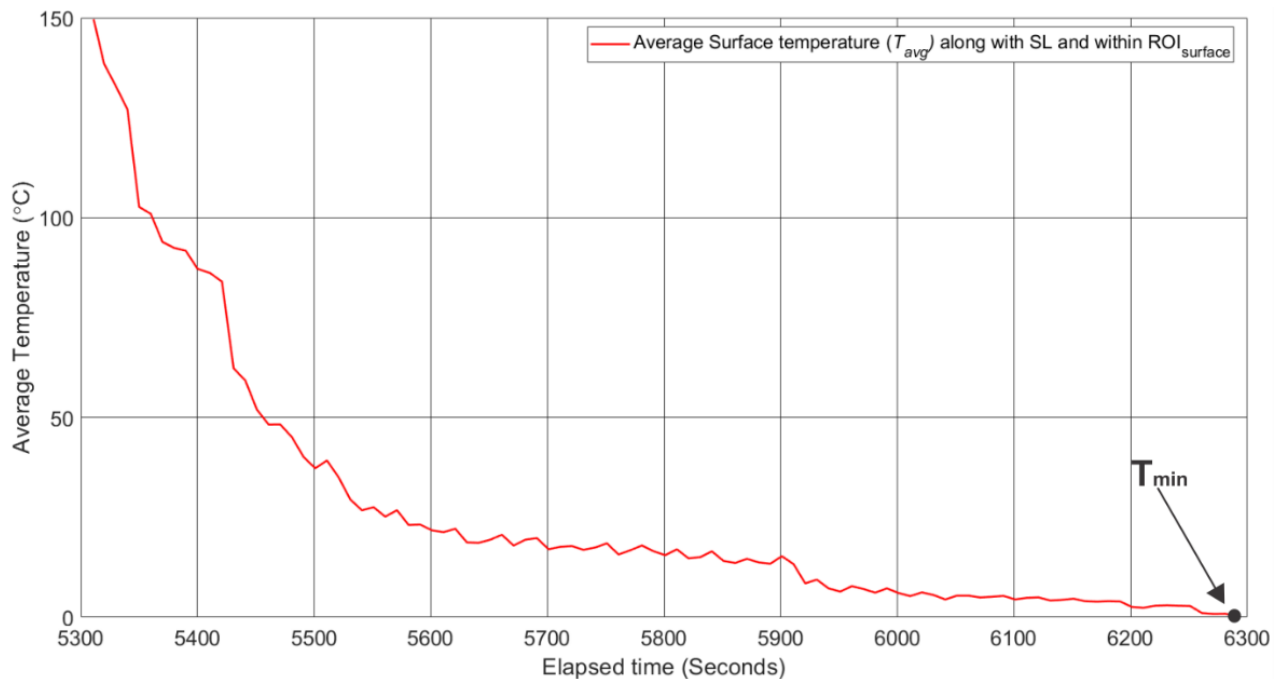


Figure 4.29 Tracking average surface temperature during relaxation

4.5.4 The Integrated System

Figure (4.30) shows the response scheme of the three components as well as the interaction of their functions to form an integrated system. They are the process of the ice thickness tracking cycle, the process of the de-icing cycle, and the process of the relaxation cycle. Curve-A represents the average thickness of the accumulated ice within ROI_{thermal} , and along with the SL, is obtained using thermal images, while Curve-B represents the average surface temperature, T_{avg} , within ROI_{surface} , and along with the SL, is also obtained from the thermal images.

The system activates the ice tracking process, which depends on thermal image processing to obtain the average thickness of the ice accumulated on the SL surface and within ROI_{thermal} . Curve-A in Figure (4.30) shows the system response results during the ice tracking process. Simultaneously with the process of tracking the thickness of the ice, the average surface temperature T_{avg} , Curve-B, is also tracked. When the thickness of the ice reaches the setpoint value of $Thick_{\text{Upper}}$ which is predefined in the system, the system stops the ice tracking process and activates the de-icing process. During the experiment, it was realized that the term "surface saturation," as shown in Curve-A, is a useful parameter that the system can use as an indication to stop the ice tracking process and activate the de-icing process when the ice thickness does not increase any further, even if the thickness setpoint condition is not met.

During the de-icing process, the system continues tracking both average ice thickness and the average temperature, T_{avg} . At the beginning of the de-icing stage, the average ice thickness decreases due to the melting of the bottom of the ice layer interfaced with the heated region. The period from the moment the heat elements are activated to the moment the system senses the change in the average temperature of the outer ice surface is called the time to respond, t_{respond} , as shown in Curve-B of Figure (4.30). It is the period required for the heat generated beneath the ice

layer to transfer through the ice layer. The length of this period depends on the thickness of the accumulated ice layer [27, 28]. As time passes the ice disintegrates and falls to the floor. The system continues tracking the average ice thickness, and each obtained value is compared to the conditional value of $Thick_{Lower}$, as shown in Curve A. The system stops the de-icing process and activates the relaxation process when the tracked value is equal to or below the setpoint value. The parameter $Thick_{Lower}$ is a thickness value predefined in the system which indicates the target surface becomes ice-free when the tracked value of average ice thickness reaches the $Thick_{Lower}$ value.

In the case of the relaxation cycle, the only activity performed by the system is that it continuously tracks the average surface temperature, T_{avg} , as shown in Curve-B, where each obtained value is compared to the value of T_{min} , which is previously defined in the system. The temperature, T_{min} , represents the limit at which the system has to stop the relaxation cycle and terminate the experiment or restart tracking the ice if required. It is observed that if the surface temperature T_{avg} is above the freezing point or very close to it, no freezing process of water droplets occurs on the surface.

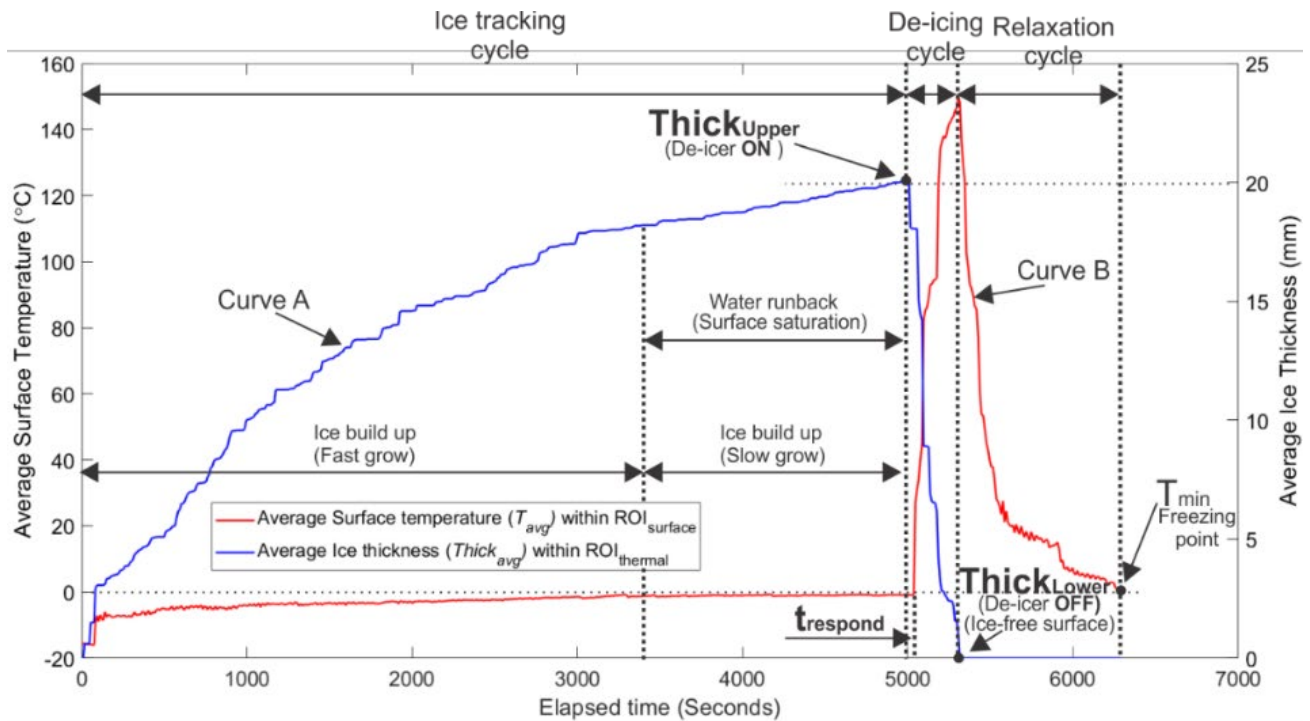


Figure 4.30 The complete system response for ice thick. 20 mm & ambient temp. -15 °C

Another experiment was conducted using the setpoints and operating conditions of Scenario-2, which are listed in Table (4.3), to study the system's reaction when it tracks and mitigates an accumulated thin thickness layer of ice at a cold environmental temperature close to the freezing point. The thickness setpoint in the system was set to a value of 8 mm, which represents the conditional value at which the ice tracking system has to stop tracking when it is reached. The test was for a cold room temperature of -5 °C. The result of the experiment is as shown in Figure (4.31). It shows two curves. Curve-A represents the system's response for tracking the average ice thickness, and Curve-B represents the system's response for tracking average surface temperature. It is clear that both Figures (4.30 and 4.31) are identical regarding the behaviour of the integrated system. Both show that the system's functions respond effectively to changes resulting from both the internal setpoints of the system and the external environmental

conditions. The only difference between the two schemes is the timing and duration of the system's response according to the changes in these variables.

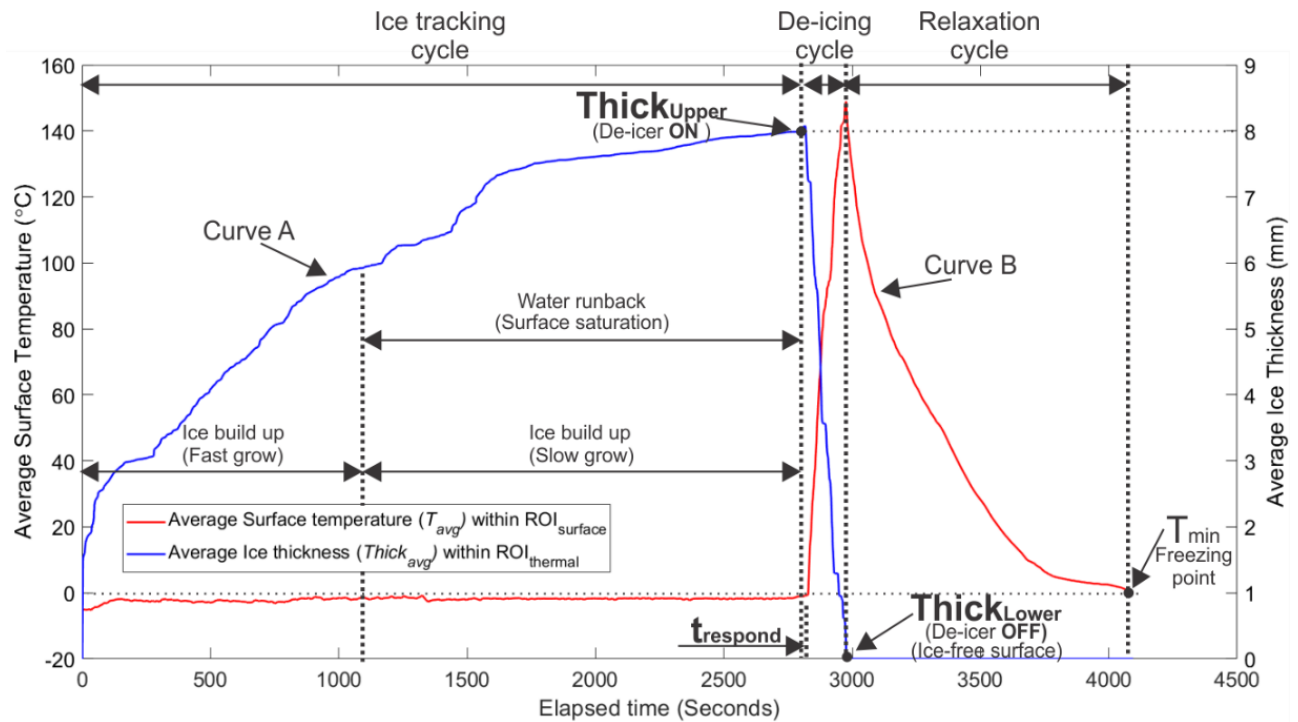


Figure 4.31 The complete system response for ice thick. 8 mm and ambient temp. -5 °C

Table (4.7) shows a comparison between the results of the two experiments regarding the time and period of the response for each component of the system; the differences among them will be explained below.

During the ice tracking cycle, the surface becomes wet at the time of 1100 s in Scenario-2 of 8 mm, which is an early stage compared to the time of 3400 s in Scenario-1 of 20 mm, due to the difference in the ambient temperature, which plays an important role in Scenario-1, reducing the surface temperature and keeping it away from the freezing point for a longer period compared to Scenario-2 of 8 mm. The period of the water runback in Scenario-2 of 8 mm lasts for 1680 s compared to Scenario-1 of 20 mm, which lasts for 1602 s for the same reason. The period of the ice tracking cycle for Scenario-2 of 8 mm is higher than half of the period of 5002 s for Scenario-

1 of 20 mm, because the ambient temperature of $-5\text{ }^{\circ}\text{C}$ in the case of Scenario-2 with 8 mm is close to the freezing point, causing slowness in the freezing process and thus increasing the time of the freezing process of successive water droplets hitting the surface. This will lead to an increase in the tracking period of ice accumulation which makes the period of the ice tracking cycle longer.

During the de-icing cycle, the time to respond period (t_{respond}) of 36 s in the case of Scenario-1 with the thickness of 20 mm is much higher than the period of 19 s of Scenario-2 with an 8 mm ice thickness, because the thicker ice slows the heat transfer from the heated surface beneath the ice layer, which increases the time of the response period, t_{respond} . Also, the very low ambient temperature of $-15\text{ }^{\circ}\text{C}$ in the case of Scenario-1 plays a role in cooling the ice surface, which increases the time of the response period compared to Scenario-2 of 8 mm. The period of 309 s for de-icing in the case of Scenario-1, with 20 mm ice thickness and an ambient temperature of $-15\text{ }^{\circ}\text{C}$, is larger than the de-icing period of 220 s for Scenario-2, with an ice thickness of 8 mm and ambient temperature of $-5\text{ }^{\circ}\text{C}$, for the same reasons.

During the relaxation cycle, the period of 983 s in the case of Scenario-1, with 20 mm ice thickness and an ambient temperature of $-15\text{ }^{\circ}\text{C}$, is less than the period of 1086 s for Scenario-2, with ice thickness of 8 mm and an ambient temperature of $-5\text{ }^{\circ}\text{C}$. This is because the surface cooling rate in the case of the very low ambient temperature of $-15\text{ }^{\circ}\text{C}$ for Scenario-1 is much higher than in the case of the temperature of $-5\text{ }^{\circ}\text{C}$ for Scenario-2.

In summary, both examples show that the proposed integrated system can detect, track, and mitigate the accumulated ice at different ice thicknesses and under different cold environmental temperatures. Moreover, both examples show that the relationship between the integrated system functions is a harmonic relationship. In other words, the system components

interact with each other according to the order of the functional purpose and under the conditions of predefined operational information.

Table 4.7 The system response comparison according to the two experiments' results

No.	Scenario	Surface wet start @ (s)	Runback period (s)	Ice track period (s)	Response period (s)	De-icing period (s)	Relaxation to 0 °C period (s)
1	20 mm @ -15 °C	3400	1602	5002	36	309	983
2	8 mm @ -5 °C	1100	1680	2780	19	220	1086

The ice tracking method is based on detecting and capturing thermal images of the released heat caused by the freezing process of water droplets that hit a cold surface. This means that a reduction in surface temperature caused by lowering the environmental temperature within negative values does not affect the ability of the method to track and measure ice thickness. It affects the time when the surface becomes wet, and the period length at which the surface becomes saturated as long as the ice continues to build up and the surface temperature rises [16, 41]. Also, the increase of wind speed in a cold climate reduces the surface temperature [2], allowing more time for water droplets to hit and freeze [13, 42], which increases the time of surface saturation occurrence but does not affect the process of ice tracking, for the same reason. In contrast, both environmental temperature and wind speed affect the duration of the de-icing and relaxation cycles. They have a direct impact on the surface cooling rate. As the ice surface temperature decreases, the time required for de-icing increases. In the same manner as for a cold wind speed, the time required for de-icing increases.

A study found that certain factors must be considered in order to increase the accuracy of temperature measurements [43]. The first consideration is the size of source effect (SSE), which is the effect of reflected thermal radiation from the surrounding environment on measurements. To mitigate the effect of SSE, the IR camera E-60 has an anti-reflective coating on the lens and a

high lens transmittance [35, 44]. Furthermore, the camera is housed in a box, which assists in decreasing the effect of SSE. The second determining factor is the region of interest, which must contain at least (10×10) pixels of homogenous temperature as specified in the references [43, 45]. The present study's ROI_{thermal} is substantially greater than the desired size, indicating that it fits the criterion. The third component is the spot size, which should be 1 pixel or a (3×3) pixel grid to ensure that the measurement is as accurate as possible [43, 45, 46]. In this investigation, the spot size ratio was calculated using the reference [46] and found to be 2:1500. This is the quantifiable size of a single pixel (1×1) . Since these factors have been taken into account, as a result, the temperature measurements in this study have an appropriate accuracy and are close to the actual ones. This fact leads to the conclusion that the source of ice thickness errors in thermal images is that the produced heat radiation from the freezing process generates a thin thermal layer in front of the actual ice layer, increasing the thickness of the ice, and impairing the accuracy of the thermal image readings. This thin layer has lower intensities than the active ice region, and its influence can be reduced by applying the mean intensity thresholding value to the image [2]. It cannot, however, be completely eradicated, and it continues to have a little influence on the accuracy of the number of pixels that represent ice thickness when extracted from the thermal image. The ice thickness is defined as the number of pixels in the X-axis direction, and it is calibrated using spatial calibration factor (SCF) to acquire the closest value to the real ice thickness in the X-direction [2]. Using the average ice thickness of all pixels' rows serves to decrease ice thickness inconsistencies along the SL (Y-direction) and approximate the average value to the actual ice thickness average value.

The ice in the thermal image in the case of the ice tracking process is the region with the highest brightness and the background is the region with the lowest brightness. Here, the

contour of the accumulated ice is separated from the background using the contrast difference between them within the ROI. In contrast, the ice region in the thermal image in the case of the de-icing process is the dark region with a low brightness, compared to the warm region of the heated beds, which has the highest brightness. Here, the ice region is obtained from both the warm and the previous ice regions. The warm region is also separated from the background using the contrast difference between them within the ROI. In both cases, the detection accuracy depends on the degree to which the pixel brightness gradient is distinguished. This means that the quality of the thermal image can affect the accuracy of measurement. The factors that can affect image quality include image resolution and image noise, and their effects are explained below.

Image resolution is considered a factor that can increase measurement accuracy. Usually, images of objects are represented by the number of pixels that form the object's shape in the image. Clearly, when more pixels represent the object in the image, the object's image quality improves and becomes more explicit, and vice versa. Low-resolution images can cause inaccurate measurements due to image blurring [2]. Even though the IR camera FLIR-E60 gives sufficient information about the ice thickness and surface temperature, which are considered acceptable, as discussed, the recent development of IR cameras with a higher resolution can give better image quality and better measurement accuracy.

Another consideration is the image's noise. In the thermal image of the ice buildup case, certain noise pixels can be found attached or adjacent to the actual pixels of the ice layer, or in the warm region in the thermal image of the de-icing case. The undesirable noises become part of the pixels that form the actual object image, regardless of whether the object is in an ice region or a warm region, which affects the average ice thickness measurement accuracy when extracted from the thermal image. Morphological reconstruction methods [2, 33, x40] are used to fill any holes in

the white object by replacing 0 with 1 and to eliminate unwanted little white connected pixels in the black background region by replacing 1 with 0. However, this cannot eliminate the image's noise completely, and it still has a slight effect on the accuracy of measuring the ice thickness [2].

Thermal de-icing systems are used to prevent the formation of ice on wind turbine blades. These systems can be powered by electrical heating or hot air. Electrical heating systems require temperatures above 0°C to melt the ice, while hot air systems use temperatures above 100°C to blow hot air onto the blade's surface to achieve the same effect. The temperature required for de-icing a wind turbine blade can vary depending on factors such as the type of icing and the materials used in the blade's construction. However, typically, the temperature of the heat elements used for de-icing wind turbine blades ranges from 60 to 80°C.

In the current study, heat elements were used to de-ice the leading edge of a cylindrical surface. It was found that these heat elements take 30 seconds to reach the maximum operating temperature of 149°C and require certain arrangements to limit their operating temperature. Although this temperature is higher than the typical range for de-icing wind turbine blades, it provides a clear indication of the effectiveness of the de-icing method and allows for accurate tracking and measurement of the de-icing process. Therefore, this method can still be used within the acceptable range of temperature for de-icing using heat elements.

Our earlier research [1] looked into the conceptual design of integrating ice detecting and mitigation systems using IR thermal imaging and electro-thermal elements. The evaluation was based on several key parameters, as shown in Table (4.8). Based on the conceptual design's evaluation, it was determined that the combination is applicable and deemed a promising integrated method. However, the result of the current study, as shown in Table (4.8), proves this

concept experimentally; that is, the IR thermal imaging and the electro-thermal elements can be combined to meet the essential requirements of the integrated system.

Table 4.8 The applicability of the proposed integrated system based on two studies

Feature	Previous study	Current study
System Response	Fast	1 f/s is found sufficient for tracking both thickness and temperature
Physical Integration at Workplace	Applicable	Both techniques work without interfering with each other
Closed-Loop System	Yes	The experiment proves this
Multiple Input Multiple Output System	Yes	The number of ROI can be increased
Coverage Area	Limited	It is wide as is proved experimentally
System Complicity	Medium	Because of heat beds' wiring
System Resolution	High	It is high because it depends on the thermal pixel map and number of heat beds
Energy Consumption	Low	It is low because it can be controlled, especially if the entire LE is heated
Analysis System	Image	It uses thermal image processing algorithms
System Concept	Applicable	It is applicable and the experiment proves this
System Interaction	Acceptable	The experiment proves integrated functions interact with each other

Moreover, the results of both experiments show that the proposed integrated technique can track and measure ice thickness on an SL surface remotely in a cold environmental condition, and obtain good results of average ice thickness with time. It is also established that T_{avg} tracking includes a feature that can instruct the system to activate the de-icing unit when the surface is saturated, even if the tracked average thickness value does not reach the upper thickness setpoint, $Thick_{Upper}$, requirement.

The proposed integrated technique can add some benefits to ice sensing methods. One advantage is the use of an arithmetic mean of the ice thickness along the SL to reduce the inherent discrepancy in the thickness of the ice caused by the ice's uneven accumulation, resulting in a rough surface with ridges of varying heights on the surface. Therefore, the average thickness of the ice derived from the thermal image provides acceptable findings that are near to the actual

results, as demonstrated in the experiment. The obtained average uncertainty values of ± 0.16 mm for the ice accumulation tracking cycle and ± 0.1 mm for the de-icing cycle are considered acceptable values and prove the benefit of using average thickness to track accumulated ice during ice buildup and mitigating processes.

It is found that using the time frame rate of 1 f/s is sufficient to perform the necessary operations of image processing, which need fractions of a second. The conducted experiment also showed there is no lag of the extracted information from the processed sequenced thermal images using this frame rate, which is considered another advantage of using the proposed technique for ice tracking and mitigation.

An additional benefit of utilizing an IR camera to detect and monitor heat created by both ice build-up and de-icing is that an IR camera can detect heat radiating from an object even when visibility is poor [47]. A comparison study reported that with four different weather conditions: urban pollution, light rain, fog, and heavy rain, the highest attenuation in thermal radiation occurred in thick fog [48]. Other studies stated that thermal radiation emitted by objects can be seen in the thermal image taken in heavy rain or in complete darkness [47, 48].

Infrared cameras have proven to be effective tools for tracking ice accumulation due to their ability to detect temperature differences and operate in low-light conditions. In contrast to optical imaging, infrared cameras excel at producing high-contrast images that enable the identification of ice accumulation from the surrounding environment. While the image quality of infrared cameras may not be as high as that of optical imaging, the temperature differences detected by infrared cameras are more relevant for the specific application of tracking ice accumulation. Near the boundary that separates the object from its background, there exists a significant similarity in contrast, which poses a challenge for the accurate extraction of the object's image

from the background. This difficulty, in turn, renders optical images unsuitable for tracking the accumulation of ice. The determination of the average ice thickness from optical images acquired within a cold room setting involved human visual inspection, with each measurement per image typically requiring a duration of 10 to 15 minutes. This approach, however, is insufficient for tracking the accumulation of ice, rendering it inadequate for this purpose. Furthermore, infrared cameras are less affected by surface reflectivity, which can pose challenges for optical imaging. Overall, thermal imaging with infrared cameras is superior for tracking ice accumulation, particularly in terms of visibility, image contrast and surface reflection.

Furthermore, the method can be used to keep the surface temperature above freezing point during icing events in order to avoid the accumulation of ice on the surface. The process of tracking surface temperature and turning on and off the heaters is an iterative cycle. As long as it is running, the average surface temperature, T_{avg} , is measured every second within the region's $ROI_{surface}$. Once T_{avg} meets T_{max} or T_{min} of the predefined conditions, the system reacts accordingly by activating or deactivating the heat elements.

The results obtained using a cylindrical surface are of utmost importance as they can be directly related to wind turbine blade surfaces. Despite the differences in their aerodynamic properties, both objects share the location of the stagnation zone where ice buildup often occurs, and the maximum amount of accumulated ice mass is located. To track the ice accumulation and de-icing processes, this study has adopted a small-scale circular shape of a cylinder to conduct necessary experiments around the stagnation zone. Furthermore, studies have shown that the shape of the ice profile closely resembles the contours of the airfoil's curved surface as more ice builds up on the surface. This finding highlights the relevance of the results obtained using the cylindrical surface to be applied to wind turbine blades, which are airfoil objects. The results obtained so far

are promising. The integrated system has been shown to be capable of detecting, tracking, and mitigating accumulated ice at different thicknesses and under different cold environmental temperatures using a small-scale cylinder as the target surface. However, further testing is necessary to confirm its performance on a larger scale, such as a real-world setting involving the wind turbine blade surface.

The de-icing system of a wind turbine is powered differently depending on whether the turbine is in shutdown or operational mode. In shutdown mode, an auxiliary power supply is used to heat elements on the leading-edge surface of the turbine, while in operational mode, the system is directly powered by the wind turbine itself. This is because the wind turbine does not generate electricity during shutdown mode, and thus requires an auxiliary power supply to provide the necessary electricity for heating the elements. However, during operational mode, using the wind turbine to power the de-icing system is a more efficient and cost-effective method as it eliminates the need for an auxiliary power supply and reduces energy consumption. Efficient utilization of resources in this manner ensures that the wind turbine operates reliably and effectively, which is essential for maximizing energy production and minimizing downtime.

The use of de-icing systems employing heat elements on the leading edge of wind turbine blades can result in additional weight being added to the turbine. Such weight may be attributed to the heat elements, associated wiring, and control systems. Nevertheless, the extent of additional weight is typically insignificant, and its impact on the overall mass of the turbine is considered minimal. The de-icing system may also have a slight effect on the turbine's speed, but its impact is generally considered to be negligible. The additional weight resulting from the system may lead to a slightly slower acceleration of the blades. However, once the turbine attains its operating speed, the influence on the overall turbine performance is deemed to be minimal.

While the current study shows acceptable results regarding the performance of de-icing systems on a cylindrical surface, which may not fully capture the complexities of real-world conditions, further research is necessary on the use of the proposed de-icing system on actual wind turbine blades to accurately quantify the system's effect on the turbine's weight, speed, and cost. Such studies can help provide a more comprehensive understanding of the performance of the proposed integrated system in real-world conditions and ultimately aid in optimizing the integrated system for improved energy efficiency, reliability, and cost-effectiveness.

The installation of an integrated ice monitoring and de-icing system in wind turbines requires several components such as an IR camera, an insulated box, wiring, a pole, heat elements, an auxiliary power supply, and a controller and computer. The material cost of these components can vary depending on the specific turbine and requirements needed, and the IR camera can be particularly costly due to its high-resolution features and long-life battery. Additionally, installation costs can be significant as the system requires the installation of a pole, wiring, and heat elements on the blade surfaces. Furthermore, maintenance costs should be considered since the system requires periodic inspection and repair.

However, the absence of an integrated ice monitoring and de-icing system can result in greater expenses compared to the cost of installing and maintaining the system. The lack of the system makes wind turbines more vulnerable to ice buildup, which can lead to reduced efficiency, increased wear and tear, and potential blade damage. The expense of repairing or replacing damaged blades, as well as the power generation loss due to reduced efficiency, can be substantial. Therefore, integrating an ice monitoring and de-icing system in wind turbines can be a beneficial investment in the long run. It can help guarantee efficient and dependable power generation, while also reducing maintenance costs.

4.6 Conclusions

This study investigated and developed an integrated system to detect, track, measure, and remove the accumulated ice above the SL of the circular surface and within the ROI, using thermal imaging and heat elements.

A literature review was performed to investigate the profile shape of the accumulated ice on the LE of both the airfoil and cylinder surfaces. It showed that most of the ice load on both surfaces was accumulated on the LE and that its peak points were around the SL, which was the reason for using the small-scale of a cylinder to carry out the experiments in the current study. Also, the review showed that the surface's temperature distribution changes over time as the ice grows on the surface and that its temperature signature can be used to detect, track and measure ice accumulation using processed thermal images. Furthermore, it confirmed that utilizing a morphological transformation method to process thermal images of the warm region caused by heated beds and the preceding ice region can identify the remaining ice layer and obtain the average ice thickness.

The proposed integrated system included three components. Both ice tracking and mitigation components used thermal images and image processing algorithms to obtain average ice thickness within the ROI_{thermal} . The role of the third component was to track the T_{avg} until it reached the freezing point to cause the system to terminate the experiment or track the ice build-up again if required. Three predefined setpoint values were used to operate the system, including the upper setpoint thickness (≥ 20 mm), lower setpoint thickness (≤ 1 mm), and minimum temperature (0° C). During the experiment, the time frame rate of 1 f/s was found sufficient to extract a single image and process it using the image processing algorithms described earlier. The extracted sequential thermal images and image processing algorithms were used to track changes both in ice accumulation during an ice event and ice decrease during ice mitigation, while the mean

surface temperature obtained by an infrared camera was used to track the relaxation process from 149° C until it reached 0° C. The optical camera's data were utilised to confirm the thermal images' results. The experiment showed that the average values of ice thickness in both the thermal image and the optical image when the de-icing process was activated, were 20.16 mm and 19.72 mm respectively, and the average values of ice thickness when the de-icing process was stopped, were 0 mm and 0 mm respectively. The findings of thermal and optical images taken during ice buildup and mitigation showed a good agreement.; the average uncertainty value for ice accumulation tracking was ± 0.16 mm with a standard deviation of 0.034 mm, and for ice mitigation tracking was ± 0.1 mm and the standard deviation was 0.018 mm. These findings are satisfactory and support the use of thermal imaging in tracking ice accumulation and de-icing. The study also stressed the importance of employing image processing techniques on grayscale thermal images to enhance image contrast, as well as using the mean threshold approach to improve measurement accuracy and minimize uncertainty.

Two experiments were conducted using two different average ice thicknesses as predefined setpoints and two different cold environmental temperatures. The combination for the first experiment was (20mm, -15° C) and for the second was (8 mm, -5° C). The results showed that the response behaviours of both experiments were identical. In the first scenario where the conditions were (20 mm, -15° C), it took 5002 seconds for the ice to accumulate and reach the upper setpoint of 20 mm. Whereas in the second case where the conditions were (8 mm, -5° C), it took 2700 seconds for the ice to reach the upper setpoint of 8 mm. Furthermore, the de-icing cycle length in the first case was 89 seconds longer than in the second case because the larger the thickness of the ice, the longer the period of de-icing. This means that pre-setting the upper value for measuring the average ice thickness is important procedure because it allowed the system to

directly manage the amount of the accumulated ice mass, whereas the length of the ice tracking period was restricted by environmental conditions. The length of the de-icing period was directly dependent on the amount of the accumulated ice mass, and the role of the setpoint of the lower value of ice thickness was to stop the de-icing process when the measured value of ice thickness met this conditional setpoint. The experimental results showed that the system responded according to both the system settings and the changes in cold environment conditions.

Previous research has shown that thermal images can be utilized to extract vital information [2], while the current study showed that the obtained data can be used to track not only ice buildup but also de-icing. Furthermore, this experiment confirmed the findings of our earlier study [1], which found that it is feasible to combine an infrared camera and heat elements at the same workspace without physical contact and acquire a rapid reaction, as well as construct an integrated ice detection and mitigation system. Based on the findings, it is expected that the proposed methodology will be a new contribution to airfoil surface ice sensing and mitigating methods and merit further investigation in the future.

4.7 References

- [1] Madi E, Pope K, Huang W, Iqbal T. A review of integrating ice detection and mitigation for wind turbine blades. *Renew. Sust. Energ. Rev*; 2019; 103:269-281.
- [2] E. Madi, K. Pope, and W. Huang. Estimating the volume of frozen water droplets on a cold surface during the phase change with thermal image processing. *Measurement*; 2021;183:109907.
- [3] Thomas, S. K., Cassoni, R. P., & MacArthur, C. D. Aircraft anti-icing and de-icing techniques and modeling. *Journal of Aircraft*; 1996; 33(5), 841-854.
- [4] Kibler, Elijah Mendoza. Determination of adhesive strength and freezing rate of ice on aircraft structures at subcooled temperatures. 2013. Theses. 297.
- [5] Pierre Lavoie. Modeling of thin water films on swept wings in icing condition. 2017; Thesis. Université de Montréal.

- [6] Anderson, John D. Fundamentals of aerodynamics. 4th Edition. New York: McGrawHill, 2007.
- [7] A. Ebrahimi. Atmospheric icing effects of S816 airfoil on a 600 kW wind turbine's performance. *Scientia Iranica B*; 2018; 25(5), 2693-2705.
- [8] Fortin, G. and Perron, J. Wind turbine icing and deicing. AIAA 2009-274, Orlando, Florida: 47th AIAA. Aerospace Sciences Meeting; 2009.
- [9] M. Bragg, A. Broeren, H. Addy, M. Potapczuk, D. Guffond, and E. ontreuil. Airfoil ice-accretion aerodynamic simulation. in 45th AIAA Aerospace Sciences Meeting and Exhibit, p. 85, 2007.
- [10] D. Switchenko, W. G. Habashi, G. Baruzzi, and I. Ozcer. Fensap-ice simulation of complex wind turbine icing events, and comparison to observed performance data. in 32nd ASME Wind Energy Symposium; p. 1399, 2014.
- [11] Pedersen, M. C. Modelling Icing on Structures for Wind Power Applications. Ph.D. thesis. Aalborg University, Denmark; 2018.
- [12] Hudecz, A., Hansen, M. O. L., Battisti, L., & Villumsen, A. Icing problems of wind turbine blades in cold climates. Department of wind energy, Technical University of Denmark; 2014.
- [13] Liu, Yang & Waldman, Rye & Hu, Hui. An experimental investigation on the unsteady heat transfer process over an ice accreting NACA 0012 Airfoil; 2015; 10.2514/6.2015-0035.
- [14] Virk, Muhammad & Ghani, Rizwan. Experimental study of atmospheric ice detection on wind turbine blade using thermal infrared technique. *Wind Engineering*. 2013; 7: 71-78.
- [15] Peter Suke, B.Eng. Analysis of heating systems to mitigate ice accretion on wind turbine blades. Master thesis. McMaster University. 2014.
- [16] G.M. Ibrahim, K. Pope, Y.S. Muzychka. Effects of blade design on ice accretion for horizontal axis wind turbines. *Journal of wind engineering & industrial aerodynamics*. 2018; 173: 39–52
- [17] M. Papadakis, G.W. Zumwalt, R. Elangonan, G.A. Freund, M. Breer, L. Whitmer, An experimental method for measuring water droplet impingement efficiency on two- and three-dimensional bodies, Technical report; 1989; NASACR- 4257.
- [18] Atmospheric icing of structures, ISO 12494; 2001.
- [19] Dershowitz, Adam & Hansman, & Hansman, R. Experimental investigation of passive infrared ice detection for helicopter applications. 1992; 10.2514/6.1991-667.
- [20] Karev, Anatolij & Farzaneh, Masoud & Kollár, László. Measuring temperature of the ice surface during its formation by using infrared instrumentation. *INT J heat mass transfer*. 2007; 50: 566-579.
- [21] S. Jung, M.K. Tiwari, N.V. Doan, D. Poulikakos, Mechanism of supercooled droplet freezing on surfaces, *Nat. Commun*. 2012; 3: 615.
- [22] Ryerson Charles C. Assessment of superstructure ice protection as applied to offshore oil operations safety. US Army Research; 2009; 49.

- [23] Lasse Makkonen. Ice Adhesion-Theory, Measurements and Countermeasures. *Journal of Adhesion Science and Technology* 26(4-5):413-445. 2012. DOI: 10.1163/016942411X574583
- [24] Natural Resources Canada. Image interpretation & analysis- Image Transformations. 2015. Retrieved from: <https://www.nrcan.gc.ca/maps-tools-and-publications/satellite-imagery-and-air-photos/tutorial-fundamentals-remote-sensing/image-interpretation-analysis/image-transformations/9377> [Accessed 1 January 2022].
- [25] MathWorks. 2022. Types of Morphological Operations. Retrieved from: <https://www.mathworks.com/help/images/morphological-dilation-and-erosion.html> [Accessed 1 January 2022].
- [26] Open-Source Computer Vision. Morphological Transformations. Retrieved from: https://docs.opencv.org/3.4/d9/d61/tutorial_py_morphological_ops.html [Accessed 1 January 2022].
- [27] Rashid, Taimur & Khawaja, Hassan & Edvardsen, Kåre. Measuring thickness of marine ice using IR thermography. *Cold Regions Science and Technology*. 2018; 158.
- [28] Taimur Rashid. Monitoring of Marine Ice and its Thickness for Ship Anti-/De-icing Experimental and Analytical Study using Infrared Thermography. PhD thesis. The Arctic University of Tromsø. Norway; 2018.
- [29] National Instruments (2016). cdaq-9171 user manual. Retrieved from www.ni.com [Accessed 2 May 2021].
- [30] National Instruments (2016). ni-9375 datasheet. Retrieved from www.ni.com [Accessed 2 May 2021].
- [31] Omega (2009). ome-db-24r-24rd datasheet. Retrieved from www.omega.ca [Accessed 2 May 2021].
- [32] Tempco Flexible Heater. shs80300 datasheet. Retrieved from <https://www.tempco.com> [Accessed 15 June 2020].
- [33] MATLAB 2018a. The MathWorks, Inc., Natick, Massachusetts, United States.
- [34] FLIR. Atlas SDK for MATLAB. Retrieved from <https://www.flir.ca/support/products/flir-atlas-sdk-for-matlab>. [Accessed 15 June 2020].
- [35] FLIR (2013). IR camera E-60 user manual. Retrieved from www.flir.com. [Accessed 15 June 2020].
- [36] Al-Obaidy F. IC testing using thermal image based on intelligent classification methods. Master thesis; 1996; University of Technology, Baghdad, Iraq.
- [37] Zuiderveld K. Contrast limited adaptive histogram equalization. *Graphic Gems IV*.
- [38] Bradley D, Roth G. Adapting Thresholding Using the Integral Image. *JGT*; 2007;12:2,13-21.
- [39] Otsu N. A threshold selection method from gray-level histograms. *IEEE T Syst Man Cy C*; 1979; 9:1, 62-66.
- [40] McAndrew A. An introduction to digital image processing with MATLAB; 2004.

- [41] Jia Yi Jin, Muhammad Shakeel Virk. Study of ice accretion along symmetric and asymmetric airfoils. *Journal of Wind engineering & industrial aerodynamics*. 2018; 179: 240–249.
- [42] Lasse Makkonen, J R Stallabrass. The effect of roughness on the rate of ice accretion on a cylinder. *Annals of Glaciology*, 6; 1985.
- [43] Pušnik, Igor & Geršak, Gregor. (2021). Evaluation of the Size-of-Source Effect in Thermal Imaging Cameras. *Sensors*. 21. 10.3390/s21020607.
- [44] Howard W Yoon David W Allen Robert D Saunders. Methods to reduce the size-of-source effect in radiometers. *Metrologia*; 2005; 42(2):89. DOI: 10.1088/0026-1394/42/2/003
- [45] Ward, B. IFOV, Spatial Resolution, Spot Measurement Size, Distance to Spot Ratios... What do They all Mean? 2017. Available online: <https://www.linkedin.com/pulse/fof-spatial-resolution-spot-measurement-size-distance-brenton-ward/> (accessed on 18 May 2022).
- [46] Baker, A. How far can I measure with a thermal imaging camera? FLIR Systems. Available online: <https://www.controlengurope.com/article/163635/How-far-can-I-measure-with-a-thermal-imaging-camera-.aspx> (accessed on 18 May 2022).
- [47] Iwasaki Y, Misumi M, Nakamiya T. Robust vehicle detection under various environmental conditions using an infrared thermal camera and its application to road traffic flow monitoring. *Sensors*; 2013;13: 7756-73.
- [48] Iwasaki. A method of robust moving vehicle detection for bad weather using an infrared thermography camera; 2008; 1: 86 - 90.

Chapter 5: A New Method to Limit Thermal Energy Required to De-Ice the Leading Edge of A Cylindrical Surface*

** The materials in this chapter were submitted to Cold Regions Science and Technology; 2023. Authors Ezieddin Madi, Dr. Kevin Pope, and Dr. Weimin Huang collaborated on the paper. Madi conducted research, analyzed data, and wrote the original draft. Pope provided supervision and his extensive knowledge and expertise played a crucial role in ensuring the quality and accuracy of the research., while Huang offered guidance, support, and also assisted with reviewing and editing the manuscript.*

5.1 Introduction

Ice formation on structures in cold regions can pose serious dangers [1], especially on curved surfaces' leading edges (LE), such as airfoils or cylinder surfaces. An ice detector combined with a de-icer is necessary to avoid ice development on an LE's surface.

There are two types of ice mitigation techniques: passive ice prevention and active ice mitigation. For passive ice prevention techniques, no ice detector is typically involved. The process is typically carried out manually by spraying anti-freezing chemicals on the surface or coating it with an ice-repellent coating. However, in light icing conditions, these coatings are only helpful for short-term operations; they are useless in severe cold conditions. Passive ice protection methods were shown to be insufficiently durable when examined on airfoil surfaces [2, 3]. The other type is active ice mitigation techniques. They are used for removing ice from the leading edge of airfoil surfaces and are either anti-icing or de-icing. An anti-icing technique averts ice accretion during icing events while a de-icing technique removes accreted ice after ice accretion events. An active anti-icing technique usually uses power to prevent ice formation on an airfoil surface, compared to an active de-icing technique which is activated only after ice formation [4]. A de-icing system is typically initiated after the deposited ice has been recognized and stays active until the leading edge of the airfoil surface is free of ice. Active de-icing can be implemented either through open loop or closed loop actuation. In closed loop active de-icing, ice sensing is used in the loop. Then a signal is sent to activate the de-icing unit to remove the accreted ice, based on the output of the sensing system. Active de-icing techniques are more efficient in removing ice during moderate to severe icing circumstances when combined with a trustworthy and precise ice detector. [1].

A previous study [1] ascertained that ice detection with an infrared camera and ice mitigation with electrical heat elements are promising for de-icing a wind turbine blade. The infrared camera can detect heat emitted by heat elements from a distance. As a result, both may be coupled to create a closed loop system that can respond remotely and accurately. An earlier study [5] developed an integrated ice detection and mitigation system that uses thermal imaging and thermal elements. In addition to monitoring the heat radiated by the de-icing process, the integrated system tracks and calculates the amount of ice that remains on the surface until it is cleared.

The LE surface's stagnation zone (SZ) is where ice accretion frequently occurs and is also the location where the highest concentration of ice mass accretes [5-9]. Heat elements are typically placed at the SZ where ice accretes. As additional ice builds on the SZ, the profile shape of the accreted ice enlarges, and the ice distribution area over the leading edge (LE) of the cylinder surface expands, leading to ice that thickens outside the heating area. This causes an increase in the strength of the adhesive ice layer that is outside the heating zone [5, 10, 11], increasing the amount of heat energy required to weaken and remove it.

The front edge of an airfoil surface's stagnation zone (SZ) is especially sensitive to ice buildup [5, 10, 12]. The mass of ice accreted near the SZ creates a peak, which drops to zero on the lower and upper surfaces [7, 8]. The shape of the building ice will be similar to the curved surface of the airfoil. Over time, the ice profile on the airfoil's leading edge gradually transforms into an elliptical shape [13-16].

Therefore, as more ice accretes on the SZ surface, the elliptical geometry of the accreted ice shape expands, as does the ice thickness at the stagnation point (SP) and the heater's edge. The aerodynamic properties of an airfoil object may differ from those of a circular object, but both are

characterized by the presence of a stagnation zone where ice buildup commonly occurs and the maximum amount of ice mass is found [10, 12].

Furthermore, an airfoil's leading edge (LE) has a rounded shape that can be approximated by a cylindrical leading edge [17]. The unknown ice thickness at the heater's edge can be calculated using the known ice thickness at the stagnation point (SP) by applying the correlation between the elliptical shape of ice accretion on a cylindrical surface and the circular form of the cylinder.

Monitoring the thickness of the ice near the heater's edge and keeping it as thin as possible will assist in minimizing the thermal energy required for de-icing. This concept was the motivation of our interest in performing this study in order to find a geometric relationship between the thickness of the ice at the stagnation line and the thickness of the ice at the heater's edge, which can then be used to analyze the effect of ice thickness at the heater's edge on the amount of heat energy needed for ice removal.

This chapter establishes a relationship between ice thickness along the stagnation line (SL) and ice thickness at the heater's edge. The relationship is used to control ice mass and, subsequently, the required thermal energy for ice removal. To obtain accreted ice samples and perform the de-icing process on a round surface, this study adopts a small-scale circular cylinder shape to conduct the necessary experiments around the stagnation zone.

5.2 The Theoretical Background

Studies have reported that the shape of the ice profile will closely resemble the contours of the airfoil's curved surface as more ice builds up on the surface [13-16]. Figure (5.1) illustrates the evolution of the ice accretion profile shape on the stagnation point (SP) over time. It shows the incrementation of ice profile shape after t_1 and t_2 of ice accretion. As the ice accretion progresses, the ice mass collection efficiency reaches a maximum in the vicinity of the stagnation point (SP)

and decreases to zero at the lower and upper surfaces [8, 9, 18]. The ice formation follows the shape of the curved surface of the airfoil. Over a period, the ice profile transforms into an elliptical shape on the leading edge of the airfoil, as illustrated in Figure (5.1).

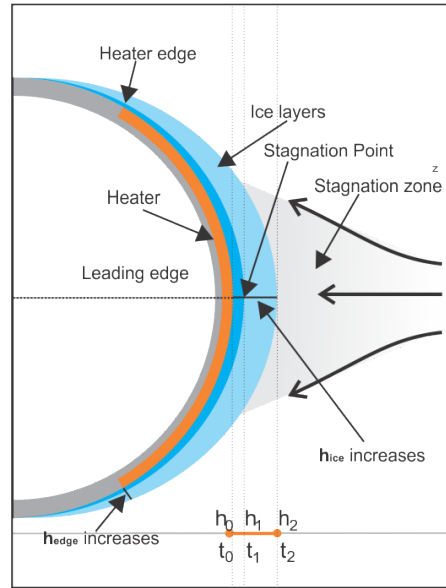


Figure 5.1 An illustration of ice profile shape increments with time

Ice accretion initially occurs on the leading edge, which is the heater's location. The constant heat flux of the heater will melt and shed the thin ice layer in a short period, as illustrated in Figure (5.2). However, as the ice continues to accrete, it will eventually surpass the boundaries of the heater. This leads to an increase in ice thickness, as demonstrated in Figure (5.2). If ice accretion extends past the edges of the heater, it can be difficult to remove. The constant heat flux generated by the heater will cause the ice layer interfaced within the heated area to melt [15]. However, the ice block remains attached to the surface, as it is still attached outside the heating zone. As more heat diffuses into the ice above the heated zone, the ice continues to fracture, as seen at t_2 , t_3 , and t_4 in Figure (5.2). Over time, the heat penetrates the ice at the edge of the heater, causing the attached ice block to disintegrate and collapse, as seen at t_5 in Figure (5.2). The thermal elements under the ice layer typically generate relatively steady heat [19]. Therefore, the amount

of heat energy, Q , required to melt all of the accreted ice on the heater surface can be determined by Eq. (5.1), where Q is the amount of heat, P_{heater} is the total energy of the heat elements, and t_{de-ice} is the time required for melting.

$$Q = P_{heater} \times t_{de-ice} \quad (5.1)$$

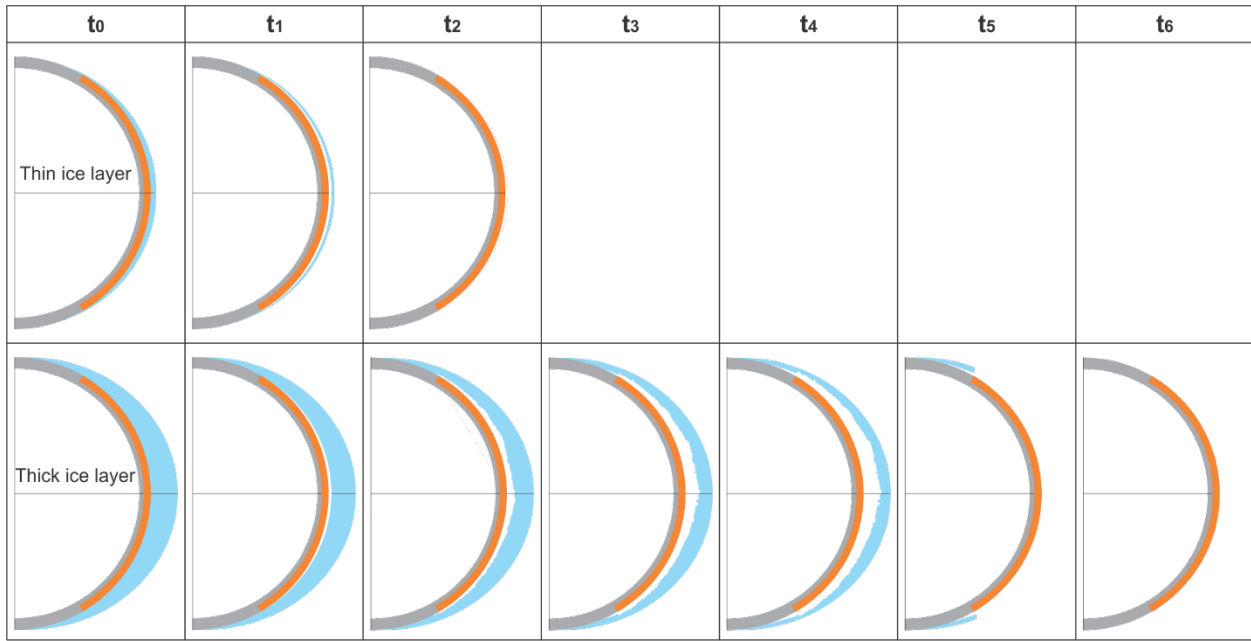


Figure 5.2 The effect of the ice thickness at heater’s edge on de-icing process

Studies have reported that as the thickness and distribution area of the ice layer grows on the LE surface, its adhesion strength to the LE surface increases [5, 10, 11], increasing the amount of heat energy required to weaken and remove it. As the ice thickness, h_{sl} , at SP increases, the ice thickness, h_e , at the heater edge increases, leading to a rise in the heat energy required for de-icing. Therefore, the geometric correlation between the elliptical shape of the accreted ice on a cylinder surface may help calculate the unknown value of the ice thickness at the edge of the heater, h_e , when the value of ice thickness at the SP is known. It may be concluded that by monitoring the ice thickness at the heater's edge and continuing to prevent it from significantly extending past the

heater's edge, a minimal requirement for de-icing heat energy can be attained by maximizing the effect of ice fracturing and shedding.

Figure (5.3) illustrates the heater placement in front of the LE of the cylindrical surface, where ice mass commonly forms. The heater's edge makes an angle $\angle\theta$ with the cylinder's center. The accretion of ice on the front of the leading edge of the cylinder surface is expected to have a form that closely mirrors the curved shape of the cylinder. As time passes, the ice profile gradually transforms into an elliptical shape [10-13]. The line AB in Figure (5.3) represents the ice thickness at the heater's edge (h_e). The line AC indicates a line drawn from the ellipse's center (C) to a point on its edge (A), while the line CB represents the cylinder's radius (r), and the angle ($\angle\theta$) is the anticlockwise rotation angle formed between the heater's edge and the cylinder's center. The geometrical correlation between a circle and an ellipse, as seen in Figure (5.3), is utilized to determine the length of CA, using the cylinder's radius and the angle $\angle\theta$, as described in Eq. (5.2). As a result, the relationship between ice thickness at the SP and ice thickness at the heater's edge can be determined by substituting CD with $(r + h_{sl})$ and CA with $(r + h_e)$, yielding Eq. (5.3).

$$CA = \sqrt{\frac{r^2(CD)^2(1 + \tan(\theta)^2)}{r^2 + (CD)^2\tan(\theta)^2}} \quad (5.2)$$

$$h_e = \sqrt{\frac{r^2(r + h_{sl})^2(1 + \tan(\theta)^2)}{r^2 + (r + h_{sl})^2\tan(\theta)^2}} - r \quad (5.3)$$

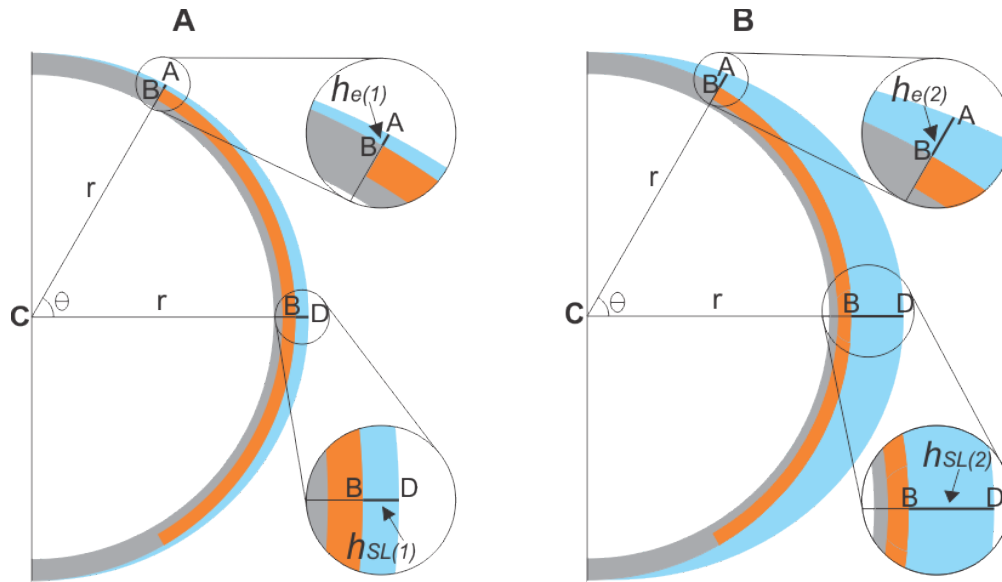


Figure 5.3 The relation of the ice thicknesses at SP and heater's edge

The formation of ice along the LE's surface is uneven, leading to a rough surface with ridges of different heights, as demonstrated in Figure (5.4-A). To address the variance in ice thickness caused by this uneven ice buildup, an arithmetic mean is employed to average the ice thickness values along the surface level [5]. In order to determine the average ice thickness along the SL, a technique involving the analysis of ice accretion images is employed. This method involves determining the average thickness of the ice within a specified region of interest (ROI), as shown in Figure (5.4-B). The ROI's dimensions are known, and its width corresponds to the ice's thickness along the SL. Using Eq. (5.4), the average thickness of the accreted ice along the SL, $\overline{h_{SL}}$, is calculated in millimeters, where $h_{SL}(i)$ is the quantity of pixels in the line (i), (n) is the number of lines within the region of interest, ROI, and SCF is the spatial calibration factor of the ROI.

$$\overline{h_{SL}} \text{ (mm)} = \frac{1}{n} \left(\sum_{i=1}^{i=n} h_{SL}(i) \right) \times SCF \quad (5.4)$$

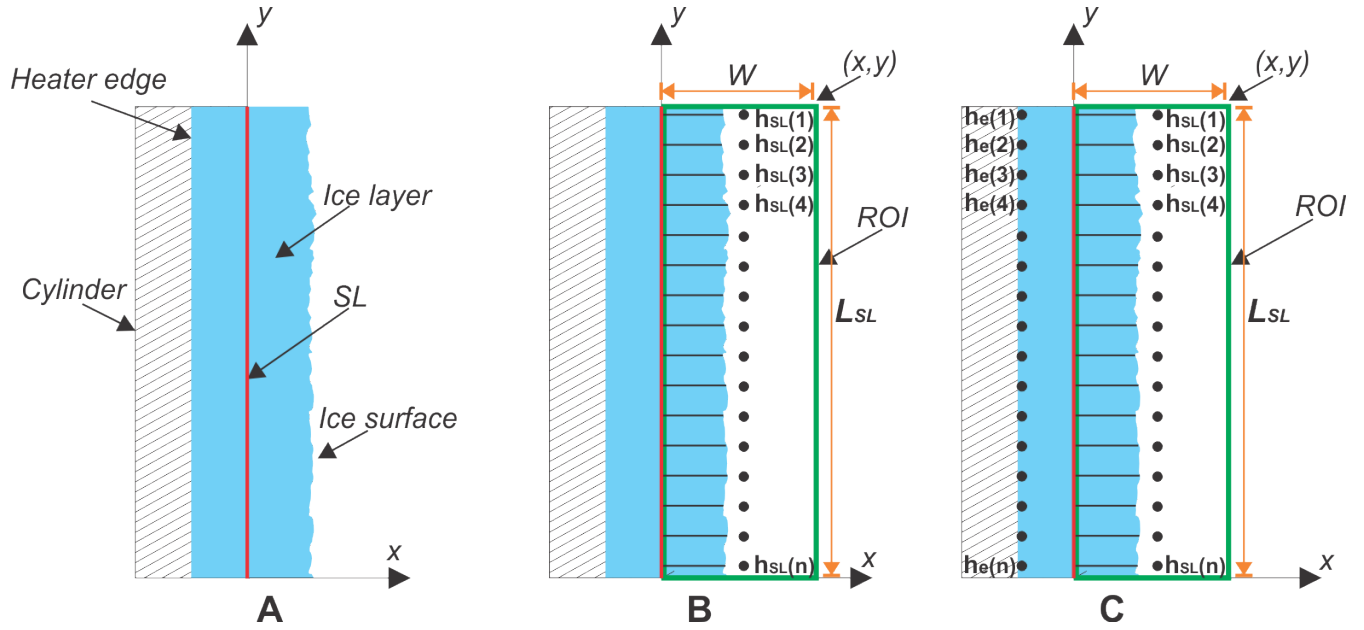


Figure 5.4: Measuring average ice thicknesses along SL and at heater's edge

As demonstrated by Eq. (5.3), the thickness of the ice at any position along the heater's edge is related to the thickness of the ice at the SP corresponding to that same position, as illustrated in Figure (5.4-C). This relationship allows for the prediction of ice thickness at various locations along the heater's edge based on the measured thickness at the SP. Using the average of the ice thicknesses along the SL in Eq. (5.4) yields the average of the ice thicknesses along the heater's edge, as in Eq. (5.5).

$$\bar{h}_e = \sqrt{\frac{r^2(r + \bar{h}_{SL})^2(1 + \tan(\theta)^2)}{r^2 + (r + \bar{h}_{SL})^2 \tan(\theta)^2}} - r \quad (5.5)$$

The accreted ice mass around and along the LE has a linear relation to the ice thickness at the SL, as shown in Eq. (5.6), where m_{ice} is the ice mass, L_{SL} is the length of the SL, ρ_{ice} is the density of the ice, and r is the radius of the cylinder. Furthermore, Eq. (5.5) shows that ice thickness at the SL, h_{SL} , has a relation with ice thickness at the heater's edge, h_e . Both Eq. (5.5) and Eq. (5.6) lead to conclude that the bigger h_{SL} value at the SL, and the thicker the value of ice thickness, h_e ,

at the heater's edge, the larger the amount of accreted ice mass will be. The correlation between h_{SL} and h_e in Eq. (5.5) can assist in managing h_{SL} to stay within the confines of h_e , therefore regulating the accumulating ice mass and modifying the heat energy necessary for de-icing.

$$m_{ice} = h_{SL} \left[\frac{\pi r L_{SL} \rho_{ice}}{2} \right] \quad (5.6)$$

5.3 Experimental Method

The experiment aims to demonstrate the effect of ice thickness at the heater's edge on the amount of thermal energy required to remove the ice accreted on a cylindrical surface. Furthermore, it demonstrates that the relationship between ice thickness at the stagnation line (SL) and the thickness of ice at the heater's edge can be used to control the amount of energy required for removal. De-icing experiments use ice samples of varying thicknesses accreted on a cylindrical surface.

The experiment's setup includes a fiberglass cylinder. The outer diameter (r) and height (L_{SL}) of the cylinder were both measured with corresponding uncertainties. The outer diameter was measured using a Mitutoyo 500-173 digital caliper, resulting in an average diameter of 254.46 mm, with an associated uncertainty of ± 0.05 mm. The cylinder height was measured using a metal ruler, yielding a result of 610 mm, with an associated uncertainty of ± 1 mm. Heat elements were also included, which were positioned on half of the cylinder's surface, upstream of the wind flow. The heating area on the cylinder surface was made up of 4x7 thermal elements arranged in a grid that covered the frontal portion of the cylinder where the LE surface's SZ was located, as shown in Figures (5.5) and (5.6). The position of the heating zone with respect to the cylinder's center was determined by measuring the angle between the cylinder's center and the heater's edge using a Digital Angle Ruler (AccuMASTER 7455), resulting in an angle, θ , of $65^\circ \pm 0.03^\circ$. The heat

elements were protected from damage through the use of thin fiberglass tape coverings. Upon activation, the heaters consistently generated a constant amount of heat. The average computing power produced by the heat elements, P_{heater} , was 1271.1 ± 4.95 W. (Please refer to Appendix-A for more details about power measurement and uncertainty analysis).

The hardware setup is presented in Figure (5.7) and comprised a National Instruments-made compact cDAQ-9171 chassis hosting a data acquisition module, the NI9375 [20, 21]. The digital output channels of the DAQ unit were linked to switching relays, as depicted in Figures (5.5 and 5.7), to control the activation and deactivation of the thermal elements. The hardware setup was connected to a computer and operates through custom software that was developed using MATLAB [22] and FLIR SDK [23, 24]. The software's user interface offered communication signals to the DAQ unit, which managed the latch circuit and heating elements. The heating components could be switched on or off using a corresponding operating signal, by setting the outputs of the DAQ unit (NI9375) to either 1 or 0.

A Canon-7D camera was used in the experiment to capture a visible image that was used to calculate the average ice thickness that accreted on the cylinder's SL. Also, the temperature variation during the de-icing process was captured using an IR camera (FLIR E60). As illustrated in Figure (5.5), the two cameras were housed in a styrofoam box and had their lenses adjusted to focus on the SL of the target surface. The thermal camera featured a 320×240 image resolution. Its emissivity was set to 0.95, which corresponded to the ice emissivity [24]. The experiment was carried out in a controlled environment with a temperature of -15°C . A fan was employed to generate an air stream within the cooler, and the wind speed inside the cooler was measured to be 4 m/s.

Pneumatic spray nozzles were mounted in front of the fan to produce water droplets as tiny as microns in the direction of the air stream toward the target surface. The nozzles produced a consistent spray distribution at a rate of 0.29 to 92 liters per minute. The volume of water injected into the airflow could be modified by adjusting the pressure regulators, which adjusted the liquid water content (LWC) of the airflow inside the cooler. The liquid water content (LWC) is 0.6 and the mean volume diameter of the spray is $50\ \mu\text{m}$. As the spray moved toward the target cold surface, it cooled to near the freezing point due to the low temperature of the cold airflow.

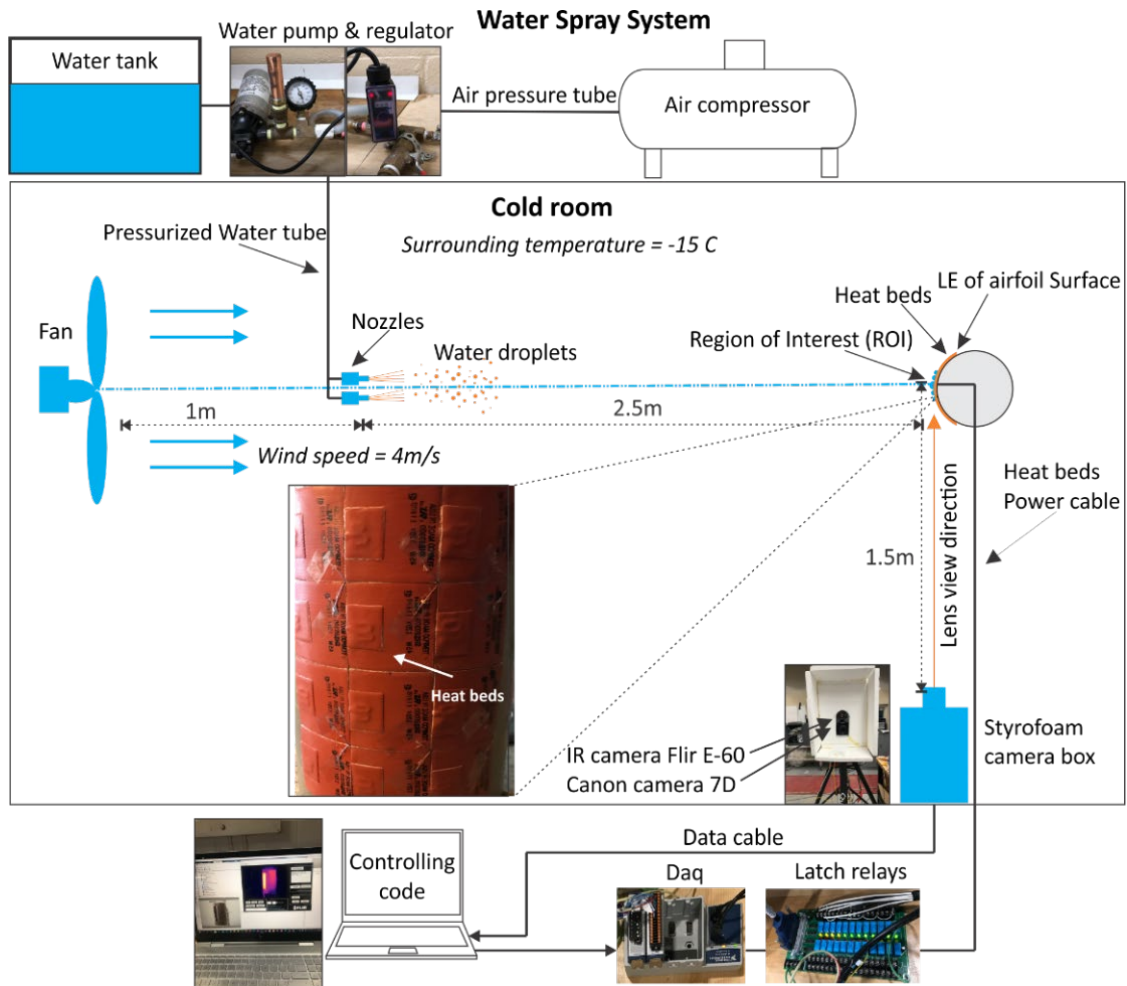


Figure 5.5: The experiment setup of managing heat energy needed for de-icing, top view.

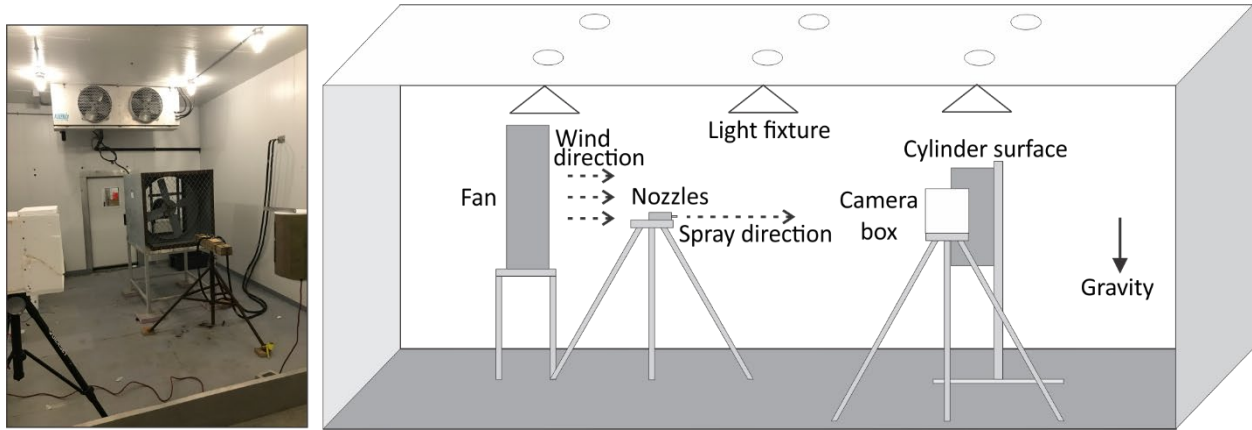


Figure 5.6: The experiment setup of managing heat energy needed for de-icing, side view

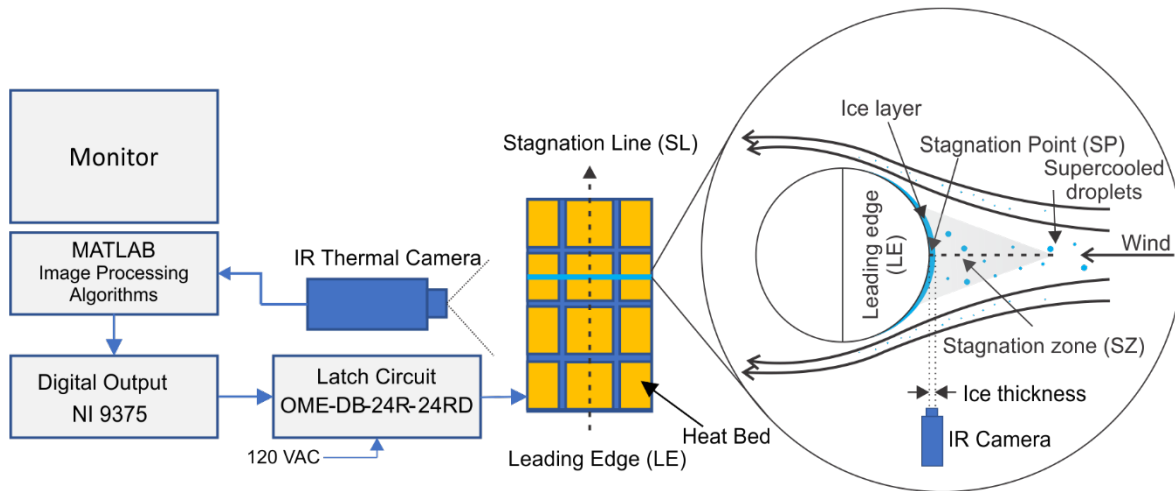


Figure 5.7: The hardware configuration required for ice buildup and de-icing.

The experiment was performed multiple times to obtain a range of de-icing results from various ice samples of different thicknesses. Each experiment was divided into three stages, (i) ice growth, (ii) ice sample measurements, and (iii) ice removal. The first involved accumulating ice on a cylindrical surface to obtain an ice sample of a certain thickness at the SL. The second step was to measure the thickness of the ice at the SL and the heater's edge. The third was the ice removal stage, which focused on de-icing time.

The initial step in each experiment was obtaining the accreted ice sample. The water spray system was turned on to start the ice accretion process. On the target surface, the deposited droplets froze, and their freezing behavior was observable. To generate progressively thicker ice samples, the duration of the ice accretion was increased. Table (5.1) presents the duration of the ice accretion processes of the obtained ice samples.

The second step of the experiment was the measuring stage. Once the ice accretion process was completed and an ice sample was acquired, an optical image of the obtained ice sample was captured using a CANON-7D camera, as shown in Figure (8). The MATLAB tool "imtool" was used to determine the average ice thickness. The region of interest (ROI) had known dimensions and was divided into 15 lines of equal spacing, as shown in Figure (5.8-A). Then, the thickness of the ice at each separate line was measured in pixels, as shown in Figure (5.8-A). Both the spatial calibration factor (*SCF*) and the formula in Eq. (5.4) were used to measure the average thickness, h_{SL} , in millimeters, along the SL of the accreted ice sample. (Please refer to Appendix-A for more details about the measurement and uncertainty analysis).

The average thickness of ice near the heater's edge was measured using a digital Vernier caliper, as shown in Figure (5.8-B). Figure (5.9) displays the collected accreted ice samples. Table (5.1) lists the measurement data for the average ice thickness at the SL, h_{SL} , and the measured average ice thickness at the heater's edge, h_e , for the collected ice samples. The detailed measurements of h_{SL} , Δh_{SL} , h_e and Δh_e are in Appendix-A, including measurement and uncertainty analysis.

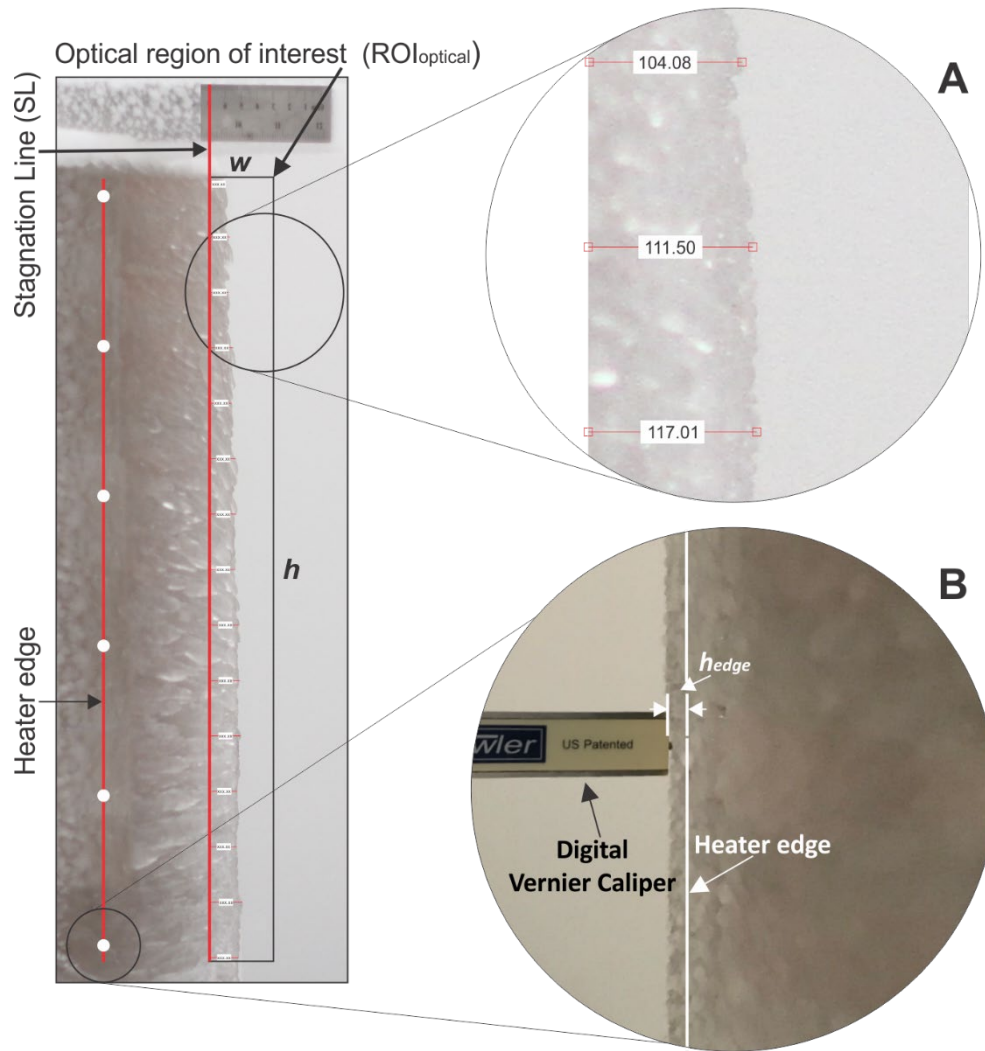


Figure 5.8: Measuring average ice thickness along SL using ROI (A) and at the heater edge (B)

The third step of the experiment was the de-icing stage for the obtained ice sample. The IR camera and heat elements were switched on simultaneously to begin the ice removal process. IR and optical cameras were used to record the thermal de-icing process. The experiment ended when the cylinder's target surface became free of ice. The duration of the de-icing process, t_{de-ice} , was extracted from the recorded thermal images using MATLAB and Flair SDK code.

5.4 Results and Discussion

This section presents the experimental results of ice accretion and de-icing. The section is divided into two sub-sections: ice accretion and de-icing.

5.4.1 Ice Accretion

This section presents the results of the ice samples obtained from experiments on ice accretion. Table (5.1) lists the measurement data and includes average ice thickness at the SL (h_{sl}), uncertainty of ice thickness at the SL (Δh_{sl}), average ice thickness at the heater's edge (h_e), uncertainty of ice thickness at the heater's edge (Δh_e), and the time of ice accretion (t_{ice}). (For additional details concerning the measured values of h_{SL} and Δh_{SL} h_e and Δh_e , please refer to Appendix-A).

The captured visual images for the ice samples are listed, as shown in Figure (5.9). The images are displayed in the order of the experiment's sequences, starting from left to right and then from top to bottom. The extracted readings consist of average ice thicknesses in millimeters at both the SL and the heater's edge. These readings provide quantitative information about the ice thickness at these locations, allowing for further analysis and comparison.

Table 5.1: Measured values of accreted ice samples

Ice samples	h_{SL} (mm)	$\pm\Delta h_{SL}$ (mm)	h_e (mm)	$\pm\Delta h_e$ (mm)	t_{ice} (s)
S1	3.48	± 0.03	0.32	± 0.06	279
S2	5.49	± 0.03	0.74	± 0.06	582
S3	7.97	± 0.03	1.52	± 0.06	877
S4	10.03	± 0.03	1.71	± 0.06	1170
S5	13.06	± 0.04	2.21	± 0.06	1522
S6	15.08	± 0.04	2.61	± 0.06	2071
S7	17.98	± 0.05	3.23	± 0.06	3274
S8	20.03	± 0.05	3.64	± 0.06	4816

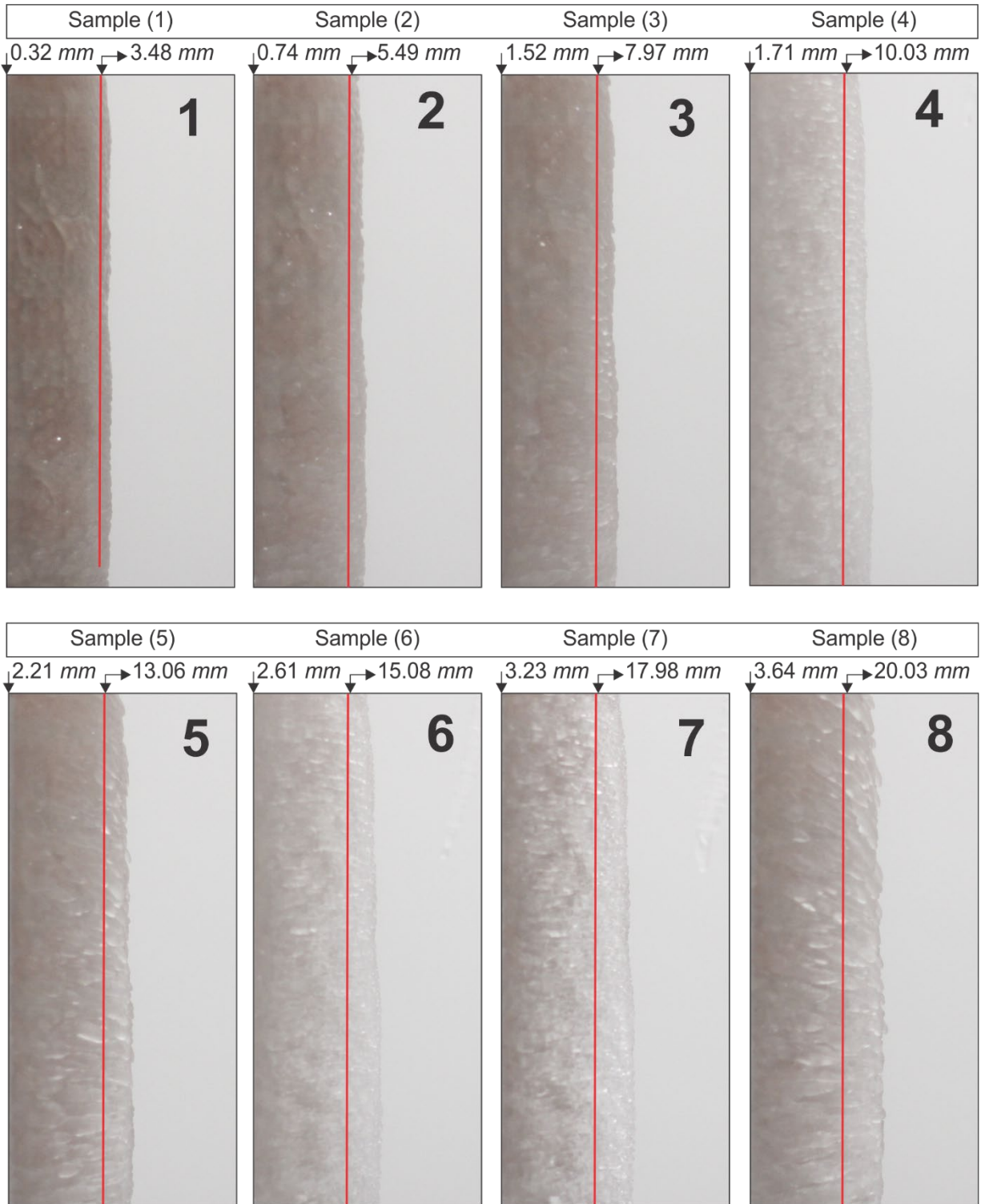


Figure 5.9: Ice samples on leading edge of cylinder

Table (5.2) presents the measured and calculated ice thickness values near the heater's edge, h_e , and their uncertainties. The measured values indicate the outcomes of the experiment, whereas the calculated values are obtained using Eq. (5.5). For further information on the measured and computed values of (h_e , and Δh_e), (please refer to Appendix-A for more details about measurement and uncertainty analysis).

To evaluate the values of measured h_e and computed h_e , the percent error (err%) for each sample is obtained using Eq. (5.7). err% describes how much the computed value of h_e , differs from the measured value of h_e , as a percentage of the measured value. The combined uncertainty (ΔU) for each sample is calculated using Eq. (5.8), which considers the uncertainties of both the measured and computed values.

Table (5.2) shows the results of the percent error for each sample, and they range from 4.09% to 46.67%. Samples S1 and S2 have the highest percent errors, indicating that the computed values for these samples differ significantly from the measured values. During the initial stages of icing, ice accumulation usually starts in the stagnation zone and then spreads beyond it. As a result of this behavior, the actual values of S1 and S2 may have a higher percentage error than their corresponding calculated samples. The reason for this is that the calculated samples rely on a geometrical relationship for their calculation, while the actual values are obtained from direct measurement. Samples S4, S5, S6, and S7 have relatively low percent errors, indicating good agreement between the measured and computed values. For ice sample S8, the percentage of error increases a little. The results indicate that the average percentage error of 16.4% falls within the acceptable range and can be considered satisfactory. The combined uncertainty for each sample is the same (± 0.078), indicating that the computation process is reliable and produces consistent results.

$$err\% = |(mrd(h_e) - est(h_e))/mrd(h_e)| \times 100\% \quad (5.7)$$

$$\Delta U = \sqrt{(mrd(\Delta h_e)^2 + est(\Delta h_e)^2)} \quad (5.8)$$

Table 5.2: A comparison between measured and computed values of h_e and their %error

Sample	Measured $h_e (mm)$	Measured $\Delta h_e(mm)$	Computed $h_e (mm)$	Computed $\Delta h_e(mm)$	Err %	ΔU mm
S1	0.32	± 0.06	0.60	± 0.05	46.67%	± 0.078
S2	0.74	± 0.06	0.93	± 0.05	20.43%	± 0.078
S3	1.52	± 0.06	1.33	± 0.05	12.50%	± 0.078
S4	1.71	± 0.06	1.64	± 0.05	4.09%	± 0.078
S5	2.21	± 0.06	2.08	± 0.05	5.88%	± 0.078
S6	2.61	± 0.06	2.36	± 0.05	9.58%	± 0.078
S7	3.23	± 0.06	2.75	± 0.05	14.86%	± 0.078
S8	3.64	± 0.06	3.01	± 0.05	17.31%	± 0.078

The graph in Figure (5.10) is created using the findings of the ice accretion experiments. It shows the ice thickness at SL, h_{SL} , the measured ice thickness at the heater edge, h_e , and the calculated ice thickness at the heater's edge, h_e .

The graphs in Figure (5.10) show that as the samples' ice thicknesses along the SL grow, so do their measured and calculated ice thicknesses at the heater's edge. The average ice thicknesses along the SL for ice samples S1 and S2 are 3.48 mm and 5.49 mm, respectively, and the calculated ice thicknesses at the heater's edge are 0.60 mm and 0.93 mm, but the measured thicknesses are smaller, 0.32 mm and 0.74 mm. Multiple studies have reported that the ice accretion process initiates around the SZ and expands beyond this region as it thickens at the SL [8, 9, 18]. This phenomenon may explain why the measured ice thickness at the heater edge for ice samples S1 and S2 was thinner than the calculated values. This is because the duration of their ice accretion process was short, leading to a thin ice layer along the SL with a correspondingly thin ice layer beyond the SZ.

This minor discrepancy in ice thicknesses at the heater's edge is because the latter thickness is dependent on the geometric correlation of Eq. (5.5), whereas the first is based on actual measurement. Moreover, the graph shows that when the average ice thickness along the SL for ice samples S1 and S2 is thin ($h_{SL} < 5.5$ mm), both the measured and computed ice thicknesses at the heater's edge are less than 1 mm. A very thin layer indicates that the actual area of the accreted ice layer does not exceed the SZ, and that the ice thickness at the heater's boundary is quite thin. Typically, when the ice layer is thin, it is within the heating zone. The small discrepancy between the measured (actual) and calculated ice thickness near the heater's edge can be ignored because the actual value is less than the calculated value. This indicates that the computed values reasonably approximate the actual ice thickness in these cases.

When more droplets hit the SZ surface, the ice mass collection distribution forms a peak at the SP, resulting in some of the water droplets deviating and freezing around the stagnation zone, causing the ice layer surrounding the heater's edge to thicken somewhat [7, 15]. Figure (5.10) shows that the measured and calculated ice thicknesses at the heater's edge in ice samples S3, S4, and S5 are almost comparable. Therefore, as ice accretes on a cylindrical surface, its geometrical shape along the SL becomes elliptical [13-16], which explains why the measured and calculated values of ice thicknesses at the heater's edge compare well.

Over time and as the ice accretion continues, the peak near the SZ grows, causing the airflow around a circular airfoil surface to deflect more supercooled water droplets upward and downward along the circular surface, increasing the ice area above the LE, and thickening the ice beyond the SZ [7, 15]. Figure (5.10) shows that the slope between ice samples S6, S7, and S8 is less steep than the slopes between the previous ice samples. This suggests that, despite the longer ice accretion periods in ice samples S7 and S8, there is slow ice growth near the SL and an increase

in ice thickness around the stagnation zone. This may explain why the measured ice thickness at the heater edge for ice samples S7 and S8 is slightly greater than the calculated value, and why their percentage errors are 14.86% and 17.31%, respectively. This is because the calculated value is dependent on its relationship with the ice thickness at the SL in Eq. (5.5), which does not vary significantly in these cases.

In summary, the results show that ice accretion on a cylindrical surface form an elliptical shape, with the most significant ice thickness at the SP, corresponding to the largest diameter of the produced ellipse. The results also confirm that as the thickness of the ice at the SL increases, the elliptical shape expands, increasing the ice thickness at the heater's edge, as predicted by Eq. (5.5). The overall average percentage error of the ice thickness values at the heater's edge was calculated to be 16.4%, which is within an acceptable range. These findings contribute significantly to the understanding of the process of ice accretion on cylindrical surfaces and may have potential applications in various fields.

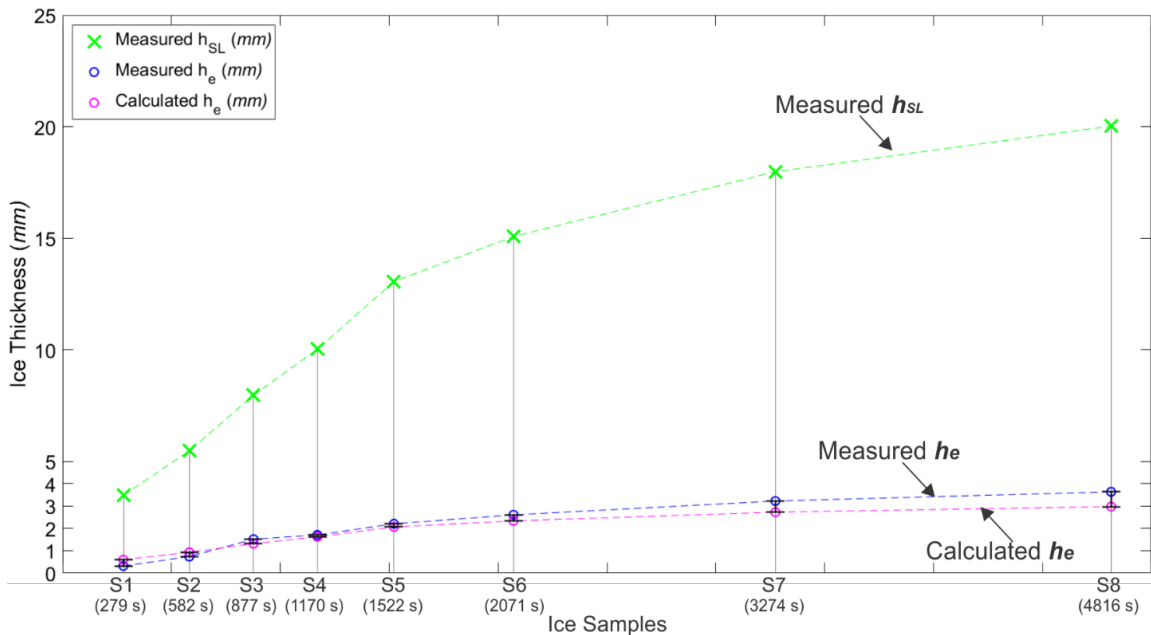


Figure 5.10: Ice thicknesses at SL and heater's edge over time

5.4.2 De-icing

Table (5.3) presents the data of the ice samples and the results of the de-icing experiments, including the measured average ice thickness at the SL (h_{SL}), the calculated average ice thickness at the heater's edge (h_e), and the time required to de-ice each ice sample (t_{de-ice}). The data also include the mass of the accumulated ice sample (m_{ice}) as calculated by Eq. (5.6), the uncertainty in mass (Δm_{ice}), the heat energy (Q) required to remove the ice sample, and the uncertainty in heat energy (ΔQ), the ratio of heat energy to ice mass (R) which is a relative measure of the thermal energy required for de-icing, and the uncertainty in the ratio (ΔR). (For further information on the measured and computed values of Q , ΔQ , m_{ice} , and Δm_{ice} , please refer to Appendix-A which includes measurement and uncertainty analysis).

The ratio (R) of heat energy (Q) to ice mass (m_{ice}) is represented by Eq. (5.9), which is a relative measure of the thermal energy required for de-icing. The propagation of error formula shown in Eq. (5.10) is used to compute the uncertainty of the ratio. where ΔQ is the uncertainty in the heat energy, and Δm_{ice} is the uncertainty in the ice mass.

Table (5.3) shows the effect of increasing ice thickness at the heater's edge, h_e , on the de-icing time, t_{de-ice} , de-icing thermal energy, Q , and the thermal energy to ice mass ratio, R . The heat generated by the heat elements in the cases of ice samples S1 and S2 takes 38 s and 61 s, which are relatively short time periods to melt the ice layer interfaced with the LE's surface, because the ice layer at the heater's edge is very thin ($h_e < 1$ mm). As the ice layer thickens at the heater's edge in cases S3, S4, and S5, which are 1.32 mm, 1.63 mm, and 2.07 mm respectively, their de-icing periods are 93 s, 121 s, and 166 s respectively. The de-icing periods for ice samples S6, S7, and S8 are the longest, at 200 s, 255 s, and 303 s, because they have thicker ice layers at the heater's edge, 2.36 mm, 2.75 mm, and 3.01 mm respectively. The results showed that as the ice layer of

the ice sample becomes thicker beyond the SZ, it takes longer to diffuse into the layer near the heater's edge.

The results in Table (5.3) show that the ratio of heat energy to ice mass (R) required for de-icing increases as the ice mass increases. This finding is consistent with the intuitive perception that larger masses of ice require more energy to melt or break up than smaller masses of ice. The increasing trend in the ratio is consistent across all the samples, and the ratio ranges from 124.336 J/g for Sample S1 to 171.962 J/g for Sample S8. It can be concluded that the ratio (R) can serve as a useful relative measure of the thermal energy required for de-icing, particularly in applications when the amount of ice to be melted or removed varies.

$$R = \frac{Q}{m_{ice}} \quad (5.9)$$

$$\Delta R = \sqrt{\left[\left(\frac{\Delta Q}{m_{ice}}\right)^2 + \left(\frac{Q \times \Delta m_{ice}}{m_{ice}^2}\right)^2\right]} \quad (5.10)$$

Table 5.3: The ice sample data and the results of de-icing experiments

Sample	h_{SL} (mm)	h_e (mm)	t (s)	m_{ice} (kg)	$\pm\Delta m_{ice}$ (kg)	Q (kJ)	$\pm\Delta Q$ (kJ)	R (J/g)	$\pm\Delta R$ (J/g)
S1	3.48	0.60	38	0.389	± 0.004	48.378	± 0.193	124.336	± 1.248
S2	5.49	0.93	61	0.613	± 0.004	77.531	± 0.305	126.538	± 0.949
S3	7.97	1.33	93	0.891	± 0.004	118.203	± 0.462	132.647	± 0.841
S4	10.03	1.64	121	1.121	± 0.005	153.891	± 0.600	137.227	± 0.814
S5	13.06	2.08	166	1.460	± 0.007	210.486	± 0.823	144.148	± 0.860
S6	15.08	2.36	200	1.686	± 0.007	254.200	± 0.991	150.765	± 0.869
S7	17.98	2.75	255	2.010	± 0.009	324.405	± 1.263	161.371	± 0.938
S8	20.03	3.01	303	2.240	± 0.009	385.113	± 1.500	171.962	± 0.978

Figure (5.11) illustrates the relationship between the ice thickness at the edge of the heater and the ratio of de-icing heat energy to ice mass (R). The graph demonstrates that as the ice

thickness of the h_e increases, a greater amount of heat energy is required to melt a given mass of ice. This is reflected in the higher values of the ratio of (R) as the ice thickness increases. The graph also shows that when the ice thickness, h_e , is very thin, the de-icing process is rapid and a lower ratio of (R) is required. These findings suggest that the thickness of the ice at the edge of the heater plays a significant role in determining the amount of heat energy required for de-icing and the duration of the de-icing process.

Figure (5.11) demonstrates that the lowest ratio values of (R) were observed for ice samples S1 and S2, with values of 124.336 J/g and 126.538 J/g, respectively. These samples had less ice mass and thin ice thickness values at the edge of the heater, less than 1 mm. The highest ratio values of (R) were found for ice samples S6, S7, and S8, with values of 150.765 J/g, 161.371 J/g, and 171.962 J/g, respectively. These samples had the largest ice mass; the thick ice thickness values at the edge of the heater were greater than 2.5 mm. The results of the study suggest that even a small increase in ice thickness at the edge of the heater leads to an increase in the mass of ice formed on the surface. This, in turn, results in a significant increase in the de-icing heat energy required and a corresponding increase in the ratio of heat energy to ice mass.

The line plotted between ice samples S1 and S2 exhibits a steeper slope compared to the lines plotted between the other ice samples. This can be attributed to the fact that the ice layer in these samples is relatively thin, with almost negligible ice beyond the heating zone. This means that the accreted ice on the surface of the heater is primarily within the SZ and requires a minimal ratio of (R) and, therefore, a relatively small amount of heat energy to melt the interfacial ice layer above the SZ and cause the ice to shed via gravity. In contrast, the slope of the lines plotted between ice samples S3 to S8 shows a steady increase. This suggests that as the mass of ice accreted around the SZ increases, leading to a gradual increase in the ice thickness outside the SZ, there is a

corresponding increase in the de-icing heat energy required for ice removal. This results in an increase in the ratio value of Q/m .

The results of this study indicate that both the correlation between h_e and R in Figure (5.11) and the relationship between h_{SL} and h_e described in Eq. (5.5) are valid and can be used to predict the amount of thermal energy required to remove accreted ice. These findings highlight the importance of minimizing the ice thickness at the edge of the heater in order to optimize the de-icing process and reduce the amount of heat energy needed.

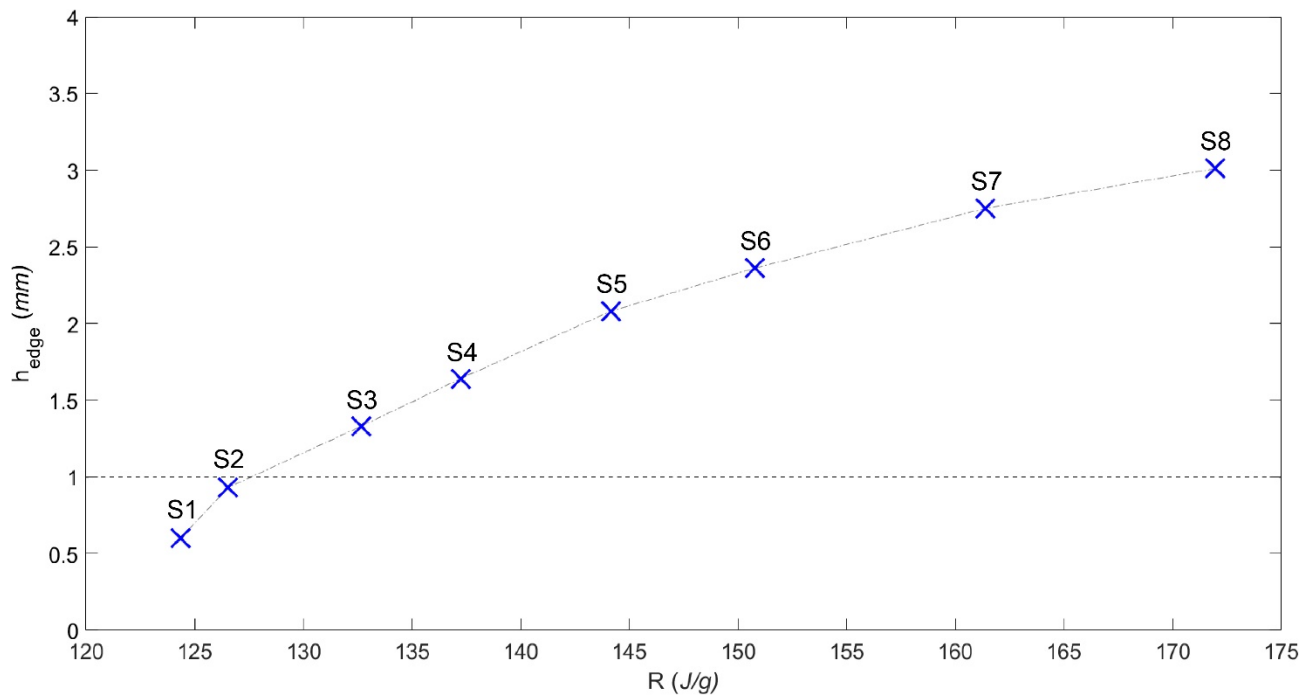


Figure 5.11: The effect of ice thickness at heater’s edge on the ratio of (R)

The study's findings show that when the ice layer is thin, its bottom interfaced area is within the heating area. The generated heat rapidly melts the ice-interfaced layer, and gravity sheds the ice [1, 19]. As the ice layer becomes thicker, the de-icing process takes longer and behaves differently. The images shown in Figure (5.12) describe the de-icing behavior for a thick ice layer. The de-icing process in Figure (5.12) was monitored using both an IR thermal camera (Flir E-60)

and an optical camera (Canon 7D). The images were taken at different times during the de-icing event.

Figure (5.12-A) shows that the accreted ice layer has a rough surface with ridges of varying heights along the LE's surface of the cylinder. The ice distribution over the surface is uneven, which means ice thickness beyond the SZ is also uneven, as seen in the optical image in Figure (5.12-A).

When the thermal elements beneath the ice layer are triggered, they generate relatively constant heat [19]. Most of the heat energy the heaters produce diffuses directly into the ice above the heated region [19]. Even though the heat causes the bottom of the ice layer that interfaces with the heating zone to melt, the ice block remains attached to the cylinder's cold surface, due to the strong adhesion strength of the ice surrounding the heated zone, as seen in the thermal image in Figure (5.12-A). Since the heat diffuses faster in thinner regions than in thicker regions [19], the thin ice near the heater's edge begins to fracture, loosen, and fall, leaving a warm region, as seen in Figure (5.12-B).

The remaining ice block is still adhering to the cold surface of the cylinder, as seen in Figure (5.12-B). The ice continues to fracture over time, and the warm region expands as more heat diffuses into the thicker ice regions near the heater's edge, as seen in Figure (5.12-C). The ice surrounding the heated zone has a high adhesion strength, allowing the entire ice block to adhere to the surface [11], as seen in Figures (5.12-B and C). Over time, the heat penetrates the ice beyond the edge of the heater, causing the remaining attached ice to disintegrate and collapse, as seen in Figure (5.12-D).

It is clear that as the ice beyond the SZ becomes thicker, the de-icing period increases, causing an increase in the heat energy of de-icing. Ice usually forms unevenly on the surface of

the LE, resulting in a rough surface. The surface roughness of the accreted ice varies, resulting in ice regions of varying thicknesses around the heater's edge. As a result, the ice block does not collapse completely at once, but progressively disintegrates and collapses over time. This is because heat typically diffuses faster in the thin regions near and along the heater's edge, where ice begins to break and disintegrate, and then expands in the thicker regions along the heater's edge, as shown in Figure (5.11).

The average ice thickness near the heater's edge, as calculated by Eq. (5.5), effectively eliminates the discrepancy caused by uneven ice accretion and offers acceptable findings that are near the actual results, as demonstrated in the experiment. The calculated average percentage error value of 16.4% for the examined ice samples is considered acceptable. It illustrates the usefulness of the obtained results demonstrated in Figure (5.11) for predicting the de-icing heat energy when the average ice thickness at the heater's edge is known, as is discussed in the next section.

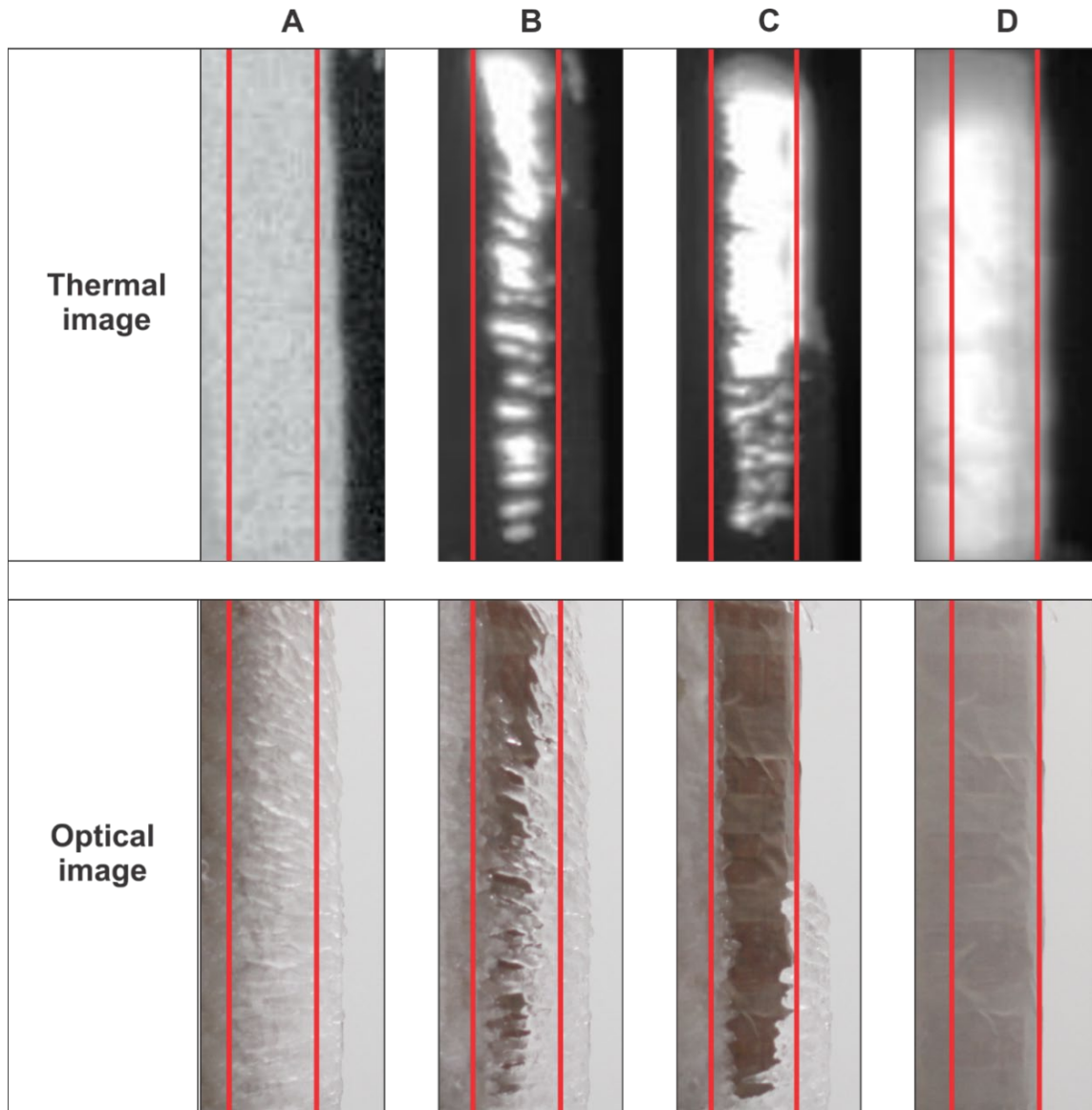


Figure 5.12: Thermal and optical images describe the de-icing process using thermal elements

The findings for all ice samples, which are illustrated in Figures (5.10) and (5.11), are combined in Figure (5.13). The combined graph illustrates a correlation between average ice thickness at the SL and average ice thickness at the heater's edge. It also presents the results of the relationship between the average thickness of ice at the heater's edge and the ratio of de-icing thermal energy to ice mass (R).

The curve of the measured ice thickness at the stagnation line, h_{SL} , as shown in Figure (5.13), demonstrates that as the average ice thickness at the SL increases, the mass of ice formed on the surface also increases. This results in a larger amount of thermal energy being required to remove the accreted ice, leading to an increase in the ratio of (R). Similarly, the curve of the calculated average ice thickness near the heater's edge, h_e , demonstrates that even a slight increase in ice thickness at the heater's edge causes an increase in the amount of heat energy needed to clear the ice buildup as well as the ratio (R).

The relationship between the average ice thickness at the SL, h_{SL} , and the average ice thickness at the heater's edge, h_e , is reciprocal, such that when the average ice thickness at the SL is thin, the average ice thickness at the edge of the heater is also thin. This leads to a lower requirement for heat energy, Q , to de-ice the surface, and a smaller ratio of (R). Conversely, when the average ice thickness at the SL is thick, h_{SL} , the average ice thickness at the edge of the heater, h_e , is also thick, requiring a larger amount of heat energy to de-ice and a larger ratio of (R). This indicates that the value of the ice thickness near the edge of the heater, h_e , directly influences the amount of heat energy, Q , required for the de-icing process.

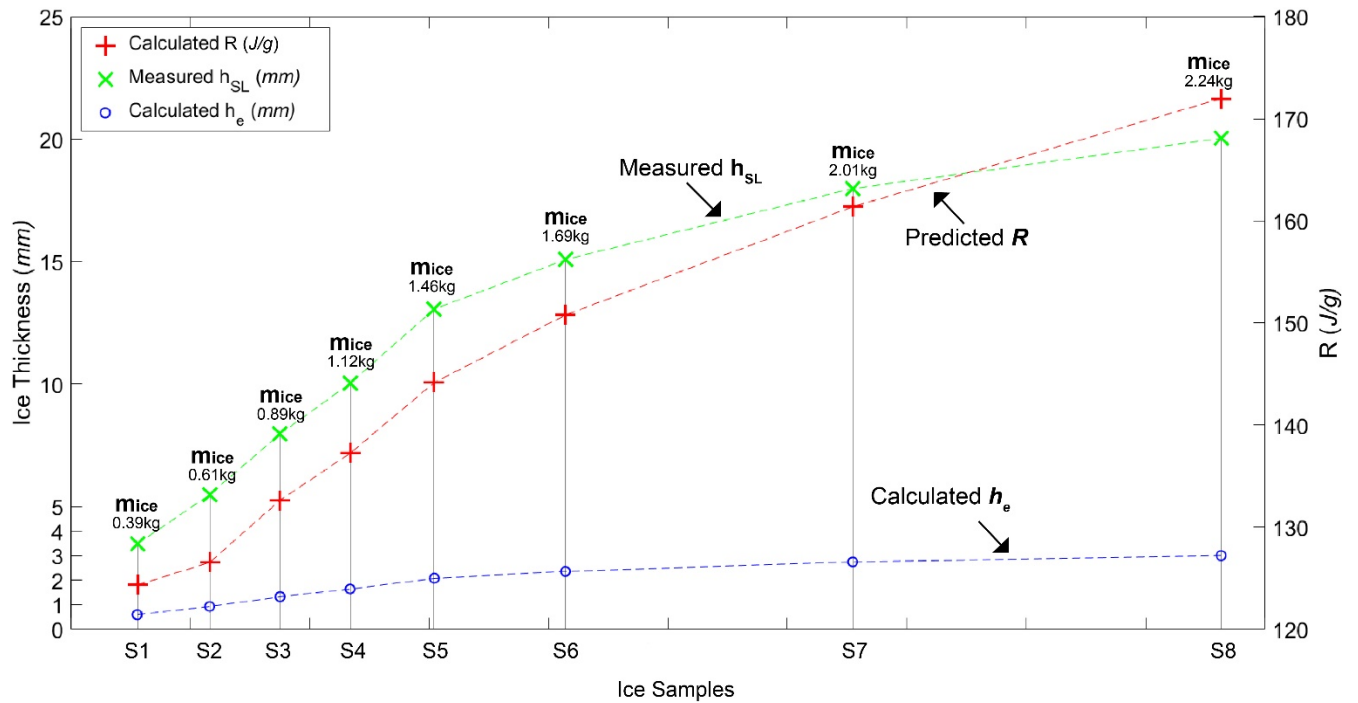


Figure 5.13: Ice thicknesses at both SL and heater's edge and the ratio of Q/m_{ice}

When the value of the ice layer thickness at the heater's edge is computed using Eq. (5.5), the amount of heat energy required to remove the accreted ice may be roughly predicted using Figure (5.11). Therefore, the results of the study are significant and may be utilized as the basis for generating a graphical tool for predicting the heat energy required to remove ice mass formed on a cylindrical surface when the ice thickness at the heater's edge is determined.

Figure (5.14) demonstrates how to use the graph to predict heat energy. For example, if the ice thickness at the SL is 12.5 mm, the calculated ice thickness at the heater's edge is 2.0 mm. According to Figure (5.14), this value of ice thickness at the heater's edge requires an amount of heat energy of 200 KJ to remove the ice mass accreted above the LE's surface.

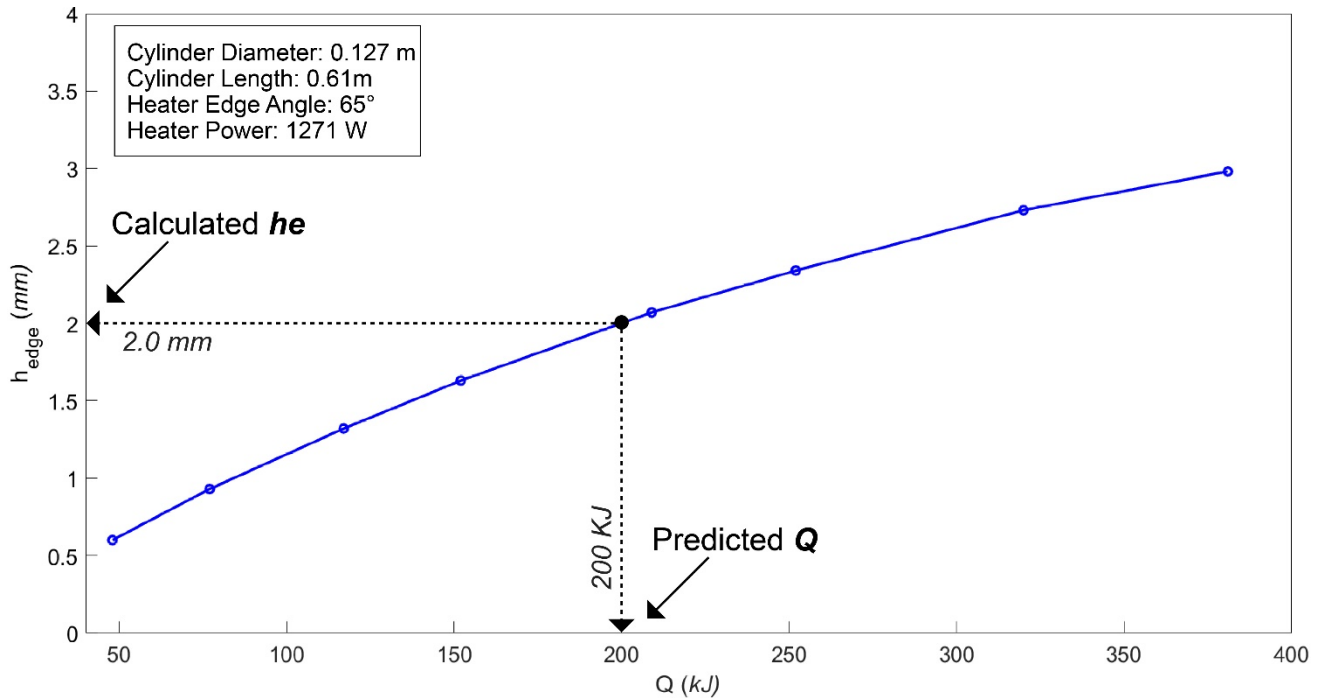


Figure 5.14: An example to predict the heat energy using the computed ice thickness at heater edge

Using the proposed integrated system indicated in Chapter-4, the average ice thickness along the stagnation line (SL) can be accurately determined [5]. This enables the system to incorporate Eq. (5.5) to compute and monitor ice thickness near the heater's edge. Consequently, heat energy can be predicted using a predefined graph like the one presented in Figure (5.14). In order to utilize the thermal energy graph effectively, it must be established in advance based on the parameters of the current study, including the diameter and height of the cylinder employed, as well as the heating angle created by the heater's edge with the center of the cylinder's center, as shown in Figure (5.14).

Figure (5.15) describes the effect of increasing the heating angle on the heating area above the LE surface and hence on the ice thickness near the heater's edge. In Case A, the heating angle is $\angle 85^\circ$, while in Case B, it is $\angle 65^\circ$. The results presented in Table (5.4) are generated based on the

heating angles for both Case A and Case B, for both thin and thick ice layers. The ice thickness at the SL of the thin layer is 5.5 mm, while the thick ice layer is 10 mm. The heating area in Case A is large and needs a heater power of 1780 W, whereas the heating area in Case B is small and requires a heater power of 1271 W. When the heating angle increases, the heater's wattage increases to cover the expansion in the heated area above the LE surface.

Table (5.4) demonstrates that while the ice layer is thin (5.5 mm) in both cases of heating angles, the de-icing period is short, implying that the heat energy utilized in Case A is more than in Case B, due to the difference in heating area. When the thickness of the ice layer along the SL is 10 mm, the ice layer near the edge of the heater is thin in Case A, but thick in Case B. This implies that the de-icing period is shorter in Case A than in Case B, indicating that the heat energy required in Case B is much more than in Case A, due to the difference in ice thickness near the heater's edge.

A study reported that airfoil's surfaces are highly susceptible to icing, noting that any small change in the blade surface roughness will negatively affect the turbine's aerodynamic characteristics, even with little icing [1, 5, 6]. In fact, Case A is favored in all circumstances listed in Table (5.4). However, if the ice layer must not extend beyond the SZ and the heater power must be kept low, Case B is preferred. The current study employs a small heating angle of $\angle 65^\circ$ within the SZ region in order to demonstrate the relationship between ice thickness at the SL and at the edge of the heater, as well as the effect of ice thickness at the edge of the heater on the amount of heat energy required for de-icing. This approach allows for a simplified investigation of these correlations.

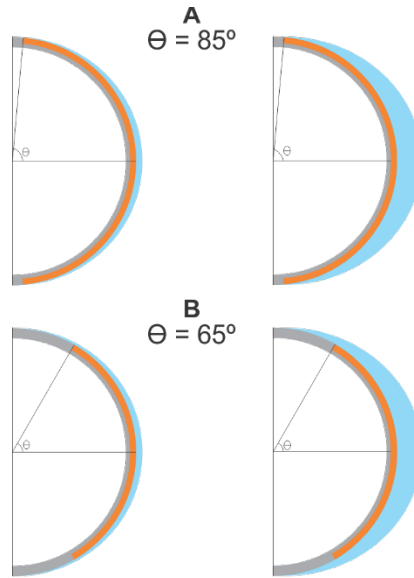


Figure 5.15: The effect of the heating angle on the heating area above the LE surface

Table 5.4: The effect of the heating angle on the ice thickness near the heater's edge

Case	Theta (θ°)	Heat area	Heater power (W)	h_{SL} (mm)	h_e (mm)	De-ice period
Case-A	85	Large	1780	10	0.10	Short
	85	Large	1780	5.5	0.04	Short
Case-B	65	Small	1271	10	1.63	Long
	65	Small	1271	5.5	0.93	Short

Table (5.5) provides information about ice samples accumulated on a cylindrical surface, including the ice thickness at the heater edge (h_e), ice mass (m_{ice}), heat energy required for de-icing (Q), heat energy to melt the ice (Q_{melt}), and overall efficiency for each sample (eff%). Efficiency is defined as the ratio of heat energy required for de-icing to the heat energy required for melting the ice.

The thickness of ice at the heater edge (h_e) has a significant effect on the overall efficiency of de-icing. As the thickness of ice increases, the efficiency decreases, indicating that more heat energy is required for de-icing. This effect can be attributed to the increased thermal resistance of thicker ice layers, which makes it more difficult to transfer heat to the ice surface at the heater

edge. Furthermore, the low ambient temperature of the cooler also has an impact on de-icing efficiency. The colder the environment, the more heat energy is required to de-ice the ice surface. This effect can be explained by the fact that the thermal gradient between the heater and the ice surface is greater at lower ambient temperatures, resulting in more heat loss from the heater. The cold wind speed also increases the convective heat transfer coefficient and therefore increases the heat loss from the heater. This effect leads to a decrease in the overall efficiency of de-icing. The average overall efficiency for all samples can be calculated as the mean value of the efficiency for all samples, which is approximately 60%. This value indicates that approximately 60% of the heat energy required to melt the ice is needed to de-ice the ice surface. The efficiency value can be used to optimize the design of de-icing systems and to estimate the amount of heat energy required to de-ice ice surfaces of a particular thickness. For example, increasing the heating angle (θ) increases the heating area which is in turn increases the de-icing efficiency.

Table 5.5: The effect of the ice thickness at heater edge on the de-icing efficiency

Sample	h_e (mm)	m_{ice} (kg)	Q (kJ)	Q_{melt} (kJ)	eff%
S1	0.6	0.39	48.38	32.76	68%
S2	0.93	0.61	77.53	51.24	66%
S3	1.33	0.89	118.20	74.76	63%
S4	1.64	1.12	153.89	94.08	61%
S5	2.08	1.46	210.49	122.64	58%
S6	2.36	1.69	254.20	141.96	56%
S7	2.75	2.01	324.41	168.84	52%
S8	3.01	2.24	385.11	188.16	49%

5.5 Conclusions

This chapter investigated the role of the ice thickness at a heater's edge for minimizing the thermal energy necessary to remove the ice accreted above the stagnation zone of a cylindrical surface by using the relationship between the thickness of the ice at both the stagnation line and

the edge of the heater. As ice thickness at the heater's edge grows, de-icing duration increases, increasing the heat energy required for de-icing. The results of the conducted experiments showed that the lower the value of ice thickness at the heater's edge, the less heat energy is needed to de-ice and the shorter the period of de-icing. The results of the de-icing experiments indicate that by controlling the ice thickness at the heater's edge, it is possible to reduce the amount of heat energy required to remove the ice accreted above the LE's surface of a cylinder by utilizing the relationship between the ice thickness at the SL and at the heater's edge. The results demonstrate the potential for this relationship to improve the efficacy of the de-icing process on cylindrical and airfoil surfaces.

5.6 References

- [1] E. Madi, K. Pope, and W. Huang, T. Iqbal. A review of integrating ice detection and mitigation for wind turbine blades. *Renew. Sust. Energ. Rev*; 2019; 103:269-281.
- [2] Quiterio Gómez Muñoz C, Pedro García Márquez F, Sánchez Tomás J. Ice detection using thermal infrared radiometry on wind turbine blades. *Measurement* 2016;93:157–63.
- [3] Pappalardo G, Mineo S, Perriello ZS, Cubito A, Calcaterra D. Infrared thermography proposed for the estimation of the cooling rate index in the remote survey of rock masses. *Int Jnl Rock Mech Min Sci* 2016;83:182–96.
- [4] Mughal UN, Virk MS. Atmospheric icing sensors - an insight. *SENSORCOMM*; 2013. p. 191–9.
- [5] E. Madi, K. Pope, and W. Huang. An integrated ice tracking and mitigation system on the stagnation line of a cylindrical surface based on thermal imaging and electro-thermal elements. *Measurement*; 2022; 199: 111539, 2022.
- [6] Pierre Lavoie. Modeling of thin water films on swept wings in icing condition. 2017; Thesis. Université de Montréal.
- [7] Anderson, John D. *Fundamentals of aerodynamics*. 4th Edition. New York: McGrawHill, 2007.
- [8] A. Ebrahimi. Atmospheric icing effects of S816 airfoil on a 600 kW wind turbine's performance. *Scientia Iranica B*; 2018; 25(5), 2693-2705.
- [9] Fortin, G. and Perron, J. Wind turbine icing and deicing. *AIAA 2009-274*, Orlando, Florida: 47th AIAA. Aerospace Sciences Meeting; 2009.
- [10] Kibler, Elijah Mendoza. Determination of adhesive strength and freezing rate of ice on aircraft structures at subcooled temperatures. 2013. Thesis. 297.

- [11] Lasse Makkonen. Ice Adhesion-Theory, Measurements and Countermeasures. *Journal of Adhesion Science and Technology* 26(4-5):413-445. 2012. DOI: 10.1163/016942411X574583
- [12] Thomas, S. K., Cassoni, R. P., & MacArthur, C. D. Aircraft anti-icing and de-icing techniques and modeling. *Journal of Aircraft*; 1996; 33(5), 841-854
- [13] M. Bragg, A. Broeren, H. Addy, M. Potapczuk, D. Guffond, and E. ontreuil. Airfoil ice-accretion aerodynamic simulation. in 45th AIAA Aerospace Sciences Meeting and Exhibit, p. 85, 2007.
- [14] D. Switchenko, W. G. Habashi, G. Baruzzi, and I. Ozcer. Fensap-ice simulation of complex wind turbine icing events, and comparison to observed performance data. in 32nd ASME Wind Energy Symposium; p. 1399, 2014.
- [15] Pedersen, M. C. Modelling Icing on Structures for Wind Power Applications. Ph.D. thesis. Aalborg University, Denmark; 2018.
- [16] Hudecz, A., Hansen, M. O. L., Battisti, L., & Villumsen, A. Icing problems of wind turbine blades in cold climates. Department of wind energy, Technical University of Denmark; 2014.
- [17] Birajdar, Mahasidha & Kale, Sandip. (2015). Effect of Leading Edge Radius and Blending Distance from Leading Edge on the Aerodynamic Performance of Small Wind Turbine Blade Airfoils. 4. 5-1. 10.11648/j.ijjepe.s.2015040501.19.
- [18] G.M. Ibrahim, K. Pope, Y.S. Muzychka. Effects of blade design on ice accretion for horizontal axis wind turbines. *Journal of wind engineering & industrial aerodynamics*. 2018; 173: 39–52
- [19] Peter Suke, B.Eng. Analysis of heating systems to mitigate ice accretion on wind turbine blades. Master thesis. McMaster University. 2014.
- [20] National Instruments (2016). cdaq-9171 user manual. Retrieved from www.ni.com [Accessed 2 May 2021].
- [21] National Instruments (2016). ni-9375 datasheet. Retrieved from www.ni.com [Accessed 2 May 2021].
- [22] MATLAB 2018a. The MathWorks, Inc., Natick, Massachusetts, United States.
- [23] FLIR. Atlas SDK for MATLAB. Retrieved from <https://www.flir.ca/support/products/flir-atlas-sdk-for-matlab>. [Accessed 15 June 2020].
- [24] FLIR (2013). IR camera E-60 user manual. Retrieved from www.flir.com. [Accessed 15 June 2022].
- [25] E. Madi, K. Pope, and W. Huang. Estimating the volume of frozen water droplets on a cold surface during the phase change with thermal image processing. *Measurement*; 2021;183:109907.
- [26] Virk, M.S., Homola, M.C., Nicklasson, P.J. Atmospheric icing on large wind turbine blades. *Int. J. Energy Environ*. 2012; 3 (1), 1–8.

- [27] Jia Yi Jin, Muhammad Shakeel Virk. Study of ice accretion along symmetric and asymmetric airfoils. *Journal of Wind engineering & industrial aerodynamics*. 2018; 179: 240–249.
- [28] Fu, P., Farzaneh, M. A CFD approach for modeling the rime ice accretion process on a horizontal axis wind turbine. *J. Wind Eng. Industrial Aerodynamics*; 2010; 98 (4), 181–188.
- [29] Jared Soltis, Jose Palacios, Douglas Wolfe. Design and testing of an erosion resistant ultrasonic de-icing system for rotorcraft blades. Pennsylvania State University. technical report No. TR 14-007. 2013
- [30] Staffan Rydholm, Benny Thörnberg. Liquid Water Content and Droplet Sizing Shadowgraph Measuring System for Wind Turbine Icing Detection. *IEEE SENSORS JOURNAL*. 2016; 16: 8.
- [31] Robert J. Moffat. *Describing the Uncertainties in Experimental Results*. Experimental Thermal and Fluid Science. 1988.
- [32] Huda Jawad, Tahseen Husain. Measuring object dimensions and its distances based on image processing technique by analysis the image using sony camera. *Eurasian Journal of Science & Engineering*. 2017. doi: 10.23918/eajse.v3i2p100
- [33] The t-distribution table values retrieved from <https://www.ttable.org/> [Accessed 12 February 2023].

Chapter 6: Conclusions and Recommendation

6.1 Summary and Conclusions

The purpose of this dissertation is to design and implement an integrated system for detecting, tracking, and extracting information about ice accumulation on the leading edge of a cylindrical surface using thermal imaging, image processing, and a heat element. The ultimate goal of this research is to mitigate the negative impacts of icing events by reducing the mass of ice on the surface. The dissertation is organized into several chapters, each of which outlines a specific stage of the project.

Chapter 2 presents a review of various ice detection and mitigation techniques that have been proposed for use on wind turbine blades in cold regions. While some of these techniques demonstrated potential for detecting certain aspects of ice accretion and mitigating its impact, there remained limitations that needed to be addressed in order to effectively integrate these techniques into a cohesive system. Further research was required to enhance the properties and capabilities of these techniques in order to achieve optimal integration.

In Chapter 3, a remote method for estimating the volume of a frozen water droplet on a cold solid surface was presented using thermal imaging and image processing. This method involved the investigation of the effects of temperature, surface roughness, and droplet size on the contact angle. It also demonstrated the efficacy of using thermal imaging and image processing techniques to track and calculate the equivalent diameters of a group of frozen droplets, with promising results. Uncertainty evaluations revealed an average overestimation in droplet volumes of approximately 19%, indicating that the proposed method exhibited acceptable accuracy for a range of applications.

In Chapter 4, a proposed integrated system for detecting, tracking, measuring, and removing ice on the stagnation line of a cylindrical surface was developed. Thermal imaging, heat elements, and image processing algorithms were used to accurately track changes in ice accumulation during an ice event and ice decrease during de-icing. The results of the experiments showed good agreement between thermal and optical images, with low uncertainty values for both ice accumulation tracking and de-icing tracking. The response behaviors of the system were found to be consistent with different average ice thicknesses and cold environmental temperatures. The importance of image processing techniques and the mean threshold approach in improving measurement accuracy and minimizing uncertainty were also highlighted in the chapter. The results demonstrated that the proposed integrated system can assist in reducing de-icing energy consumption and de-icing time.

In Chapter 5, it was demonstrated through a literature review that the geometric relationship between the circular shape of the cylinder and the elliptical shape of the accumulated ice on the surface of the cylinder can be utilized to control the ice thickness at the stagnation line within the minimal limit of the ice thickness at the edge of the heater. This allows for the management of the accumulated ice mass and the heat energy required for de-icing. Experimental results showed that by controlling the ice thickness at the heater's edge, it is possible to reduce the amount of heat energy needed to remove the ice accumulated on the surface of a cylinder.

In conclusion, the research presented in this dissertation represents a novel contribution to the field of ice sensing and mitigation techniques for cylindrical and airfoil surfaces. The results of this study warrant further investigation and exploration in order to fully realize the potential of these techniques and to explore their applications in cold regions.

6.2 Recommendations for Future Studies

In this dissertation, the effectiveness of using thermal imaging, image processing, and heat element techniques to track and extract valuable information about ice accumulation in order to mitigate the ice mass during icing events has been demonstrated. Below, some recommendations and potential avenues for future work are discussed.

1. It is recommended that future research involve testing the proposed integrated system on a large blade scale in order to determine its feasibility and effectiveness in a real-world setting. While the system has been shown to be capable of detecting, tracking, and mitigating accumulated ice at different ice thicknesses and under different cold environmental temperatures using a small-scale cylinder as the target surface, further testing is necessary to confirm its performance on a larger scale.
2. It is recommended that future research explore the potential for enhanced accuracy and precision in thermal imaging through the use of advanced techniques. While the IR camera FLIR-E60 has been shown to provide sufficient information about ice thickness and surface temperature, the potential benefits of incorporating new and advanced techniques warrant further investigation.
3. Develop image algorithms that use reference points along the leading edge to detect the location of the front-line edge of the blade where the stagnation line is located. This is particularly relevant given that the width dimension along the blade may vary, making it challenging to accurately determine the location of the stagnation line using traditional methods. By using reference points and advanced algorithms, it may be possible to more accurately detect the stagnation line and thus improve the effectiveness of ice management strategies.

6.3 A List of Publications and Co-Authorship Statement

- Madi E, Pope K, Huang W, Iqbal T. A review of integrating ice detection and mitigation for wind turbine blades. *Renewable and Sustainable Energy. Rev*; 2019; 103:269-281.
- E. Madi, K. Pope, and W. Huang. Estimating the volume of frozen water droplets on a cold surface during the phase change with thermal image processing. *Measurement*; 2021;183:109907.
- E. Madi, K. Pope, and W. Huang. An integrated ice tracking and mitigation system on the stagnation line of a cylindrical surface based on thermal imaging and electro-thermal elements. *Measurement*; 2022; 199: 111539, 2022.
- E. Madi, K. Pope, and W. Huang. A new method to limit thermal energy required to de-ice the leading edge of a cylindrical surface. (*Submitted to Cold Regions Science and Technology*; 2023).

Appendix A: Measurements and Uncertainty Analysis

Measurement and uncertainty analysis are critical aspects of any experimental study, Accurate estimates of the uncertainty around these measurements can be derived by examining the uncertainty associated with each measurement. Here, we concentrate on examining the uncertainty around the measurements of ice thickness along heater edges (h_e), ice thickness along stagnation lines (h_{SL}), spatial calibration factors (SCF), computing ice thickness along heater edges (h_e), ice mass (m), average power (P_{heater}), and heat energy (Q). Calculations for error propagation and uncertainty are made in accordance with reference [31].

Ice Thickness Along the Heater Edge (h_e)

The results of the measurements and uncertainty analysis of 8 ice thickness samples are presented in Table (A-1). For each sample, 15 measurements were taken at different positions along the heater edge using a digital caliper instrument. The average ice thickness (h_e) for each sample was obtained by summing all 15 measurements using Eq. (A-1). The uncertainty in the caliper measurement (δh_e) was ± 0.05 mm. The variability in the ice thickness (σh_e) was calculated for each ice sample by finding the standard deviation of the 15 measured values using Eq. (A-2). Both uncertainties (δh_e and σh_e) were involved in the calculation of the overall uncertainty (Δh_e) in the average ice thickness, using Eq. (A-3). The results show that the overall uncertainty in the average ice thickness for each ice sample was around ± 0.06 mm. This uncertainty reflects the confidence interval for the true value of the average ice thickness. The similarities in the uncertainties are due to the constant uncertainty in the caliper measurement, as well as the relatively similar variability in the ice thickness for all obtained samples.

$$\text{Average } h_e = \frac{1}{n} \times \sum_i^n \left(\frac{h_e(i)}{n} \right) \quad (A - 1)$$

$$\sigma h_e = \sqrt{\frac{\sum_i^n (h_e(i) - \bar{h}_e)^2}{n - 1}} \quad (A - 2)$$

$$\Delta h_e = \sqrt{\sigma h_e^2 + \delta h_e^2} \quad (A - 3)$$

Table A.1: Measurements of ice thickness at heater edge (h_e) and its uncertainty (Δh_e)

Ice Sample	Average h_e (mm)	σh_e (mm)	δh_e (mm)	Δh_e (mm)
S1	0.32	± 0.04	± 0.05	± 0.06
S2	0.74	± 0.03	± 0.05	± 0.06
S3	1.52	± 0.04	± 0.05	± 0.06
S4	1.71	± 0.04	± 0.05	± 0.06
S5	2.21	± 0.03	± 0.05	± 0.06
S6	2.61	± 0.03	± 0.05	± 0.06
S7	3.23	± 0.03	± 0.05	± 0.06
S8	3.64	± 0.03	± 0.05	± 0.06

Spatial Calibration Factor (*SCF*)

The spatial calibration factor (SCF) [5, 25, 32] in pixels to millimeters for a region of interest (ROI) was determined by placing a ruler with an accuracy of ± 0.5 mm at a distance of 1.5 m in front of a Canon 7D camera. The actual width of the ROI, which was known to be 70 ± 0.5 mm, was measured from the captured image of the ruler's scale. The camera had a resolution of 5184 x 3456 pixels. To ensure measurement accuracy, several factors, including camera settings, position, and focus, as well as environmental conditions such as light and temperature, were held constant throughout the experiment.

Ten image samples of the ruler scale were captured, and the width of the ROI in pixels was measured in each image using the MATLAB image processing tool. The average SCF was then calculated by taking the average of the width values (x_i) obtained from the ten image samples, using Eq. (A-4). The value of (x_i) represents the width in pixels for the current measurement (i), the value (y) represents the actual width in millimeters, and (n) represents the number of measurement samples. The calculated average SCF was found to be 6.537 pixel/mm. Table (A-2) shows the obtained results.

The uncertainty in the SCF value, which is a measure of the degree of error or variability in the calibration factor, was determined by calculating the standard deviation of the SCF values using Eq. (A-5). The uncertainties in the pixel measurement (Δx_i), actual width of the ROI (Δy), and the number of measurements (n) were considered. The resulting ΔSCF value was found to be ± 0.01 pixel/mm.

A t-distribution table was used [33] with 9 degrees of freedom and a confidence level of 95% to determine the range within which the true value of the SCF lies. The t-value was found to be approximately ± 1.833 . Multiplying this value by the standard error of the mean (0.019) gave a confidence interval (CI) of 0.035 pixel/mm. Therefore, it can be concluded with 95% confidence that the true value of the SCF lies between 6.572 pixel/mm and 6.502 pixel/mm.

$$\text{Average SCF} = \frac{1}{n} \times \sum_i^n \left(\frac{x_i}{y} \right) \quad (A - 4)$$

$$\Delta SCF = SCF \times \sqrt{\frac{\sum_i^n \left(\left(\frac{\Delta x_i}{x_i} \right)^2 \right) + \left(\frac{\Delta y}{y} \right)^2}{n}} \quad (A - 5)$$

Table A.2: Samples of measuring average SCF and ΔSCF

Sample	x (pixel)	SCF (pixel/mm)
S1	454	6.486
S2	463	6.614
S3	457	6.529
S4	462	6.600
S5	452	6.457
S6	455	6.500
S7	465	6.643
S8	456	6.514
S9	459	6.557
S10	453	6.471

Ice Thickness Along the Stagnation Line (h_{SL})

The average ice thickness (h_{SL}) along the stagnation line and within the ROI is measured from the captured image using Eq. (A-6), where h_{SL} is average ice thickness, $h_p(i)$ is the number of pixels at line i , n is the number of lines within the ROI, and SCF is the spatial calibration factor. The uncertainty in the measured ice thickness, Δh_{SL} , is derived using the propagation of errors as in Eq. (A-7), where n is the number of measured lines, $h_p(i)$ is the number of pixels at line (i), SCF is the spatial calibration factor, and ΔSCF is the uncertainty in the spatial calibration factor, expressed in pixel units. Since the camera resolution is high and the light distribution inside the cold room is uniform, the uncertainties of the measurements of pixels which are extracted from the images are assumed to be a fixed unit of (± 0.1 pixel). The term $(\partial h_{SL} / \partial SCF)$ is the partial derivative of h_{SL} with respect to SCF , which measures how much the thickness changes with respect to changes in the spatial calibration factor, and it is calculated using Eq. (A-8).

Table (A-3) demonstrates the obtained measurements results of ice samples' thicknesses and uncertainties. It can be concluded that thickness of the ice samples increases as we move from sample S1 to sample S8. The thickness of the samples ranges from 3.44 mm for sample S1 to 19.98

mm for sample S8, with incremental increases in thickness between samples. The uncertainties for each measurement are relatively small, ranging from 0.03 mm to 0.05 mm, indicating a good measurement process.

$$h_{SL} = \frac{1}{n} \times \frac{\sum_i^n h_{p(i)}}{SCF} \quad (A-6)$$

$$\Delta h_{SL} = \sqrt{\left(\frac{\partial h_{SL}}{\partial SCF} \times \Delta SCF\right)^2 + \left(\frac{1}{n} \times \sqrt{\sum_i^n (h_{p(i)})^2}\right)^2} \quad (A-7)$$

$$\frac{\partial h_{SL}}{\partial SCF} = -\frac{\frac{1}{n} \sum_i^n (h_{p(i)})}{SCF^2} \quad (A-8)$$

Table A.3: Measurements of average ice thickness (h_{SL}) along SL and its uncertainty (Δh_{SL})

Sample	Avg h_{SL} (pixel)	Avg h_{SL} (mm)	$\pm \Delta h_{SL}$ (mm)
S1	22.56	3.48	± 0.03
S2	35.75	5.49	± 0.03
S3	51.73	7.97	± 0.03
S4	65.87	10.03	± 0.03
S5	85.17	13.06	± 0.04
S6	98.61	15.08	± 0.04
S7	117.36	17.98	± 0.05
S8	131.09	20.03	± 0.05

Computing Ice Thickness Along the Heater Edge (h_e)

The computed average ice thickness (h_e) along the heater's edge is obtained using the formula of Eq. (A-9), where h_{SL} is average ice thickness along the SL, the radius of the cylinder is (r), the length of the cylinder (L_{SL}), and (θ) is the heating angle. To obtain the propagation of error of h_e , the formula in Eq. (A-10) is used, where ($\partial h_e / \partial r$) is the partial derivative for h_e with respect

to each r obtained by Eq.(A-11), $(\partial h_e/\partial h_{SL})$ is the partial derivative for h_e with respect to each h_{SL} obtained using Eq. (A-12), and $(\partial h_e/\partial \theta)$ is the partial derivative for h_e with respect to each θ obtained using Eq. (A-13). The formula of propagation of error in Eq. (A-10) calculates the value of Δh_e based on the given values of $r = 127.23 \pm 0.05$ mm, and $\theta = 65^\circ \pm 0.03^\circ$. The values of ice thickness, h_{SL} , and Δh_{SL} change according to ice samples and they are listed in Table (A-4). The computed results of h_e and Δh_e are listed in Table (A-4).

The results of h_e and Δh_e suggest that the ice thickness (h_e) along the heater's edge increases as the ice thickness (h_{SL}) along the SL increases, which is expected. The values of h_e ranges from 0.60 for S1 to 3.01 for S8, with a corresponding range of uncertainty (Δh_e) of 0.05. The consistent value of Δh_e for all ice samples indicates that the method used to calculate the uncertainty is robust and reliable. The propagation of error formula used in this study provides an efficient and accurate method to estimate the uncertainty in h_e based on the given parameters.

$$\bar{h}_e = \sqrt{\frac{r^2(r + \bar{h}_{SL})^2(1 + \tan(\theta)^2)}{r^2 + (r + \bar{h}_{SL})^2 \tan(\theta)^2}} - r \quad (\text{A} - 9)$$

$$\Delta h_e = \sqrt{\left(\frac{\partial h_e}{\partial r} \times \Delta h_r\right)^2 + \left(\frac{\partial h_e}{\partial h_{SL}} \times \Delta h_s\right)^2 + \left(\frac{\partial h_e}{\partial \theta} \times \Delta \theta\right)^2} \quad (\text{A} - 10)$$

$$\frac{\partial h_e}{\partial r} = \left(r \times (r + \bar{h}_{SL})^2 \times (1 + \tan\theta^2) / (r^2 + (r + \bar{h}_{SL})^2 \times \tan\theta^2) \right)^{1.5} - 1 \quad (\text{A} - 11)$$

$$\frac{\partial h_e}{\partial h_{SL}} = \left(r^2 \times (r + \bar{h}_{SL}) \times (1 + \tan\theta^2) / (r^2 + (r + \bar{h}_{SL})^2 \times \tan\theta^2) \right)^{1.5} \quad (\text{A} - 12)$$

$$\frac{\partial h_e}{\partial \theta} = \left(r^2 \times (r + \bar{h}_{SL})^2 \times (2 \times \tan\theta) / (r^2 + (r + \bar{h}_{SL})^2 \times \tan\theta^2) \right)^{1.5} \quad (\text{A} - 13)$$

Table A.4: The computed h_e and its uncertainty Δh_e based on the propagation of error.

Sample	h_{SL}	$\pm\Delta h_{SL}$	h_e	$\pm\Delta h_e$
S1	3.48	± 0.03	0.60	± 0.05
S2	5.49	± 0.03	0.93	± 0.05
S3	7.97	± 0.03	1.33	± 0.05
S4	10.03	± 0.03	1.64	± 0.05
S5	13.06	± 0.04	2.08	± 0.05
S6	15.08	± 0.04	2.36	± 0.05
S7	17.98	± 0.05	2.75	± 0.05
S8	20.03	± 0.05	3.01	± 0.05

Computing Ice Mass (m_{ice})

The ice mass (m) is obtained using the formula of Eq. (A-14), where h_s = ice thickness, r = the radius of the cylinder, L_s = the length of the cylinder, and ρ = the density of the ice. To derive the propagation of error formula, the partial derivative of each variable has to be derived first. Eq. (A-15) is the partial derivative of m with respect to h_{SL} . Eq. (A-16) is the partial derivative of m with respect to r . Eq. (A-17) is the partial derivative of m with respect to L_s , and Eq. (A-18) is the partial derivative of m with respect to ρ . Then to calculate the uncertainty (Δm) in the mass (m), these partial derivatives are plugged into Eq. (A-19), where $\Delta r = \pm 0.0005$ m, $\Delta L_{SL} = \pm 0.001$ m, and $\Delta \rho = \pm 0.2$ kg/m³ are the uncertainties of $r = 0.127$ m, $L_{SL} = 0.61$ m, and $\rho = 917.1$ kg/m³, respectively. The values of ice thickness, h_{SL} , and its uncertainty, Δh_{SL} , change according to ice sample and they are listed in Table (A-5). The calculated ice mass, m , and its uncertainty, Δm , are shown in Table (A-5).

From the results in Table (A-5), it can be seen that as the ice thickness and mass of the samples increase, the uncertainties in the mass also increase. The uncertainty in the calculated mass ranges from ± 0.004 kg for the smallest ice sample (S1) to ± 0.009 kg for the largest ice sample

(S8). These uncertainties are relatively small compared to the mass of the ice samples, which indicates that the calculated mass values are precise.

$$m_{ice} = h_{SL} \times \left[\frac{\pi \times r \times L_{SL} \times \rho}{2} \right] \quad (A - 14)$$

$$\frac{\partial m_{ice}}{\partial h_{SL}} = \left[\frac{\pi \times r \times L_{SL} \times \rho}{2} \right] \quad (A - 15)$$

$$\frac{\partial m_{ice}}{\partial r} = h_{SL} \times \left[\frac{\pi \times L_{SL} \times \rho}{2} \right] \quad (A - 16)$$

$$\frac{\partial m_{ice}}{\partial L_{SL}} = h_{SL} \times \left[\frac{\pi \times r \times \rho}{2} \right] \quad (A - 17)$$

$$\frac{\partial m_{ice}}{\partial \rho} = h_{SL} \times \left[\frac{\pi \times r \times L_{SL}}{2} \right] \quad (A - 18)$$

$$\Delta m_{ice} = \sqrt{\left[\left(\frac{\partial m_{ice}}{\partial h_{SL}} \times \Delta h_{SL} \right)^2 + \left(\frac{\partial m_{ice}}{\partial r} \times \Delta r \right)^2 + \left(\frac{\partial m_{ice}}{\partial L_{SL}} \times \Delta L_{SL} \right)^2 + \left(\frac{\partial m_{ice}}{\partial \rho} \times \Delta \rho \right)^2 \right]} \quad (A - 19)$$

Table A.5: Ice mass (m_{ice}) and uncertainties for each ice sample

Sample	h_{SL} (m)	$\pm \Delta h_{SL}$ (m)	m_{ice} (kg)	$\pm \Delta m_{ice}$ (kg)
S1	0.00344	± 0.00003	0.38909	± 0.00358
S2	0.00545	± 0.00003	0.61271	± 0.00391
S3	0.00789	± 0.00003	0.89111	± 0.00445
S4	0.01004	± 0.00003	1.12143	± 0.00501
S5	0.01298	± 0.00004	1.46021	± 0.00657
S6	0.01503	± 0.00004	1.68607	± 0.00715
S7	0.01789	± 0.00005	2.01031	± 0.00868
S8	0.01998	± 0.00005	2.23952	± 0.00929

Heater Power (P_{heater})

The power required to operate heater beds is an essential factor to consider for their effective functioning. It is achieved by measuring the voltage and current. The environmental conditions within the cold room were considered during all the power measurements to ensure stability. The temperature was maintained at -15°C , and the wind speed was 4 m/s during the measurements.

To obtain stable measurements, the heaters were operated for a few seconds until the heat produced became relatively constant. Table (A-6) lists 10 measurements of voltage and current samples which were taken at different stages of time while the heaters continued to operate. A Digital multimeter Fluke 789, with an accuracy of 0.7%, was used for measuring the voltage, while a Fluke clamp meter 355, with an accuracy value of 1.5%, was used for measuring the current.

The variability uncertainty in the voltage was obtained using Eq. (A-20). The variability uncertainty in the current was obtained using Eq. (A-21). The overall uncertainty for the voltage was computed using Eq. (A-22) and found to be (± 0.14 V), while the overall uncertainty for the current was computed using Eq. (A-23) and found to be (± 0.04 A). The power (P) for each sample was calculated using Eq. (A-24), and the uncertainty of power (ΔP) for each sample was determined using Eq. (A-25). The measured and calculated values are listed in Table (A-6). The average power was found to be (1271.1 W) and a standard deviation was obtained using Eq. (A-26) and was found to be $\Delta P = \pm 4.95$ W. The standard error of the mean (SEM) was calculated using Eq. (A-27) and it was found to be 1.57 W. To determine the confidence level, a t-distribution table was used [33] with 9 degrees of freedom and a 95% confidence level. The t-value was found to be (± 1.833). The formula in Eq. (A-28) was used to calculate the confidence interval.

Substituting the values for P, ΔP, and SEM, the confidence interval (CI) was found to be (1273.95 W, 1268.22 W).

Therefore, based on the 10 measured values and the associated uncertainty using the propagation of error method, a 95% level of confidence can be obtained that the true average power required to operate the heat beds is between 1268.22 W and 1273.95 W. This level of confidence takes into account the measurement accuracy and variability of the voltage and current instruments used in the experiment, as well as the stability of the environmental conditions in the cold room.

$$\sigma V = \sqrt{\frac{\sum_i^n (V_i - \bar{V})^2}{n - 1}} \quad (A - 20)$$

$$\Delta V = \sqrt{(\sigma V^2 + (\bar{V} \times \delta V)^2)} \quad (A - 21)$$

$$\sigma I = \sqrt{\frac{\sum_i^n (I_i - \bar{I})^2}{n - 1}} \quad (A - 22)$$

$$\Delta I = \sqrt{(\sigma I^2 + (\bar{I} \times \delta I)^2)} \quad (A - 23)$$

$$P_{heater} = V \times I \quad (A - 24)$$

$$\Delta P = \sqrt{((\Delta V \times \bar{I})^2 + (\bar{V} \times \Delta I)^2)} \quad (A - 25)$$

$$\sigma P = \sqrt{\frac{\sum_i^n (P_i - \bar{P})^2}{n - 1}} \quad (A - 26)$$

$$SEM = \frac{\sigma P}{\sqrt{n}} \quad (A - 27)$$

$$CI = \bar{P} \pm t \times SEM \quad (A - 28)$$

Table A.6: Measurements of V, I, and calculated P and ΔP for each sample

Sample	V (V)	I (A)	P (W)	$\pm\Delta P$ (W)
1	110.00	11.55	1271.10	± 4.70
2	110.42	11.46	1271.08	± 4.70
3	110.09	11.54	1271.09	± 4.69
4	110.28	11.49	1271.09	± 4.70
5	110.37	11.47	1271.08	± 4.69
6	110.24	11.50	1271.10	± 4.69
7	110.05	11.55	1271.09	± 4.69
8	110.33	11.48	1271.08	± 4.70
9	110.14	11.52	1271.08	± 4.69
10	110.19	11.51	1271.09	± 4.69

Heat Energy (Q)

The heat energy (Q) required to de-ice each ice sample was calculated using Eq. (A-29), using the average power (P) and time of de-icing (t). The uncertainty in the heat energy required to de-ice various ice samples was estimated by using the propagation of error method. The uncertainties in P and t were propagated using Eq. (A-30) to estimate the uncertainty in Q , where ΔP and Δt represented the uncertainties in P and t , respectively. The average power of the heating element was found to be 1271.1 ± 4.95 W, which generated a relatively constant heat. The de-icing time was obtained from the thermal images captured at a frame rate of 30 f/s. Thus, the accuracy of time was assumed to be $1/30$ s or 0.033 s.

Table (A-7) shows the heat energy (Q) required to de-ice 8 samples of different ice masses accumulated over a cylinder surface. Each sample has an associated uncertainty (ΔQ) in kJ and percentage uncertainty ($\Delta Q\%$) calculated as a percentage of the measured value. The results in Table (A-7) show that the heat energy required to remove the ice mass increases as the ice mass accumulated over the cylinder surface increases. This is expected, as larger ice mass will require

more heat energy to melt and remove. The percentage uncertainty for each sample is constant at 0.39%, which means that the uncertainty in the measured values is consistent across all samples. This is a good indication that the measurements were taken using a consistent and reliable method.

$$Q = P * t \quad (A - 29)$$

$$\Delta Q = \sqrt{[(t^2 \times \Delta P^2) + (P^2 \times \Delta t^2)]} \quad (A - 30)$$

Table A-7: Heat energy (Q) and uncertainties for each sample

Sample	t (s)	Q (kJ)	±ΔQ (kJ)	ΔQ%
S1	38	48.378	±0.19	0.39%
S2	61	77.531	±0.30	0.39%
S3	93	118.203	±0.46	0.39%
S4	121	153.891	±0.60	0.39%
S5	166	210.486	±0.82	0.39%
S6	200	254.200	±0.99	0.39%
S7	255	324.405	±1.26	0.39%
S8	303	385.113	±1.50	0.39%